Time-Dependent Ventilated Thermocline

by

Zhengyu Liu

B.S. Nanjing Institute of Meteorology,1982

M.A. Institute of Atmospheric Physics, Academia Sinica,1984

Submitted in partial fulfillment of the
requirements for the degree of

Doctor of Philosophy
at the

MASSACHUSETTS INSTITUTE OF TECHNOLOGY

and the

WOODS HOLE OCEANOGRAPHIC INSTITUTION

September 1991

Signature of Author .....
Joint Program in Physical Oceanography
Massachusetts Institute of Technology
Woods Hole Oceanographic Institution
September, 1991

Certified by .....
Joseph Pedlosky
Thesis Advisor

Accepted by .....
Larry Pratt
Chairman, Joint Committee for Physical Oceanography
Massachusetts Institute of Technology
Woods Hole Oceanographic Institution

Time-Dependent Ventilated Thermocline

by
Zhengyu Liu

Submitted in partial fulfillment of the requirements for the degree of Doctor of Philosophy
at the Massachusetts Institute of Technology and the Woods Hole Oceanographic Institution
September, 1991

Abstract

In this thesis, I study the time-varying behavior of a ventilated thermocline with basin scales at annual and decadal time scales. The variability is forced by three external forcings: the wind stress (chapter 3), the surface heat flux (chapter 4) and the upwelling along the eastern boundary (chapter 5). It is found that the thermocline variability is forced mainly by wind in a shadow zone while mainly by surface buoyancy flux in a ventilated zone.

A two-layer planetary geostrophic model is developed (chapter 2) to simulate a thermocline. The model includes some novel physical mechanisms. Most importantly, it captures the essential feature of subduction; it also is able to account for a time-varying surface temperature. The equation for the interface is a quasi-linear equation, which can be solved analytically by the method of characteristics.

The effect of a varying Ekman pumping is investigated. In a shadow zone, it is found that the driving due to the Ekman pumping is mainly balanced by the propagation of planetary waves. However, in a ventilated zone, the cold advection of subducted water plays the essential role in opposing the Ekman pumping. The different dynamics also results in different thermocline variability between the two zones. After a change of Ekman pumping, in the shadow zone, since the baroclinic Rossby wave responds to a changing Ekman pumping slowly (in years to decades), an imbalance arises between the Rossby wave and the Ekman pumping, which then excites thermocline variability. However, in the ventilated zone, both the advection and the Ekman pumping vary rapidly after a barotropic process (about one week) to reach a new steady balance, leaving little thermocline variability. In addition, the evolution of the thermocline and circulation are also discussed.

Furthermore, with a periodic Ekman pumping, it is found that linear solutions are approximate the fully nonlinear solution well, particularly for annual forcings. However, the linear disturbance is strongly affected by the basic thermocline structure and circulation. The divergent group velocity field, which is mainly caused by the divergent Sverdrup flow field, produces a decay effect on disturbances. The mean thermocline structure also strongly affects the relative importance of the local Ekman pumping and remote Rossby waves. As a result, in a shadow zone, local response dominates for a shallow interface while the remote Rossby wave dominates for a deep interface. With a strong decadal forcing, the nonlinearity becomes important in the shadow zone, particularly in the western part. The time-mean thermocline which results, becomes shallower than the steady thermocline under the mean Ekman pumping.

Then, we investigate the effect on the permanent thermocline by a moving outcrop line, which simulates the effect of a varying surface heat flux. The two layer model is modified by adding an (essentially passive) mixed layer atop. The outcrop line and the mixed layer depth are specified. It is found that, opposite to a surface wind stress, a surface buoyancy flux causes strong variability in the ventilated zone through subducted water while it affects the shadow zone very little. Furthermore, two regimes of buoyancy-forced solution are found. When the outcrop line moves slowly, the solutions are non-entrainment solutions. For these solutions, the surface heat flux is mainly balanced by the horizontal advection. The mixed layer is never entrained. The time-mean thermocline is close to the steady thermocline with the time-mean outcrop line. When the outcrop line moves southward rapidly during the cooling season, the solutions become entrainment solutions. Now, deep vertical convection must occur, because the horizontal advection in the permanent thermocline is no longer strong enough to balance the surface cooling. The mixed layer penetrates rapidly such that water mass is entrained into the mixed layer through the bottom. The time-mean thermocline resembles the steady thermocline with the early spring mixed layer, as suggested by Stommel (1979). The local variability in the permanent thermocline is most efficiently produced by decadal forcings.

Finally, two issues about the waves radiating from the eastern boundary are discussed. The first is the penetration of planetary waves across the southern boundary of a subtropical gyre. We find that the wave penetration across the southern boundary is substantially changed by the zonal variation of the thermocline structure. The zonal variation alters both the effective β and the wave front orientation. As a result, the wave penetration differs for interfaces at different depths. For an interface near the surface, part of the waves penetrate into the equatorial region. For middle depths, most waves will be trapped within the subtropical gyre. In contrast, for deep depths, all waves penetrate southward.

The second issue of the eastern boundary waves mainly concerns with the breaking of planetary waves in the presence of an Ekman pumping and the associated two-dimensional mean flow. It is found that the breaking is affected significantly by an Ekman pumping and the associated mean flow. With an Ekman pumping, downwelling breaking is suppressed and the breaking time is delayed; upwelling breaking is enhanced and their times are shortened. The breaking times and positions are mainly determined by the maximum vertical perturbation speed while the intensity of the breaking front mainly depends on the amplitude of the perturbation. The intensity of a breaking front increases with the amplitude of the forcing, but decreases with the distance from the eastern boundary. The orientation of a breaking front is overall in northeast-southwest ($x \sim -1/f^2$).

Thesis Advisor

Joseph Pedlosky

Professor of Physical Oceanography

Acknowledgments

I am deeply indebted to my advisor Joseph Pedlosky, who has guided me through these years with a great deal of patience. His deep insight in physics and pin-point criticism have helped me very much. In particular, I would like to thank him for Chapter 4 of this thesis, which was motivated by his persistent enthusiasm.

I would like to thank other members of my thesis committee: Drs. Carl Wunsch, Glenn Flierl, Dave Chapman and Rui Xin Huang. They have always been very helpful to me over the past few years. In addition, I am grateful to many other professors of the MIT/WHOI joint program. I have had very useful discussions with Drs. Jim Price and Ken Brink on the puzzling mixed layer; Dr. Bill Young was my advisor for the first summer and has since offered me advice from time to time; Dr. Nelson Hogg willingly accepted the Chairmanship of my thesis defense committee; Drs. Glenn Flierl and Paola Rizzoli generously let me use their computers. I would also like to thank Dr. Toshio Yamagata for introducing me to the field of physical oceanography.

I have spent four excellent years in the Joint Program. I have learned many things in addition to physical oceanography. I have had many wounderful friends, among whom are Dave Walsh, Jamie McLaren, Susan Wijffels, Molly Baringer, Antonietta Capotondi, Cecilie Mauritzen, Shuntai Zhou, and Changshen Chen. Their friendship and help have been an essential part of my life. The staff of the education office at WHOI, the Center for Meteorology and Physical Oceanography at MIT, and the International Student Office at MIT have given me much help. I like this program. Before my leave, the only regret is that I should have come here earlier.

Diana Spiegel, Steve Meacham and Roberta Young have offered me a lot of assistance with the computers. The patient tutoring of Anne-Marie Michael has made the typing of the thesis possible.

Most of all, I thank my parents and my grandmother. For so many years, wherever and whenever needed, their love and care always accompanied me and gave me strength. I owe so much to my wife, Huixia Wu. Without her understanding and support, this thesis would not have been possible.

This thesis is supported by National Science Foundation, Division of Atmospheric Sciences.

Table of Contents

Chapter 1
Introduction

1 Motivation

Recently, knowledge about steady thermocline circulation has been substantially improved by the potential vorticity homogenization theory (Rhines and Young, 1981) and the ventilated thermocline theory (Luyten, Pedlosky and Stommel, 1983). Relatively little progress has been made towards understanding time-dependent thermocline circulation.

On the other hand, observations show that there is strong variability in the surface wind and surface heat flux. In addition, strong variability is also observed along the eastern boundary region. For example, Fig.1.1 presents a recent estimate of the annual cycle of the Ekman pumping volume integrated along a latitude belt in the Pacific (Levitus, 1988). One sees that the strength of the annual surface Ekman pumping changes more than 50 percent from its mean. Qiu and Joyce (1991) also show that, at interannual time scales (about 4 years), in the subtropical North Pacific, the intensity of the wind stress exhibits variation of about 20 percent from its mean (see Fig.1.2).

The annual surface heat flux changes significantly as well. The resulting mixed layer depth in the northern part of a subtropical gyre varies from 25 meters in summer (see the North Atlantic and North Pacific in Fig.1.3b) to more than 200 meters in winter (Fig.1.3a) (Levitus, 1982). At the same time, the surface density also varies substantially. Fig.1.3c and d (from Levitus, 1982) present the surface density of the world ocean in spring and fall respectively. The dot-connected lines mark the 24 σ_t in the North Pacific and the 26 σ_t in the North Atlantic. Both isolines vary from about 25 N^o to 50 N^o from spring to fall. This north-south migration distance is about the width of the subtropical gyres in both oceans.

Finally, interannual variability of isopycnals along the eastern boundary has been observed. Kessler (in section 4b, 1989) has reported about a ± 15 meters anomaly of the 20^oC isotherm along the eastern boundary of the tropic and subtropical North Pacific (Fig.1.4). Near the eastern boundary in middle and high latitudes (at the ocean Station P at $50^oN, 145^oW$), Tabara *et. al*

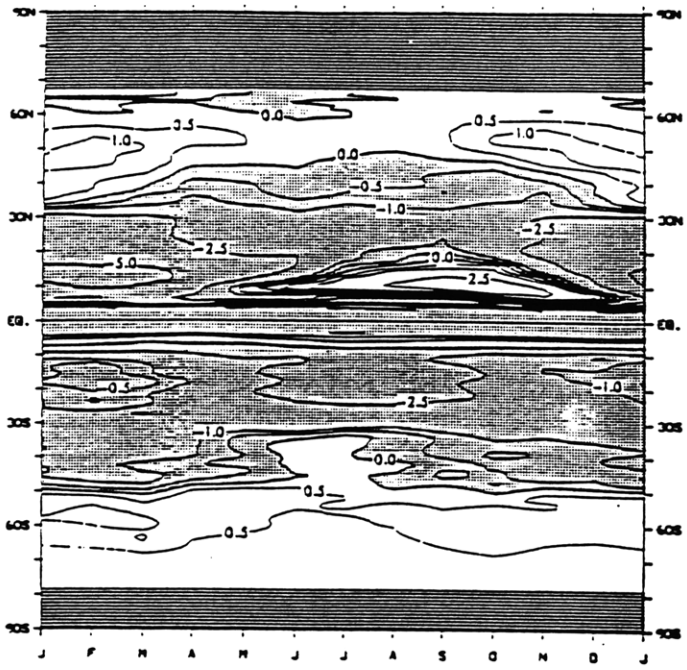

Figure 1.1: The annual variation of the Pacific Ocean zonally integrated vertical Ekman volume flux ($10^6 m^3 s^{-1}$) at the base of the Ekman layer per one-degree latitude belt as a function of month and latitude. Shading indicates a negative flux (downward). (After Levitus, 1988, Fig. 6)

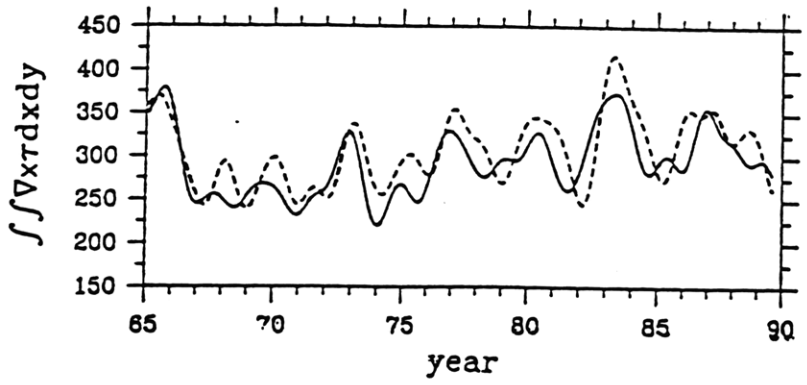

Figure 1.2: The interannual variation of wind stress curl. Time series of the wind stress curl intensity over the tropical (solid line) and the subtropical (dashed line) ocean gyres. In the calculation, the solid (dashed) line in the figure is obtained by integrating the positive (negative) wind stress curl values in the region of $0^o - 20^oN$ ($10^o - 30^oN$) based on the low-pass filtered FSU wind data. Units in $4 \times 10^3 N/m$ (After Qiu and Joyce, 1991).

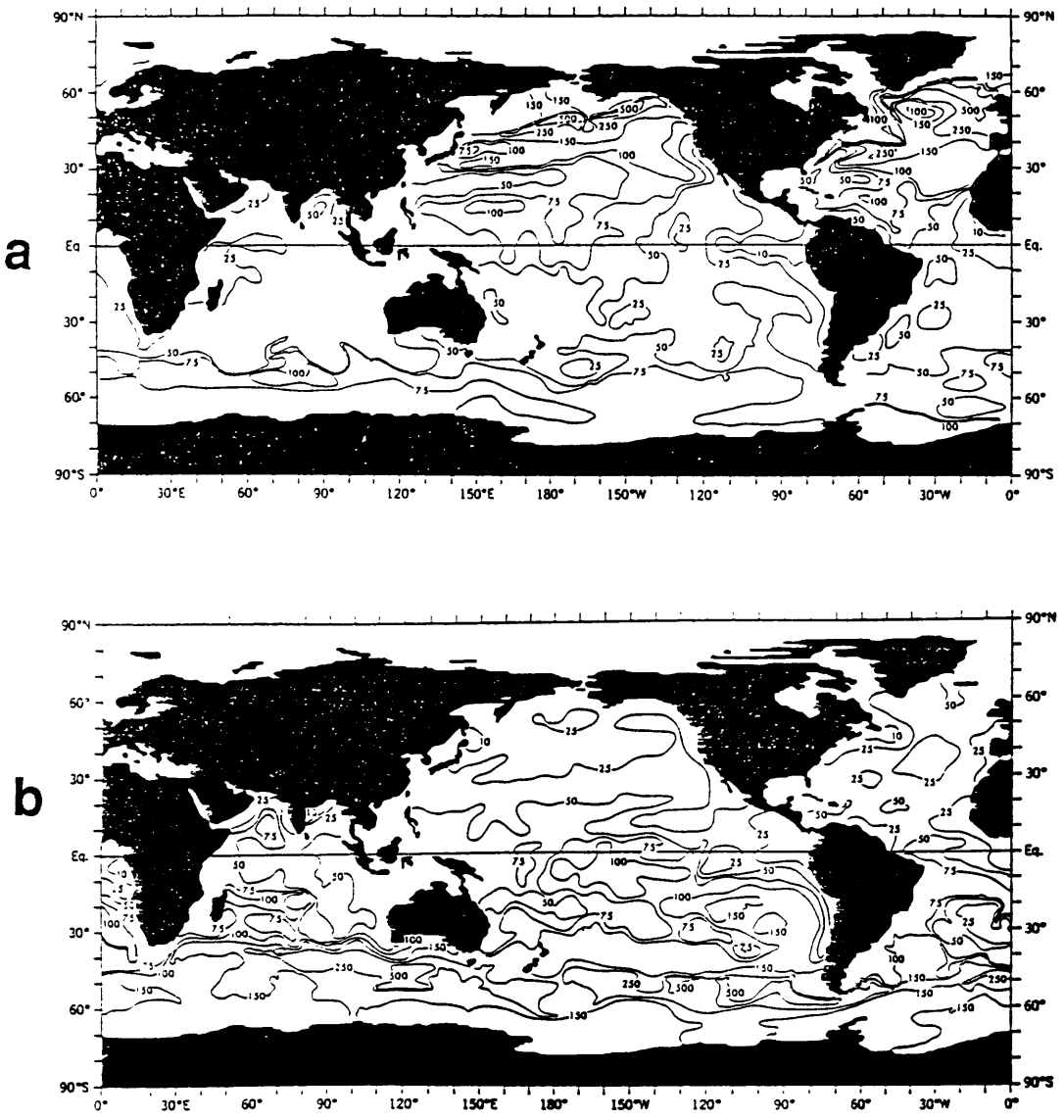

Figure 1.3: The mixed layer depths based on a temperature criterion of $0.5°C$ for (a) March and (b) September. (after Levitus, 1982). To be continued.

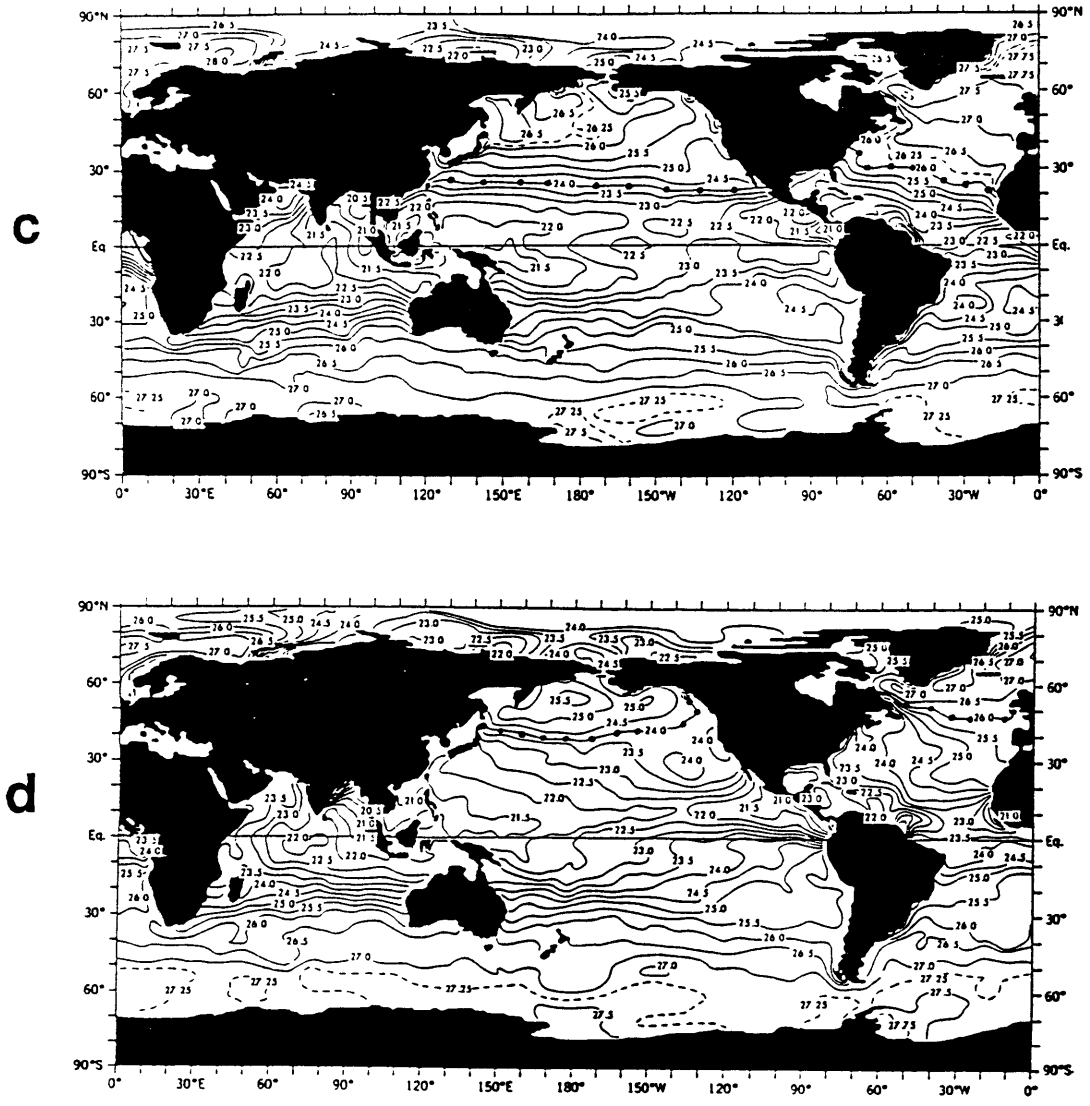

Figure 1.3: (continued) The sea surface density (sigma-t ($10^{-3}g/cm^3$)) for (c) the mean of **February, March and April** and (d) the mean of August, September and October. The dot-connected lines **represent the 24 and 26** sigma-t lines in the North Pacific and North Atlantic respectively. (after Levitus, 1982)

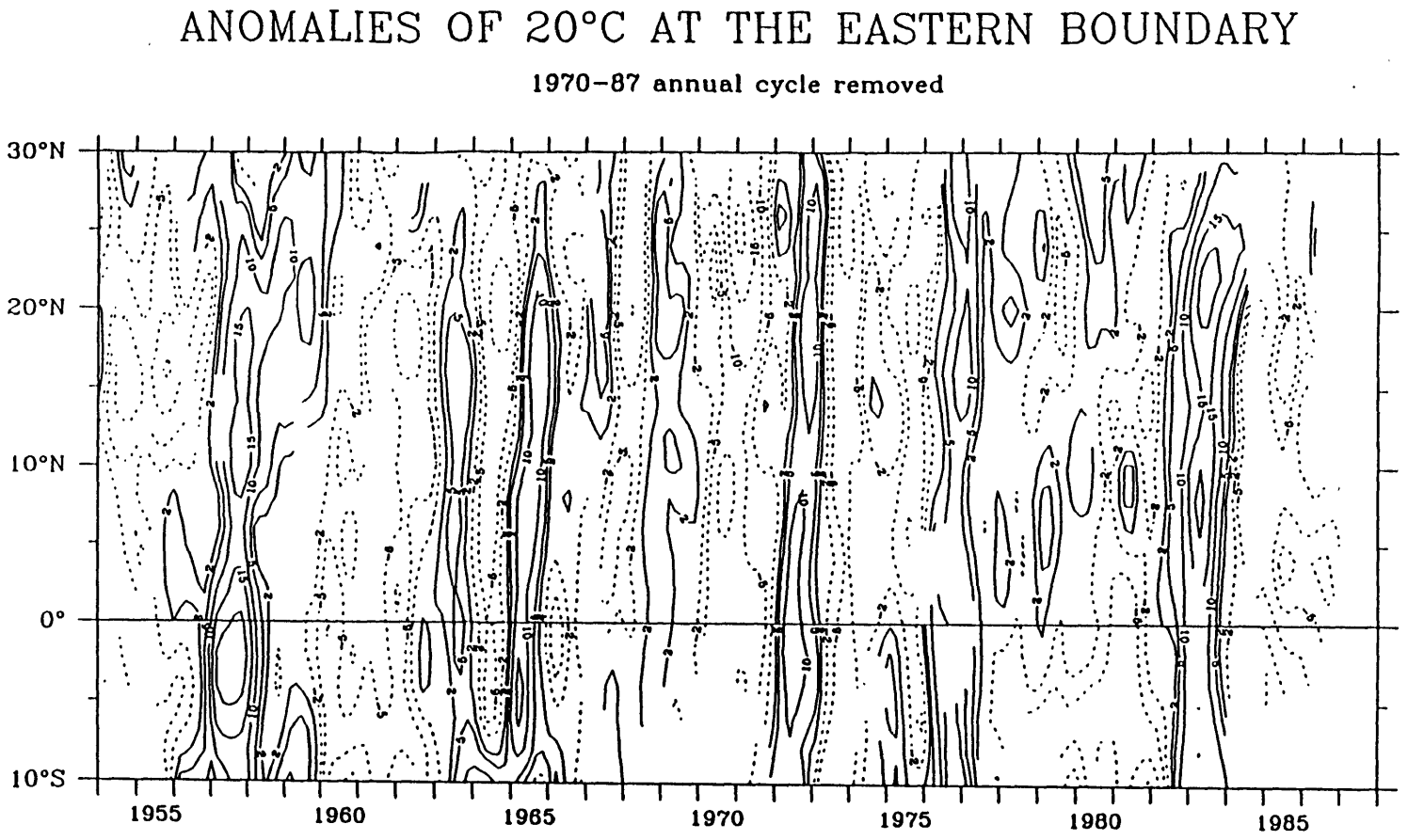

Figure.1.4: The interannual anomalies of $20°C$ depth (m) along the American coast. Contours are given at $\pm 2, 5, 10, 15$ and 20 m, with positive (deep) anomalies solid, negative (shallow) anolalies dashed. (After Kessler, 1989).

(1986) have found variability of isopycnals of about $\pm$10 meters at the annual period and about $\pm$50 meters at interannual periods (about 5 years) (Fig.1.5). Under such a strong variability in the external forcing, one naturally wonders how the ocean responds to the variable forcing; what the main physical mechanisms are behind the thermocline evolution; what the relation is between the time-mean circulation and the thermocline predicted by a steady thermocline theory with the time-mean forcing. This thesis is an attempt towards understanding the physics of the time-varying oceanic circulation. We choose to concentrate on basin scale variability with short climate time scales (years to decades).

To highlight the basic physics, a simple theoretical model is developed in chapter 2. The effect of a variable wind forcing is discussed in chapter 3 and the variability caused by a variable surface heat flux is investigated in chapter 4. In chapter 5, we will study some dynamic aspects relevant to upwelling and downwelling along the eastern boundary.

Theoretically, there are several difficulties in the problem of the externally forced basin-scale thermocline circulation. One is the strong nonlinearity caused by the advection of the density field, which also occurs in the study of steady general oceanic circulations. Another arises from the lateral boundaries. Within the geometry of an ocean basin, the basic flows are no longer one dimensional. Therefore, classical theories for disturbances in the presence of a parallel flow can not be applied directly to the study here. In addition, as far as a variable surface heat flux is concerned, there is an extra difficulty. Because the varying surface heat flux causes a strong variation of the mixed layer or a seasonal thermocline, the the thermocline is closely coupled with a mixed layer (Woods, 1985), which is strongly turbulent and whose dynamics is not well understood, particularly at interannual time scales.

Finally, it should be pointed out that the variability of a basin scale circulation can also be affected by the eddies produced by instabilities of the basic circulation. Recent numerical studies (Cox,1985; Cox,1987) suggest that these eddies are important for the transport of physical quantities on the basin scale circulation. This effect will not be considered in the thesis.

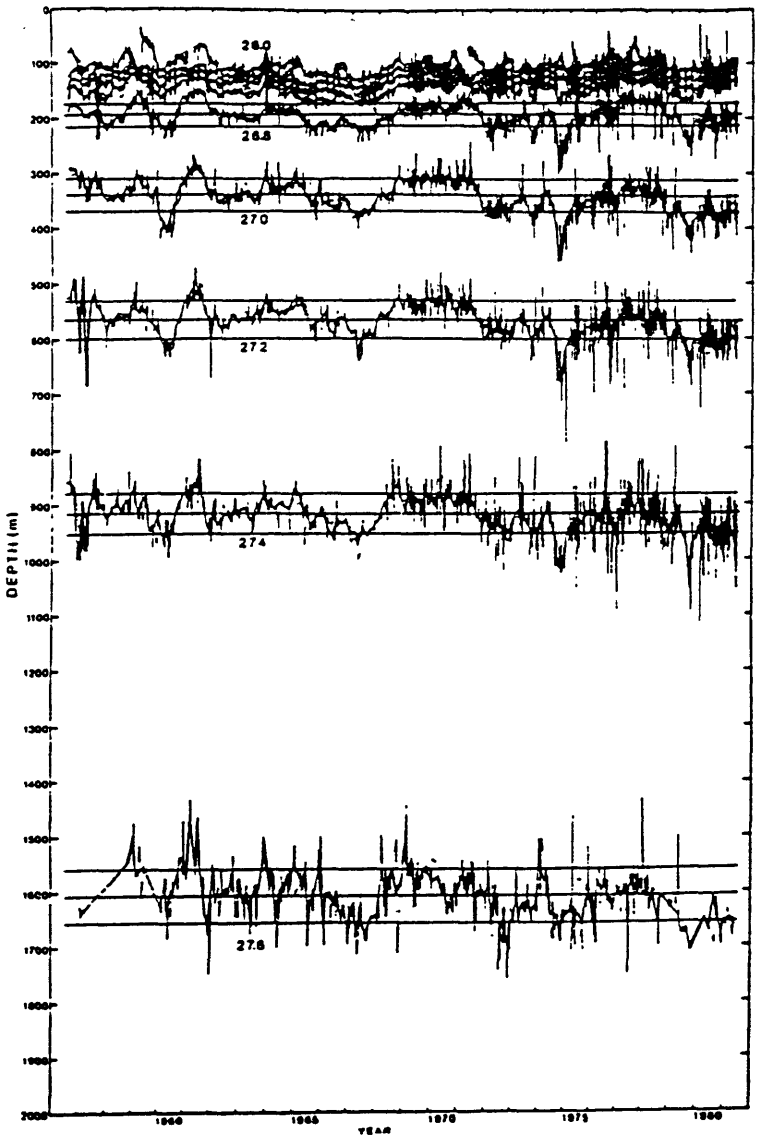

Figure 1.5: The amplitudes of annual and interannual variations. Depth (m) of isopycnal surfaces (σ_t = 26.0 – 27.6) for Station P. The heavy straight dashed and light lines represent, respectively, the means and standard deviations. The heavy lines through the data points denote monthly means. The values for σ_t = 27.6) are based on hydrographic-cast data only, whereas the others are based on STD data as well. "Annual" cycle has not been removed from the dataset. (after Tabara *et.al.*, 1986).

2 Observations of Annual and Interannual Variability

Observing annual and interannual variability in the basin scale has remained to be an extraordinarily difficult task for oceanographers (Wunsch, 1991). Nevertheless, in the last decade or so, great efforts have been made towards observing annual and interannual variability. Preliminary results are encouraging, which at least give us a sense of the long-term variability of the thermocline. Most of the data analyzed so far were adopted from XBT or hydrographic (CTD) surveys in the North Pacific and the North Atlantic. Annual and interannual signals have been clearly identified in most of the studies. Regarding these observations, we will concern ourselves with the observations possibly relevant to the thesis. The questions that we are interested in are as follows: a) How strong are these long-term signals? b) Is there any evidence of baroclinic Rossby waves? What are their space and time scales? d) What are the energy sources and generating mechanisms for the observed anomalies?

Amplitude

In mid-latitudes, annual variations are clear in the upper 500 m, with the strongest anomalies occurring in the upper 200 m (Emery et al, 1984). The latter anomalies are mainly caused by the seasonal thermocline. At a depth of about 300 m, typical annual vertical displacements of isopycnal surfaces (or isothermal surfaces) have maximum amplitude of about $\pm$10 meters, with the corresponding steric sea level changes of $\pm$1 cm to $\pm$2 cm (e.g. Kang and Magaard,1980; Price and Magaard, 1983; White and Saur, 1981). Fig.1.5 (from Tabara *et. al*, 1986) shows an example of time series of isopycnals in the Northeastern Pacific (Station P). The annual signal can be clearly seen in the upper 300 meters of the ocean. Observations also demonstrate that the amplitude usually is stronger in the western part of the ocean than in the central and eastern part of the ocean (Talley and White, 1987).

Interannual variations of isopycnals can often reach $\pm$50 meters in the main thermocline, with equivalent steric sea level changes of about $\pm$ 5 cm (White and Tabara,1987; Tabara *et. al*,1986; White,1983; Talley and White, 1987; Roemmich and Wunsch,1984; Qiu and Joyce,1991). Differing from the rapid vertical decay of annual signals, interannual anomalies extend deeper than the

bottom of the thermocline (greater than 1500 meters) as shown in Fig.1.5. Thus, within and below the middle and lower thermocline, interannual variability is much stronger than the annual one (Tabara *et. al*,1986;Roden, 1977). Spatially, interannual variations change in a fashion similar to annual variations; i.e., they are stronger in the western part than in the central and eastern part. Annual and interannual variability of the eighteen degree water in the North Atlantic has also been observed. It was found that the interannual variation is much stronger than the annual variation. This feature can be identified in Fig.1.6 (Talley and Raymer, 1982).

Rossby waves, space and time scales

Most studies of the long-term anomalies have concentrated on identifying baroclinic Rossby waves. Westward propagation of disturbances is salient in most observations except in the Kuroshio extension and the North Atlantic Current. In the southern part of subtropical gyres (roughly south of 30^oN), baroclinic Rossby waves have been clearly identified at annual as well as interannual periods in both the North Pacific and North Atlantic. For instance, annual Rossby waves of the first baroclinic mode have been found in the southern part of the Eastern North Pacific (e.g. White and Saur,1981;Kessler,1989). Kang and Magaard (1980) also found annual Rossby waves in the northern part of the North Pacific. The annual Rossby waves are found to account for more than fifty percent of the total annual variability. Their zonal wave lengths range from 300 km to 1500 km; their westward propagation speeds vary from 1 cms^{-1} to 5 cms^{-1}. Usually the waves propagate their phase towards the northwest, implying a radiation of energy southwestward. Nevertheless, interannual baroclinic Rossby waves are observed clearly only in the southern parts of both the North Pacific and the North Atlantic (Price and Magaard,1980; 1986; White and Saur, 1983). Spectral analyses show peaks at about 10 years and 6 years. The dominant wavelengths vary from 1500 km to 3000 km.

For baroclinic Rossby waves, although analyses about wave amplitudes and wave vectors often agree with each other, analyses of wave phases have reached two totally opposite conclusions. Some analyses show that the phase increases in randomness westward (e.g. Kang and Magaard,1980), while others claim to have found deterministic phases (e.g.,White and Saur,1983; White and Tabara, 1987). At this stage, it seems unclear which statement is correct.

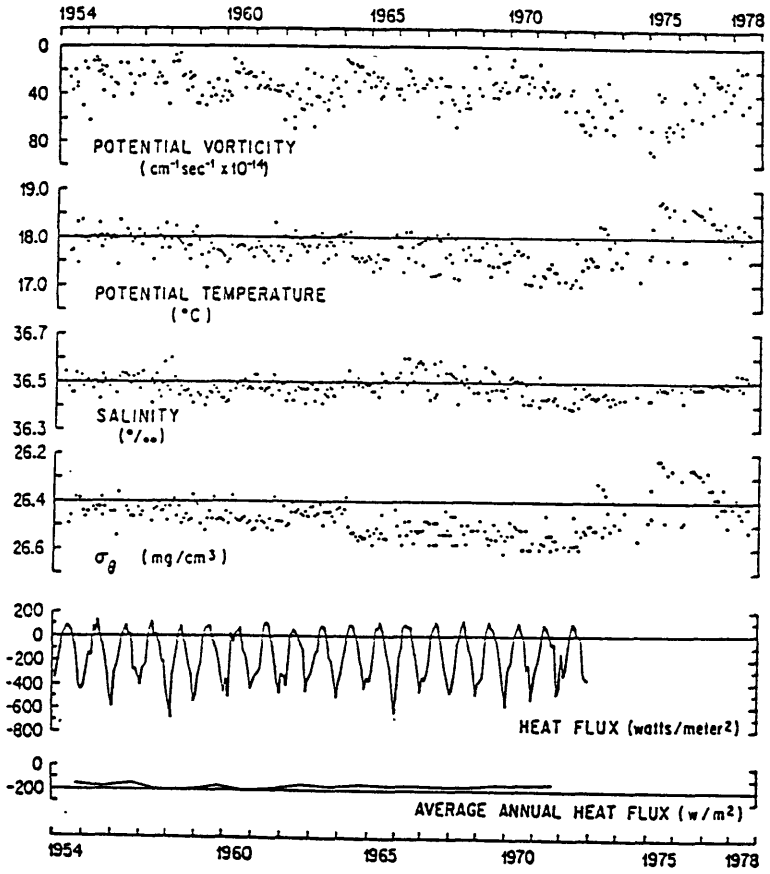

Fig.1.6 (a) Potential vorticity, (b) potential temperature, (c) salinity and (d) potential density of the Eighteen Degree Water core at the *Panulirus* station, plotted against time. Monthly and yearly averaged heat fluxes from a subset of Marsden Square 115 are plotted through 1972. The core is defined as the vertical potential vorticity minimum. From 1954 to 1958, the Eighteen Degree Water had potential temperature, salinity and density near 18°C, 36.5‰ and 26.4 mg cm^{-3}. The potential density increased slightly by 1964 and then increased more systematically to 26.6 mg cm^{-3} until 1972. Potential temperature remained nearly uniform through 1958 and then decreased to 17.9°C in 1964 to 17.1°C in 1972. Salinity increased from 36.5‰ in 1954-1958 to almost 36.6‰ in the 1960s to a low of 36.4‰ in 1972. The new Eighteen Degree Water of 1977-1978 had the characteristics of that in the 1950s: 18.1°C, 36.5‰ and 26.4 mg cm^{-3}. (after Talley and Raymer, 1982).

In contrast to the clear interannual Rossby wave signals in the southern part of the two subtropical gyres, in the northern part (north of 30^oN), interannual Rossby waves are not found in the North Pacific (Price and Magaard,1980; White and Saur,1983), and are found to be very weak in the North Atlantic (Price and Magaard,1986). The difference in the dynamics between the northern and the southern part of subtropical gyres has also been found in some earlier observations. For example, at the annual frequency, in both the North Pacific and the North Atlantic, Gill and Niiler (1973) found that in the southern parts of the Subtropical gyres, the baroclinic response dominates. In other words, the velocity variability is mainly caused by density (or isopycnal) anomaly. In the northern parts, however, the barotropic response dominates without resorting to the temporal variation of the density field. This seems to be consistent with the Rossby wave analysis, because strong baroclinic Rossby waves should produce strong baroclinic responses in the southern parts of the subtropical gyres. Later, we will return to the physical implication of this difference between the northern and the southern part.

The space and time scales of the variability can be seen in Fig.1.7 (from Talley and White, 1987). In the eastern parts of the North Pacific, energy spectra appear red subject to both time and space. Most energy is in planetary space scales and interannual time scales. For example, in the two right panels, the energy peaks have space scales longer than 3000 km and time scale longer than 6 years. This suggests that a low frequency, planetary wave model, as will be adopted in the thesis, might be valid in the eastern parts of the subtropical gyres. In the western region, disturbances tend to have a broad peak at shorter wave lengths and periods, implying different generating mechanisms such as local instabilities.

There is also evidence about the long-term variation of the background flow field (basin scale). For example, the geostrophic transport (relative to 1000 db) of the North Equatorial Current in the North Pacific deviates from its mean about 50 percent at annual (Meyers, 1975) and about 25 percent at interannual time scales (Qiu and Joyce, 1991). The baroclinic transport of the Subtropical gyre in the North Pacific and the Kuroshio current also exhibit strong long-term variability (e.g. White, 1977; He and White, 1987). There is even speculation about the existence of interannual oscillations between the two subtropical gyres in the two hemispheres (Wyrtki and Wenzel,1984).

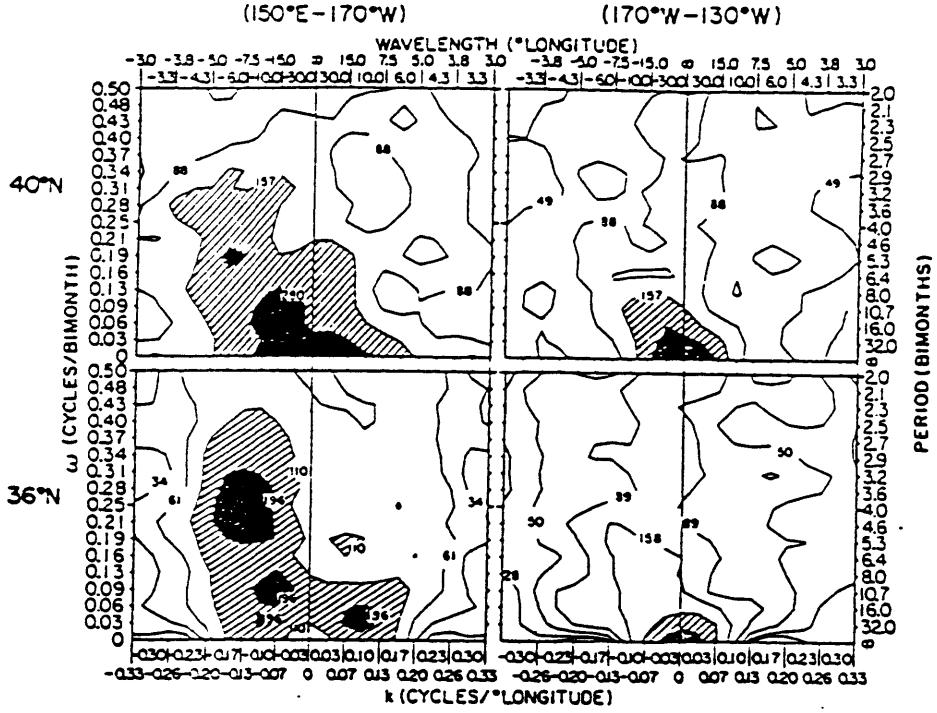

Figure 1.7: Frequency-zonal wavenumber (ω/k) spectra of anomalous 300 m temperature for the western (left panels) and eastern (right panels) mid-latitude North Pacific. Zonal wavelength is shown only to 2° although the Nyquist wavelength is 1°. (The effective Nyquist wavelength is between 3° and 4°.) Contour intervals are the 90 percent confidence intervals starting with a value slightly below the spectral maximum. The area within the first two contour levels below the maximum is shaded and the area within the third contour level is hatched. (After Talley and White, 1987).

Energy sources and generating mechanisms

This is one of the most important aspects of the study of the long-term variability. In the northwestern region, it seems to us reasonable that the variability is closely associated with the dynamics of the western boundary currents or the strongly variable surface buoyancy flux there. In other regions, the generating mechanisms are unclear. Classical explanations attribute the annual thermocline variability to the local Ekman pumping (Veronis and Stommel,1956; Gill and Niiler, 1973; Meyers, 1975). However, later studies show that this mechanism is not able to explain the observations satisfactorily (White, 1977,1978). For example, in a large area, the predicted field is poorly correlated with the observations; the amplitude is badly underpredicted. A linear model incorporating both the local Ekman pumping and the remote Rossby wave radiation from eastern boundaries improves the results substantially, particularly in the southern part of the subtropical gyres (e.g., Kang and Magaard,1980; White and Saur,1981; 1983; Kessler,1989).

However, as discussed earlier, in the northern part of the subtropic gyres, interannual Rossby waves are not evident. Therefore, a model with a local Ekman pumping and baroclinic Rossby waves may fail in these regions. So far, the reason for the lack of interannual baroclinic Rossby wave signals in the northern part of subtropical gyres is not understood. It seems to me that the difference between the northern part and the southern part of a subtropical gyre suggests different dynamics. The reason is that the data for the interannual variability are taken in the upper ocean (shallower than 500 meters). On the other hand, it is known that in the northern part of subtropic gyres, the mixed layer can penetrate very deep (deeper than 200 meters) in winter. One would imagine that the surface heat flux could contribute significantly to the observed signals. We will concern ourselves with this issue in the thesis.

Nonlinearity

The nonlinearity of the Rossby wave may also be important. Observations on the interannual variation found large amplitudes of variations on an isopycnal ($\pm 50m$). Using a decorrelation scale of 1000 km and a reduced gravity of $\gamma \sim 1\ cm/s^2$, one can calculate the corresponding anomalous velocity as $v \sim \gamma \partial_x h/f = 1\ cm/s$. This velocity is comparable to the speed of baroclinic Rossby waves. Therefore, nonlinearity might be expected to play an important role.

3 Review of Earlier Theories

Effects of Ekman pumping

Classical theories of oceanic variability have emphasized the role of Ekman pumping. Using a linear quasi-geostrophic model, Anderson and Gill (1975) studied the response of the ocean to a sudden change in wind field. They found that baroclinic Rossby waves are excited along the eastern boundary and propagate westward. The interior Sverdrup flow is realized after long baroclinic Rossby waves pass by. However, Charney and Flierl (1981) pointed out that in a linear, inviscid model, the final Sverdrup flow is confined to the surface singularly, leaving the subsurface fluid undisturbed. This is inconsistent with the observations.

The effect of the spatially varying mean thermocline structure has also been investigated, mostly in a $1\frac{1}{2}$ layer model. Anderson and Killworth (1979) found that in a subtropical gyre, the downward Ekman pumping increases the mean thermocline depth. As a result, the Rossby wave, whose speed increases with thermocline depth, accelerates westward. Cheng and Philander (1989) have studied the effect of a meridional variation of the mean thermocline. They found that a westward baroclinic flow tends to sweep disturbances westward while an eastward mean flow deflects waves towards the equator. Since the thermocline structure in the subtropical gyre is more complicated than zonal baroclinic jets, we might expect that the basic thermocline structure influences the Rossby waves significantly.

The effect of an annual periodic Ekman pumping has recently been investigated by Dewar (1989) in a quasi-geostrophic model. He found a time-mean circulation with some micro-gyres in the otherwise motionless shadow zone. These gyres are produced by the interaction between the barotropic and baroclinic flows; the former refers to the vertically averaged flow which is determined by the Ekman pumping through the Sverdrup relation while the latter is the veolcity component due to the vertical shear. Dewar's work is limited to the annual frequency. Moreover, his quasi-geostrophic model can not take into account ventilation. As a result, his result is restricted to the shadow zone and can not be extended to the ventilated zone.

These previous works have recognized two mechanisms for the thermocline variability: the local Ekman pumping and the planetary waves radiating from the eastern boundary. However, the works lack some important dynamics. One is the effect of a barotropic flow and thermocline structure. Most of the previous work have concentrated on either the local response or the linear Rossby wave in the absence of a mean thermocline circulation (e.g., Veronis and Stommel, 1956; Gill and Niiler, 1975; Gill and Anderson,1975). The effect of a shear flow has also been considered (e.g., Cheng and Philander,1989; Killworth,1979). However, these models do not include a barotropic mean flow, or a Sverdrup flow. Because the wave speed of a baroclinic planetary wave in the mid-latitude is comparable to that of the Sverdrup mean flow, we should expect that the mean flow has a strong influence on the planetary waves and the thermocline circulation. Indeed, in both of the two recent steady thermocline theories (Rhines and Young, 1982; Luyten *et.al.*, 1983), the barotropic mean flow plays the crucial role. Without a mean barotropic flow, there will be neither a Rhines-Young pool (Dewar *et. al*, 1984; Dewar, 1989) nor a ventilated zone. In addition, the observed mean thermocline structure varies significantly in space (Emery *et.al.*, 1984). Thus, the effect of the mean thermocline may become significant, too. In this thesis, the mean flow and thermocline structure will be considered and will be seen to play crucial roles.

The other part of the physics is even more fundamental because it addresses a new mechanism for the thermocline variability-- the ventilation and the associated advection effect. None of the previous work on time-varying thermocline has included the subduction effect. Hence, they could not study the temporal behavior of a ventilated thermocline. The subduction effect will be emphasized and investigated in detail in this thesis.

Variable surface heat flux

The importance of a varying surface heat flux on the thermocline has been recognized in recent years. Stommel (1979) first pointed out that it is the water subducted from the rising mixed layer during early spring that forms the permanent thermocline. Woods (1985) further pointed out that the upper part of the ocean responds to a varying surface heat flux through a complicated coupling between the mixed layer and the thermocline. During the cooling season when the mixed layer penetrates rapidly, some water is entrained from the thermocline into the mixed layer. On the

other hand, when the heating starts and the mixed layer retreats, water is detrained from the mixed layer to the thermocline.

However, so far, the study on the effect of variable surface heat flux has mainly based on physical speculation and has been descriptive. There has been no theory which is developed from rigorous physical equations and which is able to study the physical process in a quantitative way. Indeed, even in steady thermocline models, the effect of a surface heat flux has only be studied implicitly and partially (they either have no mixed layer or their mixed layer models are essentially passive) (e.g. Luyten, *et.al.*, 1983; Huang, 1986; Pedlosky *et.al.*, 1984; Pedlosky and Robins, 1991; Marshall and Nurser, 1991). The major difficulty lies in the coupling between a mixed layer and a ventilated thermocline. In this thesis, we will attempt to study the effect of a variable surface heat flux on the permanent thermocline.

Waves from the eastern boundary

Observations also showed variability of isopycnals along the eastern boundary (e.g. section 4B of Kessler, 1989). These variability can be caused either by wind forcings and buoyancy forcings along the eastern boundary, or by Kelvin waves from the equator. It has been argued theoretically that the Rossby waves forced by annual upwelling on the eastern boundary are more efficient than the interior annual wind stress in producing oceanic variability (Anderson and Killworth, 1979).

The impact of eastern boundary Rossby waves on the interior ocean is profound. One issue concerns the penetration of waves across the southern boundary of a subtropical gyre, which is related to the equatorial and extra-equatorial interaction. With an basic ocean at rest, Schopf *et. al* (1981) demonstrated that waves generated in the extra-equatorial region along the eastern boundary can penetrate into the equatorial region, causing strong variability. This occurs because the Rossby wave speed increases rapidly towards the equator with the decrease of the Coriolis parameter f (the long Rossby wave speed is proportional to $C \sim 1/f^2$). They called this phenomenon the β-dispersion. In more realistic situation, however, it is still controversial if the planetary wave can penetrate to the equator. Indeed, as demonstrated by Cheng and Philander (1989), the wave rays can be substantially distorted by mean baroclinic jets.

So far, the effect of the zonal variation of the basic state stratification has not been noted. This variation may be particularly important in the vicinity of the southern boundary of a subtropical gyre. The reason is that in those regions (about 15^oN), using observations, Emery *et. al* (1984) have shown that the internal deformation radius almost doubles from the eastern to the western sides in both the North Pacific and North Atlantic. This implies about a four times increase of long Rossby wave speed from the east to the west because $C \sim (radius)^2$. This thesis will pay particular attention to the zonal variation of the basic state on the wave penetration.

The other aspect that will be studied is the breaking of nonlinear planetary waves, which is related to large scale frontal structures. It has been shown theoretically that under an annual upwelling in the eastern boundary (Anderson and Killworth,1979) or a strong local anomalous thermal forcing (Dewar, 1987), planetary waves may break within the subtropical gyre. A more detailed investigation, particularly in the presence of Ekman pumping and a mean Sverdrup flow, is needed.

4 Novel Physical Mechanisms in the Thesis

As seen in the review, previous works have left several key elements not understood for the time-varying thermocline. These elements will be studied in detail in the thesis and are summarized in the following. The most important two dynamical features are:

a) The variable surface heat flux: This will be investigated in chapter 4. It will be shown that, as the wind stress does, the surface heat flux may play an important role in forcing variability in the ocean. Yet, the two mechanism have completely different natures and result in different variability in different regions.

b) The subduction effect: In chapter 3 and 4 of the thesis, we will see that the subduction effect is essential for suppressing the local Ekman pumping variability within a ventilated zone. On the other hand, the advection may help the surface heat flux to produce strong thermocline variability at interannual periods .

In addition, there are some other aspects to be explored. c) The barotropic flow and basic thermocline structure; the former refers to the vertically averaged flow (determined by the surface

wind from the Sverdrup relation) while the latter refers to the steady thermocline structure forced by the time-mean Ekman pumping. This effect is included in all the case studies. It will be seen that both the mean flow and the thermocline structure are important in determining regions of different dynamics and variability. They also significantly affect the behavior of perturbations such as the propagation, the amplitude and the breaking. d) The response on decadal time scales: Most of the earlier works investigated the annual forcing. For the purpose of climate change, in the thesis, we will consider time scales from annual to inter-decadal. e) The nonlinear interaction: Here, by nonlinear interaction, we refer to both the nonlinear planetary wave and the interaction between the barotropic and baroclinic flows. Previous studies have concentrated either on the nonlinear Rossby wave (e.g. Anderson and Killworth, 1979) or on the interaction between the barotropic and baroclinic modes (Dewar, 1989). In this thesis, we will combine them together. In chapter 5, we will see that an Ekman pumping and the associated mean flow affect the planetary wave breaking significantly. f) The dynamics at different depths: To date, few works have examined the different dynamics on isopycnals at different depths. Here, we are going to pay attention to this aspect. The model we are going to use is a two-layer model, which is too crude a representation in the vertical direction (see §2.6). Nevertheless, the study may suggest that, on interfaces at different depths, the wave propagation varies substantially (chapter 3) and the wave breaking might differ dramatically (chapter 5).

5 Overview of the Thesis

This thesis investigates some basic aspects of the time-dependent thermocline on annual and decadal time and basin spatial scales. The temporal variation is forced by varying external forces: the surface wind stress, the surface heat flux and the eastern boundary upwelling. We tend to focus on the basic physics for the time-varying ventilated thermocline. The main body of the thesis is organized in four chapters, which are

Ch.2. The Model, its Physics and Characteristic Solutions

Ch.3. Thermocline Forced by Varying Ekman Pumping

Ch.4. Thermocline Forced by Varying Surface Temperature

Ch.5. Propagation and Breaking of Planetary Waves Radiating From the Eastern Boundary

Chapter 2 introduces the basic model of the thesis-- a two-layer planetary geostrophic model. The governing equation for the baroclinic mode is derived as a quasi-linear equation which is solved analytically by the method of characteristics. Characteristic solutions are derived. For the thermocline variability, this model has three mechanisms: Ekman pumping, baroclinic Rossby wave and density advection. As an example, the steady thermocline case is investigated to illustrate the different nature of the dynamic balance between a ventilated zone and a shadow zone. Later, this fact will be seen crucial for explaining thermocline variability. The limitation of the model is also discussed at the end.

In chapter 3, we investigate the evolution of the thermocline under a variable Ekman pumping. To highlight the physics, we first study a simpler case, in which the Ekman pumping is suddenly increased (spin-up) or decreased (spin-down). It is found that the dynamics of a ventilated zone differs substantially from a shadow zone. In the shadow zone, the Ekman pumping is mainly opposed by the Rossby wave, which is in accordance with previous studies. After a rapid change of the Ekman pumping, the baroclinic Rossby wave evolves at a much slower time scale (years to decades). This creates a great imbalance in forcings and results in a strong thermocline variability. However, in the ventilated zone, instead of the Rossby wave, (cold) density advection plays the essential role in balancing the driving Ekman pumping on the surface. When the Ekman pumping changes rapidly, the cold advection also varies rapidly at the time scale of barotropic Rossby waves (about one week) to achieve a new steady balance, leaving little thermocline variability. In addition to the above dynamics, the development of the thermocline circulation is also interesting. The evolution differs dramatically between a spin-up and a spin-down. For example, with a change in the Ekman pumping field, the lower layer fluid in the shadow zone is no longer motionless. During

a spin-up, the lower layer water moves southward and the circulation is an anticyclonic gyre. In contrast, during a spin-down, the water moves northward and the lower layer circulation consists of two counter-rotating gyres: an anticyclonic gyre to the north and a cyclonic gyre to the south.

Then, a periodic Ekman pumping is adopted to simulate a variable Ekman pumping more realistically. The features found in the spin-up and spin-down also exist in the periodic Ekman pumping case, with the seasons of an increasing and a decreasing Ekman pumping resembling the spin-up and spin-down respectively. This is so particularly for annual forcings (i.e. with periods comparable to one year). Therefore, under a varying Ekman pumping, the thermocline variability is much stronger in the shadow zone than in the ventilated zone. The direction of the lower layer circulation in the shadow zone oscillates southward and northward.

Furthermore, it is found that for annual forcings, the disturbance is essentially linear. Nevertheless, the linear perturbation is influenced substantially by the basic state thermocline structure. In the ventilated zone, the advection due to the subducted water has the same importance as the local response and they tend to cancel each other. In the shadow zone, if the interface is shallower, local responses dominate; if the interface is deep, remote Rossby waves dominate.

For a strong decadal forcing, the nonlinearity is still weak in the eastern part of the shadow zone but is no longer negligible in the western part of the shadow zone. The time-mean thermocline in the shadow zone is always shallower than the steady thermocline under the time-mean Ekman pumping. The difference may be significant, especially in the western part of a shadow zone. This shallower mean thermocline is mainly caused by the nonlinear Rossby wave. The accompanying mean flow in the shadow zone is southward.

In chapter 4, we consider the variability relevant to a varying surface buoyancy flux. As a first step, here in the thesis, we simulate the effect of a periodic surface buoyancy flux by specifying a periodically moving outcrop line in a ventilated thermocline. Under this simulated surface buoyancy flux, the thermocline variability is in sharp contrast to that forced by the surface wind stress previously discussed in chapter 3. Now, the thermocline in the ventilated zone has a strong variability while the thermocline in the shadow zone exhibits weak variation.

Furthermore, the variability in the ventilated zone has two different regimes. When the outcrop line moves slowly (under a weak cooling), the thermocline variability is dominated by horizontal density advection (i.e. the advection of the interface). Even without a varying mixed layer, the solution remains gravitationally stable. Waters always detrain into the permanent thermocline. Therefore, this regime of solution is called the non-entrainment solution. For a non-entrainment solution, the time-mean thermocline resembles the steady thermocline with the time-mean outcrop line.

When the southward speed of the outcrop line is faster than the particle speed (under a strong cooling) during part of a cycle, a solution without a varying mixed layer depth breaks down due to gravitational instability. This implies that horizontal advection is no longer strong enough and cold vertical convection must occur to balance the strong anomalous surface cooling. Therefore, an (essentially passive) time-dependent mixed layer is superposed on the two-layer thermocline model with the outcrop line and the mixed layer depth specified. Then, we find another regime of solution called the entrainment solution. The solution is so named because when the outcrop line moves faster than the particle speed, waters must be entrained from the permanent thermocline into the mixed layer in order to assure the stable thermocline structure. During the entraining, a fast penetration of the mixed layer must occur. In contrast to the non-entrainment solution, the time-mean profile of an entrainment solution is close to the steady thermocline with the outcrop line and mixed layer depth at early spring position (or when the mixed layer is deepest). During one cycle of the evolution of an entrainment solution, there are three stages: the seasonally subducting stage, the entraining stage and the subducting stage. Waters subducted during the seasonally subducting stage will be re-entrained in the following entraining stage as high potential vorticity waters to form the seasonal thermocline. The water subducted during the subducting stage has a lower potential vorticity and establishes the permanent thermocline. The local variability of permanent thermocline is most efficiently produced by interannual and decadal forcings. At annual frequency, there is very little water subducted into the permanent thermocline each year, causing weak variability.

In chapter 5, we examine the behavior of planetary waves radiating from the eastern boundary in the presence of an external Ekman pumping and the associated mean flow. Two issues will be addressed. The first is how planetary waves originating within the subtropical gyre propagate, in particularly, whether these waves penetrate across the southern boundary of the subtropical gyre into the tropics ? In this issue, the role of the zonal variation of the mean thermocline is emphasized in changing the wave front propagation and effective β (potential vorticity gradient), which further determines the wave penetration across a southern boundary. The result is that the penetration for an interface at different depth differs significantly.

The other issue in chapter 5 deals with the breaking of nonlinear planetary waves forced by an upwelling or a downwelling at the eastern boundary. We are interested in the effect of an Ekman pumping and a mean flow on the breaking of planetary waves. In particular, when and where does breaking occur ? Furthermore, what are the structures of breaking fronts? It is found that the planetary wave breaking is affected significantly by an Ekman pumping and the associated mean flow. In the presence of an Ekman pumping, the breaking of disturbances caused by a downwelling is suppressed and the breaking time is delayed. To the contrary, the breaking caused by an upwelling is enhanced and their times are shortened. The breaking of annual and interannual disturbances will be significantly altered.

In short, chapter 2 develops the model for the thesis. Chapter 3 discusses the effect of a variable Ekman pumping while chapter 4 studies the effect of variable surface heat flux. Chapter 5 investigates two issues related to planetary waves radiating from the eastern boundary.

Chapter 2
The Model, Its Physics and Characteristic Solutions

1 The Model and Basic Equations

In this thesis, we adopt the perhaps simplest ventilated thermocline model which allows subduction--a two-layer, ideal fluid, planetary geostrophic model. The three dimensional geometry of the model is displayed in Fig.2.1a. ρ_1 and ρ_2 represent the densities of the upper and lower layer respectively. h is the thickness of the upper layer while H is the total depth. A downward Ekman pumping $w_e(x,y,t)$ is imposed on the top. The top-plane view of the model is shown in Fig.2.1b, where for convenience the meridional coordinate is chosen as the Coriolis parameter $f = 2\Omega sin\theta$, with θ being the latitude. The northern and southern boundaries of a subtropical gyre where Ekman pumping vanishes are located at f_n and f_s. The lower layer outcrops at f_o. The eastern and western boundaries are set at $x_e = 0$ and $x_w < 0$.

The difference between the present model and the layered model used in classical ventilated thermocline theory (Luyten *et.al.*, 1983) lies on the bottom. Now, instead of using a motionless abyss, we use a rigid and flat bottom

$$H = constant. \tag{1.1}$$

The flat bottom is adopted in the thesis mainly for simplicity. Later, we will see that this model has the advantage of being relatively simple and analytically tractable. Most importantly, it still captures the essential feature of a ventilated thermocline by allowing fluid to subduct. However, we should point out that for the application to the real ocean, in our mind, the bottom of the model ocean is the bottom of the main thermocline, or the depth where the direct wind-driven gyre penetrates. This imagined bottom is neither rigid nor flat. Thus, this flat bottom is very artificial. However, qualitatively, this flat bottom will not change our conclusions. For more details, the reader should refer to section 6 at the end of this chapter.

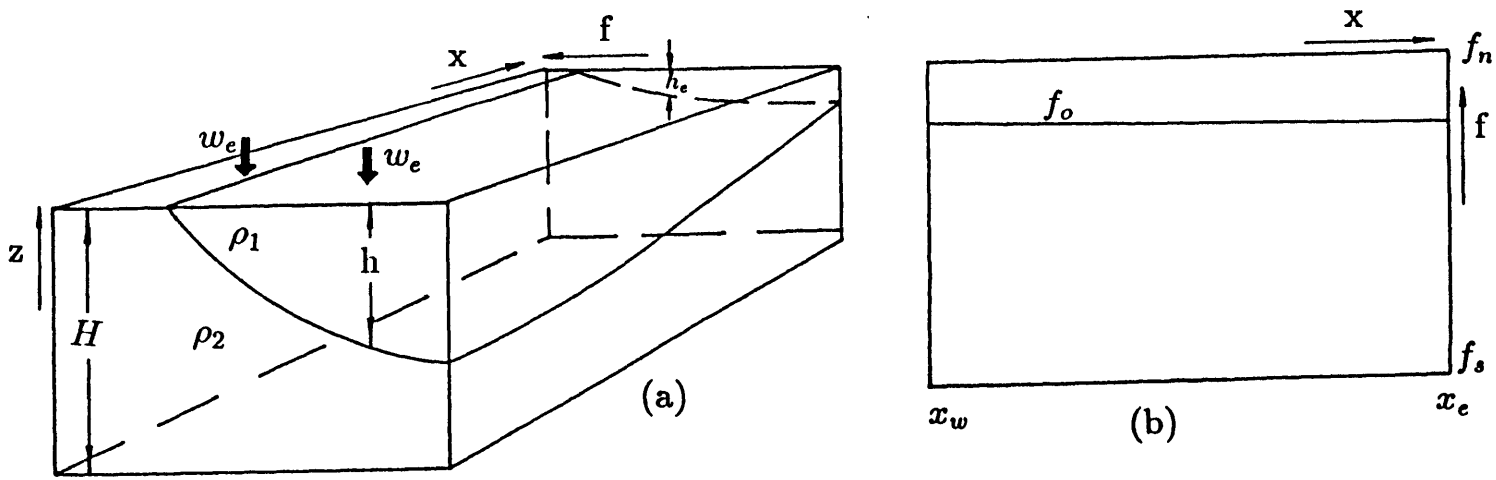

Fig.2.1: The geometry of the model. a) the three dimensional prospective view. b) the top-plane view. Notations are explained in the text.

Now we derive the governing equation. For a gyre-scale circulation, the hydrostatic balance yields the dynamic pressures in both layers as

$$p_1 = \rho_0 \gamma \eta, \quad p_2 = \rho_0 \gamma (\eta - h), \tag{1.2a}$$

Here, ρ_0 is the mean density and $\gamma = g(\rho_2 - \rho_1)/\rho_0$ is the reduced gravity. η is the elevation equivalent to the upper layer pressure such that $\rho_0 \gamma \eta = p_{surface} + \rho_0 g \xi$ where ξ is the surface elevation. Implicitly, it has been assumed that $(\rho_2 - \rho_1)/\rho_0 \ll 1$. Using planetary geostrophic approximation, the momentum equations are simply the geostrophic balance in each layer.

$$v_n = p_{nx}/\rho_0 f, \quad u_n = -p_{ny}/\rho_0 f, \quad n = 1, 2. \tag{1.2b}$$

In addition, we have the Sverdrup relation and the potential vorticity conservation (in this thesis, the potential vorticity always refers to that of the bottom layer):

$$\beta[v_1 h + v_2(H - h)] = f w_e, \tag{1.2c}$$

$$(\partial_t + \vec{v}_2 \cdot \nabla) q = 0, \qquad where \;\; q = \frac{f}{H - h}. \tag{1.2d}$$

(1.2c,d) can also be replaced by the mass conservation equation of both layers.

Using (1.1) and (1.2a,b), the Sverdrup relation (1.2c) can be integrated as

$$[2H\eta + (H - h)^2] \,|_0^x = \frac{2f^2}{\beta \gamma} \int_0^x w_e dx.$$

On the other hand, using (1.2a,b) and the geostrophic balance for the barotropic velocity $\vec{v}_B = (u_B, v_B)$, we have

$$\frac{1}{f\rho_0}(-p_{By},\, p_{Bx}) = (u_B,\, v_B) = \frac{\vec{v}_1 h + \vec{v}_2(H - h)}{H} = \frac{\gamma}{2fH}\left(-[2H\eta + (H - h)^2]_y,\;\; [2H\eta + (H - h)^2]_x\right).$$

The barotropic pressure p_B is then identified as

$$p_B = \frac{\rho_0 \gamma}{2H}[2H\eta + (H - h)^2]. \tag{1.3a}$$

The above Sverdrup relation can be rewritten in terms of p_B as

$$p_B = \frac{\rho_0 \gamma D^2}{2H} + p_{BE} \tag{1.3b}$$

where

$$D^2 = \frac{2f^2}{\beta\gamma}\int_0^x w_e(x,f,t)dx; \quad p_{BE} = p_B\mid_{x=0} = \frac{\rho_0\gamma}{2H}[2H\eta_e + (H-h_e)^2]. \tag{1.3c}$$

where $\eta_e = \eta\mid_{x=0}, h_e = h\mid_{x=0}$. (1.3b) states explicitly that the barotropic mode is determined instantaneously by the Ekman pumping at any time. This occurs because the fast barotropic Rossby wave (with a time scale of about one week) has been filtered out by the Sverdrup relation (for a more rigorous derivation, see Dewar, 1989). In other words, in our model, the adjustment time for a barotropic process is infinitesimal. This assumption is reasonable because we are interested in annual and decadal time scales.

For the baroclinic mode, from the definition of p_B in (1.3a), we have

$$\eta - h = p_B/(\rho_0\gamma) - (H-h)^2/2H - h = p_B/(\rho_0\gamma) - (H^2+h^2)/2H.$$

By virtue of (1.1a,b), we obtain the velocities in layer two as $(u_2, v_2) = \frac{\gamma\vec{k}}{f}\times\nabla[p_B/(\rho_0\gamma) - (H^2 + h^2)/(2H)]$. Substituting these velocities into (1.2d) and noticing (1.1) yield the evolution equation for the baroclinic mode

$$h_t + v_B h_y + [u_B + C(h)]h_x = -(1-\frac{h}{H})w_e, \tag{1.4a}$$

Here, u_B,v_B and $C(h)$ are barotropic velocities and the speed of the non-dispersive Rossby wave, respectively,

$$\begin{aligned}(u_B,\ v_B) &\equiv \frac{h\vec{v_1} + (H-h)\vec{v_2}}{H} = \frac{1}{f\rho_0}(-p_{By}, p_{Bx}) = [-\frac{(\rho_0\gamma D^2 + 2Hp_{BE})_y}{2Hf\rho_0},\ \frac{fw_e}{H\beta}],\\ C(h) &= -\frac{\beta\gamma h(H-h)}{f^2H}.\end{aligned} \tag{1.4b}$$

where the barotropic flow in (1.4d) is completely determined by the Sverdrup relation in (1.3b). Since the continuity equation gives $-\nabla\cdot\vec{v}_B = w_e/H$, (1.4a) can also be put in the conservation form

$$h_t + (v_B h)_y + (u_B h)_x + C(h)h_x = -w_e. \tag{1.4c}$$

The evolution equation (1.4a) is a quasilinear equation. The characteristics are simply the group velocities of baroclinic planetary waves in the presence of a barotropic mean flow. This equation has

been derived by Rhines (1986) and Dewar (1987). This set of equations can be easily generalized to the case with a rigid bottom varying in y direction and with an internal entrainment flux.

Now, we non-dimensionalize the equations. For convenience, the meridional coordinate will be chosen as the Coriolis parameter f. Superscripting a dimensional quantity by a star, we have the non-dimensional quantities:

$$f = \frac{f^*}{f_n}, \quad \beta = \frac{\beta^*}{\beta_0}, \quad t = \frac{t^*}{T_W}, \quad x = \frac{x^*}{L}, \quad h = \frac{h^*}{H}, \quad \eta = \frac{\eta^*}{H}, \quad w = \frac{w^*}{W}, \bar{p} = \frac{p^*}{\rho_0 \gamma H} \tag{1.5a}$$

where $\bar{p}$ stands for any pressure. In (1.5a), W, f_n, β_0, H represent respectively the typical Ekman pumping velocity, the Coriolis parameter at the northern boundary of the subtropical gyre, the mean β value in a subtropical gyre and the total depth. In addition, $T_W = H/W$, $\gamma = 2cms^{-2}$, $L = C_{\beta H} \times T_W$, and $C_{\beta H} = \beta_0 \times L_D^2$, $L_D^2 = \gamma H / f_n^2$ with L_D and $C_{\beta H}$ being the deformation radius and the typical mid-latitude Rossby wave speed. T_W is then the advective time scale for a particle to sink to the bottom of the main thermocline and L is the zonal scale across which a mid-latitude planetary wave travels in one advective time scale. If we choose the parameters as $W = 10^{-4} cm/s$, $f_n = 2\Omega sin(45^o) = 10^{-4} s^{-1}$, $H = 800\ m$, $\beta_0 = \frac{2\Omega}{a} \cos(35^o) = 1.87 \times 10^{-13} s^{-1} cm^{-1}$, it follows that

$$T_W \approx 27\ years, \quad L \approx 16000\ km, \quad C_{\beta H} \approx 2.1\ cms^{-1}, \quad L_D \approx 38\ km. \tag{1.5b}$$

The time and spatial scales are sensitive to the choice of the total depth H, especially the horizontal length L which is proportional to the square of H. This sensitivity is noticeable because the bottom of the thermocline varies greatly from middle latitudes to lower latitudes. Therefore, the horizontal scale should vary accordingly. The values in (1.5b) are proper for mid-latitudes. In lower latitudes, H is 300 m, giving much shorter time and spatial scales than in (1.5b)

$$T_W \approx 10\ years, \quad L \approx 2250\ km. \tag{1.5c}$$

The non-dimensional width of the Pacific (say about 20000 km in lower latitudes) is about 1.2 with (1.5b), but it becomes 8.8 with (1.5c).

The non-dimensional form for the Sverdrup relation (1.3b) is now

$$p_B = \frac{D^2}{2} + p_{BE}, \tag{1.6a}$$

where

$$D^2(x,f,t) = 2f^2 \int_0^x w_e(x,f,t)dx, \quad p_B = \eta + \frac{(1-h)^2}{2}, \quad p_{BE} = p_B \mid_{x=0} . \tag{1.6b}$$

The baroclinic evolution equation (1.4a) becomes

$$\boxed{h_t + \vec{v_B} \cdot \nabla h + C(h)h_x = -(1-h)w_e.} \tag{1.7a}$$

where

$$u_B = -\frac{p_{Bf}}{f} = -\frac{1}{2f}[D^2 + p_{BE}]_f, \quad v_B(\equiv \frac{df}{dt}) = \frac{p_{Bx}}{f} = fw_e, \quad C(h) = -\frac{h(1-h)}{f^2}. \tag{1.7b}$$

For simplicity, in (1.6) and (1.7), we have chosen an exact β-plane such that $f = f_m + \beta_0 y$ where f_m is the mean latitude of a subtropical gyre. [1] The non-dimensional $\beta = 1$. (1.7a) is the basic equation of the thesis.

2 Physical Interpretation of the Evolution Equation

One striking feature suggested by (1.7a) (or (1.4a)) is that the baroclinic field is determined completely by the evolution of the first baroclinic mode propagating in the *known* barotropic mean flow. This phenomenon is caused by the decoupling of the first baroclinic mode from other modes and is satisfied only in the two-layer PG model with a flat bottom. In fact, the two-layer system filters out other baroclinic modes and prohibits baroclinic mode-mode interactions. The planetary geostrophic approximation neglects relative vorticity. Thus, the barotropic mode is completely determined by the Ekman pumping and is therefore independent of the baroclinic evolution. The flat bottom (actually, a meridional variation of the bottom could also be allowed) will not force topographic waves which otherwise would interact with the first baroclinic mode. Any one of the above three mechanisms will result in equations with Jacobian form coupling terms between different modes.

Another question closely relevant to the discussion above is : in the evolution equation (1.7a) (or (1.4a)), why there is neither the baroclinic advection nor the potential vorticity field altered by

[1] This exact β plane differs from the standard β plane often used in quasi-geostrophic theory. In the latter case, f is taken to be a constant except when being differentiated. One direct difference between the standard β plane and exact β plane is on the long Rossby wave speed $C \sim 1/f^2$. In a standard β plane, the wave speed is constant because $f = f_m = constant$. But in an exact β plane, the wave speed increases rapidly towards the equator because $C \sim 1/(f_m + \beta_o y)^2$.

the mean baroclinic thermocline structure ? This occurs because of the non-Doppler shift effect of planetary waves (Held, 1983; Cheng and Philander, 1989).

The physics behind (1.7a) (or (1.4a)) can be made clear as follows. First, we rewrite (1.4a) as

$$h_t = -\vec{v_B} \cdot \nabla h - Ch_x - (1 - \frac{h}{H})w_e(f), \tag{2.1}$$

The right-hand side terms in order will be called the density advection, the Rossby wave and the effective local Ekman pumping. The corresponding energy equation is

$$P_t = -\vec{v_B} \cdot \nabla P - CP_x - (1 - \frac{h}{H})hw_e(f),$$

where $P = h^2/2$ is the available potential energy; $-\vec{v_B} \cdot \nabla P$ is the energy advection by the barotropic flow; $-CP_x$ is the energy radiated by Rossby waves and $-(1 - \frac{h}{H})hw_e(f)$ is the rate of work done by the effective local Ekman pumping. The dynamic effects of these three mechanisms are illustrated below.

The effective local Ekman pumping $-(1 - \frac{h}{H})w_e(f)$, roughly speaking, consists of two parts: the surface Ekman pumping $-w_e$ and the divergent Ekman pumping mass flux in the upper layer $-\frac{h}{H}w_e = h\nabla \cdot \vec{v_B}$, as shown schematically in Fig.2.2a. Since the later part of mass input diverges in the upper layer before it reaches the interface, it will not affect the evolution of the interface. As a result, the surface Ekman pumping effective to influence the interface is the remaining part $-w_e - (-hw_e/H) = -(1 - \frac{h}{H})w_e(f)$. This effective Ekman pumping is still downward but weaker than the surface Ekman pumping. The response is a deepening of the interface $h_t > 0$ as stated in (2.1). From the energy viewpoint, the local Ekman pumping is an external energy source which forces lighter fluid to descend. Hereafter, without confusion, the effective local Ekman pumping is simply called Ekman pumping.

The Rossby wave mechanism $-Ch_x$ is caused by the westward propagation of a planetary wave. In a subtropical gyre, an isopycnal usually deepens westward, i.e. $h_x < 0$ on the gyre scale. Thus, the westward propagation of a Rossby wave produces a local ascent of the interface, i.e. $h_t < 0$ as observed from (2.1) (Fig.2.2b). In other words, a Rossby wave locally transports available potential energy westward.

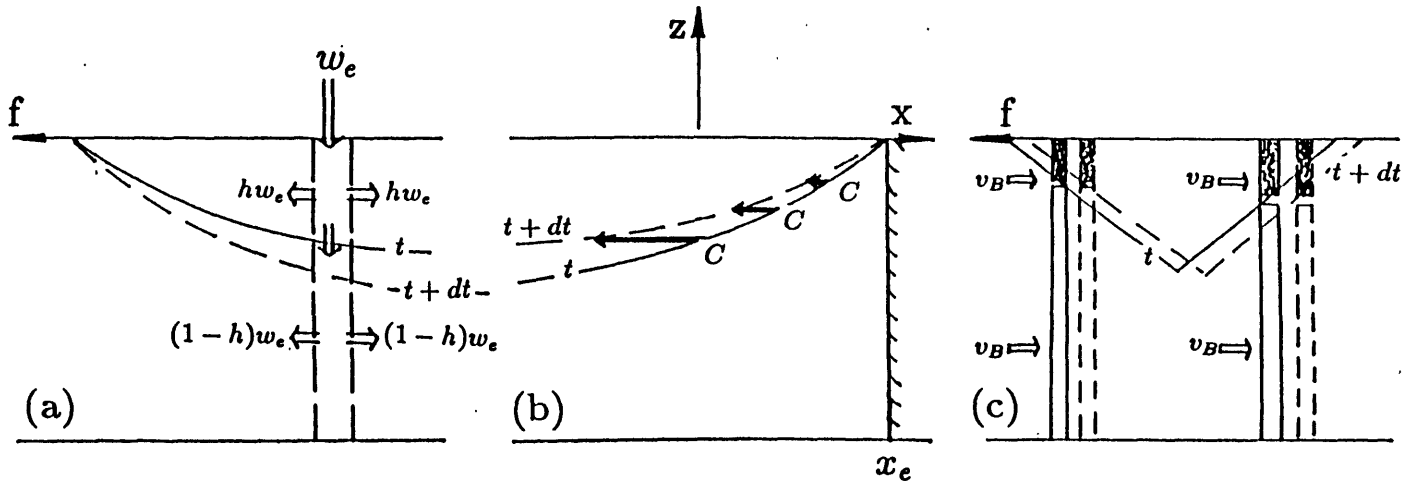

Fig.2.2: A schematic figure for each dynamic mechanism in the the present model. a) The effective Ekman pumping, which tends to deepen the interface. b) The Rossby wave effect which tends to shallow the interface by propagating the westward deepening interface; c) The density advection effect, which can cause a shallowing of the interface for a cold advection (left half) and cause a deepening for a warm advection (right half).

The term $-\vec{v_B}\cdot\nabla h$ is called the density advection because in a two-layer model, the advection of the interface h is the analogy of a density advection. Here, a dense fluid advection (cold advection) $-\vec{v_B}\cdot\nabla h < 0$ is simulated by an excess lower layer fluid advection. This advection locally produces a thicker lower layer ($h_t < 0$), which implies a local reduction of heat storage or energy. The opposite occurs for a light fluid advection (warm advection)(see Fig.2.2c).

Hence, the Ekman pumping provides the driving force for the thermocline circulation. In balancing this driving to achieve a steady state, either a Rossby wave or a cold advection has to function. This will be seen clearly in the next section.

Finally, it is interesting to see a relation between the density advection and the β-spiral which is a measure of the vertical velocity shear. In the light of (1.2a,b) and (1.4c), one obtains

$$\vec{k}\cdot(\vec{v_1}\times\vec{v_2}) = \vec{v_B}\cdot\nabla h \tag{2.2}$$

This relation means that a β-spiral structure ($\vec{k}\cdot(\vec{v_1}\times\vec{v_2}) < 0$) corresponds to a cold advection while an anti-β-spiral structure ($\vec{k}\cdot(\vec{v_1}\times\vec{v_2}) > 0$) gives a warm advection. This relation between density advection and vertical shear can be easily proven in a continuously stratified model even in the presence of temporal variations. Therefore, the observed β-spiral in the interior mean thermocline in the subtropical gyre (Stommel and Schott, 1977) implies a mean southward cold advection there, which is consistent with our intuition.

3 The Dynamics of a Steady Ventilated Thermocline

Before we analyze a time-dependent thermocline, it is helpful to briefly discuss a steady ventilated thermocline in our two-layer model. For simplicity, we only consider the case in which both the Ekman pumping w_e and outcrop line f_o are zonal. In addition, as in the classical LPS model (Luyten *et. al*,1983), we assume that there is no mass flux into the eastern boundary in each layer, i.e. $p_{1f}\,|_{x=0} = p_{2f}\,|_{x=0} = 0$. From (1.2a), this means $\eta_e = constant, h_e = h_e(f_o) = 0$. Thus,

$$w_e = w_1(f), \quad f_o = constant, \quad \eta_e = constant, \quad h_e = 0. \tag{3.1}$$

Following Luyten *et. al* (1983), we derive the solution. In the ventilated zone, the steady form of potential vorticity conservation (1.2d) and the geostrophic balance (1.2b) give $f/(1-h) = Q(p_2)$.

Along the outcrop line, this becomes $Q(p_2) = f_o = constant$. Thus, we have the solution for the ventilated zone as

$$\frac{f}{1-h} = f_o = constant, \quad or \quad h = 1 - f/f_o. \tag{3.2}$$

In the shadow zone, $\vec{v_2} = 0$. With the aid of (1.2a,b), this means $p_2 = \eta - h = constant$. Using the Sverdrup relation (1.3b), we have the shadow zone solution

$$h^2 = D_1^2 \equiv 2f^2 w_1 x. \tag{3.3}$$

The shadow zone boundary will be denoted by B_1. The continuity of the solution (3.2) and (3.3) along B_1 gives the expression for B_1 as

$$x_{B1}(f) = \frac{(1 - \frac{f}{f_o})^2}{2f^2 w_1(f)}. \tag{3.4}$$

Now, we analyze the dynamic balance for the steady solution (3.2) and (3.3). In the steady case, equation (1.7a) degenerates to

$$\vec{v_B} \cdot \nabla h + C h_x = -(1-h) w_e. \tag{3.5}$$

In the ventilated zone, the solution (3.2) has no zonal slope $h_x = 0$. Thus, in the ventilated zone, the Rossby wave term vanishes $Ch_x = 0$ and the dynamic balance is achieved between the cold advection energy sink and the Ekman pumping energy source, i.e.

$$\vec{v_B} \cdot \nabla h = -(1-h) w_e > 0. \tag{3.6}$$

Rossby waves play no role in the dynamic balance in the ventilated zone here. The cold advection in (3.6) also means a β-spiral velocity shear in the ventilated zone.

In contrast, in the shadow zone, $\vec{v_2} = 0$ and (2.2) yields $-\vec{v_B} \cdot \nabla h = 0$. Therefore, the dynamic balance is such that all the energy input from the Ekman pumping is transported westward by planetary waves, i.e.

$$C h_x = -(1-h) w_e > 0. \tag{3.7}$$

This simple example illustrates the intrinsic dynamic difference between a ventilated zone and a shadow zone. The Ekman pumping is important for both regions as the driving mechanism.

However, in balancing this driving, the ventilated zone is dominated by density advection while the shadow zone is controlled by planetary waves. Intuitively, this difference of dynamics in the two zones is sensible. In a ventilated zone, the subduction of waters play a crucial role. Thus, advection is important. In a shadow zone, however, there is no motion except in the surface layer. Thus, advection is not crucial.

As far as time variability is concerned, the dynamic balances (3.6) and (3.7) have completely different nature and may result in totally different variability. For instance, we consider the case in which the wind stress suddenly changes. Let's tentatively analyze the dynamics balance in the two zones. In the ventilated zone, both the Ekman pumping $-(1-h)w_e$ and the density advection $\vec{v}_B \cdot \nabla h$ vary rapidly after a barotropic Rossby time scale (in our model, this time is zero). Therefore, a new steady dynamics balance (3.6) may be rapidly achieved. This may imply little variability of the interface. In the shadow zone, the situation is totally different. The baroclinic Rossby wave $C(h)h_x$ varies only after a slow baroclinic Rossby wave time scale while the Ekman pumping has been changed rapidly right after the change of the wind stress. Therefore, the steady balance (3.7) can not be maintained any more. An imbalance in the steady dynamic balance is produced, which may excite strong temporal variability of the interface. Consequently, in responding to this changing wind, one may speculate that there is little variability in the ventilated zone but there is a strong variability in the shadow zone. In chapter 3, this will be proven is indeed the case.

Finally, one notices that the ventilated zone solution (3.2) is peculiar because of its uniform potential vorticity $f/(1-h) = f_o = constant$. This uniform potential vorticity is an artificial feature of our model. Indeed, it is the flat bottom, together with a zonal outcrop line, that produces a constant subduction potential vorticity f_o along the outcrop line and in turn the uniform potential vorticity in the whole ventilated zone. The absence of Rossby waves is caused by this uniform potential vorticity because there is no background potential vorticity gradient to provide the restoring mechanism for a Rossby wave. If the outcrop line depends on latitude, the potential vorticity along the outcrop line would not be uniform. Thus, the potential vorticity in the lower layer would not be uniform and Rossby waves may appear in the ventilated zone. For a more general model or even the real ocean, the potential vorticity in a ventilated zone is definitely not

uniform. One naturally wonders whether the different dynamic natures between the two zones still exist. I speculate that qualitatively this is still true. In fact, in observations (e.g. Keffer,1985; Talley, 1988), numerical models (Cox and Bryan, 1984; Cox, 1985, 1987) and theories with more complex models (e.g. Luyten *et. al*,1983; Pedlosky and Young, 1983; Liu *et. al*,1991), it has been observed that the potential vorticity in a ventilated zone, although not uniform, is much more uniform than that in a shadow zone. This suggests that the planetary wave activity would be much weaker in a ventilated zone than that in a shadow zone. For a more detailed discussion, the reader should refer to section 6 of this chapter.

4 Characteristic Equations

Now, we return to the time-dependent evolution. We want to solve (1.7a) by the method of characteristics. The characteristic equations for (1.7a) are given by

$$\frac{dt}{ds} = 1 \tag{4.1a}$$

$$\frac{df}{ds} = f w_e(x,f,t) \tag{4.1b}$$

$$\frac{dh}{ds} = -(1-h) w_e(x,f,t) \tag{4.1c}$$

$$\frac{dx}{ds} = -\frac{1}{2f}[D^2(x,f,t) + p_{BE}(f,t)]_f - \frac{h(1-h)}{f^2}. \tag{4.1d}$$

where s is the variable along a characteristic. The initial condition for characteristics in (4.1) is

$$(t,f,x,h)\mid_{s=0} = [t_i, f_i, x_i, h_i(x_i,f_i,t_i)]. \tag{4.2}$$

This is different from the real time initial condition at $t = 0$ with $h(x,f,t)\mid_{t=0}$. (4.1) is a set of ordinary differential equations. A simple case occurs when the Ekman pumping is independent of longitude, i.e. $w_e = w_e(f,t)$. In this case, this set of equations can be solved one by one: (4.1a) for t, (4.1b) for f, (4.1c) for h and finally (4.1d) for x. In addition, for a general Ekman pumping, the division of (4.1b) and (4.1c) yields

$$\frac{d}{ds}\left(\frac{f}{1-h}\right) = 0, \quad or \quad \frac{f}{1-h} = \frac{f_i}{1-h_i}. \tag{4.3}$$

This is just the conservation of potential vorticity (1.2d) represented in the characteristic coordinate.

Here, for simplicity, we adopt the eastern boundary condition that there is no barotropic zonal transport into the eastern boundary (Pedlosky, 1983). Hence, it follows that

$$u_B \mid_{x=0} = \frac{-1}{f}\partial_f p_{BE} = 0 \tag{4.4}$$

The simplest interface structure to satisfy this eastern boundary condition is $h_e = 0$ as is the case in Luyten et al.(1983). However, the eastern boundary condition (4.4) allows any $h_e(f,t)$ once the corresponding $\eta_e(f,t)$ makes p_{BE} in (1.6b) spatially constant.

Thus, for a zonally independent Ekman pumping and a zero barotropic transport into the eastern boundary (4.4), using (4.3) to replace the h equation (4.1c) and noticing D^2 in (1.6b), (4.1) can be simplified as

$$t = t_i + s, \tag{4.5a}$$

$$\frac{df}{ds} = f w_e(f,t), \tag{4.5b}$$

$$\frac{f}{1-h} = \frac{f_i}{1-h_i}, \tag{4.5c}$$

$$\frac{dx}{ds} = -\frac{x}{f}[f^2 w_e(f,t)]_f - \frac{h(1-h)}{f^2}. \tag{4.5d}$$

Now, the x equation is a linear equation since f and h are solved from (4.5b,c)

An example

Here, we consider a special but useful case of spin-up or spin-down. Before an initial time, say, $t = 0$, we assume that the thermocline is a steady thermocline under an old Ekman pumping $w_1(f)$ (as in the example in last section of (3.1)). Then, the Ekman pumping is changed abruptly to a new Ekman pumping w_2, i.e.

$$w_e(f,t) = \begin{cases} w_1(f) & if\ t < 0 \\ w_2(f) & if\ t \geq 0 \end{cases} \tag{4.6}$$

With (4.6), we can integrate (4.5b) to yield

$$s = \int_{f_i}^{f} \frac{df}{f w_2(f)}. \tag{4.7}$$

This equation can then be used to replace (4.5b). In addition, the differential form of (4.7) is $ds = df/fw_2(f)$. This allows us to use f to replace s as the characteristic variable. Substituting

this into (4.5d) and noticing (4.5c), the x equation (4.5d) can be written as an differential equation for the new characteristic variable f

$$\frac{d[f^2 w_2(f)x]}{df} = -\frac{1-h_i}{f_i}h$$

Using the initial conditions (4.2) and using (4.5c) again for the h, this can be integrated explicitly. Eventually, we end up with the characteristic equations

---

$$t = t_i + s, \qquad t \geq 0 \tag{4.8a}$$

$$f = \hat{f}(f_i, s), \tag{4.8b}$$

$$\frac{f}{1-h} = \frac{f_i}{1-h_i}, \tag{4.8c}$$

$$x = \frac{f_i^2 w_2(f_i)}{f^2 w_2(f)} x_i + \frac{h^2 - h_i^2}{2f^2 w_2(f)}. \tag{4.8d}$$

Here, for later convenience, s in (4.7) (or (4.5b) under (4.6)) has been replaced by $\hat{f}$ in (4.8b), which is determined implicitly by (4.7) as

$$s \equiv \int_{f_i}^{\hat{f}(f_i,s)} \frac{df}{f w_2(f)}.$$

In other words, $\hat{f}$ is the f solution (4.7) in the characteristic coordinate. (4.8b) can also be replaced by the inverse function $\hat{f}_i$

$$f_i = \hat{f}_i(f, s). \tag{4.8e}$$

which satisfies $f \equiv \hat{f}[\hat{f}_i(f,s), s]$. For illustration, here, we present two examples of the $\hat{f}$ characteristic solution, which will be frequently used in the rest of the thesis. The first is a spatially uniform Ekman pumping

$$w_e(f) = W_0, \tag{4.9a}$$

where $W_0 < 0$ is a constant. (4.7) then gives the $\hat{f}$ and $\hat{f}_i$ as :

$$\hat{f} = f_i e^{W_0 s} \quad and \quad \hat{f}_i = f e^{-W_0 s}. \tag{4.9b}$$

The second is a parabolic Ekman pumping

$$w_e(f) = W_0(1-f)(f-f_s), \quad where\ f_n = 1 \tag{4.10a}$$

This will be adopted to study an entire subtropical gyre for the spin-up problem. Its $\hat{f}$ function is implicitly determined by

$$\frac{1-\frac{f_s}{\hat{f}}}{(\frac{1}{\hat{f}}-1)^{f_s}} = \frac{1-\frac{f_s}{f_i}}{(\frac{1}{f_i}-1)^{f_s}} exp[f_s(1-f_s)W_0 s]. \tag{4.10b}$$

(4.8a-d) are essentially a set of algebraic equations. When the initial condition (4.2) is specified, (4.8) can be solved. After solving for h from this set of equations, the non-dimensional pressures are readily obtained from the non-dimensional form of (1.1a) and the Sverdrup relation (1.6b)

$$p_1 = \eta = h + (D^2 - h^2)/2, \quad p_2 = \eta - h = (D^2 - h^2)/2. \tag{4.11}$$

Here a spatial constant p_{BE} has been neglected due to (4.4). Then, the velocities is determined by the non-dimensional form of (1.2b) as

$$(u_n, v_n) = \frac{1}{f}(-p_{nf}, p_{nx}), \quad n = 1, 2 \tag{4.12}$$

It should be pointed out that (4.8) can actually be used cases other than spin-up and spin-down. If we set $w_1 = w_2$, the Ekman pumping remains unchanged. (4.8) is also for a steady thermocline. Moreover, in spite of the special form of Ekman pumping in (4.6), (4.8) still allows a moving outcrop line $f_o(t)$ as well as upwelling and downwelling along the eastern boundary $h_e(t)$. Thus, this system contains a rich variety of time variability. Indeed, (4.8) are the main characteristic equations for the thesis. It is used in chapter 3 (section 2) for the spin-up problem; it is used in chapter 4 to study the effect of a moving outcrop line, which simulates a varying surface temperature; it is used in chapter 5 for studing perturbations caused by eastern boundary upwelling and downwelling. For a periodically varying Ekman pumping in section 3 and 4 of chapter 3, (4.8) is no longer valid and therefore other approaches will be adopted.

5 Characteristic Solutions

With the characteristic equations in (4.8), for the entire gyre, solutions at different times can be derived. Suppose we want to derive the solution at the time $t = T$. The solution is formed by

characteristics starting from the eastern boundary, the outcrop line and the initial time $t = 0$ plane. Different zones will be determined by characteristics coming from different starting points. We start with the part of the solution established by the characteristics originating from the eastern boundary.

The new shadow zone

For the part of the solution due to characteristics from the eastern boundary, each characteristic curve must start at a time t_i before T on the eastern boundary, i.e. $0 < t_i < T, x_i = x_e = 0$. In the (t_i, x_i, f_i) space, one example characteristic line is shown schematically in Fig.2.3a by the thick, dark arrow. This characteristic curve starts from the surface $0 < t_i < T, x_i = x_e$ and ends on the plane $t_i = T$. If the interface depth at the eastern boundary is

$$h\,|_{x=0} = h_e(f,t), \tag{5.1a}$$

we have the initial condition for the characteristics

$$x_i = 0, h_i = h_e(f_i, t_i), \quad 0 < t_i < T, f_s < f_i < f_o. \tag{5.1b}$$

In particular, for the special case

$$h_e = 0, \tag{5.1c}$$

the characteristic solution (denoted by h_s) established by the initial characteristic surface (5.1b,c) is obtained from (4.8) as:

$$t = t_i + s, \tag{5.2a}$$

$$f = \hat{f}(s, f_i), \tag{5.2b}$$

$$h_s = 1 - \frac{f}{f_i}, \qquad 0 \le s \le T - t_i, \tag{5.2c}$$

$$x = \frac{h_s^2}{2f^2 w_2(f)} \tag{5.2d}$$

(5.2d) immediately gives an explicit solution $h_s = \sqrt{2f^2 w_2(f) x}$. This is the same as the steady shadow zone solution in (3.3) except for a new Ekman pumping w_2. Therefore, the solution in (5.2) is called the new shadow zone solution.

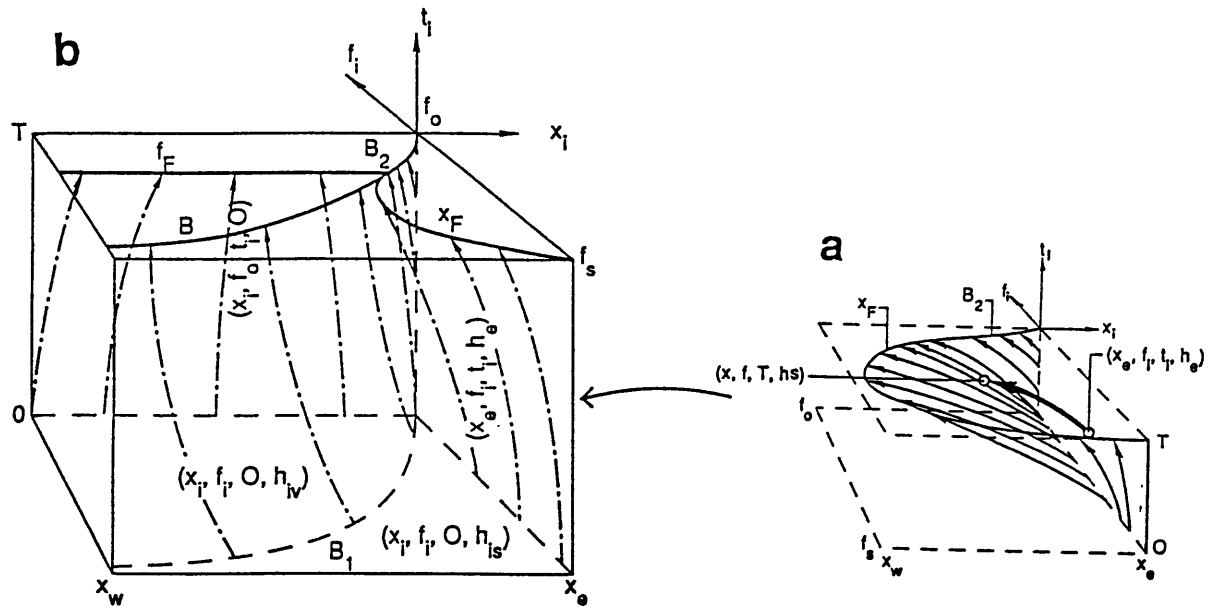

Figure 2.3: Schematic figures for characteristics and the wave fronts. (a) shows the new shadow zone. The thick, dark arrow represents a typical characteristic line originating from the eastern boundary and form the new shadow. $t = 0$ and $t = T$ are the initial and end times. The dashed lines are the boundaries of the isopycnal (the outcrop line, the eastern boundary and the western boundary). Two groups of characteristics are also drawn with thin arrowed curves. The first group initiates from the eastern boundary x_e at the initial time and form the front x_F later. The second group starts from the corner (x_e, f_o) at times after the initial time $0 < t_i < T$ and form the new new shadow zone boundary B_2. (The characteristics for the new ventilated zone and for the original ventilated and shadow zone are not presented here). b) The wave fronts and the associated characteristics in the (t_i, x_i, f_i) characteristic space. Four groups of characteristics are drawn. The first group start from the eastern boundary $x_i = x_e$ at the initial time $t_i = 0$ and form x_F, which separates the new shadow zone and the original shadow zone. The second group start from the outcrop line f_o at the initial time $t_i = 0$ and form f_F, which separates the new ventilated zone and the original ventilated zone. The third group start from the corner $(x_i, f_i) = (x_e, f_o)$ at times after the initial time $0 < t < T$ and form the new shadow zone boundary B_2, which separates the new ventilated zone and the new shadow zone. The last group start from the old shadow zone boundary B_1 at the initial time $t_i = 0$ and form the internal front B, which separates the original ventilated and shadow zone.

However, different from the steady case in (3.3), at a finite time, the solution (5.2) is valid only behind (to the east of) the earliest wave front which is established by the characteristics starting at the beginning time $t = 0$. This wave front will be denoted by x_F and is shown schematically in Fig.3.1a. In the figure, the characteristics (thin arrowed curves) forming x_F start from the line $t_i = 0$ and $x_i = 0$, and end on the x_F at $t_i = T$. To show the wave front and the associated characteristics more clearly, Fig.2.3b is plotted which shows wave front x_F (and other wave fronts which will be discussed later) and the associated characteristics in the whole (t_i, x_i, f_i) space (for $0 < t_i < T$). This includes the part of the space in Fig.2.3a near the eastern boundary. The initial condition of x_F is derived by substituting $t_i = 0$ into (5.1b). For the special eastern boundary (5.1c), the x_F is obtained in (5.2) by letting $t_i = 0$:

$$x_F(f,t) = \frac{[1 - \frac{f}{\hat{f}_i(f,t)}]^2}{2f^2 w_2(f)}, \tag{5.3}$$

where the inverse $\hat{f}_i$ function in (4.8e) has been used. This is a planetary wave front in the presence of a Sverdrup flow. It propagates westward at the characteristic speed $dx/dt = u_B + C(h)$. [1] As time goes on, x_F propagates, behind which the new shadow zone is expanded. The expansion can be seen in Fig.2.3a or b on succeeding t_i planes. More clearly, the evolution is seen in the top view in Fig.2.4. At the initial time $t = 0$ (Fig.2.4a), x_F has not propagated yet. There is no new shadow zone. The gyre is filled with the initial steady ventilated thermocline (h_{iv} as in (3.2) and h_{is} as in (3.3)). Later (in Fig.2.4b), x_F advances westward and near the eastern boundary a new shadow zone has been established. Even later (in Fig.2.4c), the x_F reaches further west and the new shadow zone is greatly expanded.

In addition, similar to the steady case of (3.4), to the north of the new shadow zone, there is a new shadow zone boundary B_2. This B_2 is formed by the characteristics (also shown as thin arrows in Fig.2.3a,b) starting from the line $x_i = 0, f_i = f_o$ and $0 < t_i < T$. The equation for B_2 is then readily obtained from (5.2) as

$$x_{B2}(f) = \frac{(1 - \frac{f}{f_o})^2}{2f^2 w_2(f)}. \tag{5.4}$$

[1] With the special eastern boundary condition (5.1c), at the southern boundary f_s, x_F is always stagnant on the eastern boundary. Detailed discussion about the behavior of x_F will be given in appendix B of chapter 5.

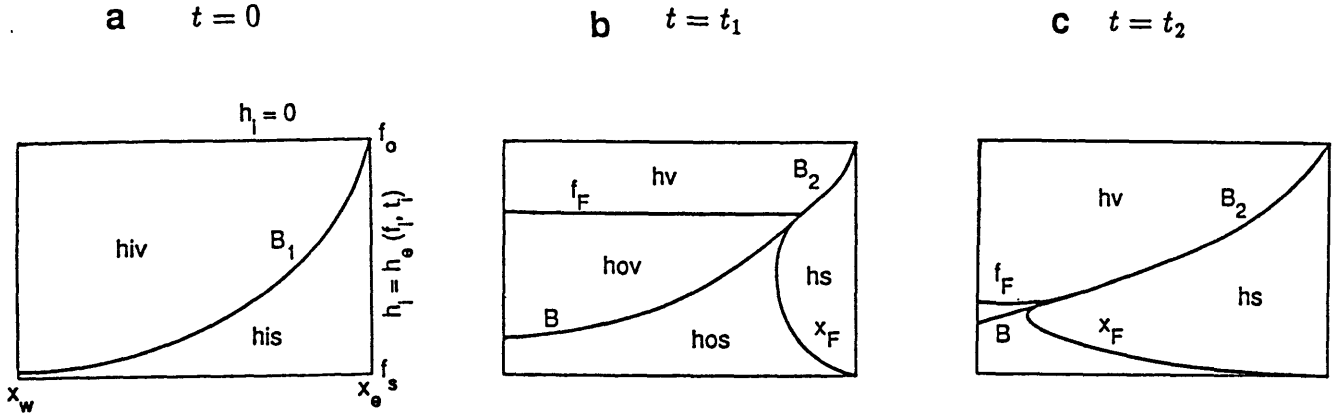

Figure 2.4: The schematic top-view of the evolution of the zone boundaries at succeeding times. (a) The initial time t=0. The gyre is occupied by the old steady ventilated thermocline. (b) At a later time, x_F and f_F have advanced westward and southward respectively, establishing a new shadow zone near the eastern boundary and a new shadow zone near the outcrop line. The original ventilated zone and shadow zone have shrunk. (c) At an even later time, the new ventilated zone and the new shadow zone have occupied almost all the basin except in the southwest corner. A new ventilated thermocline is almost established over the whole basin.

This is the same as the old shadow zone boundary B_1 in the steady circulation (see (3.4)) except with a new Ekman pumping w_2.

It should be noticed that for a general eastern boundary condition (5.1a), the solution in (5.2) may not be a true shadow zone, i.e. the lower layer fluid may be in motion. In fact, if $\partial_f h_e \neq 0$, there is an eastern boundary ventilation in this region. In this case each layer will have a non-vanishing zonal transport on the eastern boundary although there is no barotropic transport (Pedlosky, 1983). If $\partial_t h_e \neq 0$, there will be upwelling or downwelling along the eastern boundary (Anderson and Killworth, 1979). The lower layer fluid will be forced to move, too. This case will be studied in detail in chapter 5. Nevertheless, without confusion, we will still use the name new shadow zone.

The new ventilated zone

Similar to the new shadow zone, there is another group of characteristics originating from the outcrop line f_o at $0 < t_i < T$ (the figure similar to Fig.2.3a is not presented). In general, the outcrop line can take the form

$$f_o = f_o(x, t). \tag{5.5a}$$

The initial surface for characteristics is:

$$f_i = f_o(x_i, t_i), h_i = 0, \quad 0 < t_i < T, x_w < x_i < 0. \tag{5.5b}$$

Particularly for the special case with a steady and zonal outcrop line

$$f_o = constant, \tag{5.5c}$$

the solution (h_v) is derived by substituting (5.5b,c) into (4.8):

$$t = t_i + s, \tag{5.6a}$$

$$f = \hat{f}[f_o, s] \tag{5.6b}$$

$$h_v = 1 - \frac{f}{f_o}, \qquad 0 \leq s \leq T - t_i, \tag{5.6c}$$

$$x = \frac{f_o^2 w_2(f_o)}{f^2 w_2(f)} x_i + \frac{h_v^2}{2 f^2 w_2(f)} \tag{5.6d}$$

(5.6c) is already an explicit solution which is the same as the steady ventilated zone in (3.2) with the new boundary B_2 in (5.4) on the eastern flank. Therefore, solution (5.6) is called the new ventilated zone solution.

In the time-varying case, similarly to the new shadow zone discussed above, the new ventilated zone is established after the passing of the earliest wave front f_F, which starts from the outcrop line f_o at the beginning $t_i = 0$ and which advances southward. f_F is then formed by a part of characteristics in (5.5b) with $t_i = 0$ (the line with $t_i = 0, f_i = f_o$ in Fig.2.3b). These characteristics and f_F are also shown in Fig.2.3b. In the case of (5.5c), substituting $t_i = 0$ into (5.6b), this wave front can be derived as

$$f_F(t) = \hat{f}(f_o, t). \tag{5.7}$$

For instance, a uniform Ekman pumping in (4.9) has $f_F(t) = f_o e^{W_0 t}$. In general, an f_F advances southward at the characteristic speed (in our model, this is also the Sverdrup velocity) $df/dt = v_B = f w_2$. As time goes on, f_F travels more south, and thus the new ventilated zone is expanded. The expansion can be seen in Fig.2.4 at succeeding times.

It should be recognized that with a general form of outcrop line (5.5a), the solution in the new ventilated zone could be much more complicated than (5.6c). The whole chapter 4 will be devoted to the case with a moving outcrop line $f_o = f_o(t)$, which simulates a surface variable heat flux. In that case, the flow in the new ventilated zone varies with time.

The newly formed ventilated zone (h_v) and shadow zone (h_s) are due to information coming from the boundaries of the gyre. Therefore, they are boundary value solutions for the partial differential equation (1.7a). The Ekman pumping (4.6) is steady after the initial time. The boundary conditions h_e or f_o are also steady ((5.1c) and (5.5c)). Thus, the solutions (5.2) and (5.6) are steady.

The original ventilated zone and original shadow zone

From Fig.2.4, we see that, at each time, before the arrival of the wave front f_F and x_F, the gyre is occupied by some other solution. This solution is due to the real time initial value (at $t = 0$) and is formed by the characteristics starting from the plane with $t_i = 0$ and within the gyre $x_w < x_i < x_e, f_s < f_i < f_o$ (the figure similar to Fig.2.3a is not presented). Thus, the initial surface for the characteristics is

$$t_i = 0, h_i = h_i(x_i, f_i), \quad x_w < x_i < 0, f_s < f_i < f_o. \tag{5.8}$$

Furthermore, initially at time $t = 0$, there are two different zones in the gyre (see Fig.2.4a): the old ventilated zone in (3.2) and the old shadow zone in (3.3), which are denoted respectively by

$$h_i = h_{iv}(x_i, f_i) = 1 - \frac{f_i}{f_o}, \quad for \;\; x_i < x_{B1}(f_i), \tag{5.9}$$

and

$$h_i = h_{is}(x_i, f_i) = f_i\sqrt{2w_1(f_i)x_i}, \quad for \;\; x_i > x_{B1}(f_i). \tag{5.10}$$

The solution obtained from (5.8), (5.9) and (4.8) will be named the original ventilated zone (h_{ov})

$$t = s, \tag{5.11a}$$

$$f = \hat{f}(f_i, s), \tag{5.11b}$$

$$h_{ov} = 1 - [1 - h_{iv}(x_i, f_i)]\frac{f}{f_i}, \qquad 0 \le s \le T, \tag{5.11c}$$

$$x = \frac{f_i^2 w_2(f_i)}{f^2 w_2(f)}x_i + \frac{h_{ov}^2 - h_{iv}^2}{2f^2 w_2(f)}. \tag{5.11d}$$

The solution derived from (5.8), (5.10) and (4.8) will be called the original shadow zone (h_{os})

$$t = s, \tag{5.12a}$$

$$f = \hat{f}(f_i, s), \tag{5.12b}$$

$$h_{os} = 1 - [1 - h_{is}(x_i, f_i)]\frac{f}{f_i}, \qquad 0 \le s \le T, \tag{5.12c}$$

$$x = \frac{f_i^2 w_2(f_i)}{f^2 w_2(f)}x_i + \frac{h_{os}^2 - h_{is}^2}{2f^2 w_2(f)}. \tag{5.12d}$$

The boundary between h_{ov} and h_{os}, denoted by B, is at the old shadow zone boundary $x = x_{B1}(f)$ (see (3.4)). Later, B evolves with time. The B and the associated characteristics are illustrated schematically in Fig.2.3b. After using the initial curve $x_i = x_{B1}(f_i)$, B is derived from (5.11) or (5.12) as

$$x_B(f, t) = \frac{(1 - \frac{f}{f_o})^2 - (1 - \frac{\hat{f}_i}{f_o})^2\delta(\hat{f}_i)}{2f^2 w_2(f)}. \tag{5.13}$$

where $\delta(\hat{f}_i) \equiv 1 - \frac{w_2(\hat{f}_i)}{w_1(\hat{f}_i)}$. B varies with time. It forms an internal wave front starting on B_1, as opposed to a boundary wave front x_F or f_F. As shown schematically in Fig.2.4, initially, the h_{ov} (or h_{iv} at $t = 0$) and h_{os} (or h_{is} at $t = 0$) occupies the whole gyre. Later, x_F propagates westward and

f_F advances southward, the new shadow zone and the new ventilated zone are expanded. At the same time, the original ventilated zone and the original shadow zone shrink. At the last time shown in Fig.2.4c, the new shadow zone and the new ventilated zone have occupied almost all the gyre except the southwestern corner. A new ventilated thermocline is almost established. Eventually, the new shadow zone and ventilated zone will overtake the entire gyre, establishing a new ventilated thermocline.

6 Remarks on the Limitations of the Model

Our model has the advantage of being relatively simple and analytically tractable. Most importantly, it captures the essential feature of a ventilated thermocline by allowing fluid to subduct. In fact, this model is perhaps the simplest model to take into account ventilation effect.

However, we are fully aware of the limitations of the model. As in most previous thermocline theories, we have assumed that the Ekman pumping and the outcrop line do not depend on longitude. The western boundary currents are passive in the sense that they do not directly affect the thermocline in the interior. Finally, there are two important and perhaps serious presumptions. The first is the rigid and flat bottom. The second is the two layer representation of a continuously stratified thermocline. Since they have important impact on our model dynamics and on the interpretation of our model results, these two assumptions deserve more attention.

The rigid and flat bottom

The flat bottom assumption is adopted here mainly for simplicity. Particularly in the time-dependent problem, this rigid bottom filters a second baroclinic mode. As a result, there is no baroclinic mode-mode interaction. Furthermore, a flat bottom does not excite topographic Rossby waves which would otherwise interact with the baroclinic mode. These points have been illustrated at the beginning of section 2.

One artificial feature related to the flat bottom is a uniform potential vorticity in the ventilated zone provided that a zonal outcrop line is also imposed. This occurs because the subduction potential vorticity along the outcrop line now is a constant, i.e. $q_{subduction} = f/(H-h)\,|_{f=f_o=constant} = f_o/H = constant$. Then, with the flat bottom, this uniform potential vorticity results in the ab-

sence of zonal slope of the interface i.e. $h_x = 0$. This in turn yields an important dynamic result: the absence of baroclinic Rossby wave ($C(h)h_x = 0$) in the ventilated zone. Consequently, the advection dominates and the dynamic balance is (see (3.6))

$$\vec{v_B} \cdot \nabla h = -(1 - \frac{h}{H})w_e. \tag{6.1}$$

This is in sharp contrast to the dynamic balance in the shadow zone (see (3.7))

$$Ch_x = -(1 - \frac{h}{H})w_e. \tag{6.2}$$

where the baroclinic Rossby wave dominates. As speculated at the end of section 3 and as will be proven in later chapters, the difference between the dynamic balance (6.1) and (6.2) will result in totally different variability in the ventilated zone and the shadow zone.

If in the flat bottom model the outcrop line is not zonal, or if we have a $2\frac{1}{2}$ layer model, the subduction potential vorticity usually will not be a constant, because $q_{subduction} = f_o(x)/H[x, f_o(x)] \neq constant$. Therefore, the potential vorticity in the ventilated zone is no longer uniform and the dynamic balance (6.1) should be replaced by (see (3.5)) [1]

$$\vec{v_B} \cdot \nabla h + Ch_x = -(1 - \frac{h}{H})w_e. \tag{6.3}$$

Furthermore, in a more realistic model or the real ocean, the potential vorticity in the ventilated zone is obviously not uniform. One would ask: Do the density advection and the Rossby wave still dominate in the ventilated zone and in the shadow zone respectively ?

We speculate that, qualitatively, the answer is " yes". We have several reasons. The first reason uses the dynamic balance of (6.3) and applies only to a two layer flat bottom (with a tilting outcrop line) or to a $2\frac{1}{2}$ layer model (see footnote [1]). In either case, the shadow zone dynamic balance is the same as in (6.2). This is so because $\vec{v_2} = 0$ and then (2.2) shows that $-\vec{v_B} \cdot \nabla h = 0$. In the ventilated zone, however, the non-uniform potential vorticity results in the presence of the Rossby wave term. The dynamic balance (6.1) is no longer valid and should be replaced by (6.3).

[1] More precisely, instead of being (6.1), the steady dynamics balance equation should take the form $\vec{v_B} \cdot \nabla(H-h) + C(H-h)_x = (1 - \frac{h}{H})w_e$. This equation is valid for both the flat bottom two-layer model (it degenerates to (6.3) with a flat bottom) and a $2\frac{1}{2}$ layer model. For a $2\frac{1}{2}$ layer model, this equation is derived by the subtraction of equations (11a) and (11b) of Luyten and Stommel (1986). For a uniform potential vorticity, $(H-h)_x = 0$. This balance becomes $\vec{v_B} \cdot \nabla(H-h) = (1 - \frac{h}{H})w_e$. On the other hand, in the shadow zone, the balance becomes $C(H-h)_x = (1 - \frac{h}{H})w_e$.

Nevertheless, a cold advection ($-\vec{v_B} \cdot \nabla h < 0$) cancels part of the Ekman pumping. Therefore, the Rossby wave term only needs to balance the remaining part of the Ekman pumping, as opposed to balancing the total Ekman pumping in the shadow zone. Hence, we conclude that the Rossby wave effect is always more important in a shadow zone than in a ventilated zone. From another viewpoint, in the ventilated zone, we usually have $v_B h_f \sim u_B h_x$ and both do not cancel each other. Therefore, $\vec{v}_B \cdot \nabla h \approx O(u_B h_x)$. Thus, the ratio between the advection and the Rossby wave is

$$\frac{\vec{v}_B \cdot \nabla h}{C h_x} \approx \frac{u_B h_x}{C h_x} = \frac{u_B}{C}.$$

Since C is finite while $u_B \sim x$ (see (1.4c) and notice $D^2 \sim x$ there) and increases towards the west, we should expect that the ratio becomes larger westward. Thus, in the western part, the advection effect should eventually dominate.

The second reason relies on the potential vorticity gradient. In fact, the activity of the Rossby wave is related to the background potential vorticity gradient. A more uniform background potential vorticity implies a weaker restoring mechanism for the Rossby wave or a weaker Rossby wave activity. Thus, the question of the relative importance of the advection and the Rossby wave may be put in another way: Is the potential vorticity gradient in the ventilated zone still much weaker than that in the shadow zone?

The first support comes from observations (e.g. Keffer, 1985; Talley ,1988) and numerical modellings (e.g. Cox and Bryan, 1984; Cox, 1985;1987). Their results all show that, on outcropped isopycnals, the potential vorticity is much more uniform in the ventilated zone than that in the shadow zone, the latter zone being located near the eastern boundary and southern boundary of the subtropical gyre. Second, a much more uniform potential vorticity in the ventilated zone is also found in other more complicated steady circulation models. For instance, in a $3\frac{1}{2}$ model, this feature exists both in the classical LPS solution (two outcropped layer and one surface layer) (see Luyten *et. al*, 1983) and a coupled Rhines-Young pool and a ventilated thermocline solution (one unventilated layer, one outcropped layer and one surface layer) (see Pedlosky and Young, 1983; Liu *et. al*, 1991).

Finally, in a two-layer or a $2\frac{1}{2}$ layer model, we can also analyze the potential vorticity structure in more detail. Supposing a tilted outcrop line $f_o(x)$, the amplitude of the spatial variation of

potential vorticity in the ventilated is the same as that of the subduction potential vorticity on the outcrop line, i.e.

$$\Delta q_{v.z.} = \Delta q_{subduction} = \frac{f_o(x_w)}{H(x_w, f_o)} - \frac{f_o(x_e)}{H(x_e, f_o)}. \tag{6.4}$$

On the other hand, the potential vorticity range in the shadow zone is decided on the eastern boundary

$$\Delta q_{s.z.} = \frac{f_o(x_e) - f_s}{H(x_e, f_o)}. \tag{6.5}$$

where f_s is the latitude of the southern boundary of the subtropical gyre. If the zonal variation of H is small (or flat), it is clear that the condition for $\Delta q_{v.z.} \approx \Delta q_{s.z.}$ is

$$\frac{\Delta q_{v.z.}}{\Delta q_{s.z.}} \approx \frac{f_o(x_w) - f_o(x_e)}{f_o(x_e) - f_s} \sim 1. \tag{6.6}$$

This means that the outcrop line has to tilt across the whole meridional extent of the isopycnal in the subtropical gyre. This requires a zonal slope too strong for most observed outcrop lines within a subtropical gyre in early spring, particularly in the Pacific (see Fig.1.3b of chapter 1). Furthermore, if the effect of the variation of H is included, the ratio in (6.6) will be reduced further, giving an even more uniform potential vorticity in the ventilated zone. This is so because a winter outcrop line in a subtropical gyre usually tilts (but not strongly) in the northwest-southeast direction (in the northern hemisphere) i.e. $f_o(x_w) > f_o(x_e)$ (see observation in Fig.1.3b of chapter 1, particularly in the North Atlantic. Some theories have been given to explain this tilt by Pedlosky *et. al*, 1984). On the other hand, in the subtropical gyre, the thermocline depth deepens westward, i.e. $H(x_w, f_o) > H(x_e, f_o)$. As a result, the deeper $H(x_w, f_o)$ cancels part of the large $f_o(x_w)$ and the potential vorticity variation in the ventilated zone (see (6.4)) is reduced.

With the above reasoning, in general cases, we speculate: it is qualitatively true that the density advection dominates in the ventilated zone while the Rossby wave effect dominates in the shadow zone.

The two layer representation of the thermocline

The two layer model is a very crude representation in the vertical direction. It is unclear to us how exactly this representation corresponds to a continuously stratified thermocline. This gives us some difficulty in interpreting some of our model results. Those results show that different dynamic

properties occur on different depths of interfaces (or different upper layer thickness) in our model. Does this imply that the properties also vary on isopycnals with different depths in a continuously stratified thermocline ? We do not know !

Nevertheless, we tend to think of different depths of interface in two ways, although we recognize that neither of them is satisfactory. The first comes from intuition (although this intuition may very well be wrong!). We think of an interface as an isopycnal at the same depth in a continuously stratified thermocline. It seems to us that this analogy should hold to some extent. For example, a deeper interface is less affected by the surface Ekman pumping than a shallower one. This is consistent with the fact that in a continuously stratified thermocline, a deeper isopycnal is also less affected by the surface Ekman pumping than a shallower one. On the other hand, we know that stratification would change the above conclusion. A stable stratification tends to make the effect of surface Ekman pumping decay more rapidly with depth. Does this imply that an interface at certain depth resembles more to an isopycnal at an shallower depth ?

The second analogy is to relate h and $H-h$ to the equivalent depths of the first baroclinic mode in a continuously stratified ocean. For example, if $h(x_e) = 0.5H$, we infer that the stratification along the eastern boundary is a constant Brunt-Vaisala frequency N. Similarly, a shallow interface $h < H - h$ implies a stratification stronger in the upper thermocline. However, our model is a planetary geostrophic model in which one interface could vary substantially spatially. This presents some difficulties for the stratification analogy, which is usually used in the case with no spatial variation in the direction of wave propagation (or with a much larger spatial scale than that of disturbances). Even worse is the case with outcropping. This is because the N at the bottom of an outcrop line is usually finite in a continuous model. But the stratification analogy may imply a very stable ($N \rightarrow \infty$) stratification near the outcrop line because $h/(H-h) \rightarrow 0$.

In any case, we do not know the exact correspondence. Therefore, we do have difficulty in applying some of our model results to a more complex model or the real ocean.

Chapter 3
Thermocline Forced by Varying Ekman Pumping

1 Introduction

Classical theories on low frequency oceanic variability have emphasized the role of Ekman pumping (e.g., Veronis and Stommel, 1956; Gill and Niiler, 1975; Gill and Anderson, 1975). Two important mechanisms for the thermocline variability have been found: the local Ekman pumping and the Rossby waves excited at the eastern boundary. In spite of progress already made, there are still several obvious questions to be addressed.

First of all, some important aspects on the Ekman pumping and Rossby wave have not been fully explored. One example is the effect of mean flow and thermocline structure. Most of the previous works have concentrated on the local response or the linear Rossby wave in the absence of a mean thermocline circulation. However, the wave speed of a baroclinic planetary wave in the mid-latitude is comparable to that of the Sverdrup mean flow. In addition, the observed mean thermocline structure varies significantly in space. Thus, we may expect significant influence arising from the mean flow and thermocline. Indeed, preliminary studies on waves in the presence of a zonal baroclinic flow have shown that the Rossby wave propagation could be changed substantially (e.g. Anderson and Killworth, 1979; Cheng and Philander, 1989). Here, we will further explore the thermocline variability in the presence of a two-dimensional flow and thermocline structure. In particular, we are interested in the relative importance of the local Ekman pumping and the Rossby waves radiating from the eastern boundary, which has been a recent concern. Classical works claimed the local Ekman pumping to be the main driving mechanism for the variability (e.g. Gill and Niiler, 1975; Roden, 1976). However, recent studies show that the local Ekman pumping produces a poor phase correlation with the observation and underestimates the amplitude of the variability badly (e.g., White and Saur, 1983; Kessler, 1989). Instead, a model incorporating Rossby waves improves the results substantially in the southern part of subtropical North Pacific. Here,

we will explore this problem from a theoretical viewpoint with the emphasis on the role of the thermocline structure.

In addition, the nonlinearity of Rossby waves and the interaction between the barotropic and baroclinic flows have not been studied extensively. One concern is the time-mean thermocline structure. Using a quasi-geostrophic model with an annual frequency, Dewar (1989) has found some time-mean micro-gyres in the otherwise motionless shadow zone. Now, we will extend the study to a planetary geostrophic model and decadal time scales. We would ask: under a periodic Ekman pumping, how does the time-mean thermocline differ from the steady thermocline forced by the time-mean Ekman pumping ?

More fundamentally, besides the two mechanisms mentioned above, is there any other mechanism important for the thermocline variability? We will find that one crucial mechanism, which has not been realized and studied in previous theoretical works, is the ventilation effect and the advection due to the subducted waters. Indeed, none of the previous work on time-varying thermocline has included the subduction effect. Hence, they could not study the temporal behavior of a ventilated thermocline. Here, we would ask the following questions: How does a ventilated thermocline evolve in response to a varying wind ? What are the main dynamic mechanisms behind the evolution ?

The two-layer planetary geostrophic model developed in chapter 2 will be adopted. This model includes the ventilation and advection as shown in chapter 2. We will also consider both annual and decadal forcings.

First, to highlight the physics, in section 2, we study a simple case, in which the Ekman is suddenly increased (spin-up) or decreased (spin-down). It will be found that the dynamics in the shadow zone is dominated by the Rossby wave and the Ekman pumping, which is qualitatively in accordance with previous studies. After a sudden change in the surface Ekman pumping, the baroclinic Rossby wave has not developed because of its much longer time scale (years to decades). Therefore, an imbalance is produced between the two mechanisms and yields a strong thermocline variability. However, in the ventilated zone, the dynamics is totally different. Now, the advection due to the subducted waters opposes the Ekman pumping, while Rossby waves play no significant

role. The resulted variability also differs dramatically from that in the shadow zone. Now, after a change of the wind field, the Ekman pumping and the cold advection both vary rapidly at the time scale of barotropic Rossby waves (about one week) to achieve a new steady balance, leaving little thermocline variability. In addition, the evolution of the structure and circulation of the thermocline is also discussed.

Then, a periodic Ekman pumping is adopted in section 3 and 4 to simulate an annual or decadal Ekman pumping more realistically. The features of thermocline variability found in the spin-up and spin-down also exist in the periodic Ekman pumping case, with the seasons of an increasing and a decreasing Ekman pumping resembling the spin-up and spin-down respectively. Furthermore, in section 3, it is found that for annual or weak decadal forcings, the disturbance is essentially linear. Nevertheless, the linear perturbation is influenced substantially by the basic state thermocline structure. In particular, in the shadow zone, if the interface is shallow, local response dominates; if the interface is deep, remote Rossby waves are more important. Section 4 investigates the thermocline variability under a strong decadal forcing. It is found that the nonlinearity is still weak in the eastern part of the shadow zone but is no longer negligible in the western part of the shadow zone. The time-mean thermocline in the shadow zone is always shallower than the steady thermocline under the time-mean Ekman pumping. The difference may be significant, especially in the western part of a shadow zone. The physical mechanism for this time mean thermocline structure is also explored. Finally, in section 5, we discuss some other properties of thermocline variability.

2 Spin-Up and Spin-Down of a Ventilated Thermocline

To highlight the physics behind the thermocline variability, we first discuss a simple but illustrative example——the spin-up and spin-down of a ventilated thermocline.

As discussed in section 5 of chapter 2, after an abrupt change of the Ekman pumping from an old Ekman pumping (say $w_1(f)$) to a new one (say $w_2(f)$), the solution over the gyre will be established by characteristics originating from the eastern boundary, the outcrop line and the initial time plane (it will be helpful for the reader to recall Fig.2.3 of chapter 2). The part of the solution

formed by characteristics from the eastern boundary is the new shadow zone (see (5.2d) of chapter 2)

$$h_s^2 = 2f^2 w_2(f)x. \tag{2.1}$$

Here, we have chosen an eastern boundary at $x = 0$ and an eastern boundary interface depth $h_e = 0$. This part of solution is established after the passing by of the earliest eastern boundary wave front x_F and is bounded to the northwest by the new shadow zone boundary B_2. To remind the reader, x_F is formed by characteristics starting from the eastern boundary $x_i = 0$ at the earliest spin-up time $t_i = 0$, while B_2 is established by characteristics eminating from the eastern boundary at the latitude of the outcorp line $(x_i, f_i) = (0, f_0)$ after the spin-up $t_i > 0$ (see (5.3) and (5.4) of chapter 2 for x_F and B_2 respectively). Another part of the solution is established by characteristics starting from the outcrop line. This is the new ventilated zone solution

$$h_v = 1 - \frac{f}{f_o}. \tag{2.2}$$

where a zonal outcrop line $f_o = constant$ is adopted. This solution is bounded to its east by the new shadow zone boundary B_2 and is establised after the earliset outcrop line wave front f_F. To reminder the reader again, f_F is formed by characteristics starting from the outcrop line $f_i = f_0$ at the initial time $t_i = 0$ (see (5.7) of chapter 2). The thermocline in the new shadow zone (2.1) and ventilated zone (2.2) are steady. Eventually, we should expect (2.1) and (2.2) be established all over the gyre to form a new steady ventilated thermocline under w_2.

However, at a finite time, in places where x_F and f_F have not swept across, the thermocline is undergoing transient adjustment. The solutions over there are the original ventilated zone and shadow zone, which are established by characteristics starting from the initial time plane $t_i = 0$. The characteristics originating at $t_i = 0$ from the before-spin-up ventilated zone $h_{iv} = 1 - f_i/f_o$ will form the original ventilated zone $h_{ov} = 1 - (1 - h_{iv})f/f_i$ (see (5.9) and (5.11) of chapter 2). Substituting the initial condition into the h_{ov} gives the explicit solution

$$h_{ov} = 1 - \frac{f}{f_o}. \tag{2.3}$$

This solution is bounded to the north by f_F and to the east by the internal wave front B, which is formed by the characteristics starting at the initial time $t_i = 0$ on the before-spin-up shadow zone

boundary (see (5.13) of chapter 2). Surprisingly, (2.3) shows that h_{ov} is independent of time. In fact, the structure of h_{ov} is exactly the same as the initial ventilated zone h_{iv} and the new ventilated zone (2.2). This peculiar feature is due to the flat bottom model and the zonal outcrop line, which cause a uniform subduction potential vorticity independent of time ($q_s = f/(1-h)\,|_{f=f_o} = f_o = constant$) and produce a uniform potential vorticity in the ventilated zone.

Finally, south of the internal wave front B is the original shadow zone, for which characteristics start at the initial time $t_i = 0$ from the before-spin-up shadow zone. The parametric solution has been derived in (5.12) in chapter 2. To derive the explicit solution, use of $h_{is} = 1-(1-h_{os})f_i/f$ and $x_i = h_{is}^2/[2f_i^2 w_1(f_i)]$ from (5.12c) and (5.10) in chapter 2. (5.12d) of chapter 2 gives

$$2f^2 w_2(f)x = -[1-w_2(\hat{f}_i)/w_1(\hat{f}_i)][1-(1-h_{os})\hat{f}_i/f]^2 - h_{os}^2.$$

This is a quadratic equation for h_{os} because $\hat{f}_i$ is a function of f,t only (see (4.8e) of chapter 2). We can put this in the standard form as

$$G(x-x_0) = (h_{os}-h_0)^2, \tag{2.4a}$$

where

$$G = \frac{2I^2 f^2 w_2(f)}{\delta(I^2-\delta)},\quad h_0 = \frac{(I-1)\delta}{I^2-\delta},\quad x_0 = \frac{-(I-1)^2\delta}{2f^2 w_2(f)(I^2-\delta)} \tag{2.4b}$$

$$\delta(f,t) \equiv \delta(\hat{f}_i) = 1-\frac{w_2(\hat{f}_i)}{w_1(\hat{f}_i)},\quad I(f,t) \equiv \frac{f}{\hat{f}_i} \le 1 \tag{2.4c}$$

h_{os} is bounded to the west by the eastern boundary wave front x_F and to the east by the internal wave front B, i.e.

$$x_B(f,t) \le x \le x_F(f,t). \tag{2.4d}$$

(2.4a,b,c) gives a parabolic zonal profile with G as the curvature and (x_0, h_0) as the nose. The physical h_{os} part of solution is only the section between x_B and x_F as indicated in (2.4d). (2.1)-(2.4) give the explicit solution over the entire gyre.

2.1 Thermocline Evolution

We first consider the evolution of a zonal profile. Along a given latitude f, before the arrival of f_F, a zonal profile consists of three parts: a flat and unchanged h_{ov} of (2.3) to the west of B, a steady

parabolic h_s in (2.1) to the east of x_F and a changing parabolic h_{os} of (2.4) in the middle. When f_F reaches this latitude at the time t_F satisfying

$$f_F[t_F(f)] \equiv f, \tag{2.5}$$

B and x_F merges i.e. $x_B = x_F$ (this can be proven by letting $f_i = f_0$ in equations (5.3) and (5.7) of chapter 2). Therefore, the transient middle part of h_{os} diminishes. At the same time, the western side is replaced by the new ventilated zone (2.2). Later, a steady circulation is established on this latitude with the varying B replaced by the new steady B_2. Schematic figures for a spin-up and a spin-down process are respectively given in Fig.3.1a and Fig.3.1b. h_{os} is the only part whose structure varies with time and therefore deserves a detailed discussion. In (2.4), we see that the only time dependency comes from the initial latitude (for characteristics) $\hat{f}_i(f,t)$. As time evolves, the characteristics to reach a fixed latitude f will come from a more northern initial latitude because of the southward characteristic speed $df/ds = v_B < 0$. Thus, $\hat{f}_i$ increases with time or $\partial_t \hat{f}_i(f,t) > 0$. We will examining how the increase of $\hat{f}_i$ affects the parabola in (2.4) during a spin-up or a spin-down. First, in (2.4), $\hat{f}_i$ increases and then I decreases with time. For simplicity, $w_1(f)$ and $w_2(f)$ are assumed to possess the same spatial structure and thus in (2.4c) $\delta = constant$. On the whole interface it follows that

$$\frac{w_2(\hat{f}_i)}{w_1(\hat{f}_i)} = \frac{w_2(f)}{w_1(f)} = \frac{W_2}{W_1} = constant \begin{cases} > 1 & for\ spin-up \\ < 1 & for\ spin-down \end{cases} \tag{2.6}$$

where W_1 and W_2 represent the strength of Ekman pumpings.

In a spin-up process, (2.4b,c) and (2.6) give $-\infty < \delta < 0$, $G < 0$, $h_0 > 0$, $x_0 < 0$ for all times $t > 0$. Thus, a parabola must have its nose pointing towards the east because $G > 0$. Besides, the nose (x_0, h_0) is above the shadow zone profile for that $h_s(f, x_0)/h_0(f) = \sqrt{1 - I^2\delta^{-1}} > 1$. The h_{os} part of parabola always bulges downward, as does the initial steady state, and does not include its nose as drawn in Fig.3.1a ($t = t_1$ profile). (The dashed line is drawn mainly for the illustration of the position of the nose and is not the physical part of the h_{os} solution.) The thermocline simply keeps deepening in h_{os} part until it reaches the local depth of the new steady shadow zone or ventilated zone. On the latitude f, this transient process continues until the arrival of f_F at $t = t_F$.

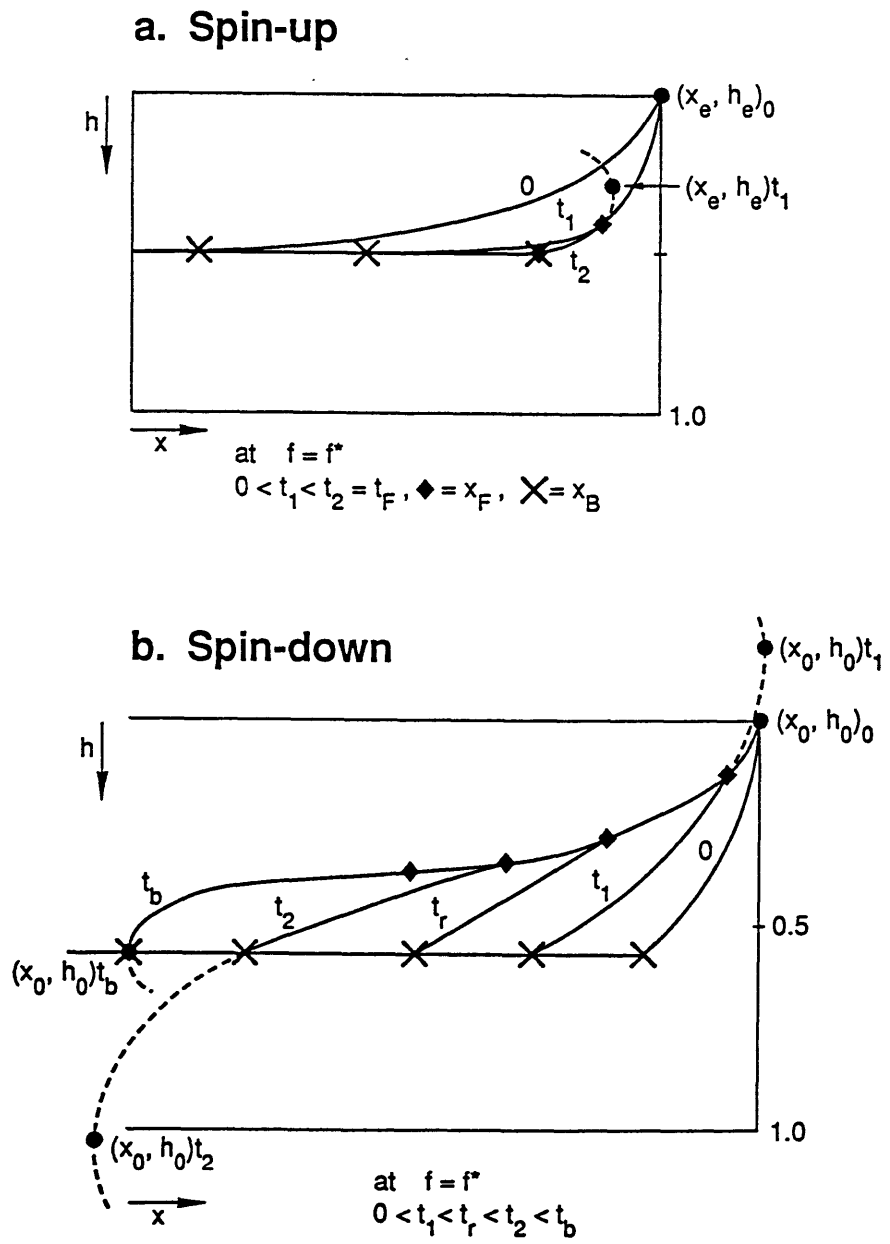

Figure 3.1: Schematic figures for the evolution of zonal profiles and the positions of x_F (black diamond), x_B (black cross) and the nose of the parabola (black dot). The dashed lines are the parabola which do not belong to the physical solution. They are drawn only for illustration of the nose of the parabola. (a) Spin-up. t_F is the time for f_o to arrive at this latitude as defined in (4.5). (b) Spin-down. In (b), it is assumed that the breaking occurs before the arrival of f_o, i.e. $t_b < t_F$ (see (4.8) for t_b).

However, the evolution in a spin-down is more complex. Now (2.4c) and (2.6) suggest $0 < \delta < 1$. As time evolves, in (2.4c), I starts from 1 to decrease. Initially, $I \approx 1$ thus $I^2 - \delta > 0$. (2.4b,c) show that $x_0 > 0, h_0 < 0, G < 0$. We will call this stage the initial stage. Now, the h_{os} part of parabola bulges downward and does not include its nose as shown in Fig.3.1b (the t_1 profile). Later, I may continue to decrease such that $I^2 - \delta = 0$ is reached at the transient time t_r satisfying

$$I^2[f, t_r(f)] - \delta \equiv 0. \tag{2.7}$$

Now, (2.4b) indicates that $G = \infty$ or the parabola degenerates to a straight line which deepens westward, as shown in Fig.3.1b. The initial stage is over and we will call the following stage the transient stage. Now, $I^2 - \delta < 0$. (2.4b,c) indicate that both the curvature and nose change sign such that $G < 0, x_0 < 0, h_0 > 0$. Thus, the parabola should have its nose pointing towards the west. Since immediately after t_r, (2.4b) and (2.7) shows that the nose is very deep and west (i.e. $x_0 \to -\infty, h_0 \to \infty$), the physical part of h_{os} in (2.4a) does not include its nose. Therefore, a typical section during the transient stage is shown as the t_2 profile in Fig.3.1b. Later, as $\hat{f}_i$ increases and I decreases further, the nose moves upward and eastward (or h_0 and $\mid x_0 \mid$ is reduced). Eventually, it may occur that $x_0 = x_B$ and $h_0 = h_{ov}$ at the time t_b such that

$$x_0[f, t_b(f)] \equiv x_B[f, t_b(f)], \quad \textit{and} \quad h_0[f, t_b(f)] \equiv h_{ov}[f, t_b(f)]. \tag{2.8}$$

(These two equations can be proven to occur simultaneously. So they give the same t_b.) Now, the nose is on the western edge of h_{os} (i.e. on B) and the interface is vertical there as shown in Fig.3.1b. This is the marginal gravitational stability state and thus t_b is the first breaking time. After t_b, the h_{os} solution (2.4) becomes gravitationally unstable on its western side. Thus, on the western side, (2.4) is no longer a physical solution. The solution enters the breaking stage. The breaking is caused by the steepening due to the nonlinear planetary wave $C(h) \sim h(1-h)$ (Anderson and Killworth, 1979; Dewar, 1987). Therefore, in principle, the evolution during a spin-down may differ significantly from that of a spin-up where breaking can never occur.

Nevertheless, it should be pointed out that the breaking for a spin-down will not occur in an ocean with a realistic width. This is mainly due to the very gentle slope of the thermocline. It takes a very long time ($t > O(1)$) for the nonlinear steepening to function. By that time, the Rossby

wave has propagated far away from the eastern boundary and the breaking position $x_0[f, t_b(f)]$ is well beyond the western boundary. Detailed calculation is not presented here. One may think that the breaking may occur if the perturbation is very localized. We speculate that this is the case. Indeed, in a later chapter 5, we will present some examples of breaking of planetary waves forced at the eastern boundary.

2.2 Circulation Evolution

Now, we analyze the two dimensional structure of the thermocline and circulation, with the emphasis on the lower layer circulation. Fig.3.2 displays a spin-up, where a parabolic Ekman pumping in (4.10) of chapter 2 is used with the maximum w_1 and w_2 being -0.5 and -1.5 respectively. Before the spin-up at $t = 0^-$, the initial state is the steady thermocline under w_1, in which the lower layer is motionless in the shadow zone. The circulation immediately after the spin-up $t = 0^+$ is shown in Fig.3.2a. Wave fronts x_F, f_F and B have not moved yet (dot-connected lines in each panel). The interface (solid lines in the upper panel) remains unchanged because baroclinic waves and advection have not developed yet. However, barotropic waves have passed across the basin and an enhanced new Sverdrup flow $v_B = fw_2$ has been established (dashed lines in the upper panel). This increased barotropic flow then intensifies the anticyclonic gyres in both layers (upper and lower layer pressures are in solid and dashed lines respectively in the middle panel). In the shadow zone, the lower layer waters are no longer motionless. They start to move southward (the lower layer flow in the shadow zone is more clearly shown in solid lines in the lower panel). These waters penetrate towards the lower $q_2 = f/(1-h)$ isolines (dashed lines in the lower panel). The penetration implies a positive lower layer potential vorticity (q_2) advection ($-\vec{v_2} \cdot \nabla(\frac{f}{1-h}) > 0$), which must produce a local increase of q_2, i.e. a local deepening of the upper layer thickness. Physically, with a spin-up, the anomalous Ekman pumping is downward, i.e. $\Delta w_e = w_2 - w_1 < 0$. After the barotropic adjustment, this downward Δw_e compresses the planetary vortex tube and produces an additional barotropic southward flow all over the basin. Therefore, the anticyclonic gyre is intensified in both layers. In particular, in the shadow zone where layer two waters were at rest before the spin-up, now waters move southward.

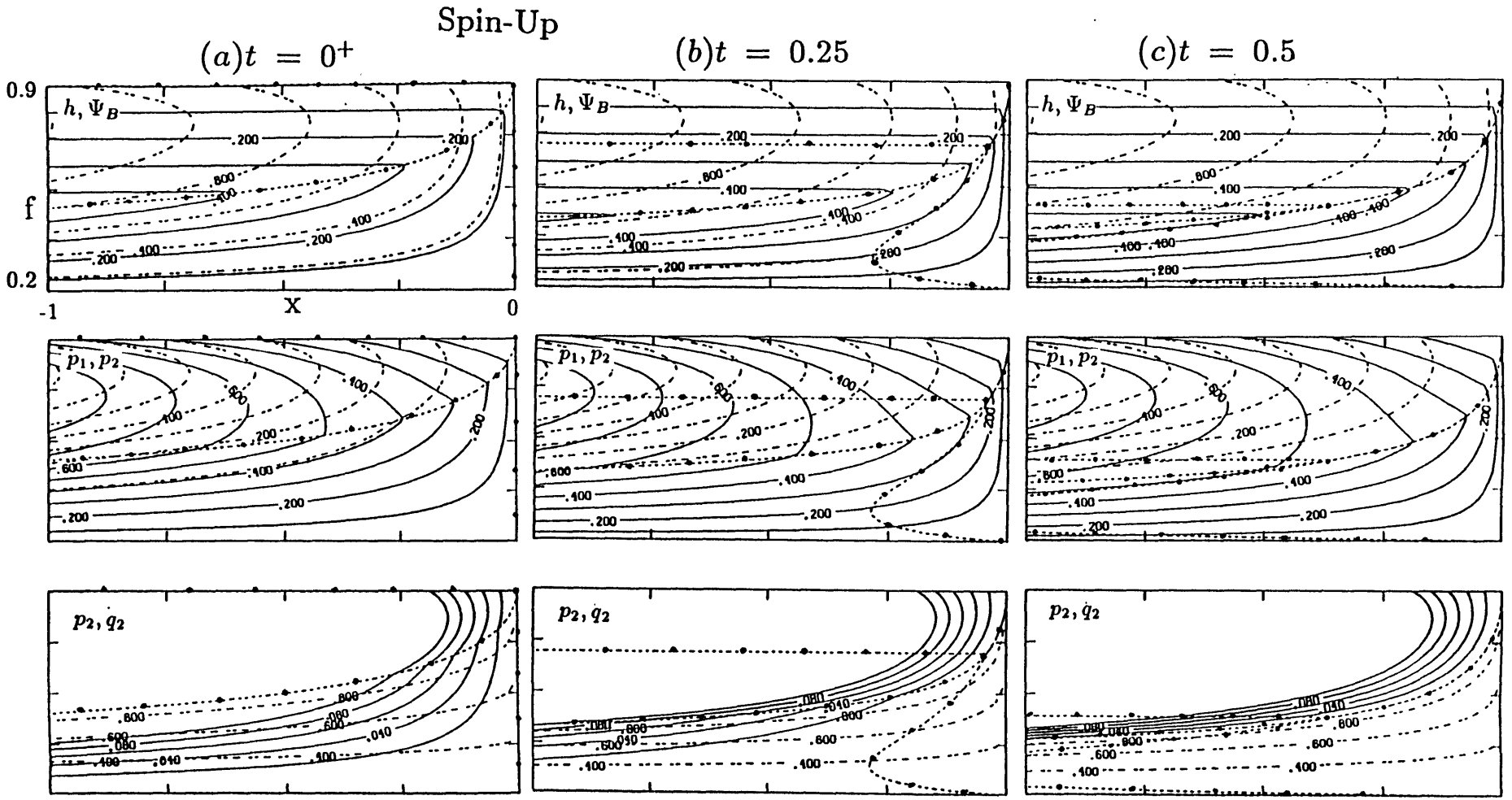

Fig.3.2: Spin-up from a maximum Ekman pumping $max(w_1) = -0.5$ to $max(w_2) = -1.5$. The parabolic Ekman pumping in (4.10) of chapter 2 is taken with other parameters as $f_0 = 0.9$, $f_s = 0.2$. $x_w = -1$. In all cases, the wave fronts x_F, f_F, B are labeled. (a) Immediately after the spin-up at $t = 0^+$. The barotropic adjustment has finished while the baroclinic adjustment was has not started. The upper panel shows the upper layer depth in solid lines (contour interval=0.1) and the barotropic streamfunction in dashed lines (contour interval=0.2). The middle panel shows the upper layer pressure (or streamfunction) in solid lines (contour interval= 0.1) and the lower layer pressure in dashed lines (contour interval=0.1). The lower panel shows the lower layer pressure (solid lines) below $p_2 = 0.1$ (which is the smallest dashed contour in the middle panel. The lower layer potential vorticity (contour interval=0.2) is plotted by dashed lines in the lower panels. (b) and (c) the same as (a) except at time in order $t = 0.25, 0.5$. Wave fronts propagate to establish new shadow zone and ventilated zone. The thermocline is deepening in the original shadow zone. In (c), the new ventilated thermocline has almost been established over the entire basin except at the southwestern corner.

The succeeding baroclinic development is plotted in Fig.3.2b,c. Fig.3.2b illustrates a later time $t = 0.25$. Compared with Fig.3.2a, now the upper layer has deepened while the barotropic flow remains unchanged (upper panel). The associated anticyclonic thermal wind intensifies the upper layer flow and reduces the lower layer flow (middle panel). There is always flow penetrating from the original ventilated zone to the original shadow zone (lower panel). The flow tends to push old waters in the original shadow zone further south-westward and to replace part of the waters. The boundary wave front x_F radiates westward and catches the newly replaced water as well as the remaining water in the original shadow zone to establish a smaller new shadow zone. On the other hand, the advection front f_F advances southward. Accompanied by a stronger subducted flow caused by the stronger w_2, f_F builds up a larger new ventilated zone. The internal front B migrates slightly eastward to expand the original ventilated zone due to the increased Ekman pumping.

Fig.3.2c is for an even later time $t = 0.5$. The upper layer further deepens in the original shadow zone (upper panel). x_F and f_F continue to propagate to enlarge the new shadow zone and ventilated zone respectively, at the expense of the original shadow zone and ventilated zone. The new ventilated thermocline is almost established over the gyre except in the southwestern corner. In the new shadow zone, the lower layer is again at rest. If the time is long enough, one can imagine that the new ventilated thermocline will be established over the entire gyre.

The opposite spin-down process is shown in Fig.3.3. Before the spin-down ($t = 0^-$), the initial state is similar to the final state of the previous spin-up in Fig.3.2c (except in the southwestern corner). After the spin-down at $t = 0^+$ in Fig.3.3a, compared with the initial stage, the interface remains unchanged. But, the anticyclonic barotropic circulation is reduced (upper panel); so are the anticyclonic gyres in both layer (middle panel). Moreover, a cyclonic gyre emerges in the southern part, which includes a northward branch of flow in the original shadow zone and a south-westward return flow in the original ventilated zone (the dashed lines in the middle panel, or more clearly the solid lines in the lower panel.) As a result, there are two counter-rotating gyres in the lower layer. Its physics is opposite to the spin-up case. Now the anomalous Ekman pumping is upward, i.e. $\Delta w_e = w_2 - w_1 > 0$. Thus, the stretching of planetary vortex tube produces an additional

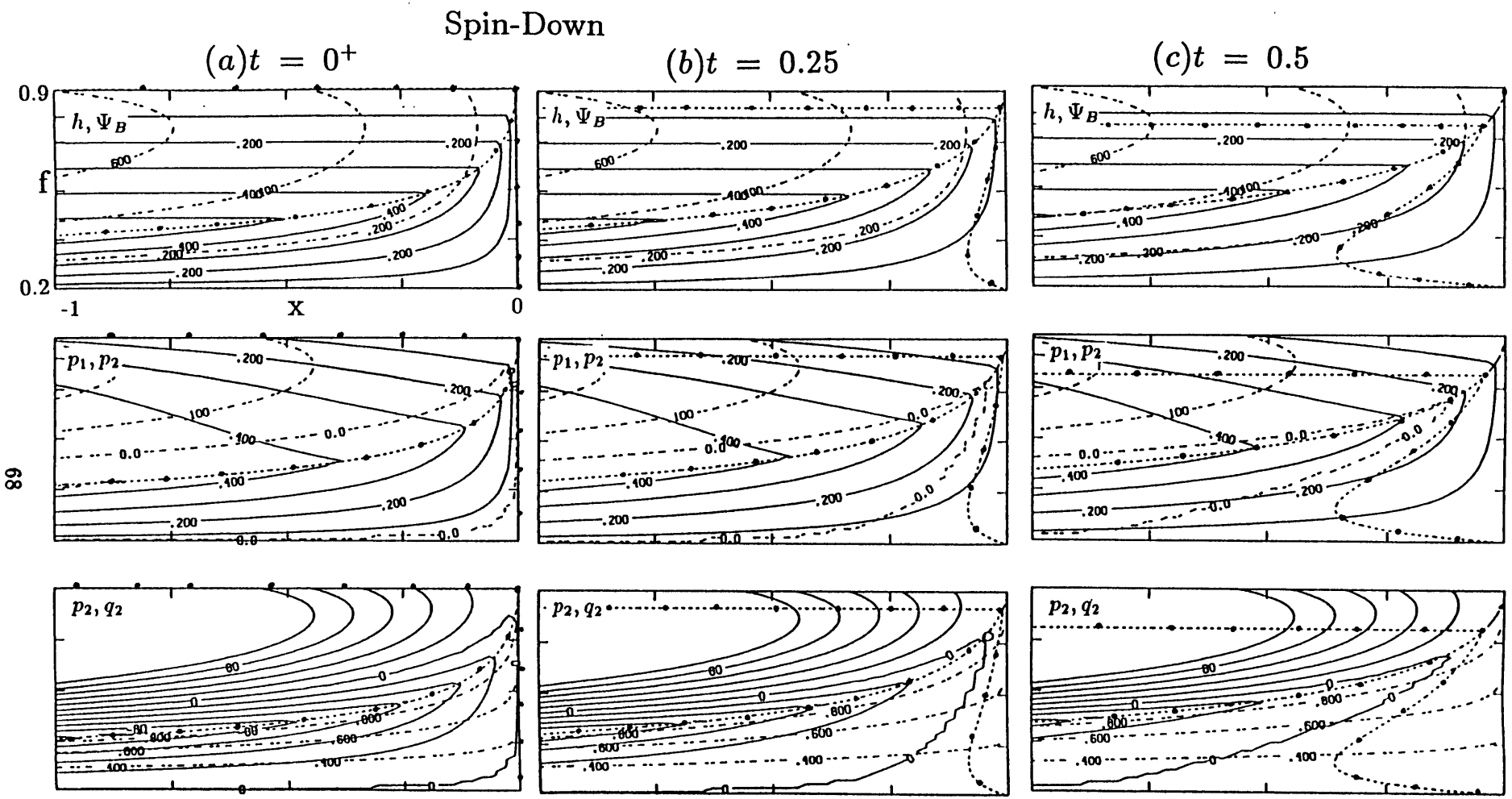

Fig.3.3: The same as Fig.3.2 except for a spin-down from a maximum Ekman pumping of -1.5 to a maximum pumping of -0.5. Now, the interface shallows in the original shadow zone, resulting northward flow in the lower layer. As a result, the lower layer fluid exhibits two counter-rotating gyres: an anticyclonic gyre to the north and a cyclonic gyre to the south. These lower layer circulation differs dramatically from that in the spin-up in Fig.3.2. Now, the x_F and f_F propagate much more slowly than in the spin-up case in Fig.3.2 mainly because of the much slower barotropic flows.

barotropic northward flow, which tends to reduce the anticyclonic gyre. In the shadow zone where the water was motionless before, now the water starts to move northward and therefore creates a cyclonic gyre.

In addition, the barotropic physics discussed above suggests that in the lower layer, the relative strength between the motion in the original ventilated zone and the original shadow zone is proportional to: $v_{2ov}/v_{2os} \sim (w_2 - w_1)/w_2$. Since in a spin-up, $w_2 < w_1 < 0$ while in a spin-down $0 > w_2 > w_1$, it follows that v_{2ov}/v_{2os} is larger in a spin-down than in the opposite spin-up. In other words, in a spin-down, the two counter-rotating gyres may be of comparable strength (once the spin-down is not too weak), while in a spin-up, the motion in the shadow zone is always weak compared with the ventilated zone. This feature can be observed in the middle and lower panels of Fig.3.3a and Fig.3.2a.

Fig.3.3b,c show the following baroclinic evolution. The interface becomes shallow while the barotropic flow remains unchanged (upper panels). The shallowing thermocline causes a weaker thermal wind, implying a weakening upper layer flow (middle panels). The x_F advances westward and expands the new shadow zone. The extra waters for the expanded shadow zone mostly come from the western boundary inflow through the northward lower layer flow in the south. The f_F front progresses slowly with a weaker subducted flow. The established new ventilated zone is smaller because the amount of subducted water is less than that going out to the western boundary. The much slower x_F and f_F (than that in Fig.3.2) are primarily caused by the much reduced barotropic velocity. Now B moves slightly westward to increase the original shadow zone due to the weakened Ekman pumping. In the lower layer (lower panels), in contrast to the spin-up, now there is always flow penetrating from the original shadow zone to the original ventilated zone, pushing waters northward. After entering the original ventilated zone, the waters turn back south-west. This penetrated water accelerates the water going out to the western boundary in the original ventilated zone.

In the limit of a complete spin-down $w_2 = 0$, after the fast barotropic adjustment, a cyclonic gyre fills out the whole basin to compensate the anticyclonic mass transport in the upper layer, resulting a zero Sverdrup flow. Then, during the slow baroclinic evolution, the thermocline evolves

as a giant purely baroclinic Rossby wave packet with the transports in each layer compensated. This packet propagates westward to cause the thermocline shallowing and deforms after meeting the western boundary.

It is interesting to see the resemblance between the flow pattern in the spin-down case (Fig.3.3) and that driven by a steady warm interface entrainment $w^* > 0$ (Luyten and Stommel,1986; Pedlosky,1986). Physically, this is because in the spin-down case, the shallowing of interface produces an upward velocity (in the shadow zone, advection is usually less important, as seen later) just like an upward entrainment velocity ($w(-h) = -\frac{dh}{dt} + w^* \approx -\partial_t h + w^*$.) Therefore, there is a stretching on the planetary vorticity. Similarly, the flow pattern in a spin-up process resembles that caused by a cold entrainment.

2.3 Dynamic balances and mechanisms

According to the zones formed by characteristics (h_v, h_s, h_{ov}, h_{os}), the dynamic balances in each zone are as follows. In a new ventilated zone, the subducted water produces a strong cold advection to balance the Ekman pumping deepening ($\vec{v}_B \cdot \nabla h = -(1-h)w_e$). In a new shadow zone, the eastern boundary Rossby wave balances the Ekman pumping ($C(h)h_x = -(1-h)w_e$). These two zones are like the steady thermocline case (see (3.6) and (3.7) of chapter 2). In an original ventilated zone, the rapidly varying cold advection dominantly balances the new Ekman pumping, leaving little variability (in the special case of (2.2), there is no variability), i.e. $h_t = -\vec{v}_B \cdot \nabla h - (1-h)w_e = 0$. In the original shadow zone, the dynamic balance is more complicated. Over most of the region, the density advection plays a secondary role. This can be observed in the upper panels of Fig.3.2 and Fig.3.3, where the barotropic flows are almost parallel to h in the original shadow zone. Nevertheless, in a spin-up, there may be a strong warm advection in the south-western corner of the basin. In contrast, in a spin-down, the density advection is always negligible. In the limiting complete spin-down case, $\vec{v}_B = 0$ and thus there is no density advection anywhere. [1]

[1] Under a general Ekman pumping, the sign of the advection is such that: in a spin-up, it is a cold advection (β spiral) in the northern and a warm advection (anti-β spiral) in the southern part of a subtropical gyre. Thus, in the south, the warm advection enhances the deepening due to the Ekman pumping; in the north, the cold advection cancels part of the Ekman pumping deepening. The opposite occurs during a spin-down, i.e. there is a cold advection in the southern part while a warm advection in the northern part. A detailed discussion is not presented here.

Local dynamics

So far, the dynamic balances are discussed according to zones formed by characteristics. The sizes of these zones vary with characteristics. Hereafter, we study the local dynamics (i.e. at a fixed location). This approach will help us to gain a better insight into the dynamics from a more conventional viewpoint.

Before going into further detail, we should realize that in the presence of a time-dependent Ekman pumping $w_e(t, x, f)$, an instantaneous ventilated zone and a shadow zone will vary in their sizes. Therefore, a ventilated zone at one time may be invaded by a shadow zone later and vice versa. Hence, unlike the case for a steady Ekman pumping, it is no longer proper to divide an isopycnal only into a ventilated zone and a shadow zone. Now, it is proper to define the ventilated zone as the instantaneous ventilated zone under the weakest Ekman pumping $(w_e)_{min}$ (the minimum is taken for $t \geq 0$), and to define the shadow zone as the instantaneous shadow zone under the strongest Ekman pumping $(w_e)_{max}$. This ventilated zone will not be invaded by any instantaneous shadow zone, and vice versa. Besides, there is a third buffer region, known as the alternative zone, between the ventilated zone and the shadow zone. The alternative zone is occupied by an instantaneous ventilated zone and shadow zone alternatively. Denoting the shadow zone boundaries B under $(w_e)_{max}$ and $(w_e)_{min}$ as B_{max} and B_{min} respectively (see (3.3) or (4.3)), the above three zones can be expressed as:

$$Shadow\ Zone \ : \quad x_{Bmax} < x, \tag{2.9a}$$

$$Alternative\ Zone \ : \quad x_{Bmin} < x < x_{Bmax}, \tag{2.9b}$$

$$Ventilated\ Zone \ : \quad x < x_{Bmin}. \tag{2.9c}$$

Fig.3.4g displays schematically the three zones. The local dynamics in each zones is also plotted in Fig.3.4 and will be examined as follows. The key for the evolution is that the density advection changes rapidly (or barotropically) with the Ekman pumping, while the Rossby wave changes slowly (baroclinically).

The local dynamics in the shadow zone

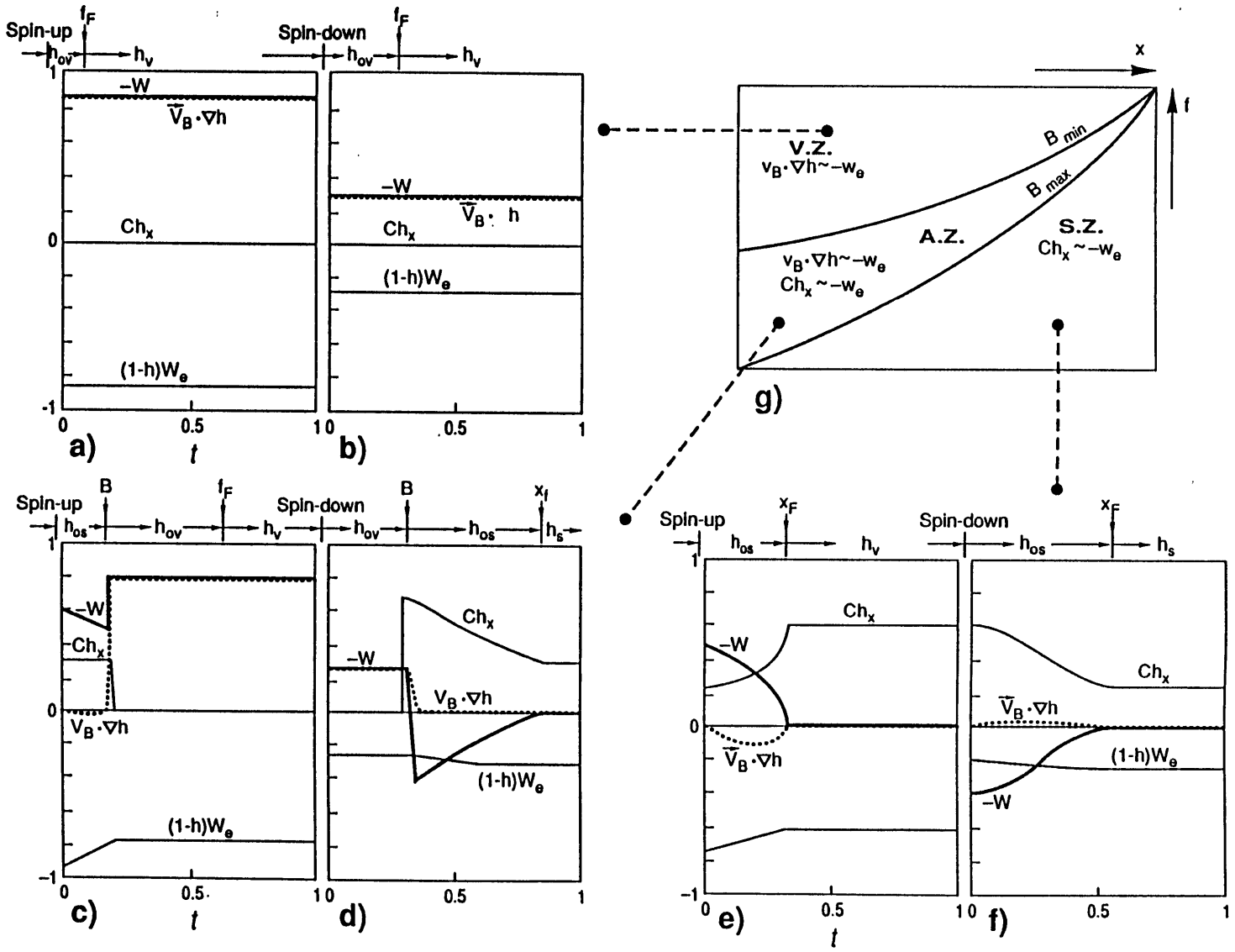

Fig.3.4: The evolution of different dynamic terms at a fixed location in different regions. The spin-up is the one in Fig.3.2 and the spin-down in the one in Fig.3.3. The arrival of each wave front is also marked (by arrow) on the top of each figure. a) spin-up at (x,f)=(-0.5,0.85) (in the ventilated zone); b) the same as a) except with a spin-down. c) spin-up at (x,f)=(-0.5,0.5) (in the alternative zone); d) the same as c) but for a spin-down. e) spin-up at (x,f)=(-0.5,-0.35) (shadow zone); f) the same as e) except a spin-down. g) a schematic figure of different zones for local dynamics and the major dynamics balances in each zone.

An example of the shadow zone dynamics is shown in Fig.3.4e,f., in which, the evolution of the four dynamic terms: the effective Ekman pumping, the Rossby wave, the density advection and the vertical velocity at the interface, are depicted at the location $(x, f) = (-0.5, 0.35)$. These four quantities can be proven to be related by

$$w|_{z=-h} = -[h_t + \vec{v_2} \cdot \nabla h] = -[h_t + \vec{v_B} \cdot \nabla h] = Ch_x + (1-h)w_e. \tag{2.10}$$

Here, we have used (1.7a) and $\vec{v}_2 = \vec{v}_B - h\vec{v}_T, \vec{v}_T = \nabla h \times \vec{k}/f$. Fig.3.4e shows the spin-up in Fig.3.2 and Fig.3.4f shows the spin-down in Fig.3.3. Thus, Fig.3.4e and f can be thought as a cycle with one spin-up and one spin-down. The arrival of each wave front is also marked on the top of the figures. Before the spin-up, the weaker Ekman pumping is balanced by the Rossby wave from the eastern boundary to maintain the old steady shadow zone with no vertical velocity at the interface (as shown in the final time of Fig.3.4f). After the spin-up, the Ekman pumping is suddenly increased while the baroclinic process (the Rossby wave) has not developed yet (Fig.3.3e). The excess Ekman pumping then forces a downward vertical velocity barotropically (through the barotropical divergence field), which in turn compresses the planetary vortex tube to make the originally motionless lower layer flow move southward. This location now is in the original shadow zone where the downward velocity starts to deepen the upper layer. This deepening suppresses the effective Ekman pumping, but causes an increase of the Rossby wave effect (both h and h_x increase). Therefore, the difference between the two mechanisms decreases monotonically. (2.10) then means that the vertical velocity is reduced, so is the lower layer southward flow and the local deepening. This baroclinic process continues until the difference between the Ekman pumping and Rossby wave vanishes at about $t \approx 0.3$, which is also the time when the newly excited eastern boundary Rossby wave (x_F) just reaches this location. Accordingly, the vertical velocity vanishes and the a steady state is achieved. Afterwards, the eastern boundary Rossby wave begins to balance the Ekman pumping to maintain the new shadow zone. The warm advection develops to about one-third of the vertical velocity at about $t \approx 0.2$, contributing a significant part of the vertical velocity. Later, it decays with time because of eastern boundary waves.

The above steady shadow zone continues until the spin-down occurs in Fig.3.4f. A sudden decrease of the Ekman pumping takes place barotropically but the Rossby wave term has not

changed yet. Therefore, the excess Rossby wave term begins to produce an upward velocity at the interface, which forces a northward flow in the lower layer. Since the advection is initially zero, this upward velocity mostly consists of a local shallowing. This location is once again in original shadow zone. The subsequent baroclinic process is opposite to the spin-up above. The shallowing increases the effective Ekman pumping, but decreases the Rossby wave effect and causes a weakening baroclinic thermal wind. Until about $t \approx 0.7$, a new balance is reached between the both mechanisms. The Rossby waves generated along the eastern boundary due to the spin-down also has just reached this point. Later, these waves balance the Ekman pumping and thus sustain the new steady shadow zone. Different from the spin-up, the advection is a cold advection and remains weak.

The local dynamics in the ventilated zone

Fig.3.4a,b give an example in the ventilated zone at the point $(x, f) = (-0.5, 0.85)$. The dynamics differs dramatically from that in the shadow zone. Before the spin-up, the cold advection balances the Ekman pumping to maintain the old ventilated zone. A strong downward velocity exists to force a southward motion in the lower layer. However, there is no local variability because the downward velocity solely consists of the advection $w(-h) = -\vec{v}_2 \cdot \nabla h$ (see (2.10)). In other words, the warm vertical advection balances the cold horizontal advection. After the spin-up, the position is in an original ventilated zone. Both the Ekman pumping and the cold advection endures a barotropic response and thus are increased linearly by the same amount. Consequently, a new balance is reached without any local baroclinic variability. In the present case with a flat bottom and a zonal profile, there is no baroclinic Rossby wave after the barotropic response. The wave front f_F from the outcrop line arrives at this location earlier than $t \approx 0.1$, which brings the newly subducted cold water. Later on, a new ventilated zone is achieved between this new cold advection and the Ekman pumping. The spin-down in Fig.3.4b can be similarly discussed. It should be noted that for a more general case such as a tilted outcrop line, Rossby wave activities would enter. The original ventilated zone and the new ventilated zone will be different from each other. Therefore, there will be some baroclinic evolution. Nevertheless, the advective nature of the ventilated zone

(see section 6 of chapter 2) suggests that the dominant balance is still between the cold advection and the Ekman pumping.

Similar analysis applies to the alternative zone, but is not presented here (see Fig.3.4c.d). Now, the internal wave front B can abruptly shut off the Rossby wave or the advection when B passes through one location. One can find that the alternative zone is controlled by the advection and Rossby wave alternatively. Both the thermocline and circulation vary dramatically. Nevertheless, the size of the alternative zone is usually smaller than the other two (see Fig.3.2 and Fig.3.3).

In summary, we see the intrinsic dynamic difference between the ventilated zone and the shadow zone. In a ventilated zone, the advection plays a crucial rule. The advection varies rapidly with the Ekman pumping to achieve a new steady balance, leaving little thermocline variability. However, in the shadow zone, the baroclinic Rossby wave evolves slowly (or baroclinically) while the Ekman pumping has changed rapidly. This mismatch of time scales produces an imbalance in the steady dynamic balance and therefore results in strong thermocline variability. In addition, the circulation also changes significantly. For instance, in the shadow zone, the lower layer is no longer motionless. The flow in the lower layer there changes its direction from a southward flow in a spin-up to a northward flow in a spin-down. Later, this will also be seen during a periodic Ekman pumping case, with the increasing and decreasing Ekman seasons corresponding respectively to spin-up and spin-down.

3 Periodic Ekman Pumping: I. Linear Theory

From this section, we investigate thermocline variability under a periodic Ekman pumping. First, in this section, we study the linear theory. Later, it will be shown that with an annual forcing or a weak decadal forcing, the linear solution approximates the fully nonlinear solution excellently. The linear theory here highlights the physics of planetary wave propagation in the presence of a basic ventilated thermocline. One issue we are particularly interested in is the relative importance of the local Ekman pumping and remote eastern boundary waves.

The two-layer model gives the non-dimensional equation governing the upper layer thickness as (see (1.7b) of chapter 2):

$$h_t + \nabla \cdot (\vec{v_B} h) + C(h) h_x = -w_e. \tag{3.1}$$

with the barotropic velocity $(u_B, v_B) = [-(f^2 w_e)_f x/f, f w_e]$ and the planetary wave speed $C(h) = -h(1-h)/f^2$. The periodic Ekman pumping is assumed of the form:

$$w_e(f,t) = w_0(f) + a w_1(f,t). \tag{3.2a}$$

Here the perturbation forcing w_1 is periodic in time with a period T and has a zero mean. w_0 is the time-mean Ekman pumping

$$w_0(f) = < w_e(f,t) > \sim O(1), \quad where \ < > = \frac{1}{T}\int_0^T dt. \tag{3.2b}$$

Further, the perturbation Ekman pumping is chosen to be

$$w_1 = w_0(f) g(t), \quad where \ g(t) = \sin \omega t. \tag{3.2c}$$

Therefore, a represents the strength of the perturbation forcing. With (3.2c), the total Ekman pumping $w_e = w_0(f)(1 + a \sin \omega t)$ varies in its intensity but not its position. ω is the non-dimensional frequency of the forcing. For a mean thermocline depth $H = 600$ m, the dimensional time scale $T_w = H/W$ (see (1.5a) of chapter 2) is about 20 years. This gives the dimensionless frequencies: *annual* : $\omega \sim 100$, *decadal* : $\omega \sim 10$. In physical terms, at an annual frequency, it takes a planetary wave several periods to cross the ocean basin, while at a decadal frequency it takes a planetary wave less than or about one period to reach the western boundary.

3.1 The Linear Solution

With weak perturbation $a \ll 1$, h can be expanded as

$$h = h_0 + a h_1 + a^2 h_2 + ... \tag{3.3}$$

If the barotropic velocity is decomposed into the time-mean component $\vec{v}_{B0}$ and the perturbation component $\vec{v}_{B1}$, the Sverdrup relation and the Ekman pumping (3.2a) require that

$$\vec{v_B} = \vec{v}_{B0} + a\vec{v}_{B1}; \quad \nabla \cdot \vec{v}_{B0} = -w_0, \quad \nabla \cdot \vec{v}_{B1} = -w_1. \tag{3.4}$$

The basic state

Substituting (3.2a),(3.3) and (3.4) into (3.1), at the leading order, we obtain the basic state equation:

$$\nabla \cdot (v\vec{_{B0}} h_0) + C(h_0) h_{0x} = -w_0. \tag{3.5}$$

This gives the steady LPS thermocline (Luyten *et.al.*,1983). (3.5) has been solved in (4.8b,c,d) of chapter 2 (using $w_1 = w_2$). The characteristic solution for the basic state is

$$s = \int_{f_i}^{f} \frac{df}{f w_0}, \quad or \quad f = \hat{f}(s, f_i), \tag{3.6a}$$

$$\frac{f}{1-h_0} = \frac{f_i}{1-h_i}, \tag{3.6b}$$

$$2f^2 w_0(f) x = 2f_i^2 w_0(f_i) x_i + h^2 - h_i^2. \tag{3.6c}$$

For simplicity, we will adopt: a zonal outcrop line at $f = f_o$, a meridional eastern boundary at $x = 0$ and a flat interface at the eastern boundary $h_e(f) = H_s$. On an unventilated interface ($H_s > 0$), the interface depth at the northern boundary of the subtropical gyre ($f_n = 1$) is also H_s. A Rhines-Young pool exists west of the shadow zone (Rhines and Young,1982; Pedlosky and Young,1983). Hence, in the ventilated zone (for ventilated interfaces) or the pool zone (for unventilated interfaces), the initial conditions for characteristics are $f_i = f_o, h_i = H_s$. The solution is derived from (3.6b) directly as

$$h_0 = 1 - (1 - H_s)\frac{f}{f_o}, \qquad for \;\; x < x_{b0}(f); \;\; in \; V.Z.(if \; H_s = 0) \; or \; P.Z.(if \; H_s > 0). \tag{3.7a}$$

In the shadow zone, the initial condition is $x_i = 0, h_i = H_s$. (3.6c) yields the solution

$$h_0^2 = H_s^2 + 2f^2 w_0(f) x, \quad for \; x > x_{b0}(f) \; in \; S.Z. \tag{3.7b}$$

Here x_{b0} is the shadow zone boundary of the basic thermocline and is formed by the characteristics initiating from the corner $x_i = 0, f_i = f_o$, i.e.

$$x_{b0}(f) = \frac{[1 - (1 - H_s)\frac{f}{f_0}]^2 - H_s^2}{2f^2 w_0(f)}. \tag{3.7c}$$

(3.7) are generalized solutions for the steady thermocline with a non-vanishing $h_e(f) = H_s = constant$ (compared with the case of $h_e = 0$ in (3.2), (3.3) and (3.4) in chapter 2). Finally, we

discuss the characteristics. This turns out to be necessary in deriving explicit solutions at higher orders. Through any point (x,f), we can trace the characteristic curve back to its initial position (x_i, f_i) (on the outcrop line or eastern boundary). By virtue of (3.6b,c), the initial position can be calculated explicitly as

$$f_i = F_i(x,f) \equiv f\frac{1-H_s}{1-h_0(x,f)}, \tag{3.8a}$$

$$x_i = X_i(x,f) \equiv \frac{2f^2 w_0(f)x - h_0^2(x,f) + H_s^2}{2F_i^2(x,f)w_0(F_i)}. \tag{3.8b}$$

where h_0 is determined in (3.7). Between (x,f) and its initial position (x_i, f_i), the distance along the characteristic coordinate can be derived from (3.6a) and (3.8a) explicitly as

$$s = S(x,f) = \int_{F_i(x,f)}^{f} \frac{df}{f w_0(f)}. \tag{3.8c}$$

Indeed, for the steady basic thermocline, the characteristics are isolines of potential vorticity. In the ventilated zone, they are also the streamlines.

The equation for linear disturbances: a decaying effect

To obtain the linear solution, we first derive its governing equation at the next order from (3.1) and (3.3).

$$h_{1t} + \vec{v}_{B0}\cdot\nabla h_1 + C(h_0)h_{1x} - \mu h_1 = -(1-h_0)w_1 - \vec{v}_{B1}\cdot\nabla h_0, \tag{3.9a}$$

where

$$\mu \equiv \mu_a + \mu_R, \qquad \mu_a = -\nabla\cdot\vec{v}_{B0}, \quad \mu_R = -\nabla\cdot\vec{C}(h_0) = -\partial_x C(h_0) = \frac{(1-2h_0)}{f^2}h_{0x}. \tag{3.9b}$$

Since we only consider the forced response after the initial adjustment, the initial conditions for characteristics start either from the outcrop line (for the ventilated zone) or from the eastern boundary (for the shadow zone), i.e.

$$h_{1i} = 0, f_i = f_0 \quad \textit{in V.Z. or P.Z.}; \qquad h_{1i} = 0, x_i = 0 \quad \textit{in S.Z.} \tag{3.9c}$$

The two terms on the right hand side of (3.9a) are the perturbation Ekman pumping and the advection of perturbation velocity on the mean thermocline, respectively. The left hand side has the same characteristics or wave rays as the basic state in (3.5). Hence, linear waves propagate along

the basic state characteristics (3.8). This occurs because for weak perturbations, the alteration of characteristics due to nonlinearity is small. However, if the perturbation becomes strong, the characteristics may be changed substantially due to either the barotropic-baroclinic interaction ($\vec{v_B} \cdot \nabla h$) or nonlinear Rossby wave velocity ($C(h)$). These nonlinear effects will be discussed in the next section.

The most interesting feature in (3.9a) is the term $-\mu h_1$, which is caused by the divergence of the characteristic velocity as shown in (3.9b). Note (3.7a) in the ventilated (or pool) zone, (3.9b) yields $\mu_R = 0$. This leads to

$$\mu = \mu_a = -\nabla \cdot \vec{v}_{B0} = w_0 < 0 \qquad in\ V.Z.\ or\ P.Z. \tag{3.10a}$$

where we have used the Sverdrup relation for the basic state in (3.4). In the shadow zone, noting (3.7b) and (3.9b), we have $\mu_R = w_0(\frac{1}{h_0} - 2)$. Combining this with (3.10a), we obtain

$$\mu = \mu_a + \mu_R = w_0 + w_0(\frac{1}{h_0} - 2) = \frac{w_0}{h_0}(1 - h_0) < 0. \tag{3.10b}$$

Therefore, $\mu < 0$ always holds. This, as suggested by (3.9a), will make a disturbance decay along a characteristic line. Physically, this occurs because, with an approximate energy flux conservation, a divergent group velocity field $\mu = -\nabla \cdot (\vec{v}_B + \vec{C}) < 0$ (see (3.9b)) implies that the energy of waves should decrease downstream. (3.10a,b) show that this divergent group velocity is mainly caused by the divergent barotropic flow field. Nevertheless, on shallow interfaces ($h_0 \to 0$), the Rossby wave velocity field has a dominant divergence and imposes a strong decay effect on disturbances ($\mu_R \sim \frac{1}{h_0} \to \infty$). This occurs because of the rapid deepening of the basic thermocline near the eastern boundary on shallow interfaces.

The characteristic equations for (3.9a) are

$$\frac{dt}{ds} = 1, \tag{3.11a}$$

$$\frac{df}{ds} = f w_0(f), \tag{3.11b}$$

$$\frac{dx}{ds} = -\frac{x}{f}[f^2 w_0(f)]_f - \frac{h_0(1 - h_0)}{f^2}, \tag{3.11c}$$

$$\frac{dh_1}{ds} = \mu h_1 - (1 - h_0)w_1 - \vec{v}_{B1} \cdot \nabla h_0, \tag{3.11d}$$

where $h_0(x, f)$ is given in (3.7a,b) and μ is given in (3.10a,b). (3.11a,b,c) have been solved in the basic state as in (3.6) (or (3.8)). Therefore, the linear wave can be obtained from the linear ordinary differential equation (3.11d) alone.

The linear solution

In the absence of a mean Ekman pumping, the basic state is at rest over the whole gyre. With an Ekman pumping, the first significant change is the creation of a ventilated zone in the basic thermocline structure. In this zone, the advection of the subducted waters dominates while Rossby wave activity is weak. Indeed, using Sverdrup relation $v_{B1} = fw_1$ and (3.7a), the perturbation forcing on the right hand of (3.9a) becomes $-(1 - h_0)w_1 - \vec{v}_{B0} \cdot \nabla h_0 = 0$ for $x < x_{b0}$. This zero perturbation forcing, together with the zero boundary condition in (3.9c), yields no thermocline variability in the ventilated zone, [1] i.e. $h_1 = 0$ for $x < x_{b0}$. This reflects the fact that in the ventilated zone, the perturbation Ekman pumping is exactly balanced by the perturbation density advection. It should be noted that the conclusion also applies to the pool zone on an unventilated interface because of the dominant advection there.

In the following, we will focus on the variability in the shadow zone. In the shadow zone, if the Ekman pumping (3.2c) is adopted, we find that the perturbation density advection vanishes, i.e. $\vec{v}_{B1} \cdot \nabla h_0 = g(t)\vec{v}_{B0} \cdot \nabla h_0 = 0$, where we have used (3.7b). The remaining perturbation forcing is the perturbation Ekman pumping

$$-(1 - h_0)w_1 = -(1 - h_0)w_0(f)g(t). \tag{3.12}$$

If $ds = df/fw_0(f)$ in (3.11b) is used, the solution to (3.11d) is represented in the characteristic coordinate as

$$\hat{h}_1 = \hat{h}_1(s, t_i, f_i) = -(\frac{1}{\hat{h}_0})(\frac{1 - \hat{h}_0}{\hat{f}}) \int_0^s g(t_i + \tilde{s})\hat{f}(\tilde{s}, f_i)w_0(\hat{f})\hat{h}_0(\tilde{s}, f_i)d\tilde{s}, \tag{3.13}$$

where $\hat{f}$ is given in (3.6a). $\hat{h}_0$ is the h solution in the characteristic coordinate, which can be derived from (3.6a,b) as

$$\hat{h}_0(s, f_i) = 1 - (1 - H_s)\frac{\hat{f}(s, f_i)}{f_i}. \tag{3.14}$$

[1] With a general Ekman pumping $w_e(x, f, t)$, the absence of variability is also true once the outcrop line is zonal. But, I can not prove it in this linear equation. In a nonlinear case, it is very easy to prove. See discussion about equation (4.5) in the next section.

where $h_e = H_s$ has been used.

If (3.8) is used, (3.13) can be expressed explicitly in (x, f) coordinate as

$$h_1 = h_1(x, f, t) = -(\frac{1}{h_0})(\frac{1-h_0}{f}) \int_0^{S(x,f)} g(t - S(x, f) + \tilde{s})\hat{f}(\tilde{s}, F_i)w_0(\hat{f})\hat{h}_0(\tilde{s}, F_i)d\tilde{s}, \qquad (3.15)$$

where $t_i = t - s = t - S(x, f)$ has been used. In (3.15), the first factor $\frac{1}{h_0}$ is caused by the decaying effect due to the divergent characteristic velocity field. Indeed, using (3.7b), (3.14) and $ds = df/fw_0(f)$ (from (3.11b)), we have

$$exp[-\int_0^s \mu ds] = exp[-\int_{f_i}^f \frac{\mu(f)df}{fw_0(f)}] = \frac{h_i}{\hat{h}_0}. \qquad (3.16)$$

Along a characteristic line, h_i is fixed while $\hat{h}_0$ deepens. Therefore, (3.16) represents the decaying factor. The second factor, however, remains unchanged along a characteristic line because of potential vorticity conservation (3.11c).

The linear solution (3.15) (or (3.13)) is derived for weak perturbations $a \ll 1$. However, we will find that for an annual frequency, (3.15) agrees with the fully nonlinear solution excellently even with a strong forcing $a \sim 1$. This point will be elaborated in the next section. For the time being, for the comparison between a linear solution and a nonlinear solution, it suffices to show an example. Fig.3.5 displays one example of some instantaneous zonal sections under a strong annual forcing ($\omega = 50, a = 0.5$). (The amplitude $a = 0.5$ has been observed for real annual Ekman pumping field (Levitus, 1988). In Fig.3.5a, two instantaneous h profiles (solid lines) on September ($\omega t = 0$) and March ($\omega t = 180^o$) are shown on the interface with $H_e = 0$. It is seen that the variability is weak. In Fig.3.5b, the perturbations $Dh = h - h_0$ of Fig.3.5a are shown (h_0 is the steady thermocline under the time-mean Ekman pumping w_0 or h_0 is the basic state in (3.7)). The linear solutions (in dot lines) approximate the nonlinear solution (in solid lines) excellently. (The nonlinear solutions will be derived in the next section.) Other figures in Fig.3.5 are similar to Fig.3.5a,b, except for deeper interfaces (with $H_e = 0.1$ in Fig.3.5c,d and $H_e = 0.6$ in Fig.3.5e,f).

3.2 Thermocline Evolution: Local or Remote Response ?

Now, we analyze the thermocline evolution. To have a better understanding of the linear response, we first derive an approximate expression for the linear wave in (3.15). Integrating the characteristic

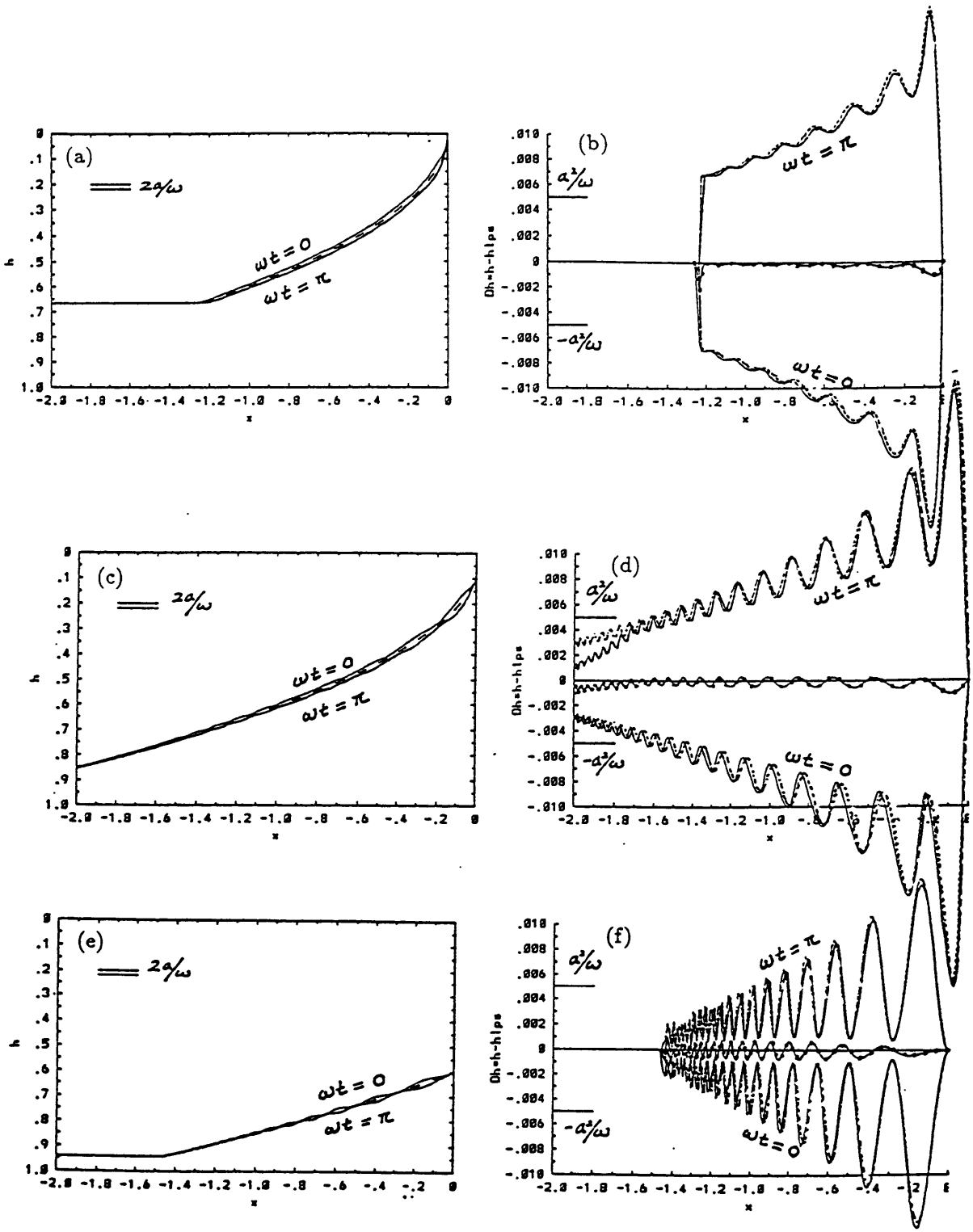

Figure 3.5: Synoptic zonal sections of interfaces (a),(c) and (e) and deviations $Dh = h - h_{steady}$ (b),(d) and (f) under a strong annual Ekman pumping $\omega = 50, a = 0.5$. The Ekman pumping function is $w_0(f) = W_0/f$, the latitude is $f = 0.3$ and $w_0(f) = -2$. a),b) $H_s = 0$; c),d)$H_s = 0.1$; e),f)$H_s = 0.6$. The solid lines are the nonlinear solutions.The dotted lines are linear solutions. The dashed lines are steady LPS solutions. The dot-connected lines are time-mean disturbances $< Dh >$.

form of solution in (3.13) by parts and using (3.8) (see appendix A), we obtain an approximate solution to (3.15) at $1/\omega$ order as (for $\omega \gg 1$)

$$h_1 = \frac{(1-h_0)w_0(f)}{\omega}[\cos\omega t - A\cos(\omega t - \Phi)] + O(\frac{1}{\omega^2}) \tag{3.17a}$$

where A and Φ are functions of x and f:

$$A = \frac{H_s F_i w_0(F_i)}{h_0 f w_0(f)}, \quad \Phi = \omega(t - t_i) = \omega S(x, f). \tag{3.17b}$$

Here, F_i, h_0 and S are given in (3.8b), (3.7b) and (3.8c) respectively. The solution is good for high frequency when the interface is not very close to the surface (see appendix A, where a solution accurate to $1/\omega^2$ is derived). The first term in (3.17a) is the local response, which lags the forcing (3.2c) by 90^o in phase. The amplitude is

$$\Delta h_{local} \approx \frac{a(1-h_0)w_0(f)}{\omega}. \tag{3.18}$$

This means that the local response decreases westward because the basic state thermocline deepens westward. This in turn weakens the effective Ekman pumping because the interface is further away from the surface towards the west. In comparison, the special case without a mean Ekman pumping has a flat basic thermocline interface and therefore the local response does not vary along a latitude.

The second term in (3.17a) is the Rossby wave which is forced mainly along the eastern boundary, where $A = 1$ (because $F_i = f, h_{os} = H_s$) and therefore the eastern boundary condition (3.9c) is satisfied. The presence of a mean Ekman pumping changes the boundary wave significantly in both its amplitude and phase. The mean Ekman pumping creates a ventilated zone which inhibits the invasion of boundary waves.

The wave amplitude decreases along a wave ray due to the divergent group velocity field. In fact, in (3.17a), we have the wave amplitude as

$$\Delta h_{wave} \approx \frac{a(1-h_0)w_0(f)}{\omega}\frac{H_s}{h_0}\frac{F_i}{f}\frac{w_0(F_i)}{w_0(f)} = \frac{(1-h_i)aw_0(F_i)}{\omega}exp(-\int_0^s \mu ds), \tag{3.19}$$

where we have used $h_i = H_s$ and (3.16). (3.19) illustrates the physics of the boundary wave elegantly. The boundary wave is excited along the eastern boundary by the perturbation forcing $(1-h_i)aw_0(F_i) = (1-h_i)w_1$ (see (3.12)). This forcing produces a local amplitude $(1-h_i)aw_0(F_i)/\omega$,

which decays according to $exp(-\int_0^s \mu ds) = h_i/h_0$ along a characteristic line due to the divergent group velocity field. For a shallow interface ($H_s \ll 1$), the decaying effect is especially strong near the eastern boundary (see discussion after (3.10b)).

The phase Φ of the free wave is also changed substantially. For example, without an Ekman pumping, the phase is always in a β dispersion orientation $\Phi \sim 1/xf^2$ (Schopf *et. al*, 1981). But, with an Ekman pumping, near the southern boundary of a subtropical gyre, the wave front varies from an β dispersion (northeast-southwest) to an northwest-southeast orientation. More details will be given in section 2 of chapter 5. Here, we only need to remember that (3.17b) implies that the Φ is approximated at the leading order by $S(x, f)$ (which is the wave front during a spin-up or spin-down as shown in last section).

Local or remote responses ?

Now, we turn to our fundamental question concerning thermocline variability: whether the disturbance is caused by a local response or a remote response. Under a local response, an interface is simply forced by the perturbation Ekman pumping to move up and down with a phase lag of 90^o to the forcing. On the other hand, remote responses have two mechanisms: the advection due to remotely subducted waters at the outcrop line and the eastern boundary Rossby waves.

In a ventilated zone, we have seen that the local response is as important as the remote advection and both tend to balance each other. This cancellation results in the absence of baroclinic variability.

In a shadow zone, the density advection is weak. The question then becomes the classical question: which is more important, the local response or the eastern boundary wave ? The solution (3.17a) consists of a local response and a remote response. The remote response is mainly caused by the eastern boundary waves. A represents the relative magnitude of the boundary wave with respect to the local response. $A < 1$ gives a local response domination while $A > 1$ a boundary wave domination. In the absence of a mean Ekman pumping, (3.9a) degenerates to

$$\partial_t h_1 + C(H_s) h_{1x} = -(1 - H_s) w_1.$$

where $C(H_s) = -H_s(1-H_s)/f^2$ is independent of x. The solution satisfying the boundary condition in (3.9c) is easily solve as

$$h_1 = \frac{(1-H_s)w_1(f)}{\omega}[cos(\omega t) - cos(\omega t - \frac{\omega}{C(H_s)}x)].$$

This suggests that $A = 1$. (This can also be obtained as the limit of $w_0 \to 0$ in (3.17b).) Thus, the local response has the same magnitude as the boundary wave, or both are equally important. Physically, at the eastern boundary, to cancel the local response and satisfy the eastern boundary condition, the amplitude of the Rossby wave must be the same as the local response. Without a mean Ekman pumping, the thermocline is flat. Thus, towards the interior, both the local response and the Rossby wave will remain their magnitude. Thus, the amplitudes are the same over the entire basin.

However, with a mean circulation, it will be seen that the above conclusion is no longer true. Fig.3.6a,b display two examples of A (solid lines) and the boundary wave phase Φ (dashed lines) with an annual frequency $\omega = 50$. The Ekman pumping takes the form $w_e(f) = W_e(1-f)(f-f_s)$. The solution accurate to $1/\omega^2$ in appendix A is used. Fig.3.6a is on a shallow interface ($H_s = 0.1$) while Fig.3.6b is on a deep interface ($H_s = 0.5$). Two features are salient. First, local responses tend to dominate on the shallow interface while boundary waves dominate on the deep interface. Secondly, local responses are stronger in the northern part of an interface while boundary waves are stronger in the southern part. These two features are also clear in Fig.3.6c,d where the forcing has a decadal frequency $\omega = 5$.

Physically, we can understand the two features from (3.18) and (3.19). First, we note that to satisfy the eastern boundary condition, the amplitudes of both the local response and the remote Rossby wave must equal along the eastern boundary or $A = 1$. Furthermore, with an Ekman pumping, the mean thermocline depth deepens westward as shown by (3.7b). Therefore, (3.18) states that the local response decays westward. On the other hand, (3.19) states that the Rossby wave amplitude also decays towards the west because of the divergent group veolcity field. Therefore, the relative importance of the local and Rossby wave responses depends on which decays less rapidly towards the interior. (3.10b) says that near the surface, the divergent group veolcity is very strong (because of the strong divergent Rossby wave speed $C \sim 1/h_0$), which implies a rapid decay

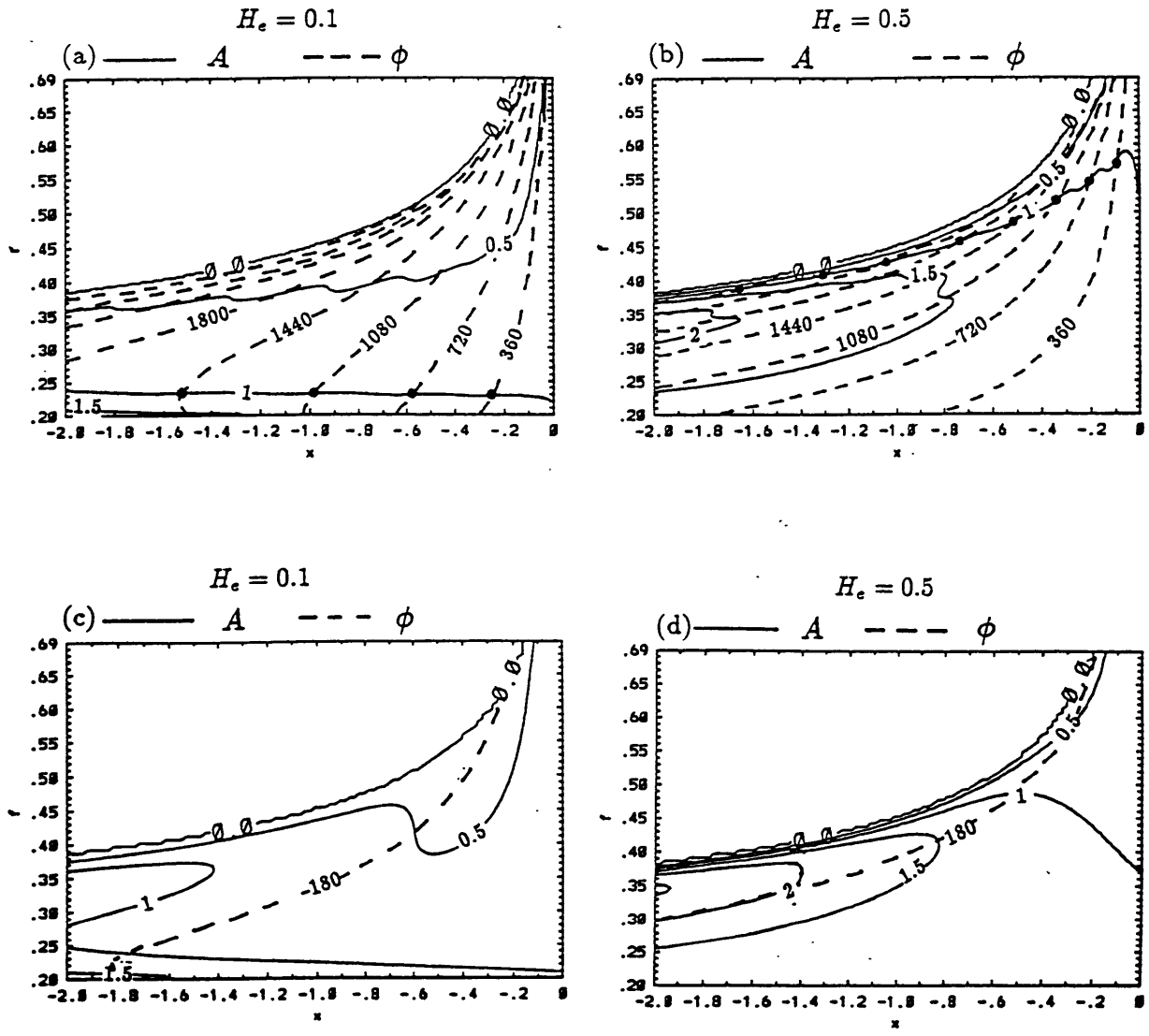

Figure 3.6: The relative amplitude A and phase Φ of the boundary waves of linear solutions of second order approximation $O(\frac{1}{\omega^2})$ in (A.1). The Ekman pumping has the form $w_0(f) = W_0(1-f)(f-f_s)$ and its amplitude is such that $w_0(f)\mid_{f=0.5(1+f_s)}$ =-1. The outcrop line is at $f_0 = 0.9$, (but the figure does not show all the interface). The frequency is an annual one $\omega = 50$ for (a) and (b) with $H_s = 0.1$ in (a) and $H_s = 0.5$ in (b). The frequency is a decadal one $\omega = 5$ in (c) and (d) with $H_s = 0.1$ in (c) and $H_s = 0.5$ in (d)

of the Rossby wave amplitude (3.19). Therefore, local response dominates near the surface. On the contray, for a deep interface, the divergent group veolcity is weak as discussed in (3.10b), the Rossby wave response dominates.

In addition, a Rossby wave is produced at latitude F_i and then propagates southward, requiring $F_i > f$. In the northern part, the local Ekman pumping $w_0(f)$ is stronger than the Ekman pumping $w_0(F_i)$ that generates boundary waves along the eastern boundary. Therefore, the local response tends to be stronger. The opposite occurs in the southern part. Particularly, near the southern boundary, where local Ekman pumping vanishes $w_0(f) \to 0$, the boundary waves are forced in the middle of the gyre where $w_0(F_i)$ is finite. Thus, $w_0(F_i)/w_0(f) \to \infty$, implying a dominant boundary wave effect.

Variability of thermocline structure and circulation

Fig.3.7a depicts the disturbance ah_1 under an strong annual frequency $a = 0.5, \omega = 50$ on September ($\omega t = 0$), December ($\omega t = 90°$), March ($\omega t = 180°$) and June ($\omega t = 270°$). The eastern boundary depth is $H_s = 0.1$ (as in Fig.3.6a). It is seen that the disturbance reaches about maximum on March while it reaches the negative maximum on September, which is typical for local response dominance. The maximum amplitude is about 0.01, corresponding to a dimensional depth of about 6 meters (if the total depth $H = 600$ meters). Fig.3.8 displays ah_1 with a weak decadal forcing $\omega = 5, a = 0.05$ (corresponding to Fig.3.6c). A positive (negative) Rossby wave anomaly is formed near the eastern boundary during winter (summer). Then, the anomaly propagates and intensifies westward to occupy the interior during fall (spring).

Lastly, we observe the variability of the circulation. Fig.3.7b,c illustrate the upper and lower layer circulation for the thermocline disturbance in Fig.3.7a. The upper layer circulation remains to be an anticyclonic gyre. This gyre reaches its maximum strength in the winter and its minimum in the summer. The lower layer is more interesting. A penetration of water towards the shadow zone appears in the winter, similar to a spin-up process in section 2 (Fig.3.2). In contrast, in the summer, the lower layer exhibits a northward flow and a cyclonic gyre in the shadow zone while the anticyclonic gyre is confined in the northern part of the ventilated zone. This agrees with the circulation during a spin-down process in section 2 (Fig.3.3). The physics has also been explained

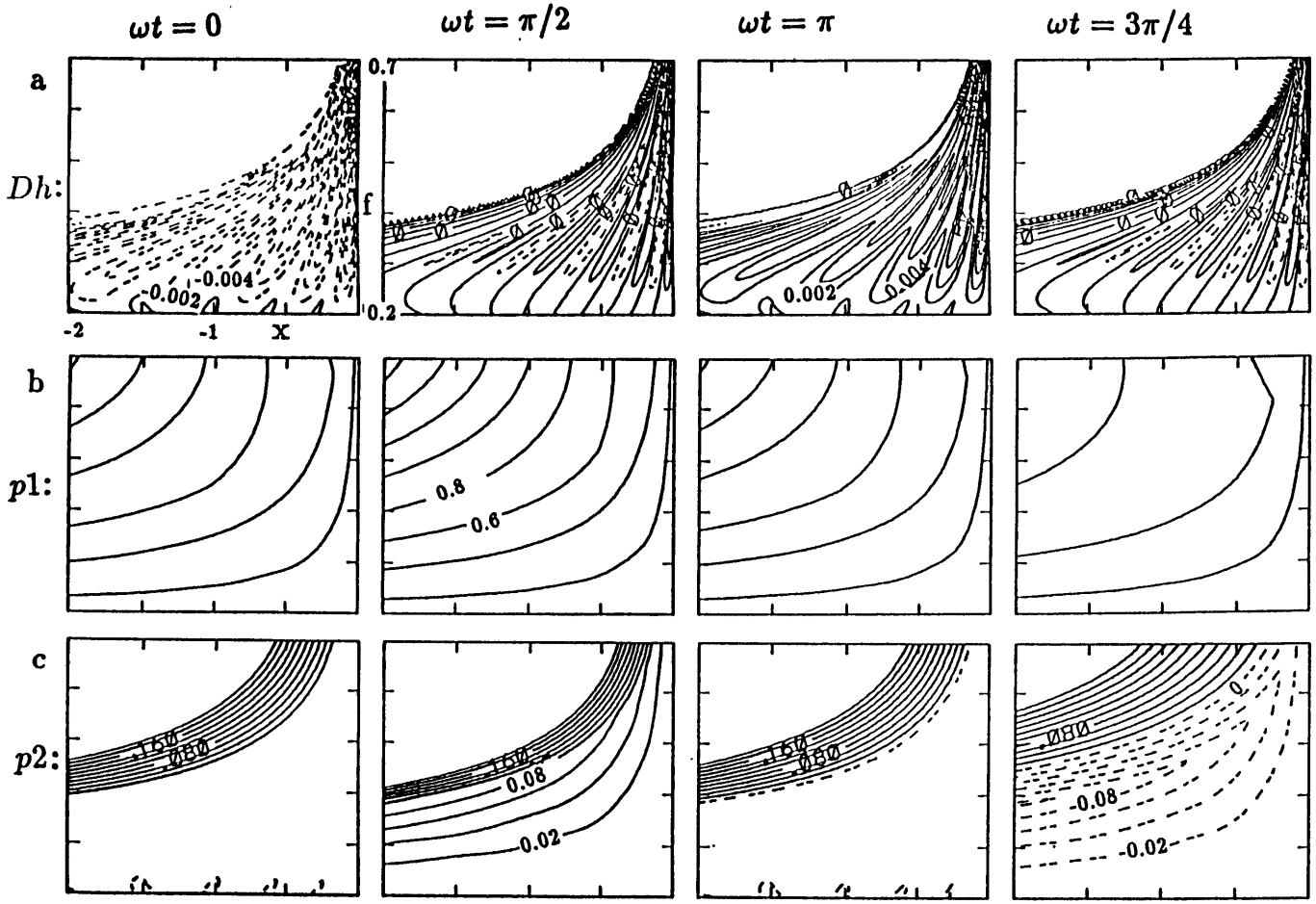

Fig.3.7: The two-dimensional structures of the linear solution of a shallow interface $H_s = 0.1$ with a strong annual forcing $\omega = 50, a = 0.5$ (corresponding to Fig.3.6a,b,c). w_e is parabolic as in Fig.3.6. a) Disturbance Dh on September ($\omega t = 0$), December ($\omega t = \pi/2$), March ($\omega t = \pi$), June ($\omega t = 3\pi/2$.) successively. b) Upper layer pressures at four seasons. c) Lower layer pressures at four seasons. In c), the contours only draw pressure with $p_2 < 0.2$. As a result, the flow in most of the ventilated zone is not shown.

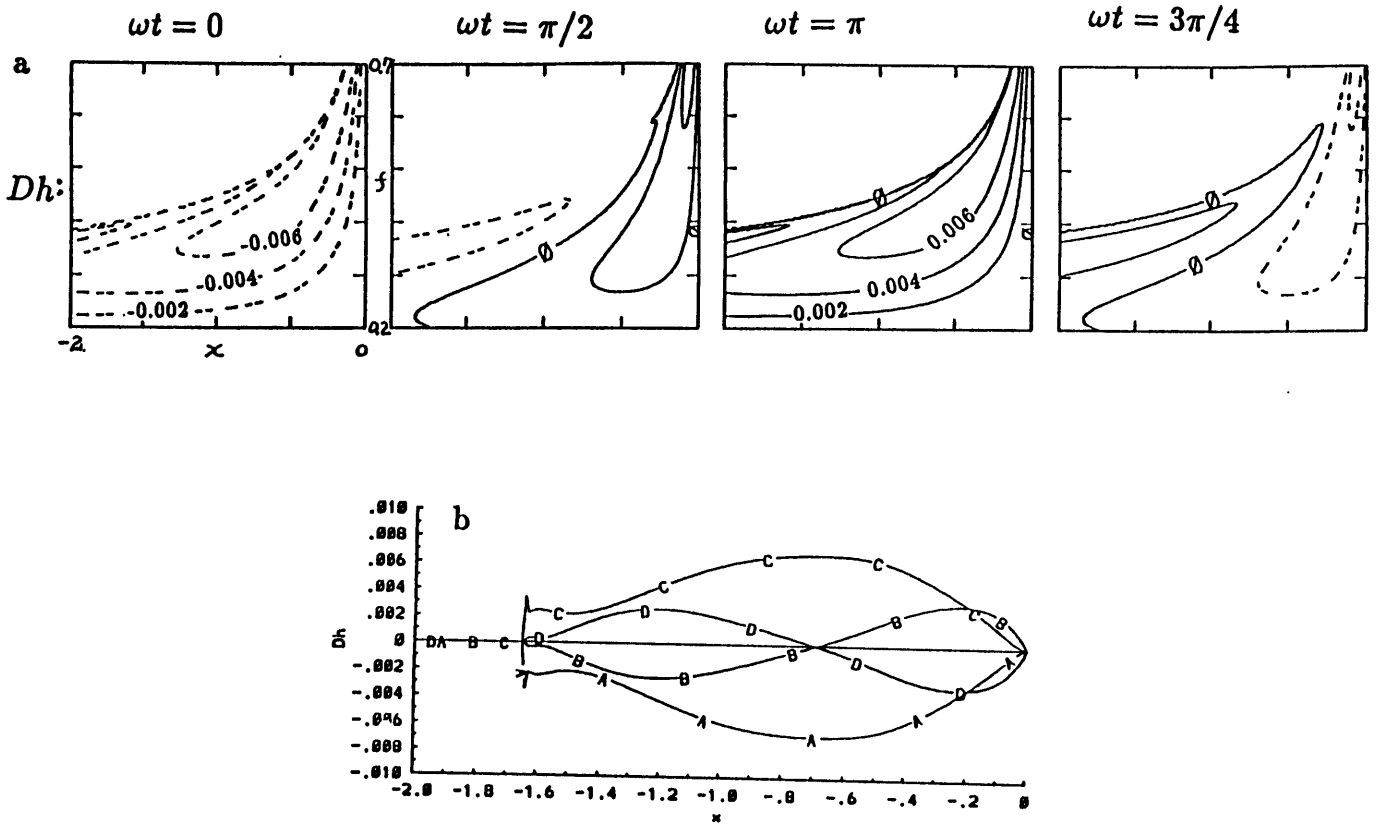

Fig.3.8: Linear deviations for a weak decadal forcing with $\omega = 5, a = 0.05$. The Ekman pumping is parabolic as in Fig.3.6. The interface is a shallow interface with $H_s = 0.1$. a) the two-dimensional structure of Dh in four seasons. b) The zonal profiles at f=0.33 during four seasons (similar to Fig.4.7a,b).

in detail there. The change of circulation is mainly caused by the barotropic response. The wavy structure is barely seen, consistent with the weak thermocline variability.

To summarize, the mean thermocline structure influences disturbances significantly. The divergent group velocity results in a decay of Rossby waves. In addition, the thermocline variability is dominated by local response on shallow interfaces but is dominated by Rossby waves on deeper interfaces. Finally, the lower layer water in the shadow zone is no longer motionless. The direction of the circulation oscillates northward and southward.

4 Periodic Ekman Pumping: II. Nonlinear Theory

Now, we investigate the nonlinear thermocline. A comparison between linear and nonlinear solutions will be carried out. It will be seen that under a strong decadal forcing, linear solutions fail to represent some important features of the nonlinear solution. Finally, we analyze the time-mean structure of the nonlinear thermocline.

4.1 The Nonlinear Solution

Following the approach in section 2 of chapter 2, we seek solutions of the nonlinear equation (3.1). With the Ekman pumping in (3.2c), the characteristic equations of (3.1) can be solved to yield parametric solutions:

$$t = t_i + s, \tag{4.1a}$$

$$\int_{f_i}^{f} \frac{df}{f w_0(f)} = s - \frac{a}{\omega}(\cos\omega t - \cos\omega t_i), \quad or \quad f = \hat{f}(s, t_i, f_i). \tag{4.1b}$$

$$\frac{f}{1-h} = \frac{f_i}{1-h_i} \qquad or \qquad h = \hat{h}(s, t_i, f_i) \tag{4.1c}$$

$$\begin{aligned} x f^2 w_0(f) &= x_i f_i^2 w_0(f_i) - \frac{1-h_i}{f_i}\int_0^s [1-(1-h_i)\frac{\hat{f}}{f_i}]\hat{f} w_0(\hat{f}) ds, \\ or \quad x &= \hat{x}(s, t_i, f_i, x_i). \end{aligned} \tag{4.1d}$$

Again, here the hatted quantities represent the solution in the characteristic coordinate. For forced solutions, the initial conditions for characteristics in the ventilated (or pool) zone and shadow zone are respectively

$$f_i = f_0, \qquad h_i = H_s \ \ in\ the\ V.Z.\ (f_o < 1)\ or\ P.Z.(f_0 = 1), \tag{4.2a}$$

$$x_i = 0, \qquad h_i = H_s \ \ in\ the\ S.Z. \tag{4.2b}$$

An example is the case with $w_0(f) = W_0/f$. Most nonlinear solutions in this chapter have this Ekman pumping (the only exception is Fig.3.11), because this Ekman pumping enables us to integrate (4.1b,d) explicityly as

$$\hat{f} = f_i + W_0[s - \frac{a}{\omega}(\cos\omega t - \cos\omega t_i)], \tag{4.3a}$$

$$x\hat{f} = x_i f_i - \frac{h_i(1-h_i)}{f_i}s + \frac{(1-h_i)^2 W_0}{f_i^2}[\frac{s^2}{2} + \frac{as}{\omega}\cos\omega t_i - \frac{a}{\omega^2}(\sin\omega t - \sin\omega t_i)]. \tag{4.3b}$$

[1] In principle, from (4.1) and (4.2), one should be able to obtain an explicit solution of the form

$$h = h(x, f, t). \tag{4.4}$$

We can prove that the general solution (4.4) possesses the primary period $T = \frac{2\pi}{\omega}$ (the proof is not presented here). This periodicity ensures that the primary frequency ω is the lowest non-zero frequency of the forced thermocline. In other words, no subharmonics will be produced except perhaps the time-mean component. Mathematically, now, a Fourier series can be used to decompose the time series of the nonlinear thermocline solution.

Now, we derive solutions in the ventilated (or pool) zone and shadow zone. In the ventilated (or pool) zone, (4.1c) and (4.2a) yield the solution

$$h = 1 - (1 - H_s)\frac{f}{f_o}, \quad x < x_b(f, t). \tag{4.5}$$

The ventilated (or pool) zone is a uniform potential vorticity pool with the constant potential vorticity $f_o/(1 - H_s)$. Therefore, no matter how strong and what pattern the Ekman pumping $w_e(x, f, t)$ is, there is no thermocline variability. (This has been discussed in section 2 for spin-up and spin-down and in the last section for linear waves.) This is so because only the potential vorticity conservation is used in (4.5). Under a zonal outcrop line (and a constant interface depth $H_s > 0$ at the northern boundary when $f_o = f_n$), the potential vorticity is always uniform. Thus, there is no variability.

[1] This Ekman pumping resumbles the middle part of a subtropic gyre fairly well, although it obviously fails to represent the region near the southern and northern boundaries simply for that it does not have the two boundaries. Therefore, this Ekman pumping is frequently used to study the variability along zonal sections resumbling those in the middle part of a subtropical gyre.

In the shadow zone, (4.1) and (4.2b) yield

$$t = t_i + s, \tag{4.6a}$$

$$f = \hat{f}(s, t_i, f_i), \tag{4.6b}$$

$$h = 1 - (1 - H_s)\frac{f}{f_i}, \tag{4.6c}$$

$$x\hat{f}^2 w_0(\hat{f}) = -\frac{1 - H_s}{f_i}\int_0^s [1 - (1 - H_s)\frac{\hat{f}}{f_i}]\hat{f}w_0(\hat{f})ds, \quad x > x_b(f,t). \tag{4.6d}$$

In (4.5) and (4.6), x_b is the shadow zone boundary which is formed by characteristics initiating from $(0, f_0)$ at successive times. x_b varies with time and is determined parametrically from (4.6b,d) as

$$f_b = \hat{f}(t - t_i, t_i, f_0), \quad x_b = -\frac{1 - H_s}{f_0 f_b^2 w_0(f_b)}\int_0^{t-t_i} [1 - (1 - H_s)\frac{\hat{f}}{f_0}]\hat{f}w_0(\hat{f})ds. \tag{4.7}$$

As has been seen in section 2, this shadow zone boundary sweeps back and forth as the Ekman pumping varies. Two examples of (4.7) are presented in Fig.3.9a and c. Follow (2.9), the region where x_b passes through is called the alternative zone. Fig.3.9a shows that the annual forcing case has a very narrow alternative zone, even with a strong perturbation (a=0.5). This occurs because the shadow zone boundary is mainly controlled by the baroclinic Rossby waves, which develops very little within one annual period. Even with a strong decadal period in Fig.3.9c, the alternative zone is not large, although it could occupy a fairly large portion of a zonal section in the southern part of a gyre. However, it is interesting to see that the wave rays (or the characteristics) starting at different times vary much more strongly than the x_b itself, as shown in Fig.3.9b,d. The shadow zone boundary of the steady thermocline under the time-mean Ekman pumping is x_{b0} ((4.8)), which is the dashed line in Fig.3.9a,c. One sees that x_b oscillates about x_{b0}. But, it should be pointed out that the time-mean x_b usually is not x_{b0}.

4.2 Time-Mean Thermocline

Thermocline equation (3.1) includes two nonlinear effects: the interaction between the barotropic and baroclinic flows ($\vec{v}_B \cdot \nabla h$) and the nonlinear Rossby wave effect ($C(h)$). The former has been studied by Dewar (1989) in a QG model under an annual forcing, while the latter was first explored by Anderson and Killworth (1980) in an $1\frac{1}{2}$ layer model. Under a periodic Ekman pumping, one

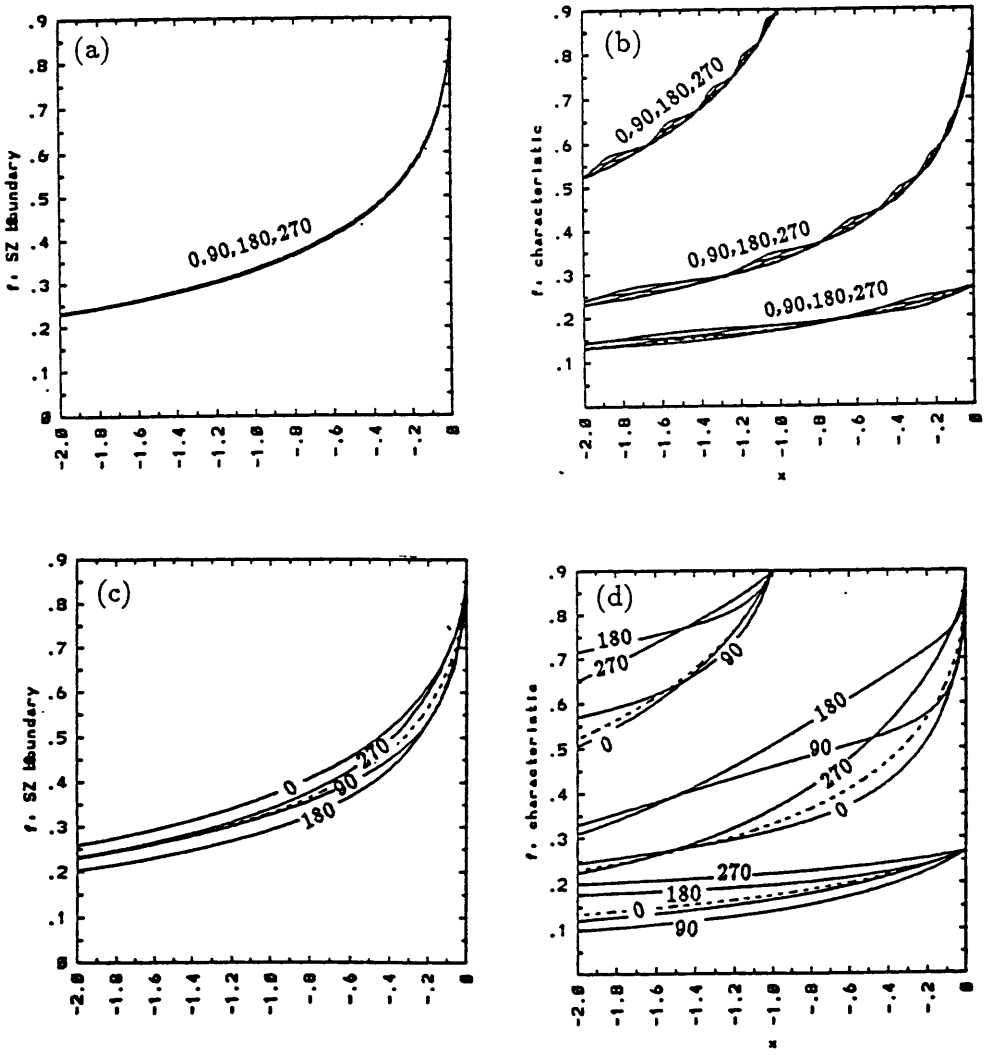

Figure 3.9: The instantaneous shadow zone boundaries and characteristics starting at different times. The Ekman pumping takes the form in Fig.3.5. $H_s = 0$ except specified. a) Shadow zone boundaries at four seasons (labeled by the phase). Under a strong annual forcing $\omega = 50$ and $a = 0.5$. b) Characteristics starting from September, December, March and June at x=0,f=0.9 (outcrop line), x=-1,f=0.9 (in the ventilated zone), x=0,f=0.25 in the shadow zone ($H_s = 0.3$). c) the same as a) except for $\omega = 5$. d) the same as b) except for $\omega = 5$.

should expect a time-mean thermocline $< h >$ differing from the steady thermocline h_0 that is forced by the time-mean Ekman pumping $< w_e >= w_0$. (Without confusion, hereafter, this steady thermocline is simply called the steady thermocline.) Here, we will investigate the time-mean thermocline.

With a strong annual forcing (see the example in Fig.3.5), one has seen that the instantaneous disturbance $Dh = h - h_0$ is at the order of a/ω, i.e.

$$Dh \leq O(\frac{a}{\omega}). \tag{4.8}$$

The non-dimensional maximum is about 0.01, which corresponds to a dimensional depth of about 6 meters (if the total depth is about 600 meters). In addition, the time-mean disturbance $< Dh >=< h - h_0 >=< h > -h_0$ (dot-connected lines in Fig.3.5: b,d,f) is not zero. The mean disturbance is no larger than a^2/ω, or

$$< Dh > \leq O(\frac{a^2}{\omega}). \tag{4.9}$$

The non-dimensional maximum is less than 0.001 or a dimensional depth of less than about 0.6 meter. Thus, $< Dh >$ is small compared with the instantaneous disturbance Dh for either a high frequency or a weak decadal frequency forcing $a \ll 1$. Nevertheless, it is interesting to observe a slightly negative $< Dh >$ component along the whole section, implying a shallower mean thermocline than the steady one. At a decadal frequency, if the forcing amplitude becomes strong, (4.9) and (4.10) suggest that $< Dh >$ may increase rapidly compared with Dh. This phenomenon is seen clearly in Fig.3.10 which plots an example at the latitude $f = 0.3$ with a strong decadal forcing $\omega = 5, a = 0.5$, the Ekman pumping $w_e = W_0/f$ is used. Fig.3.10b shows an ventilated case ($H_s = 0$). One sees that $< Dh >$ can reach about one-third of Dh. Besides, a salient feature is the strong negative $< Dh >$ along the whole zonal section. A common character of ventilated interfaces (in Fig.3.5b and Fig.3.10b) is that $< Dh >$ achieves its maximum amplitude in the alternative zone, which is located in the western flank of the shadow zone. Fig.3.10g,k show two unventilated interfaces with $H_s = 0.1$ and $H_s = 0.6$ respectively. One sees that even on unventilated interfaces, $< Dh >$ still reaches its maximum in the western shadow zone. In Fig.3.10, the non-dimensional maximum $< Dh >$ ranges from -0.02 to -0.04 at different depths, corresponding to a

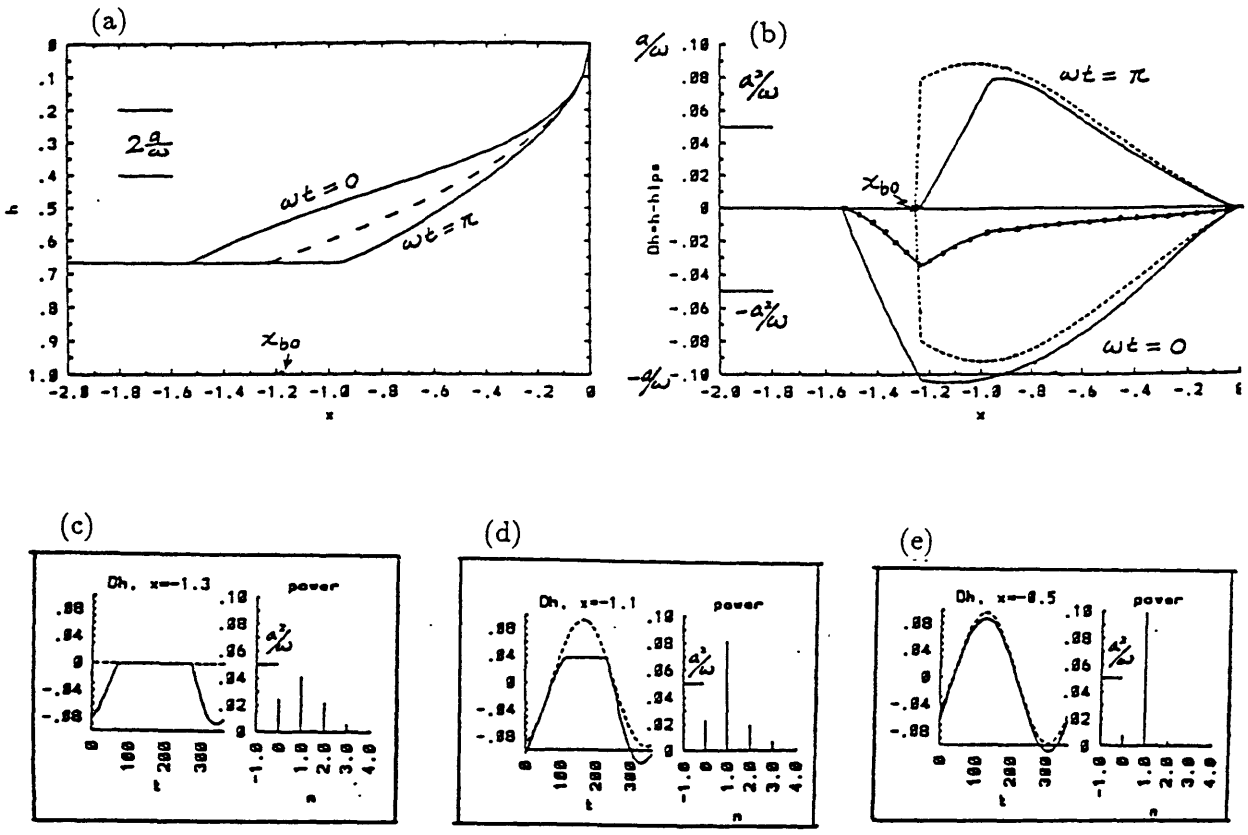

Figure 3.10: Zonal sections, time series of local interfaces and their Fourier components of nonlinear solutions under a strong decadal Ekman pumping $\omega = 5, a = 0.5$. The Ekman pumping has the form as that in Fig.3.5. a),b),f),g),j),k) are the same as in Fig.3.5 except for $\omega = 5, a = 0.5$. c,d,e) are the local time series of Dh, their Fourier components. For the Fourier components, the abscissa n refers to the frequency $n\omega$. at three locations on a),b). h),i) are two time series of Dh and Fourier components at two points on f),g). h),i) are two time series of Dh and their Fourier components at two locations on j) or k). To be continued.

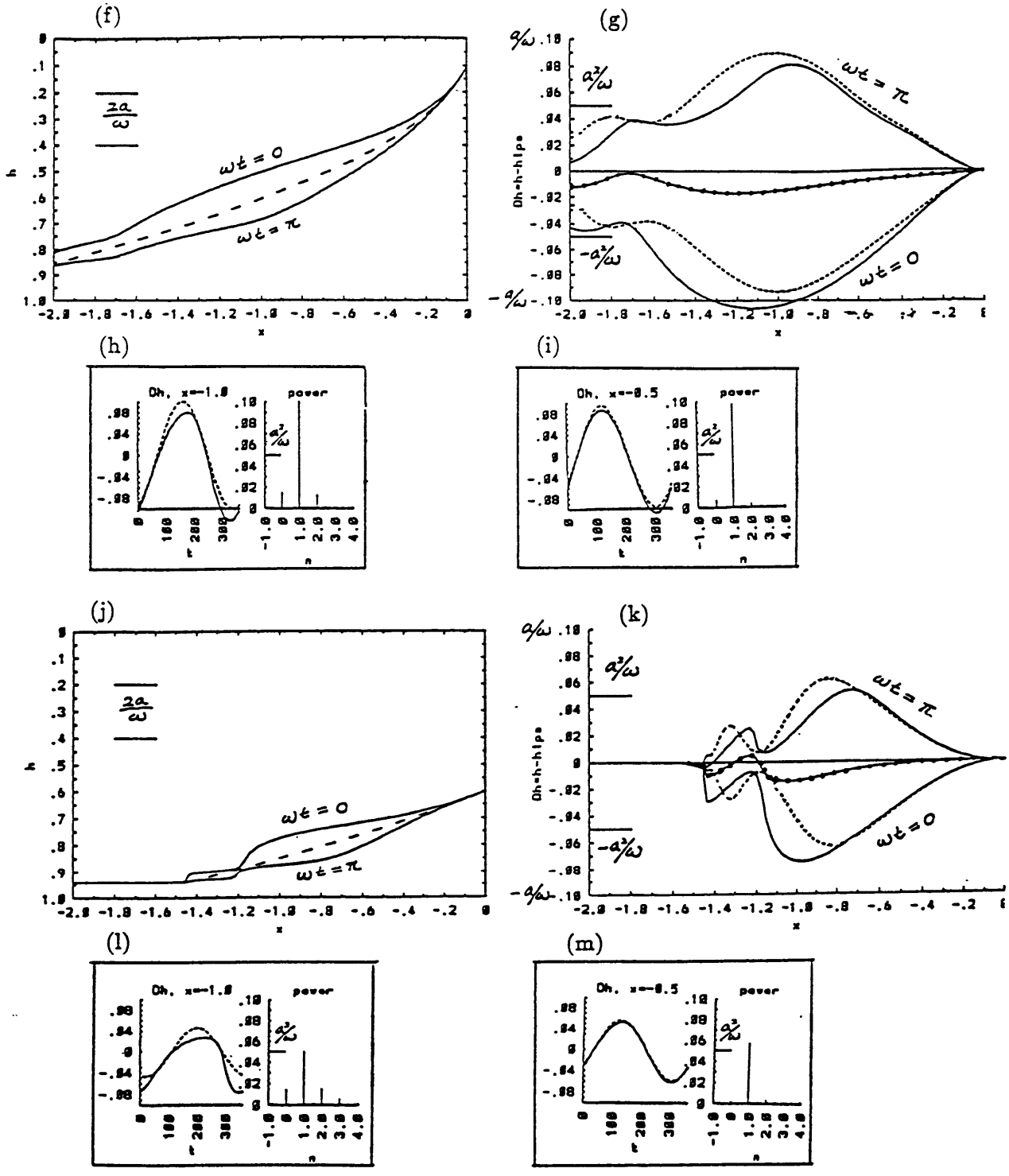

Figure 3.10: (continued)

dimensional mean deviation of -12 to -24 meters. In addition, in the region where $< Dh >$ is strong, the linear solution deviates from the nonlinear solution significantly. In contrast, in the eastern part of shadow zone where $< Dh >$ is always weak, the linear solution resembles its nonlinear solution well in all the cases.

Some time series of local interface variations and their Fourier components are also shown. Fig.3.10e is located in the eastern part of the shadow zone of the ventilated interface in Fig.3.10a,b. The number on the abscissa n corresponds to the frequency $n\omega$. The primary component (with the primary frequency ω) dominates while other components are negligible. Fig.3.10i,m give another two examples in the eastern shadow zone. Their Fourier components are similar to Fig.3.10e. A strikingly different behavior appears in the alternative zone on a ventilated interface (Fig.3.10c,d) and (somewhat less strikingly) in the western part of the shadow zone (Fig.3.10h,l). Now, both the time-mean component and the second superharmonics (with frequency 2ω) become rather strong. In addition, observing all the Fourier components of these time series, one sees that the time-mean component is about the same magnitude as the second superharmonic component while other higher superharmonics are negligible.

With a strong decadal forcing ($\omega = 5, a = 0.5$), Fig.3.11a displays the horizontal structure of the time-mean thermocline disturbance $< Dh >$ for a parabolic form $w_0(f) = W_0(1-f)(f-f_s)$ of Ekman pumping on a ventilated interface. The solution is found by first solving the characteristic equations in (4.1) using the 4th-order Runge-Kutta method at each time. Then the solution is mapped objectively on to regular grids. Finally, the time-mean is carried out at each grid point. One sees that $< Dh >$ has a negative component within the entire shadow zone. The strongest mean deviation occurs within the alternative zone. The non-dimensional maximum mean deviation is about -0.03 or dimensionally -18 meters. The instantaneous patterns in four seasons (not shown) are similar to that in Fig.3.8 except now the alternative zone is much larger. Using this time-mean thermocline, the corresponding lower layer pressure (or streamfunction) is shown in Fig.3.11b. There is a strong southward flow in the alternative zone, which weakens towards the eastern shadow zone. This southward mean flow corresponds to a mean vertical downwelling inside the shadow

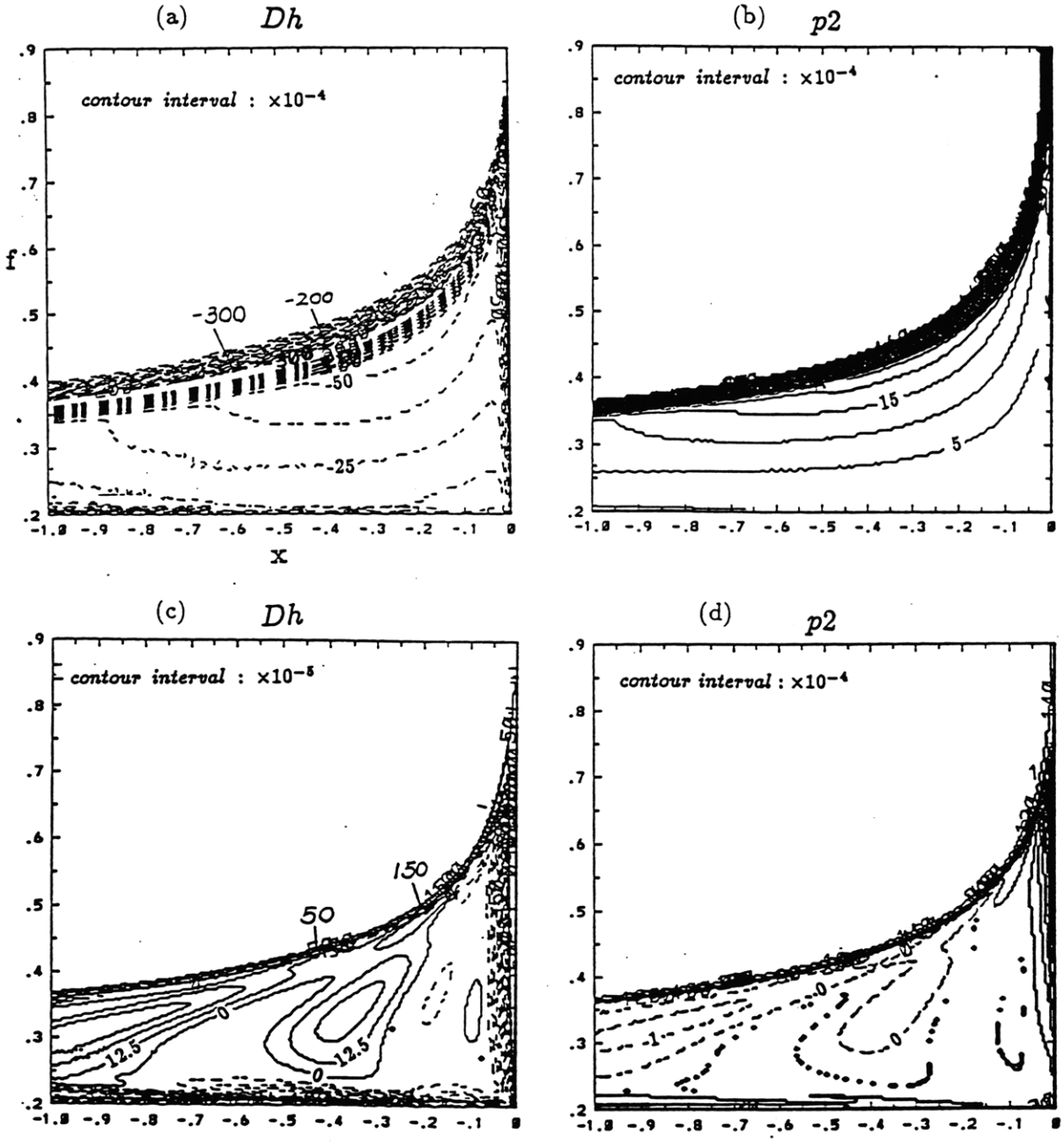

Figure 3.11: The two-dimensional time-mean structures of nonlinear solutions under the Ekman pumping $w_0(f) = W_0(1-f)(f-f_s)$ with $w_0(f)\ |_{f=0.5(1+f_s)} = -2$. The solution is obtained by integrating the characteristic equations of (1.7a) using a 4th-order RK method at each time. Then the values are objectively mapped onto regular grids and averaged. a),b) shows $< Dh >$ and the corresponding lower layer pressure p_2 for a strong decadal forcing $\omega = 5, a = 0.5$. c) and d) are the same as a) and b) except for an annual forcing $\omega = 50$. The mean lower layer pressure contours are chosen such that the flow field in the shadow zone can be seen clearly. As a result, the flow within most of the ventilated zone is not shown.

zone (not shown). As a result, in the time-mean thermocline, the lower layer fluid in the shadow zone is no longer motionless. Instead, it has a mean southward flow.

In comparison, an annual forcing produces a very different $< Dh >$ as shown in Fig.3.11c. The mean disturbance is much weaker (note the different contour intervals) than the decadal case in Fig.3.11a. The dimensional maximum value is about ± 1 meters. In addition, the pattern exhibits alternative highs and lows. In the mean lower layer pressure in Fig.3.11d, these highs and lows correspond to some micro-gyres, as found by Dewar (1989). In the previous example in Fig.3.5a, these alternative highs and lows are also obvious on the mean zonal profile (dot-connected line).

4.3 Mechanisms for the Mean Thermocline

Now we analyze the mechanism for the time-mean thermocline structure. It turns out that in different regions and for different frequencies, the mechanisms are different. We will concentrate on the shadow zone for low frequency cases.

In the shadow zone (east of the alternative zone on a ventilated interface, or the whole unventilated zone), the main mechanism is the nonlinearity of the Rossby wave that is to be explained in the following. Consider an even simpler model--a $1\frac{1}{2}$ layer model. The upper layer depth is determined by

$$h_t + C(h)h_x = -w_e(f,t), \qquad where\ C(h) = -h/f^2. \tag{4.10}$$

The only nonlinear effect in this model is the nonlinear Rossby wave. It can be proven that the solution in (4.10) is periodic if $w_e(f,t)$ is periodic in time. Thus, averaging (4.10) over one period and then integrating it along the x direction, we obtain the energy equation:

$$< h^2 >= h_0^2 \tag{4.11}$$

where h_0 is the steady thermocline (as in (3.7b)) forced by the time-mean Ekman pumping $< w_e(f,t) >= w_0(f)$. Decomposing the thermocline into $h =< h > +h'$, where h' is the perturbation with a zero mean, (4.11) becomes

$$< h >^2 + < h' >^2 = h_0^2, \quad or \quad < h >^2 = h_0^2 - < h' >^2 \ < \ h_0^2 \ . \tag{4.12}$$

This states that the mean thermocline is always shallower than the steady thermocline. Physically, (4.11) and (4.12) suggest that part of the input mean available potential energy leaks away as disturbance potential energy due to the nonlinear Rossby wave.

The above argument also applies to our two-layer model if the forcing frequency is low. Indeed, when the forcing frequency approaches zero, both the local variability (h_t) and density advection ($\vec{v_B} \cdot \nabla h$) should diminish (when $\omega = 0$, both of them vanish exactly in the shadow zone). Thus, the major dynamic balance of (4.1) degenerates to $C(h)h_x \approx -(1-h)w_e(f,t)$, where $C(h) = -h(1-h)/f^2$. This dynamic balance leads to the energy equation similar to (4.12):

$$h^2 \approx 2f^2 w_e(f,t)x + H_s^2 \qquad \textit{for very low frequency.} \tag{4.13}$$

This is the Sverdrup relation with the time as a parameter. Averaging (4.13) will give rise to the same relation as (4.11) or (4.12). With the Ekman pumping in (3.2), we can estimate the mean deviation $< Dh >$.

$$\begin{aligned} < Dh > &\equiv < h > -h_0 = < \sqrt{2f^2 w_0(f)(1+a\sin\omega t)x + H_s^2} > - \sqrt{2f^2 w_0(f)x + H_s^2} \\ &= -h_0 < 1 - \sqrt{1 + a(1 - \frac{H_s^2}{h_0^2})\sin\omega t} > \; < 0, \quad \textit{for } 0 < a < 1. \end{aligned} \tag{4.14a}$$

For a weak forcing $a \ll 1$, (4.14a) can be approximated as

$$< Dh > \approx -\frac{a^2}{16}(1 - \frac{H_s^2}{h_0^2})^2 h_0 \tag{4.14b}$$

First of all, (4.14b) shows that $< Dh >$ decreases as H_s decreases. This agrees with the examples in Fig.3.5 and Fig.3.10. Physically, this is because as the interface gets deep, the effective perturbation Ekman pumping weakens. Quantitatively, in Fig.3.10 or Fig.3.11a ($a = 0.5, h_0 \approx 500$ meters and $H_s/h_0 \ll 1$), this gives about 10 meters (or a non-dimensional value 0.017), agreeing with the maximum $< Dh >$ in the shadow zone (not in the alternative zone!). In fact, calculations show that (4.14b) gives a good approximation to (4.14a) until $a = 1$. Therefore, in a shadow zone, the time-mean disturbance seems to have the upper bound at low frequency (by letting $a \to 1$ and $H_s \to 0$)

$$\frac{< Dh >}{h_0} \leq O(\frac{1}{16}). \tag{4.15}$$

In the second place, since h_0 deepens westward, (4.14b) suggests that $< Dh >$ also increases westward. In the eastern part of the shadow zone, this westward increasing mean deviation can be observed clearly in Fig.3.10b,g,k. However, $< Dh >$ increases towards the west only to about a quarter of the wave length as seen in Fig.3.10b,g,k. This differs from (4.14) because (4.14) is valid only when $\omega \to 0$ (then the wave length goes to infinity).

With a high frequency, the advection term becomes dominate, which is response for the micro gyres in the mean thermocline. In the alternative zone, the alternating between the Rossby wave and cold advection is very efficient in producing a very shallow mean thermocline. For details, the reader should refer to appendix B.

Lastly, we point out that (4.13) (or (B.1) for high frequency case) shows that the time-mean component has the same amplitude as the second harmonics, which has been seen in the previous example Fig.3.10c,d,e,h,i,l,m. This spectrum is characterized by both a rapid rise and decrease of the local interface variability.

5 Thermocline Variability Under a Variable Ekman Pumping

Now, we further investigate the variability at different frequency and amplitude of forcing. In particular, we are interested in how important the nonlinear effect is. Visually, the examples in Fig.3.5 indicate that the linear solutions are able to represent the nonlinear solutions excellently along the whole zonal section in cases with a strong annual forcing. If the amplitude of the decadal forcing becomes strong, Fig.3.10 illustrates that the linear solution still approximates the nonlinear solution well in the eastern part of the shadow zone, but it fails in the western part of the shadow zone and the alternative zone.

As a further step to study the variability and its nonlinearity under different amplitude and frequency of forcing, we study the variability of the zonally integrated interface disturbance

$$\frac{1}{x_b}\int_0^{x_b} Dh dx, \tag{5.1}$$

where x_b is the instantaneous shadow zone boundary in (4.7). Subject to various forcing amplitudes a and frequencies ω, for the zonally averaged variability (5.1), the amplitude and phase of the

primary component, the amplitude of the time-mean component and the ratio between the time-mean component and the primary component are depicted respectively in Fig.3.12a,b,c and d. The Ekman pumping is chosen to be $w_e = W_0/f$. Qualitatively, the amplitudes of the primary component in Fig.3.12a agree with the linear solutions (3.17) or (A.1). For high frequencies (higher than decadal), their amplitudes are proportional to $\frac{a}{\omega}$ (straight lines in the $\omega - a$ plane passing through the origin) and their phases are about 90^o, reflecting properties of local responses (note that in Fig.3.12, the interface is a shallow ventilated interface.) As frequencies approach zero, the amplitudes approach finite limits and the phases decreases with frequency. It is impressive that the phase depends little on the forcing amplitude a, especially for high frequencies. This suggests the dominant linear nature of the response.

To analyze the nonlinearity quantitatively, we decompose the time series in (5.1) into a Fourier series $\int_0^{x_b} Dhdx/x_b = \Sigma_{n=0}^{\infty} A_n \sin(n\omega t - \theta)$. Then, we can judge the importance of the nonlinearity by the power ratio between the sum of all sub and superharmonics, which are generated by nonlinearity, and the primary component $P_{ratio} = (\Sigma_{n\neq 1} A_n^2/A_1^2)^{\frac{1}{2}}$. Since we have seen that the powers of the second superharmonics A_2 and the time-mean component A_0 are about the same while other components are negligible, the power ratio can be approximated as

$$P_{ratio} \approx 2A_0/A_1. \tag{5.2}$$

The A_0 and A_1 have been shown in Fig.3.12a and c. The ratio A_0/A_1 is shown in Fig.3.12d. The contour $A_0/A_1 = 0.05$ (heavy solid line on Fig.3.12d) can be taken as the criterion for $P_{ratio} = 0.1$ in the $\omega - a$ plane. Below this line the power ratio is less than 0.1 and the total power of the nonlinearly generated harmonics is one order less than that of the primary component. In other words, nonlinearity is negligible. This regime is the linear regime and mainly consists of weak decadal forcing and strong annual forcings (e.g.,Fig.3.5). Above the $P_{ratio} = 0.1$ line, the nonlinearly generated components are no longer negligible. The regime consists of strong decadal forcing and is called the nonlinear regime. (It is perhaps more proper to call it as weakly nonlinear regime because the nonlinearity is not dominant). Fig.3.10 is an example of this nonlinear regime. For the parameters $\omega = 5, a = 0.5$ in Fig.3.10, we find from Fig.3.12d that $A_0/A_1 \approx 0.17$. (5.2) then suggests that $P_{ratio} \approx 0.34$. This means that about 30 percent of the energy of this decadal forcing

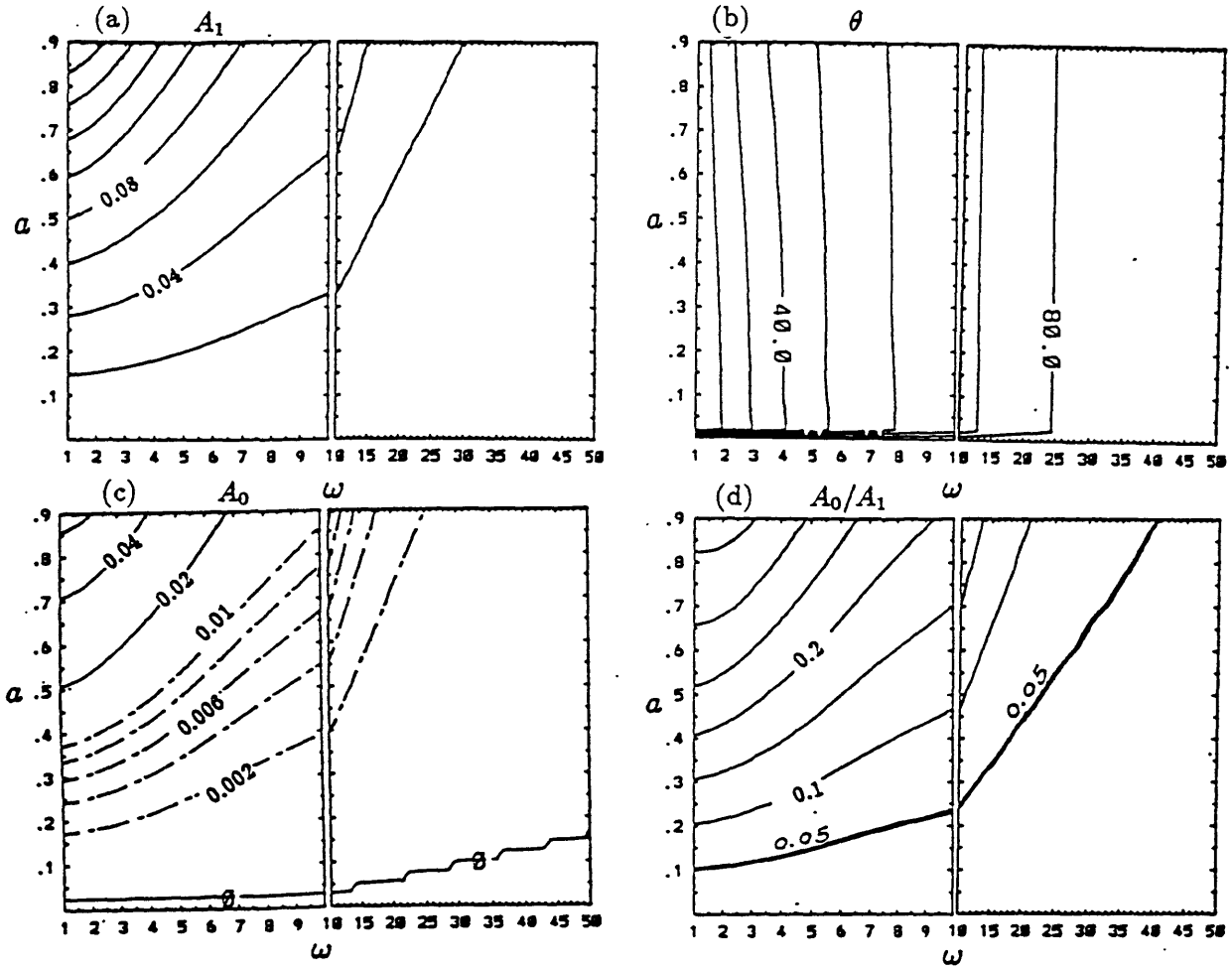

Figure 3.12: For the zonally integrated disturbance (5.1). The amplitude and phase of the primary component, the amplitude of the time-mean component, the amplitude ratio between the time-mean component and the primary component, with respect to different forcing amplitude a and frequency ω. The Ekman pumping takes the form in Fig.3.5. $H_s = 0$ is adopted. a)the primary component A_1. b) the phase of the primary component in the form of $\sin(\omega t - phase)$. c)the time-mean component A_0. d) the ratio of time-mean component to the primary component A_0/A_1.

is transferred nonlinearly to the time-mean and higher components. It should be born in mind that the zonally averaged disturbance (5.1) underestimates the maximum local nonlinearity in the western shadow zone or the alternative zone.

6 Summary

A two-layer planetary geostrophic model is used to investigate the thermocline variability under a variable Ekman pumping. This model includes a two-dimensional mean flow and thermocline structure. The effect of ventilation and advection is particularly emphasized in the ventilated zone. The analysis includes both annual and decadal forcings.

To highlight the physics, we first study a simpler case of spin-up and spin-down. It is found that the dynamics between a ventilated zone and a shadow zone differs substantially. In the ventilated zone, the cold advection balances the Ekman pumping, while in the shadow zone the Rossby wave opposes the Ekman pumping. After a change of the wind field, in the ventilated zone, the Ekman pumping and the cold advection vary rapidly at the time scale of barotropic Rossby waves (about one week) to achieve a new steady balance, leaving little thermocline variability. However, in the shadow zone, the Ekman pumping still changes rapidly, but the baroclinic Rossby wave evolves at a much slower time scale (years to decades). This creates a great imbalance in forcings and results in a strong thermocline variability. In addition, the development of the thermocline circulation is also interesting. The evolution differs dramatically between a spin-up and a spin-down. For example, with a change in the Ekman pumping field, the lower layer fluid in the shadow zone is no longer motionless. After a spin-up, the lower layer water moves southward because of the compression on planetary vortex tubes by the downward anomalous Ekman pumping. The associated circulation is an anticyclonic gyre. In contrast, during a spin-down, the water moves northward because of the stretching of planetary vortex tubes by the upward anomalous Ekman pumping. The lower layer circulation now consists of two counter-rotating gyres: an anticyclonic gyre to the north and a cyclonic gyre to the south.

Then, a periodic Ekman pumping is adopted to simulate a variable Ekman pumping more realistically. The features found in the spin-up and spin-down also exist in the periodic Ekman

pumping case, with the seasons of an increasing and a decreasing Ekman pumping resembling the spin-up and spin-down respectively. This is so particularly for annual forcings (i.e. with periods comparable to one year). Therefore, under a varying Ekman pumping, the thermocline variability is much stronger in the shadow zone than in the ventilated zone. The direction of the lower layer circulation in the shadow zone oscillates southward and northward.

Furthermore, it is somewhat surprising to see that for strong annual forcings with perturbation Ekman pumping comparable to the mean Ekman pumping, the disturbance is essentially linear. Even under a strong decadal forcing, the linear solution still approximate the nonlinear solution very well in the eastern part of the shadow zone. Nevertheless, the linear perturbation is influenced substantially by the basic state thermocline structure. The mean thermocline structure results in a divergent group velocity field. This in turn produces a decay effect on Rossby waves. In the ventilated zone, the advection due to the subducted water has the same importance as the local response and they tend to cancel each other. In the shadow zone, if the interface is shallower, local responses dominate, because the effective Ekman pumping is stronger and the Rossby wave energy flux is weaker. On the other hand, if the interface is deep, remote Rossby waves dominate, because the effective Ekman pumping diminishes while the barotropic flow supports a finite wave energy flux.

For a strong decadal forcing, the nonlinearity is still weak in the eastern part of the shadow zone but is no longer negligible in the western part of the shadow zone. The maximum nonlinearity occurs about one quarter of wave length from the eastern boundary. The time-mean thermocline in the shadow zone is always shallower than the steady thermocline under the time-mean Ekman pumping. The difference may be significant, especially in the western part of a shadow zone. This shallower mean thermocline is mainly caused by the nonlinear Rossby wave. The mean lower layer flow in the shadow zone is no longer at rest. Instead, it is southward.

We should point out some limits of the above theory. First, the eastern boundary interface depths are fixed in this chapter. This is part of the reason why the nonlinearity is always weak in the eastern part of the shadow zone. In fact, as will be shown in chapter 5, if we have a disturbance

along the eastern boundary, the nonlinearity may become very strong. The nonlinear steepening of the Rossby wave will cause breaking of interface waves.

Second, the unchanged ventilated zone is caused by the zonal outcrop line and the flat bottom. Nevertheless, the dominant subduction physics in the ventilated zone seems to suggest that the derived conclusion is qualitatively correct even for general cases (see section 6 of chapter 2).

Finally, the quiescent ventilated zone has not taken into account the surface buoyancy variability. In fact, it will be shown in chapter 4 that the surface buoyancy variability may cause strong thermocline variability in the ventilated zone but it affects the shadow zone slightly.

Much further work remains to be done even within this simple model. For example, a non-zonal outcrop line may provide a better understanding of the variability in the original ventilated zone. A north-south bottom slope may be included to simulate the bottom of the thermocline more realistically. In addition, it is interesting to study a stochastic Ekman pumping. A further step would be to study a two-and-a-half-layer model.

A The Approximate Linear Solution at $1/\omega^2$ Order

Here, we derive an approximate expression for the linear wave in (3.15) (or (3.13)) accurate to $1/\omega^2$. Noting the g in (3.2c), along characteristics (therefore f_i, t_i are constants), we can integrate (3.13) by part to yield

$$\begin{aligned}
h_1 &= \frac{1}{\hat{h_0}}\frac{1-\hat{h_0}}{\hat{f}}\left(\frac{-1}{\omega}\right)\int_0^s \hat{f}w_0(\hat{f})\hat{h_0}d[\cos\omega(t_i+s)] \\
&= \frac{1}{\hat{h_0}}\frac{1-\hat{h_0}}{\hat{f}}\left(\frac{-1}{\omega}\right)\left\{\hat{f}w_0(\hat{f})\hat{h_0}\cos\omega(t_i+s)\mid_0^s - \int_0^s \cos\omega(t_i+s)d[\hat{f}w_0(\hat{f})\hat{h_0}]\right\} \\
&= \frac{1}{\hat{h_0}}\frac{1-\hat{h_0}}{\hat{f}}\left(\frac{-1}{\omega}\right)\left\{\hat{f}w_0(\hat{f})\hat{h_0}\cos\omega(t_i+s) - f_iw_0(f_i)H_s\cos\omega t_i\right. \\
&\quad \left. -\frac{1}{\omega}\int_0^s\left[\frac{d\hat{f}}{ds}w_0(\hat{f})\hat{h_0} + \hat{f}w_{0f}\frac{d\hat{f}}{ds}\hat{h_0} + \hat{f}w_0(\hat{f})\frac{d\hat{h_0}}{ds}\right]d[\sin\omega(t_i+s)]\right\}
\end{aligned}$$

Here, we have used $f, h_0 \mid_{s=0} = f_i, H_s$ (see (3.6b,c)) In the last equality, the first two terms give the $O(1/\omega)$ solution in (3.17) if we use $t_i = t - s$ and (3.8a,c). For the $O(1/\omega^2)$ solution, we first subtitute the characteristic equations for the basic state (3.5)

$$\frac{df}{ds} = fw_0, \qquad \frac{dh_0}{ds} = -(1-h_0)w_0$$

into the integral of the last equality. Then, we integrate it by part again. Using $t_i = t - s$ and (3.8a,c), we obtain

$$h_1 = \frac{(1-h_0)w_0(f)}{\omega}[\cos\omega t - A\cos(\omega t - \Phi)] + O(\frac{1}{\omega^3}) \tag{A.1a}$$

where A and Φ are functions of x and f:

$$A = a_0\left[1 + \left(\frac{b_1}{\omega a_0}\right)^2 + \frac{a_1}{\omega a_0}\left(\frac{a_1}{\omega a_0} - 2\sin\phi + 2\frac{b_1}{\omega a_0}\cos\phi\right)\right]^{\frac{1}{2}}, \tag{A.1b}$$

$$\cos(\Phi) = \left(\cos\phi + \frac{b_1}{\omega a_0}\sin\phi\right)\frac{a_0}{A}, \qquad \sin(\Phi) = \left(\sin\phi - \frac{a_1}{\omega a_0} - \frac{b_1}{\omega a_0}\cos\phi\right)\frac{a_0}{A}, \tag{A.1c}$$

$$a_0 = \frac{H_sF_iw_0(F_i)}{h_0fw_0(f)}, \qquad \phi = \omega(t-t_i) = \omega S(x,f), \tag{A.1d}$$

$$a_1 = -\left[(2-\frac{1}{h_0})w_0(f) + fw_{0f}(f)\right], \qquad b_1 = \frac{F_iw_0(F_i)}{fw_0(f)}\left[(2-\frac{1}{h_0})w_0(f) + fw_{0f}(f)\right]. \tag{A.1e}$$

Here, F_i, h_0 and S are given in (3.8a), (3.7b) and (3.8c), respectively. (A.1) gives the approximation of (3.15) accurate to $O(1/\omega^2)$. Neglecting the second order terms (set $a_1 = b_1 = 0$), (A.1) becomes (3.17). (A.1) can be expected to be valid for frequencies higher than decadal ones ($\omega \gg 1$). The second order correction (due to a_1 and b_1) is very important for shallow interfaces ($H_s \ll 1$). Indeed, when $1/\omega h_0 \sim 1/\omega H_s \geq 1$, the second order correction becomes comparable to the first order. For the special form of Ekman pumping $w_0(f) = W_0/f$, where W_0 is a negative constant. The second order solution in (A.1) is the exact linear solution (3.15). On shallow interfaces, the failure of the first order solution in (3.17) is seen below. If $H_s \to 0$, we have $A \sim a_0 \to 0$. The solution is a purely forced response which fails to satisfy the eastern boundary condition (3.9c).

B More About the Mechanism for the Time-Mean Thermocline

Alternative zone

In the alternative zone of a ventilated interface, the mean thermocline is much shallower than the steady thermocline. In order to understand the physics, it is illuminating to observe and discuss the time series in Fig.3.10d which is located east of the steady shadow zone boundary x_{b0} in (3.7c). In the half period from September ($\omega t = 0$) to March ($\omega t = 180^o$), [1] the interface depth initially deepens because the increased effective Ekman pumping can not be balanced by the Rossby wave. During this deepening half cycle, the ventilated zone is also expanding. When the ventilated zone expands to this location, the deepening is stopped abruptly. This is because the strong invasion of cold advection of the ventilated zone successfully balances the effective Ekman pumping. Under the intensifying Ekman pumping, it is this invading cold advection that prevents the interface from further descending. The interface stays at the same depth until the other half cycle when the ventilated zone retreats and the strong cold advection vanishes. Then, the weakening Ekman pumping forces the interface to rise to its minimum depth continuously. Hence, during one period, the deepening of the interface is suddenly stopped by the advection while the shallowing of the interface is not. In this way, averaged over one period, the interface has a shallower depth than that without the invasion of the cold advection. Therefore, it is the alteration of the two different

[1] This lags the wind forcing (3.2c) by 90°, because on this near surface interface, local response dominates (see discussion in last section on linear waves)

mechanisms (the cold advection and the Rossby wave) that causes a shallower mean thermocline. The former is efficient in balancing the anomalous Ekman pumping while the latter is not. Fig.3.10g is located west of x_{b0}. The time series can be similarly explained. As a result, east of x_{b0}, the invading subduction water prohibits the thermocline deepening in the winter half year to produce a shallower mean thermocline. West of x_{b0}, the invasion of the Rossby wave during the summer half year allows the thermocline to respond to the local Ekman pumping and shallows, also causing a shallower mean thermocline.

Shadow Zone (High Frequency Case)

Compared with the decadal forcing case, the annual case exhibits substantially different time-mean thermocline structure as shown in Fig.3.5 and Fig.3.11c,d. This is because now the interaction between the barotropic and baroclinic flows becomes the dominant nonlinear effect. We can analyze the high frequency case through the weakly nonlinear theory. Inserting (3.3), (3.4) into (3.1), at $O(a^2)$ order, we have

$$h_{1t} + \vec{v}_{B0} \cdot \nabla h_1 + C(h_0) h_{1x} - \mu h_1 = -\nabla \cdot (\vec{v}_{B1} h_1) - \frac{1}{2}(\frac{dC}{dh_0} h_1^2)_x. \tag{B.1}$$

where μ is defined in (3.9b). On the right hand, the first term is the barotropic-baroclinic interaction while the second term is due to the nonlinear Rossby wave. For simplicity, in the following analysis, the h_1 solution is approximated to $O(\frac{1}{\omega}) \ll 1$ order in (3.17). $< Dh_{bb} >$ and $< Dh_{Rossby} >$ will be used to denote the part of the time-mean h_2 forced by the barotropic-baroclinic interaction and nonlinear Rossby wave respectively. After some tedious algebra, and solving the equation (B.1), at the lowest order of $O(\frac{1}{\omega})$, we obtain

$$< Dh_{bb} > \approx \frac{a^2}{2\omega} \frac{(1 - H_s) H_s}{h_0} [w_0(f) - w_0(F_i)] \sin \Phi \sim O(\frac{a^2}{\omega}), \tag{B.2a}$$

$$< Dh >_{Rossby} \approx (\frac{a w_0(f)}{\omega})^2 [\gamma_1 \cos \Phi + \gamma_2] \sim O(\frac{a^2}{\omega^2}) \tag{B.2b}$$

Here F_i, h_0, Φ are determined in (3.8a), (3.7b) (3.17b). γ_1 and γ_2 are functions of F_i, h_0 and f. (B.2) shows clearly that the barotropic-baroclinic interaction is much stronger than the nonlinear Rossby wave effect in producing the time-mean component. Since $< Dh_{bb} >$ depends on $\sin \Phi$, we should expect to see a wavy structure in $< Dh >$ field as shown in Fig.3.5b,d,e and Fig.3.11c,d. In

the figure, the time-mean deviation is very weak (about 1 meters) for an annual forcing. Dewar's result seems to over-estimate this mean deviation.

It is noteworthy that in (B.2) $< Dh >_{bb}$ depends on the meridional gradient of the Ekman pumping. If the Ekman pumping is uniform in space, i,e, $w_0(f) = W_0$, it holds that $< Dh_{bb} >= 0$ at $O(a^2/\omega)$. [1] Hence, in a subtropical gyre, the time-mean deviation $< Dh >$ will be relatively weak in the middle of the gyre (more precisely, in the region near the characteristics starting near the middle of the gyre at the eastern boundary).

[1] In the QG model of Dewar (1989), for $w_o(f) = const.$, it can be shown exactly that the mean disturbance $< Dh >= 0$ for any amplitude and frequency of forcing.

Chapter 4
Thermocline Forced by Varying Surface Temperature

1 Introduction

Just as surface wind stress does, annual and decadal variabilities of surface buoyancy flux may also force variability in the permanent thermocline. In this chapter, we attempt to investigate the effect of an annual or decadal surface buoyancy flux on the permanent thermocline.

One difficulty in dealing with a variable surface heat flux arises from the fact that the surface buoyancy flux influences the permanent thermocline through a mixed layer. Therefore, it is equally crucial to consider the dynamics of both the mixed layer and the thermocline on annual and decadal time scales. A deeper mixed layer can store more heat and therefore reduces the anomalous heat flux affecting the permanent thermocline. Hence, with a given surface buoyancy flux, the variability in the permanent thermocline depends heavily on the coupling between the mixed layer and the thermocline.

Recently, the study of the coupling between the mixed layer and thermocline has concentrated on steady cases. Either the mixed layer is essentially passive (i.e. with the density and depth specified) (e.g. Pedlosky, *et.al.*,1984; Huang, 1989; Wang, 1990; Pedlosky and Robbins, 1991) or the thermocline is somewhat specified (e.g. Marshal and Nurser, 1991). The effect of a sloping mixed layer depth has been emphasized as important in enhancing the ventilation effect. So far, there has been no theory studying a time-dependent coupling.

In this chapter, as a first step to understand the coupling between a time-varying mixed layer and the permanent thermocline, the surface buoyancy flux variation is represented by a variable surface temperature or density (if we neglect the effect of salinity), which in a two-layer model, is equivalent to a moving outcrop line. To simulate an annual or decadal cycle, a periodically moving outcrop line will be used.

First, a two-layer planetary geostrophic model is used in section 2 to investigate the case of a slowly moving outcrop line. Gravitationally stable solutions will be found. For these solutions, the

horizontal buoyancy advection is strong enough to balance the surface buoyancy flux anomaly, and therefore no convection develops. All the water subducts from the mixed layer into the thermocline and there is no entrainment occurring. Thus, these solutions will be called nonentrainment solutions. However, when the outcrop line moves southward faster than the particles near the surface, all solutions in the two-layer model become gravitationally unstable, implying the occurrence of deep convection.

To obtain stable solutions under the fast outcrop line, the two-layer model is modified in section 3 by placing a mixed layer on the top. For simplicity, we will adopt an essentially passive mixed layer by specifying the outcrop line, the depth and the density structure of the mixed layer. But, the velocity in the mixed layer is coupled with the thermocline below. The system can be solved analytically by the method of characteristics.

Section 4 is the core of the whole chapter. A general approach is developed to obtain stable solutions. It will be shown that, for a fast moving outcrop line, a stable solution must have entrainment into the mixed layer. Thus, these solutions will be called entrainment solutions. In addition, a convective scheme is used to entrain waters left behind the outcrop line into the mixed layer. In this way, stable entrainment solutions can be obtained. We will also discuss some interesting features of the entrainment solution, which differ significantly from those of the nonentrainment solution. Furthermore, since in the convective scheme, the depth of a mixed layer during one part of a cycle must be determined by the mixed layer depth during another part of the cycle, the mixed layer depth in general can not be arbitrarily specified during the whole period. It will be shown that there are three stages during one cycle: the entraining stage when the mixed layer deepens rapidly to entrain the permanent thermocline; the seasonally subducting stage during which the subducted waters prepare to be reentrained by the next entraining stage and form the water for the seasonal thermocline water; the subducting stage in which the subducted waters will never be reentrained and thus form the permanent thermocline water.

Our major question is answered in section 5. It is seen that the thermocline variability is determined by the difference of the maximum and minimum subduction potential vorticities during the subducting stage. For both very low and high frequency forcings, the response tends to be inde-

pendent of frequency. In sharp contrast, for interannual and decadal flux anomalies, the variability increases dramatically with period, implying that a decadal buoyancy forcing is efficient in forcing the permanent thermocline variability.

Lastly, the mixed layer deserves a further remark in its own right. Traditionally, the seasonal thermocline has been investigated with a 1-D model (Turner and Kraus, 1967; Kraus and Turner, 1967; Warren,1972; Gill and Turner,1976; Niiler and Kraus,1977). However, in the area where the net annual buoyancy flux is large, a 1-D model is probably no longer valid. Particularly in regions with net surface cooling in a 1-D model, either the convection has to penetrate deeper and deeper or the surface temperature has to get colder and colder, because there is no other mechanism to balance this net buoyancy loss on the surface. Thus, on climate time scales, the locally unbalanced net heat flux should be balanced by horizontal advection (Woods, 1985). Accordingly, in order to study the surface buoyancy effect on the basin scale circulation at interannual time scales, it is essential to include horizontal advection. The importance of advection in the coupling between the seasonal thermocline and permanent thermocline has been noted (Woods,1985). Since this chapter concentrates on climate scale variation, it is crucial to include the horizontal advection. This is indeed the case in our model, although the mixed layer in our model is crude and essentially passive. It turns out that our results may have important implications on the dynamics of the mixed layer.

2 Slow Outcrop Line Case: Nonentrainment Solutions

2.1 The Nonentrainment Solution

We start with the case of a slowly moving outcrop line and try to find solutions with gravitational stability. A two-layer planetary geostrophic model with a flat bottom is adopted. The upper layer depth h is governed by a quasi-linear equation, whose dimensionless form assumes (see (1.7a) of chapter 2)

$$h_t + \vec{v_B} \cdot \nabla h + C(h)h_x = -(1-h)w_e \tag{2.1}$$

where $\vec{v}_B = (u_B, v_B) = [-(f^2 \int_0^x w_e dx)_f / f, f w_e]$ is the barotropic velocity and $C(h) = -h(1-h)/f^2$ is the planetary wave speed. The Ekman pumping will be set steady throughout this chapter because our focus is on a variable surface buoyancy flux. With a zonally independent Ekman

pumping $w_e = w_e(f)$, the characteristic equations of (2.1) are solved as (see (4.8) of chapter 2)

$$t = t_i + s, \tag{2.2a}$$

$$s = \int_{f_i}^{f} \frac{df}{v_B}, \quad or\ f = \hat{f}(s, f_i) \tag{2.2b}$$

$$\frac{f}{1-h} = \frac{f_i}{1-h_i}, \tag{2.2c}$$

$$2f^2 w_e(f)x = 2f_i^2 w_e(f_i)x_i + h^2 - h_i^2 \tag{2.2d}$$

where $\hat{f}$ represents the f solution in the characteristic coordinate. (2.2) gives solutions in different regions if the initial conditions for characteristics (t_i, f_i, h_i, x_i) starts from different places. (see section 5 of chapter 2 for a detailed discussion).

Sea surface density will change if there is a temporal anomaly in surface buoyancy flux. In our layered model, the variation of sea surface density is simulated by the motion of an outcrop line. For simplicity, we adopt a zonal outcrop line varying with time, i.e. $h\,|_{f=f_o} = 0$ and

$$f_o = f_o(t). \tag{2.3}$$

We will study periodically forced solutions after the initial adjustment. Thus, characteristics for the solution in the gyre start either from the outcrop line or the eastern boundary.

Ventilated zone

If we want to derive a solution at a time t over an entire gyre, all characteristics must start before this time, i.e. $t_i \leq t$. Thus, with (2.3), characteristics originating from the outcrop line have the initial conditions

$$f_i = f_o(t_i),\ h_i = 0. \quad t_i \leq t \tag{2.4}$$

Substitution of (2.4) into (2.2a,b,c) yields the characteristic solution in its parametric form

$$f = \hat{f}[t - t_i, f_o(t_i)] \equiv f^*(t, t_i), \qquad for\ \ t_i \leq t \tag{2.5a}$$

$$h = 1 - \frac{f^*(t, t_i)}{f_o(t_i)} \equiv h^*(t, t_i) \tag{2.5b}$$

In the special case when the outcrop line in (2.3) is steady, (2.5) gives an explicit solution $h = 1 - f/f_o$, which is the same as the steady ventilated zone (see (3.2) or (5.6) of chapter 2). Thus,

hereafter, for convenience, the solution (2.5) will be called the ventilated zone solution even with a moving outcrop line (2.3).

(2.5) is independent of x. This means that the potential vorticity (in this chapter, potential vorticity always refers to that in the bottom layer) is uniform on a latitude circle. However, unlike the steady zonal outcrop line case in the previous chapter 3, the potential vorticity now can vary significantly with latitude. Therefore, the ventilated zone is no longer a uniform potential vorticity pool.

The physics of the parameteric solutions $f^*(t,t_i)$ and $h^*(t,t_i)$ in (2.5) can be made clear as follows. At a time t, a lower layer water column at a latitude f was subducted from the outcrop line at a previous time t_i, i.e.

$$t_i = \tau(f,t) \le t \qquad where \quad f \equiv f^*[t,\tau(f,t)]. \tag{2.5c}$$

The interface depth at this latitude is $h = h^*[t,\tau(f,t)] \equiv h(f,t)$. Therefore, this water column always remembers its subduction time $\tau(f,t)$. It is important to notice that the subduction time is independent of the thermocline structure h in (2.5b). In fact, τ is determined by the $\hat{f}$ in (2.5a), which is derived from the f characteristic equation $df/ds = fw_e$. This equation is solely determined by the Ekman pumping and independent of h. Hence, during the evolution, each water column in the lower layer remembers its subduction time and then can be labeled by the time according to (2.5a) or (2.5c) (not (2.5b)!). In particular, at the latitude of the outcrop line $f = f_o(t)$, the water column is subducted at the present time $t_i = t$. In (2.5c), this suggests the identity $t \equiv \tau[f_o(t),t]$.

Fig.4.1a,b demonstrate schematically how a water column is determined at latitude $f = F$ and time t. Since all subductions occur before the present time t, the subduction time τ terminates at $\tau = t$ in Fig.4.1a. In this case, the outcrop line moves so slowly such that its southward velocity is never faster than the particle velocity or $0 > \dot{f}_o > v_B(f_o)$. Therefore, no water column will be overtaken by a water column subducted later. In other words, at any time, the more north a water column is located, the later will be its subduction time; or equivalently, the $\tau(f,t)$ increases monotonically with latitude as shown in Fig.4.1a. Therefore, at each latitude F, the water column has a single subduction time $\tau(F,t)$. The labeling is done as follows. First, we find the subduction time for the water at $f = F$ from (2.5c) or (2.5a) as $\tau = \tau(F,t)$ as shown in Fig.4.1a. Then, at F,

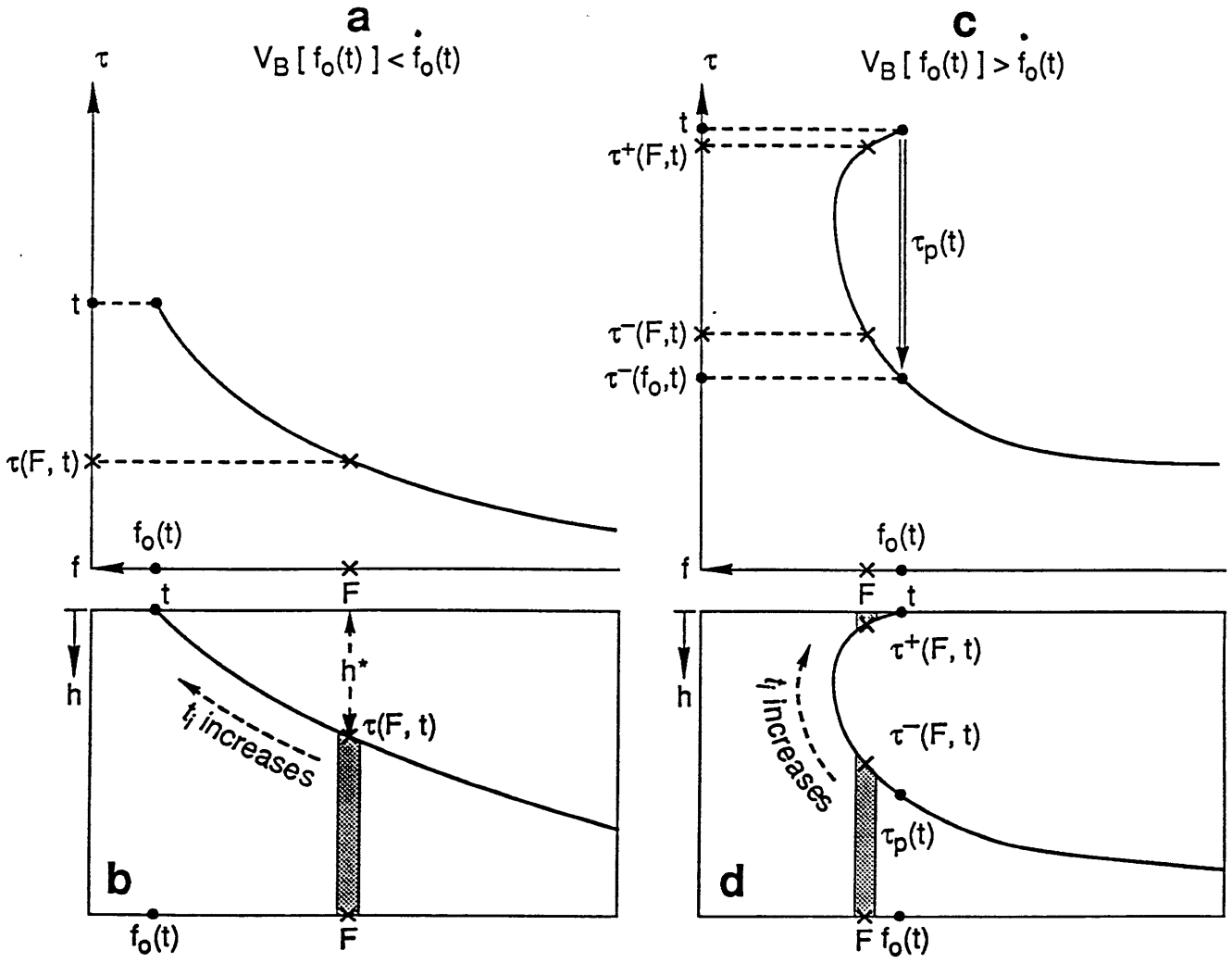

Figure 4.1: The schematic figure showing how the interface solution is determined and labeled by the subduction time $\tau(f,t)$ at a given time t. (a) and (b): Slow outcrop line case. (a) shows τ as a monotonic function of f because later water can not catch up with an earlier subducted water. τ is single-valued. (b) shows the h^* profile, which is labeled by the subduction time according to (a). The h profile is stable. (c) and (d): Fast outcrop line case (during entraining stage): Now, because a later subducted water catches up with an earlier subducted water in (d), τ is double-valued in (c), with the later branch τ^+ and the early branch τ^-. Corresponding to the double value τ function, the solution is unstable. Also shown schematically is the $\tau_p(t)$ function mapping, which gives the corresponding seasonally subducting time and determines the convective scheme used in (4.9a).

we find the depth of the interface from (2.5b) as $h = h^*[t, \tau(F,t)]$. Thus, at F, the water column has an interface at h^* and can be labeled by $\tau(F,t)$ as shown in Fig.4.1b.

Shadow zone

The solution (2.5) only occupies part of the basin. In the other part of the gyre, the solution is established by characteristics starting from the eastern boundary. For an eastern boundary at $x = 0$, the initial conditions for these characteristics are $x_i = 0, h_i = h_e(f_i, t_i) = 0$, when $f_i \leq f_o(t_i)$ and $t_i \leq t$. Here, for convenience, the depth of the eastern boundary interface has been set zero. Thus, (2.2) gives the solution

$$h^2 = 2f^2 w_e(f)x \qquad when\ x > x_b(f,t). \tag{2.6}$$

This is the same as the steady shadow zone (see (3.3) or (5.2d) in chapter 2) except now the shadow zone boundary x_b varies with time. Therefore, the solution will still be called the shadow zone solution. The resemblance between (2.6) and the steady shadow zone is not surprising because the shadow zone does not feel the motion of the outcrop line except in the most western part where the characteristics starting from the outcrop line along the eastern boundary arrive. The varying shadow zone boundary has the initial condition for characteristics as $x_i = 0, f_i = f_o(t_i), h_i = 0$. Thus, (2.2) gives the parametric form of x_b

$$x_b^*(t, t_i) \equiv (h^*)^2/2(f^*)^2 w_e(f^*) \tag{2.7}$$

where f^*, h^* are given in (2.5a,b).

Examples

(2.5), (2.6) and (2.7) form the solution in the entire gyre. As an example, we take a spatially uniform Ekman pumping

$$w_e(f) = W_0 = constant < 0. \tag{2.8}$$

(This Ekman pumping function will be used for all the calculations in this chapter.) With (2.8), (2.2b) gives the f characteristic solution

$$f = f_i e^{W_0 s} = \hat{f}(s, f_i). \tag{2.9}$$

With an outcrop line $f_o(t)$, the parametric solution in the ventilated zone is derived from (2.9) and (2.5a,b) as

$$f = f^*(t, t_i) = f_o(t_i)e^{W_0(t-t_i)} \tag{2.10a}$$

$$h = h^*(t, t_i) = 1 - e^{W_0(t-t_i)} \tag{2.10b}$$

In the rest of the chapter, the outcrop line is assumed an oscillating one with the form

$$f_o(t) = f_g(1 + a\cos\omega t), \quad 0 \le a \le 1, \tag{2.11a}$$

where f_g is the mean position of $f_o(t)$ and af_g is the amplitude of the oscillation. The most northern and southern latitudes of the outcrop line are respectively

$$f_{omax} = f_g(1 + a) \quad and \quad f_{omin} = f_g(1 - a). \tag{2.11b}$$

which are reached by f_o at the times

$$t = p_n \equiv \frac{2n\pi}{\omega} \quad and \quad t = p_n + \frac{\pi}{\omega} \qquad where \ \ n \ is \ an \ integer. \tag{2.11c}$$

In the annual period case, these two times correspond to about September and March, (for the sea surface temperature lags the surface heat flux about 90^o in phase). For a thermocline depth of about 600 meters, the dimensional time scale is $T_w = H/W_e \sim 20$ years, where we have used a typical vertical velocity of $W_e \sim 10^{-4} cms^{-1}$. Therefore, a nondimensional annual frequency is about $\omega \approx 100$ while a decadal frequency is about $\omega \approx 10$ (see the definition of scaling vairables in (1.5a) of chapter 2). Without confusion, the twelve months will still be used to refer to relative times in the oscillation even for periods other than the annual period.

Fig.4.2 displays an example of weak decadal forcing, with $W_0 = -1$ in (2.8) and $f_g = 0.7, \omega = 5, a = 0.19$ in (2.11a). Along $x = -1$, the meridional profiles at $\omega t = 0, \pi/2, \pi$ and $3\pi/2$, corresponding to "September", "December", "March" and "June", are presented in Fig.4.2a-d. The northern part that deepens southward is the ventilated zone while the southern part that shallows southward is the shadow zone. Several features are interesting. First, the interface slope near the

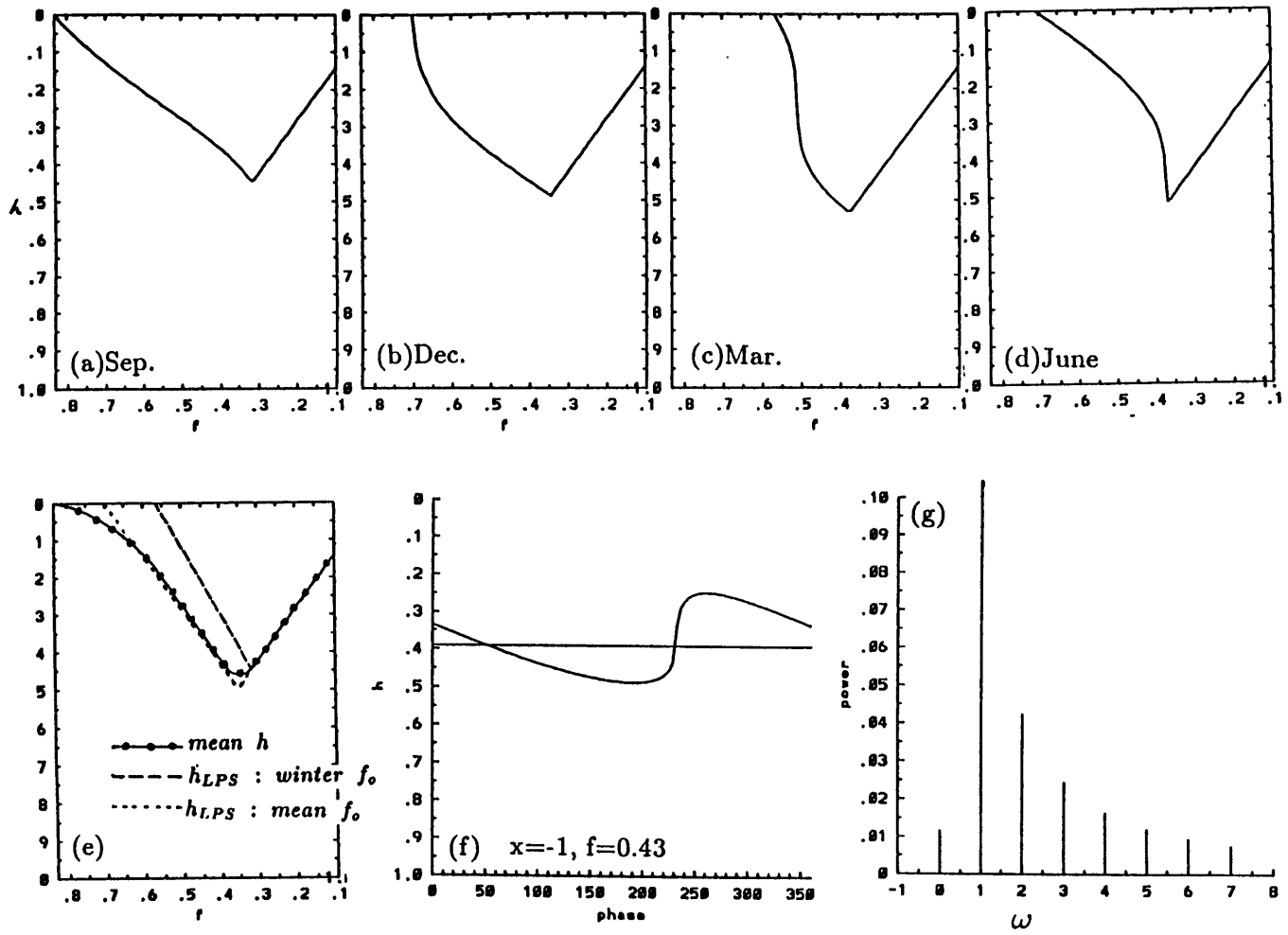

Fig.4.2: The nonentrainment solution in the absence of a mixed layer. $w_e(f) = -1, f_o(t) = f_g(1 + acos(\omega t)), \omega = 5, a = 0.19, f_g = 0.7$. (a)-(d) show the meridional sections along $x = -1$ on September ($\omega t = 0$), December ($\omega t = \pi/2$), March ($\omega t = 0$) and June ($\omega t = 0$) respectively. (e) shows the time-mean profile (dot connected line), the steady LPS thermocline with the time-mean outcrop line (short dash line) and the steady LPS thermocline with the outcrop line at March. (f) the local time series of interface during one period. (g) the Fourier components of the local time series in (f).

surface $\partial_f h$ is small at "September" (Fig.4.2a), implying a strong stratification. As the outcrop line moves southward due to cooling, the slope steepens but remains stable (Fig.4.2b) with the maximum slope (or a minimum stratification) achieved a little before "March". Later, the outcrop line returns northward due to heating. The thermocline responds with a quick decrease in the slope (Fig.4.2c.d). The second feature is the relation between the time-mean thermocline profile and some steady thermocline profiles. In Fig.4.2e, the time-mean interface $< h >$ is depicted as the dot-connected line while the short and long dashed lines respectively draw the steady LPS solutions with f_o at the time-mean position (f_g) and southernmost position (f_{omin}) ("March"). It is seen that the time-mean profile is very close to the steady thermocline with the mean outcrop line (except in the very northern part). Third, the variability in the permanent thermocline is strong as shown by a local time series of h in Fig.4.2 f. Although the outcrop line (2.11a) is harmonic, the interface variation is not ! It has a relatively slow deepening and a rapid rise and therefore possesses strong superharmonics in the power spectrum (or Fourier series) of the h time series as presented Fig.4.2g. This power spectrum differs significantly from that produced by a wind forcing. In the wind forcing case in section 4 of chapter 3, the time-mean component is comparable to the second superharmonic and other higher superharmonics are negligible (see Fig.3.10 in chapter 3). In contrast, now, the time-mean component is smaller than most superharmonics (Fig.4.2g).

The above features are also observed clearly in Fig.4.3a, where the zonal profiles are displayed. Furthermore, the shadow zone boundary x_b at four seasons are drawn in Fig.4.3b. In the region where x_B sweeps through, the shadow zone and ventilated zone dominates alternatively. A similar phenomenon has been seen with a variable wind forcing in the alternative zone.

The solution above is an example of *nonentrainment solution*, which exists in the absence of a variable mixed layer depth and remains stable. It is so named because of the absence of entrainment, as will be shown later. However, if the amplitude or frequency increases further (so that $\dot{f}_o$ increases), the solution may exhibits gravitational instability. Fig.4.4a-d shows a solution with the same frequency as that in Fig.4.2 and Fig.4.3 but with a larger amplitude of $a = 0.4$ (the shadow zone part of the solution is not shown in Fig.4.4). One sees that during "winter" when the outcrop line moves southward rapidly, the solution becomes gravitationally unstable. Later, a bulb

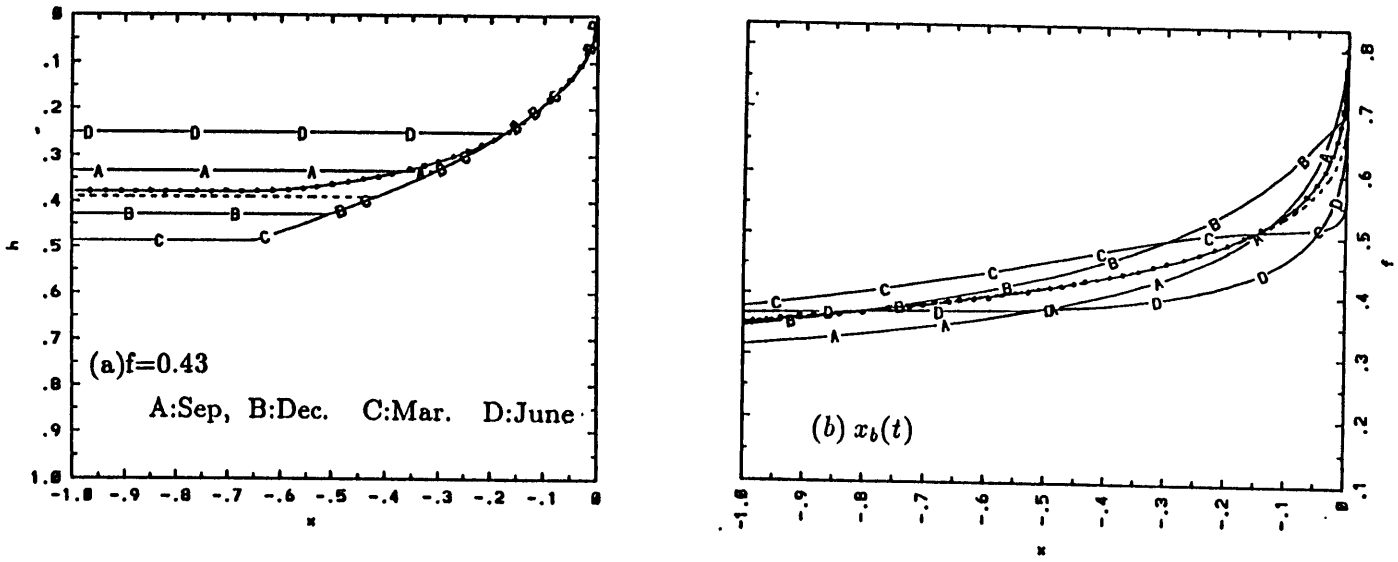

Fig.4.3: The zonal sections and shadow zone boundaries of the example in Fig.4.2. (a) the zonal sections at four seasons. The dot connected line is the time-mean profile. The short dash line is the steady LPS thermocline with the time-mean outcrop line. b) similar to a) but for the shadow zone boundary.

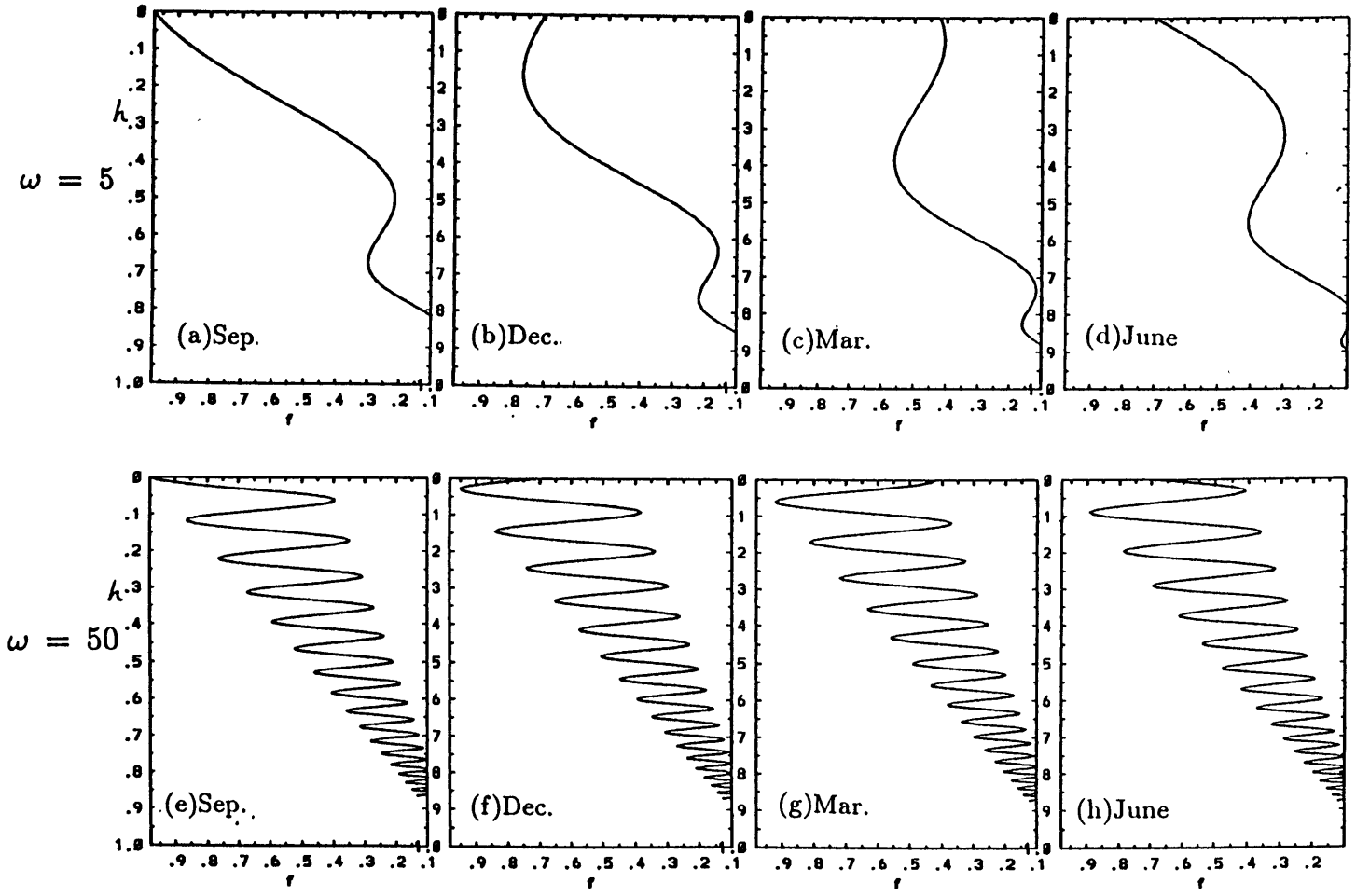

Fig.4.4: Unstable entrainment solutions. a)-d): Meridional sections at four seasons with the same parameter as in Fig.4.2 except for now $a = 0.4$. Only the ventilated zone solution is drawn. e)-h): The same as a)-d) except for $\omega = 50$.

of unstable water later is advected downward by the downward vertical velocity, and southward by the Sverdrup flow. An annual frequency case is shown in Fig.4.4e-h. The profile has many more unstable pulses of waters because of the higher frequency. The two solutions are not physically valid because of the gravitational instability. Later sections of the chapter is devoted to find stable solutions under fast outcrop lines such as those in Fig.4.4. But, first, we study the criterion for the breakdown of nonentrainment solution.

2.2 The Criterion for the Breakdown of Nonentrainment Solutions

Obviously, a gravitationally stable solution must have a stable slope of interface

$$\partial_f h \leq 0 \quad everywhere \tag{2.12a}$$

Inside the ventilated zone of our two-layer model, when the potential vorticity does not vary along a latitude, it holds that $\partial_x h = 0$ or $Ch_x = 0$ in (2.1) south of the outcrop line. Thus, there is no Rossby wave effect and the associated nonlinear steepening effect. Therefore, it seems to me that gravitational instability can only be caused on the outcrop line. (This has been seen true in all the experiments. But, I am not able to prove it mathematically.) Thus (2.12a) is equivalent to

$$\partial_f h \mid_{f=f_o(t)} = \leq 0 \qquad for\ all\ t \tag{2.12b}$$

This slope can be derived from the mass balance of the upper layer near the outcrop line. Let's take a small volume near the outcrop line in the upper layer with a δf length on its top and a δh thickness on its southern side. $-w_e \delta f$ is the downward mass flux from the top and $(v_B - \dot{f}_o)\delta h$ is the southward mass flux through the southern side (since the outcrop line is moving with the speed $\dot{f}_o$, the mass flux through the southern side is caused by the relative velocity $v_B - \dot{f}_o$). Noticing the absence of mass flux across the interface on the northern and bottom side, the mass balance for the small volume is then

$$-w_e \delta f = [v_B(f_o) - \dot{f}_o]\delta h \quad near \quad f_o, \tag{2.13a}$$

where $\dot{f}_o \equiv df(t)/dt$. (2.13a) is equivlent to

$$\frac{\partial h}{\partial f} \mid_{f=f_o} = \frac{-w_e}{v_B(f_o) - \dot{f}_o}. \tag{2.13b}$$

This slope can also be derived mathematically as in appendix B. With the aid of (2.13b), (2.12b) becomes

$$\partial_f h \mid_{f=f_o} = \frac{-w_e(f_o)}{v_B(f_o) - \dot{f}_o} \leq 0 \tag{2.14}$$

In a subtropical gyre, $w_e \leq 0$. Thus, when the outcrop line remains slower than the southward barotropic flow $v_B - \dot{f}_o < 0$, the slope (2.14) is always stable, implying the absence of convection or entrainment. Thus, these solutions will be called nonentrainment solutions or

$$\textit{nonentrainment solution}: \quad v_B[f_o(t)] - \dot{f}_o(t) \leq 0 \qquad \textit{for all } t. \tag{2.15}$$

For a nonentrainment solution, a subducted water column will never be caught by water subducted later. Thus, the more north a water column is located, the later is its subduction time. In other words, the water column of layer two at a latitude f consists solely of the water injected from the outcrop line at the time $\tau(f,t)$ (see Fig.4.1b). This suggests that the subduction time τ is single-valued with respect to f, as depicted schemetically in Fig.4.1a. This can also be proven mathematically. With the aid of (2.5a) and (2.2a,b), we have

$$t - t_i = \int_{f_o(t_i)}^{f^*(t,t_i)} \frac{df}{v_B(f)}.$$

Differentiating this equation with respect to t_i yields

$$\partial_{t_i} f^* \mid_{t \text{ fixed}} = -\frac{v_B(f^*)}{v_B(f_o)}[v_B(f_o) - \dot{f}_o]. \tag{2.16}$$

Therefore, if $v_B - \dot{f} < 0$ always holds as in (2.15), $\partial_{t_i} f^* > 0$ is always true. From (2.5c) we also have $\partial_f \tau = 1/\partial_{t_i} f^* > 0$. Thus the subduction time increases monotonically with latitude. Condition (2.15) is marginally satisfied by the solution in Fig.4.2 and Fig.4.3.

If (2.15) is violated, the solution will exhibits a unstable slope as shown in examples of Fig.4.4, implying the occurence of cold convection or entrainment. The solutions will then be called an *entrainment solution* i.e.

$$\textit{entrainment solution}: \quad v_B[f_o(t)] - \dot{f}_o(t) > 0 \qquad \textit{at some } t. \tag{2.17}$$

The two examples in Fig.4.4 can be checked to satisfy (2.17). For an entrainment solution, at a time when the southward speed of the outcrop line is faster than the particle speed, newly injected

waters will catch up with previously injected waters left behind (north of) the outcrop line. (2.16) shows that now $\partial_{t_i} f^* < 0$ or $\partial_f \tau < 0$. Thus, $\partial_f \tau$ changes sign and τ has a double-value at latitudes north of the outcrop line. This case is shown schematically in Fig.4.1c,d. We will denote the later and earlier branches of τ as τ^+ and τ^- respectively (Fig.4.1c). Correspondingly in Fig.4.1d, a water column subducted at $\tau^+(F,t)$ now overlies on the water column subducted at an earlier time $\tau^-(F,t)$, implying a gravitationally unstable solution as shown in (2.14). [1]

The unstable structure suggests the occurence of cold convection near the surface. The physics can be understood as follows. First of all, intuitively, one may think that a slow outcrop line in (2.15) is produced by a weak surface cooling (in the cooling period) while a fast outcrop line in (2.17) is forced by a strong surface cooling. This is indeed the case as illustrated in appendix A. Now, we consider an ideal fluid thermocline. If we impose a temporal surface cooling uniformly over the surface in the whole gyre, the surface temperature, and then the temperature of the whole water column, should decrease. If the stratification is stable, in a subtropical gyre, the downward vertical velocity always tends to warm the water column. Thus, the only mechanism to balance the surface cooling is a cold horizontal advection. This is the case of a nonentrainment solution. However, the horizontal cold advection can not grow very strong simply because there is no frontogensis mechanism under the uniform surface cooling. Therefore, if the surface cooling is too strong, the horizontal cold advection may not be able to balance the cooling. On the other hand, the downward vertical velocity is still forced by the surface Ekman pumping. Thus, the only way to balance the strong surface cooling is to have a unstable stratification near the surface which, together with the downward velocity, tends to cool the water column. This is the case of entrainment solution (see examples in Fig.4.1c,d and Fig.4.4). Of course, these unstable solution are not physically valid. Indeed, the unstable stratification implies a cold advection near the surface.

[1] Although the subduction time does not vary with latitude monotonically any more, the subduction time always increases as the interface shallows as shown in Fig.4.1d. This occurs because as a subducted water column moves southward, the potential vorticity conservation requires that thickness of a layer two water column $1-h$ shrinks or the interface h increases. This can be proven here. From the h characteristic equation for (2.1), we have $\frac{dh}{ds} = -(1-h)w_e > 0$. At a fixed t, noticing (2.2a) and (2.5b), we then have $\partial_{t_i} h^* = -(1-h^*)w_e > 0$.

3 A Thermocline Model With a Time-Dependent Mixed Layer Depth

For an outcrop line moving southward rapidly, we have seen that the solution derived from (2.1) becomes gravitationally unstable, implying deep cold convection. This mechanism is not included in the ideal fluid thermocline model (2.1). To develop a model accounting for convection, in our oceanic context, one proper way is to add a mixed layer onto the thermocline. As shown in Fig.4.5 our improved model has a mixed layer atop the two-layer ideal fluid thermocline. The density $\rho_m(x, f, t)$ in the mixed layer satisfies gravitational stability and equals the upper layer density at the outcrop line, i.e.

$$\rho_m \leq \rho_2 \quad for\ f > f_o; \quad \rho_m \leq \rho_1 \quad for\ f < f_o; \quad \rho_m(x, f, t)\,|_{f=f_o(t)} \equiv \rho_1. \tag{3.1}$$

$h_m(x, f, t)$ is the mixed layer depth; ρ_1 and h_1 represent the density and thickness of the upper layer respectively; ρ_2 and $h_2 = H - h_m - h_1$ are the density and thickness of the bottom layer respectively.

To derive the equations, we start with dimensional quantities. Integrating hydrodynamic equation in each layer, the dynamic pressure in each layer is obtained as

$$\frac{p_m}{\rho_m} \approx \frac{p_m}{\rho_0} = \gamma\eta + \gamma_m z \tag{3.2a}$$

$$\frac{p_1}{\rho_1} \approx \frac{p_1}{\rho_0} = \gamma\eta - \gamma_m h_m \tag{3.2b}$$

$$\frac{p_2}{\rho_2} \approx \frac{p_2}{\rho_0} = \gamma(\eta - h) - \gamma_m h_m \tag{3.2c}$$

Here η is the equivalent elevation near the surface (see (1.2a) of chapter 2), ρ_0 is the mean density and

$$h = h_m + h_1,\ h + h_2 = H,\ 0 < \gamma_m(x, f, t) = \frac{\rho_1 - \rho_m(x, f, t)}{\rho_0} g,\ \gamma = \frac{\rho_2 - \rho_1}{\rho_0} g = constant. \tag{3.3}$$

In the mixed layer pressure (3.2a), the first term is due to the pressure near the surface while the second term relates to the geostrophic vertical shear. The outcropping condition is $h_1\,|_{f=f_o} = 0$, or

$$h\,|_{f=f_o} = h_m. \tag{3.4}$$

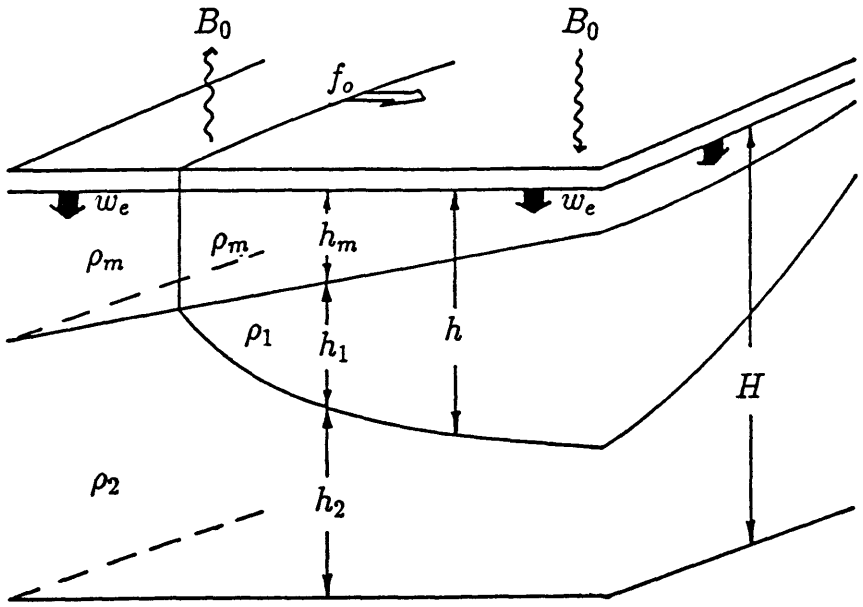

Figure 4.5: The schematic figure of the model with one mixed layer and two ideal fluid layers. The model takes the thickness of the Ekman layer zero.

As a first step to study the effect of a variable surface heat flux, we specify the mixed layer density ($\sim \gamma_m$) and depth (h_m) in this chapter, while we leave the mixed layer velocity coupled with the thermocline through the pressure. The momentum equation in each layer gives the geostrophic balance

$$(u_m, v_m) = \frac{1}{f\rho_0}(-p_{my}, p_{mx}),\ (u_1, v_1) = \frac{1}{f\rho_0}(-p_{1y}, p_{1x}),\ (u_2, v_2) = \frac{1}{f\rho_0}(-p_{2y}, p_{2x}). \tag{3.5}$$

The remaining unknowns are η and h, which can be derived from the Sverdrup relation and potential vorticity conservation in the bottom layer. Now, the barotropic velocity is

$$\frac{\int_{-h_m}^{0} \vec{v}_m dz + h_1\vec{v}_1 + h_2\vec{v}_2}{H} \equiv \vec{v}_B = \frac{1}{f\rho_0}\vec{k} \times \nabla p_B. \tag{3.6a}$$

Then, the barotropic pressure can be found from geostrophic balance as well as (3.4) and(3.5) as

$$p_B = \frac{\rho_0}{2H\gamma}[2H(\gamma\eta - \gamma_m h_m) + \gamma_m h_m^2 + \gamma(H-h)^2]. \tag{3.6b}$$

Now, the Sverdrup relation is $\beta(\int_{-h_m}^{0} v_m dz + h_1 v_1 + h_2 v_2) = f w_e$. Using (3.2), (3.5) and (3.6b), and assuming a flat bottom $H = constant$, the Sverdrup relation can be integrated explicitly as

$$p_B = \frac{\rho_0 \gamma D^2}{2H} + p_{BE} \tag{3.6c}$$

where

$$D^2 = \frac{2f^2 w_e x}{\beta\gamma},\ p_{BE} = p_B\mid_{x=0}, \tag{3.6d}$$

In the remainder of the chapter, a vanishing barotropic transport into the eastern boundary is assumed, i.e.

$$p_{BE} = 0. \tag{3.6e}$$

The potential vorticity conservation in the bottom layer is $(\partial_t + \vec{v}_2 \cdot \nabla)[f/(H-h)] = 0$. Substitution of (3.5) and (3.6) into this equation yields the equation for the depth $h = h_m + h_1$ as

$$h_t + \vec{v}_B \cdot \nabla h - \frac{1}{2Hf}J(\gamma_m h_m^2, h) - \frac{\beta}{2f^2}(1 - \frac{h}{H})(\gamma_m h_m^2 + \gamma h^2)_x = -(1 - \frac{h}{H})w_e. \tag{3.7}$$

Hereafter, the y coordinate will be changed to an f coordinate. Nondimensionalizing quantities similarly to (1.5a) in chapter 2 with the additional dimensionless quantities $\gamma_m = \gamma_m^*/\gamma^*, h_m =$

h_m^*/H (where * refers to dimensional quantities), (3.6) and (3.7) can be put in the dimensionless forms:

$$p_B = \frac{D^2}{2}, \tag{3.8a}$$

$$D^2 = 2f^2 w_e x, \quad p_B = \frac{1}{2}[2(\eta - \gamma_m h_m) + \gamma_m h_m^2 + (1-h)^2]; \tag{3.8b}$$

and

$$h_t + \vec{v}_B \cdot \nabla h - \frac{1}{2f} J(\gamma_m h_m^2, h) - \frac{1}{2f^2}(1-h)(\gamma_m h_m^2 + h^2)_x = -(1-h)w_e. \tag{3.9}$$

Here, by virtue of (3.6), the barotropic velocities are found to be $u_B = -(f^2 w_e)_f x/f$ and $v_B = f w_e$, which are the same as the two-layer case in (2.1). In our mixed layer, h_m, γ_m are specified. Thus, (3.9) is a quasi-linear equation, which is the same as (2.1) except with an additional effect arising from the thermal wind in the mixed layer. Division of the f and h characteristic equations yields the potential vorticity conservation along a characteristic line as

$$\frac{d}{ds}\left(\frac{f}{1-h}\right) = 0 \quad or \quad \frac{f}{1-h} = \frac{f_i}{1-h_i}. \tag{3.10}$$

For simplicity, a special mixed layer is adopted such that its density and depth are zonally independent, i.e., $\partial_x \gamma_m = \partial_x h_m = 0$. Thus, (3.9) reduces to

$$h_t + \vec{v}_B \cdot \nabla h + \left[\frac{1}{2f}(\gamma_m h_m^2)_f - \frac{h(1-h)}{f^2}\right] h_x = -(1-h)w_e. \tag{3.11}$$

Using (3.10) to replace the h characteristic equation, the characteristic equations for (3.11) take the forms

$$\frac{dt}{ds} = 1 \tag{3.12a}$$

$$s = \int_{f_i}^{f} \frac{df}{v_B}, \quad or \ f = \hat{f}(s, f_i) \tag{3.12b}$$

$$\frac{f}{1-h} = \frac{f_i}{1-h_i}, \tag{3.12c}$$

$$\frac{dx}{ds} = u_B + \frac{1}{2f}(\gamma_m h_m^2)_f - \frac{h(1-h)}{f^2}. \tag{3.12d}$$

These are the same as (2.2) except with the x equation. The x equation is changed by the zonal thermal wind which is produced by the meridional variation of the mixed layer.

In the rest of the chapter, we concentrate on meridional profiles inside the ventilated zone. For a zonal outcrop line $\partial_x f_o = 0$, (3.12a,b,c) show that the h solution is independent of x. This is also related to the fact that now the potential vorticity does not vary in zonal direction inside the ventilated zone or $h_x = 0$. Then (3.11) becomes

$$\boxed{h_t + v_B h_f = -(1-h)w_e} \quad \textit{in the ventilated zone, } f < f_o(t) \tag{3.13}$$

(3.13), with the outcropping condition (3.4), gives the simplest model accounting for subduction under a variable mixed layer depth. In (3.13), we see that the horizontal buoyancy advection in the thermocline is simple. The flow field is known from the Sverdrup relation and therefore is independent of the buoyancy effect. As a result, our problem is greatly simplified.

4 Fast Outcrop Line Case: Entrainment Solutions

4.1 Derivation of the Solution

Now, we present the core material of the chapter-- a general approach to obtain gravitationally stable entrainment solutions from (3.13). Our goal is to find variability in the permanent thermocline under both a moving outcrop line and a variable mixed layer depth.

We only consider the solution in the ventilated zone, which is established by characteristics originating from the outcrop line. Noticing (2.3) and (3.13b), the initial conditions are

$$f_i = f_o(t_i), \; h_i = h_m[f_o(t_i), t_i] \equiv H_m(t_i). \tag{4.1}$$

Here H_m is the depth of the mixed layer under the outcrop line. Substituting (4.1) into (3.12a,b,c) yields the solution in the ventilated zone as

$$f = \hat{f}[t - t_i, f_o(t_i)] \equiv f^*(t, t_i) \tag{4.2a}$$

$$h = 1 - [1 - H_m(t_i)]\frac{f^*(t,t_i)}{f_o(t_i)} \equiv h^*(t, t_i) \tag{4.2b}$$

(4.2) is the generalized solution of (2.5). Its physics can also be explained similarly to that of (2.5). That is: each water column remembers its subduction time

$$t_i = \tau(f,t) \le t, \quad \textit{where } \; f \equiv f^*[t, \tau(f,t)] \tag{4.2c}$$

Since (4.2a) is exactly the same as (2.5a), the subduction (4.2c) is the same as (2.5c).

(4.2a,b) give the parameteric solution for (3.13). However, the solution may not be gravitationally stable for an arbitrarily specified $f_o(t)$ and $H_m(t)$. One example we have seen is the case with a vanishing mixed layer depth $H_m(t) = 0$ (now (3.12) degenerates to (2.1)). For this case, if the outcrop line moves southward faster than the particle velocity $\dot{f}_o < v_B < 0$, the solution becomes unstable as shown by examples in Fig.4.4 and in equation (2.13b). Therefore, we need to find some constraints on the depth of the mixed layer, under which the solution (4.2) will always be stable. The necessity for these constraints is not totally surprising. This is because the mixed layer here is partially coupled with the thermocline through pressure. Consequently, the behavior and structure of the mixed layer can not be specified completely arbitrarily.

A stable slope: restraining the penetration of the mixed layer

First of all, it is obvious that a stable solution must have a stable slope all the time in the gyre, i.e.

$$\partial_f h \leq 0 \qquad everywhere; \tag{4.3}$$

Using argument similar to that for (2.12b), (4.3) seems to be equivalent to a stable slope at the outcrop line $\partial_f h \mid_{f=f_o}$. Similar to (2.13), this slope can also be derived by the mass balance of layer one near the outcrop line as

$$-w_m^* \delta f = [v_B(f_o) - \dot{f}_o]\delta h, \tag{4.4a}$$

or

$$\partial_f h \mid_{f=f_o(t)} = \frac{-w_m^*}{v_B[f_o(t)] - \dot{f}_o(t)}. \tag{4.4b}$$

where w_m^* is the mass entrainment velocity at the bottom of the mixed layer near the outcrop line. From continuity equation, we have w_m^* as

$$w_m^* = \frac{dH_m}{dt} + w_m, \tag{4.4c}$$

where $w_m = w \mid_{z=-H_m}$ is the vertical velocity at the bottom of the mixed layer at the outcrop line and can be proven to be (see appendix B)

$$w_m = (1 - H_m) w_e(f_o) \tag{4.4d}$$

With a vanishing $H_m = 0$, (4.4c,d) show that $w_m^* = w_e$. Thus, (4.4a,b) degenerate to (2.13a,b).

Hence, the stable slope (4.3) requires $\partial_f h \mid_{f=f_o(t)} = -w_m^*/[v_B(f_o) - \dot{f}_o] \leq 0$, *for all t.* or:

$$0 \;>\; w_m^* \qquad \textit{when } v_B(f_o) - \dot{f}_o < 0, \tag{4.5a}$$

$$0 \;<\; w_m^* \qquad \textit{when } v_B(f_o) - \dot{f}_o > 0 \tag{4.5b}$$

(4.5a) states that, when the outcrop line moves southward less rapidly than the particle, water mass subducts from the mixed layer into the thermocline. On the other hand, (4.5b) says that during the time interval when the outcrop line moves southward more rapidly than the particle, the mixed layer must be entrained from the thermocline below. The time interval in (4.5b) is therefore called the *entraining stage.* For a periodically moving outcrop line in (2.11), the entraining stage is

$$\textit{entraining stage} \;:\quad \tau_1^n \leq t \leq \tau_2^n. \tag{4.6a}$$

where $p_n \leq \tau_1^n, \tau_2^n \leq p_{n+1}$ with $p_n = 2n\pi/\omega$. [1] Here n refers to the entraining stage during the nth period; τ_1^n is the initial entraining time when the outcrop line just catches up the barotropic velocity; τ_2^n is the final entraining time when the outcrop line is overtaken by the barotropic velocity, i.e.

$$v_B[f_o(t)] - \dot{f}_o(t)] \mid_{t=\tau_1^n,\tau_2^n} = 0; \;\; \textit{and} \;\; \frac{d}{dt}[v_B(f_o) - \dot{f}_o] \mid_{t=\tau_1^n} > 0; \frac{d}{dt}[v_B(f_o) - \dot{f}_o] \mid_{t=\tau_2^n} < 0. \tag{4.6b}$$

It is important to remember that the entraining stage defined here is independent of the structure of the solution because the subduction time in (2.5c) (or (4.2c)) is only determined by the f equation (2.5a) (or (4.2a)). Now the physics for nonentrainment solution and entrainment solution as defined in (2.15) and (2.17) becomes clear. As stated in (4.5a,b), an entrainment solution has an entraining stage during which water is entrained into the mixed layer; a nonentrainment solution has no entraining stage and therefore water always subducts from the mixed layer into the thermocline .

(4.5) can be written as constraints on the mixed layer depth. Noticing (4.4c,d), we can rewrite (4.5a,b) as

$$-\frac{dH_m}{dt} \;>\; w_m, \qquad \textit{when } v_B(f_o) - \dot{f}_o < 0, (\textit{nonentraining}) \tag{4.7a}$$

$$-\frac{dH_m}{dt} \;<\; w_m, \qquad \textit{when } v_B(f_o) - \dot{f}_o > 0, (\textit{entraining}) \tag{4.7b}$$

[1] Obviously, an entraining stage occurs only during the half period when the outcrop line moves southward. Therefore, (4.6a) can be narrowed to $p_n \leq \tau_1^n \leq t \leq \tau_2^n \leq p_n + \frac{\pi}{\omega}$.

With $w_m = (1 - H_m)w_e < 0$, (4.7a) says that outside the entraining stage, the mixed layer depth either descends slowly or ascends at whatever speed. (4.7b) states that during the entraining stage, the mixed layer must penetrate rapidly. Considering that the dynamics of the present mixed layer differs significantly from that of a 1-D model (e.g., Kraus and Turner,1967; Turner and Kraus, 1967), it is interesting to see that the behavior of the mixed layer required by (4.7) is qualitatively consistent with that of a seasonal thermocline predicted from a 1-D model. For example, a sharp rise of the mixed layer during the heating season is allowed in (4.7a); a strong penetration during the cooling season is required by (4.7b).

A convection scheme: determing the mixed layer depth during the entraining stage

At a first sight, the stable slope (4.3) (or (4.5) or (4.7)) guarantees a physical solution. But, it does not! The problem arises during an entraining stage (4.6). Now, the outcrop line moves southward faster than the particle. The waters subducted during this stage (with $t = \tau$ satisfying (4.6)) are *always* left behind the outcrop line, no matter whether (4.3) is satisfied or not (Note that (4.6) is independent of the solution structure). This mass of water would create gravitational instability in the water column north of the outcrop line (see the schematic example in Fig.4.1d). To overcome the instability, physically, we should have a scheme to allow the unstable part of water to be entrained into the mixed layer. Here, we adopt a convective scheme which simply cuts off this part of unstable water. This scheme is illustrated schematically in Fig.4.6. where the adjustment time interval Δt is assumed to be finite. After each time step, a unstable "bulb" is produced if the mixed layer depth is not proper (say, to remain unchanged). Then, we lower the mixed layer to the stable part of the thermocline at the latitude of the outcrop line. The unstable "bulb" is then cut off and is no longer a part of our solution. Physically, after this "bulb" is entrained into the mixed layer, it is well-mixed within the mixed layer and can never be identified as an entity. In other words, after the entrainment, the unstable part of water loses memory of its subduction time because it is well-mixed with waters subducted at other times. If the time step becomes infinitesimal, these unstable bulbs will be squeezed, each having a zero volume. Consequently, our solution will have no unstable volume at any time. One should notice that this convective scheme is somewhat artificial. It says that the mixed layer entrains from below without changing its density

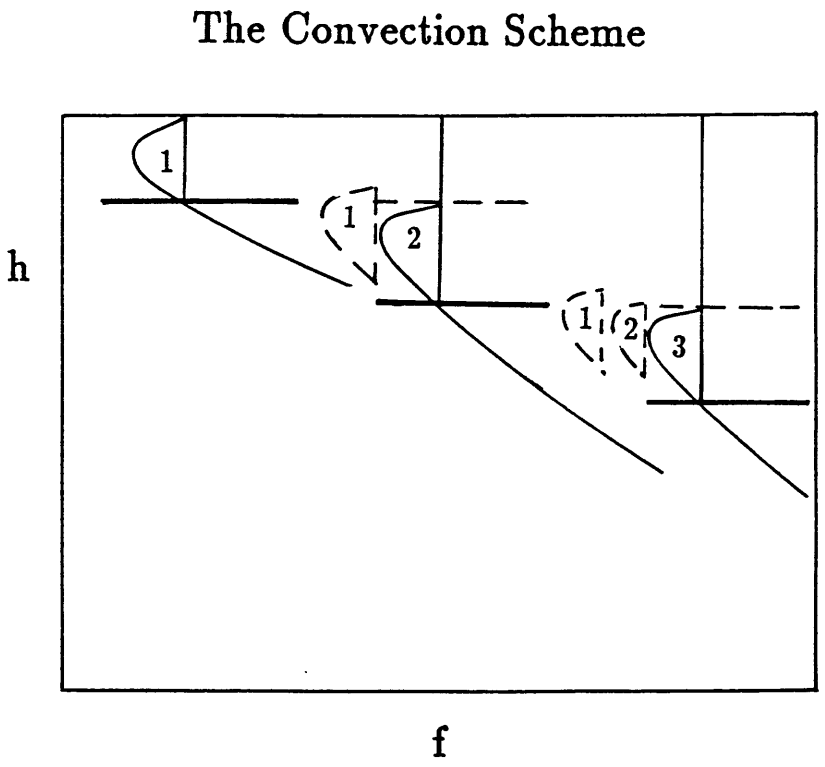

Figure 4.6: The schematic figure of the convective scheme with a finite adjustment time interval. After each time, if the mixed layer remains unchanged, a "bulb" of unstable water is produced. Our convection scheme will allow the mixed layer to descend under the outcrop line such that the "bulb" is cut off.

(or the outcrop line). In our model, we are forced to do so because our outcrop line is specified and therefore can not be altered.

The key for the above convection scheme is, at any entrainment time t, to find the stable thermocline depth below the outcrop line. Then, we lower the new mixed layer to this depth. The water column under this thermocline must have subducted at a previous time, say, denoted by $\tau_p(t)$ $(< t)$. From the subduction time function $\tau(f,t)$ (in (2.5c) or (4.5c)), this corresponding $\tau_p(t)$ can be found as follows. During an entraining stage, north of the outcrop line, $\tau(f,t)$ has double values : a later subduction time at the branch $\tau^+(f,t)$ and an earlier one at the branch $\tau^-(f,t)$ (see Fig.4.1c,d and discussion after (2.16) and (2.17)). In particular, at the outcrop line $f_o(t)$, $\tau^+(f_o,t) \equiv t$ gives the present subduction time while

$$\tau_p(t) \equiv \tau^-[f_o(t),t] \tag{4.8}$$

yields the corresponding previous subduction time, at which the injected water now arrives at $f_o(t)$. This τ_p mapping is shown schematically in Fig.4.1c. By virtue of (4.8), the stable thermocline depth with the subduction time $\tau_p(t)$ is found from (4.2b) as $h^*[t,\tau_p(t)]$ (see Fig.4.1d). Hence, our convective scheme requires a mixed layer depth

$$\boxed{H_m(t) = h^*[t,\tau_p(t)]} \quad \textit{during entraining stages.} \tag{4.9a}$$

Outside the entraining stage, this convection scheme does not impose constraint on the mixed layer depth. Thus, the stable slope (4.3) still needs to be satisfied, or

$$\boxed{H_m(t) = \hat{H}_m(t)} \quad \textit{outside entraining stages.} \tag{4.9b}$$

Here $\hat{H}_m$ satisfies (4.7a). All the corresponding previous subduction times $\tau_p(t)$ such that t is during an entraining stage $(\tau_1^n \le t \le \tau_2^n)$ form a new stage during which all the subducted waters will be reentrained in the following entraining stage (τ_1^n, τ_2^n). In other words, waters subducted during the new stage only establishes the seasonal thermocline and can never enter the permanent thermocline as an identifible entity. This stage is therefore called *the seasonally subducting stage.* The first entraining time τ_1^n entrains the water just subducted or $\tau_p(\tau_1^n) = \tau_1^n$, while the last

entraining time τ_2^n entrains the earliest seasonally subducting water at the time

$$\tau_0^n \equiv \tau_p(\tau_2^n). \tag{4.10}$$

Hence, we have

$$\textit{seasonally subducting stage}: \quad \tau_0^n \le t \le \tau_1^n. \tag{4.11}$$

In contrast, waters subducted earlier than the seasonally subducting stage will never be entrained by the mixed layer and therefore enter the permanent thermocline. This stage is called *the permanently subducting stage* or simply *subducting stage*, which is represented as

$$\textit{subducting stage}: \quad \tau_2^{n-1} \le t \le \tau_0^n. \tag{4.12}$$

It is the waters subducted during this stage that create the permanent thermocline. Consequently, the variability in the permanent thermocline is completely determined by waters subducted during the subducting stage. Like the entraining stage, the subducting and seasonally subducting stages are also independent of the solution h because they are ultimately determined only by the f solution (5.2a).

As a result, one period can be divided into three stages: the seasonally subducting stage, the entraining stage and the subducting stage. The waters injected in the seasonally subducting stage will be reentrained during the following entraining stage. In contrast, the waters subducted during the subducting stage provide water mass for the permanent thermocline. The mixed layer depth during both the subducting and the seasonally subducting stages must satisfy the stable slope condition (4.7a), which then, together with the convective scheme (4.9a) yields the mixed layer depth during the following entraining stage.

A schematic example: how to determine the solution

To have a better understanding of the physics of the three stages and the convective scheme, we investigate the thermocline evolution during one period as shown schematically in Fig.4.7. Outside the entraining stage in (4.9b), we take

$$\hat{H}_m(t) = H_{min} = \textit{constant}, \quad \textit{subducting and seasonally subducting stages.} \tag{4.13}$$

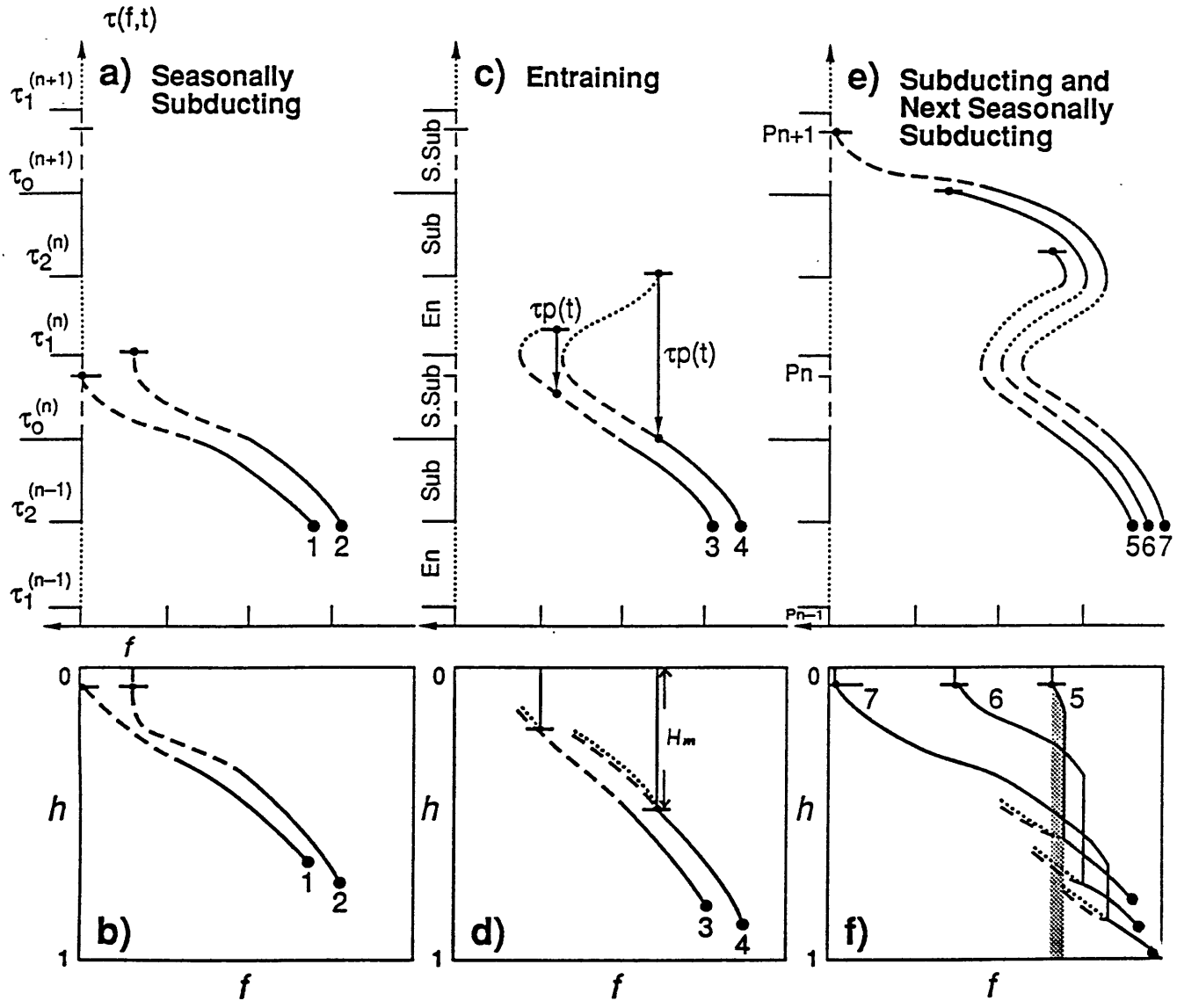

Figure 4.7: The schematic figure of showing how to determine an entrainment solution in one cycle. The seasonally subducting stage, entraining stage and subducting stage are drawn respectively in dashed lines, dotted lines and solid lines. (a), (c) and (e): show the subduction time τ as function of latitude f at different times in three stages. The times for different stages are also marked on the τ axis in (a),(c) and (e). (b), (d) and (f) show the h^* profiles corresponding to (a),(c) and (e) respectively. After one cycle, a big pulse of water is subducted into the thermocline, part of which will be reentrained during the next entraining stage. (see the text for a full discussion)

which obviously satisfies (4.7a) or a stable slope (4.3). Fig.4.7a shows some time sections of the subduction time τ in (4.2c) as a function of f (similar to Fig.4.1a), while the corresponding sections of h^* are depicted in Fig.4.7b. The dashed lines, dotted lines and solid lines respectively represent the part of τ and h^* for waters subducting during the seasonally subducting stage, the entraining stage and subducting stage. These stages are marked on the time axis in Fig.4.7a,c,e. Since we concentrate on the nth period, only the part after τ_2^{n-1} will be considered as drawn in Fig.4.7a,c,e. Curve 1 occurs at September and consists of waters from the n-1th subducting stage and part of the n-1th seasonally subducting stage. Similar to Fig.4.1a,b, τ increases monotonically northward. This reflects the fact that during the seasonally subducting stage and subducting stage, no water column will be overtaken by later subducting waters. Correspondingly, the h^* profile is stable. Curve 2 is at the last moment of seasonally subducting stage and is qualitatively the same as curve 1, except that curve 2 is south of curve 1 at each subduction time τ, reflecting the southward advection due to $v_B < 0$. Since the mixed layer remains at $\hat{H}_m = H_{min}$ according to (4.13), (4.7a) or (4.5a) says that there is no entrainment so far.

Fig.4.7c,d show time sections during the following entraining stage and therefore are similar to Fig.4.1c,d. Curve 3 is at a time during the entraining stage. Part of the τ profile has been left north of the outcrop line, because during the n-1th entraining stage, the outcrop line advances southward faster than the particles. According to our convective scheme (4.9a), the mixed layer depth is deepened to the thermocline depth which has developed from the water subducted at the corresponding seasonally subducting water at $\tau_p(t)$. Since this convection scheme is carried out from the first entraining time with infinitesimal time interval, the unstable "bulb" is squeezed such that the unstable "bulb" has a zero volume, as opposed to a finite volume in Fig.4.6. Curve 4 occurs at the last entraining moment τ_2^n and the mixed layer has captured all the water injected during the entire previous seasonally subducting stage. The mixed layer now achieves its deepest depth.

In the following time, the subducting stage starts as shown in Fig.4.7e,f. Curve 5 is at the time when the outcrop line reaches the southernmost position. South of the outcrop line, a small pulse of water (the water column shaded with grey in Fig.4.7f) is seen subducted south of the outcrop

line and under the mixed layer. This occurs because these waters are subducted after the last entraining time and thus moves southward faster than the outcrop line. This pulse of waters will not be captured by the following entraining stage because the outcrop line now is moving northward and it will come back after another period. The mixed layer suddenly (or discontinuously) rises from its deepest depth to its shallowest depth H_{min} due to (4.13). This abrupt ascent of H_m in turn produces a sharp jump of interface in front of the subducted water pulse. Curve 6 and 7 occur respectively at the last subducting time and the next September with more waters subducted while the mixed layer remains unchanged due to (4.13). One cycle is completed.

4.2 Entrainment Solutions

To see how the convective scheme overcomes instability, we choose to present two examples of entrainment solutions with the outcrop lines used in the two unstable examples in Fig.4.4. To simulate the rapid rise of a mixed layer during early spring more realistically, instead of using (4.13), we will adopt a parabolically ascending mixed layer during the subducting stage. Thus,

$$\hat{H}_m(t) = H_{min} = constant. \quad seasonally\ subducting\ stage \tag{4.14a}$$

$$\hat{H}_m(t) = H_m(\tau_2^n) - [H_m(\tau_2^n) - H_{min}]\sqrt{\frac{t-\tau_2^n}{\tau_0^{n+1}-\tau_2^n}} \quad subducting\ stage. \tag{4.14b}$$

The minimum mixed layer depth is set to be $H_{min} = 0.1$, i.e. one-tenth of the total depth. The mixed layer is then determined by (4.9a,b) and (4.14). Fig.4.8 presents an example under a strong decadal forcing $\omega = 5, a = 0.4$ (the same as in Fig.4.4a-d). Fig.4.8a-d show the meridional sections in four seasons. Solid lines are the physical solutions while dotted lines are the unstable part (with zero volume) of the solution after the use of the convection scheme (4.9a). In "September" (Fig.4.8a), the mixed layer depth is at the minimum depth. During the following cooling season, the outcrop line accelerates southward and soon catches up with the particle. In "December" (Fig.4.8b), the entraining stage has occurred for a rather long time and part of the seasonally subducted waters have been reentrained into the mixed layer (the newly formed dotted line). In "March" (Fig.4.8c), the outcrop line arrives at the southernmost position. The entraining stage has finished and the subducting stage has started for a while. More waters have been reentrained into the mixed layer. In addition, a small amount of water (barely seen in the figure. The counterpart in the schematic

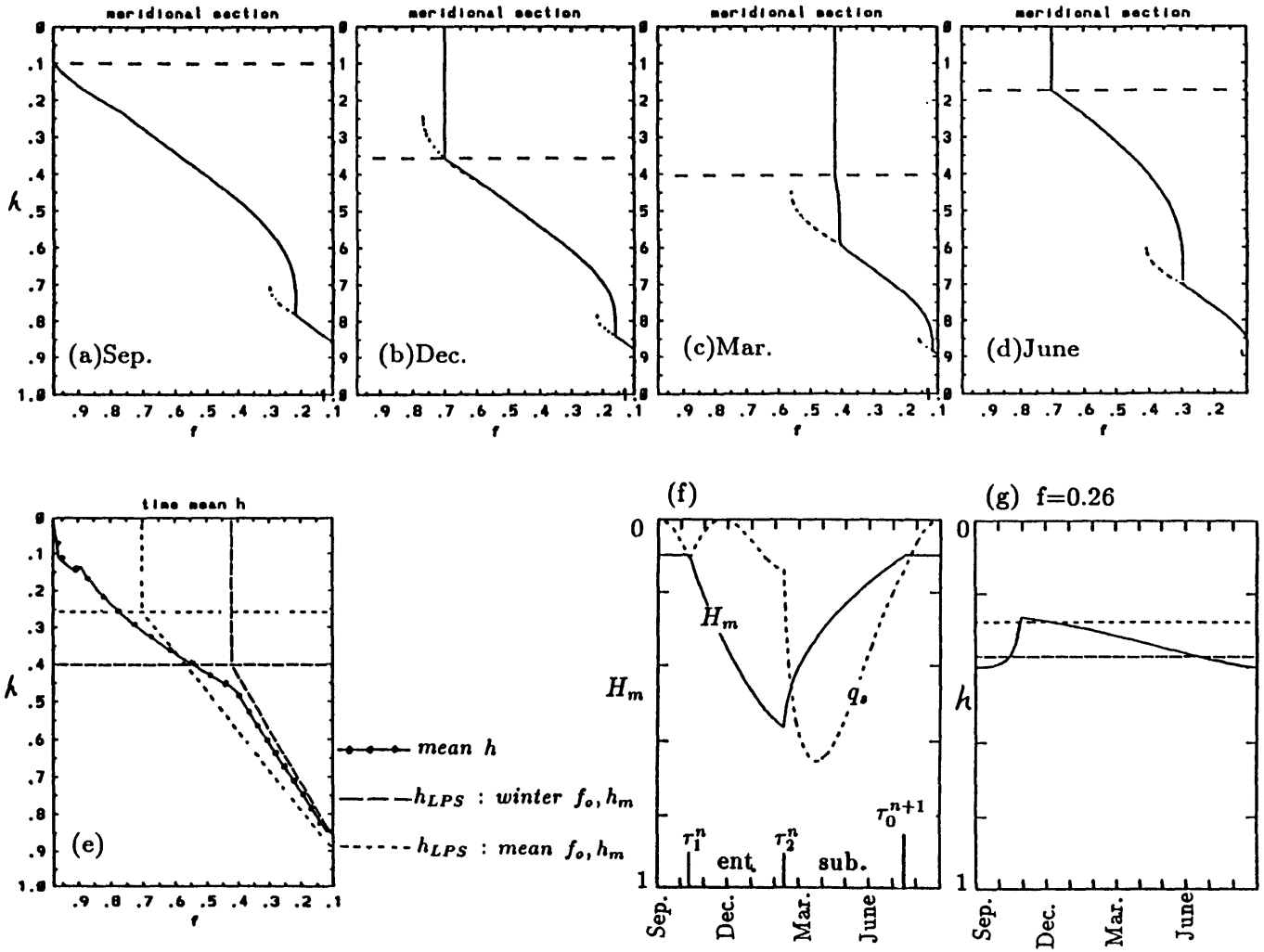

Fig.4.8: Entrainment solution with a strong decadal forcing $\omega = 5, a = 0.4$ (the same as in Fig.4.4a-d) and $H_{min} = 0.1$. (a)-(d) are the instantaneous sections at four seasons. (e) shows the time-mean profile (dot-connected line), the steady thermocline with the time-mean outcrop line and mixed layer depth (short dashed line) and the steady thermocline with the outcrop line and mixed layer at winter (actually the last entraining time τ_2) , when the mixed layer reaches the deepest (f) is the time series of the mixed layer depth according to (4.14) outside the entraining stage and (4.9a) during the entraining stage. Subduction potential vorticity $q = f_o(t)/(1 - H_m(t))$ is also shown with a relative scale. (g) shows the local interface time series with the short and long dashed line being the steady thermocline with the time-mean and later winter (actually τ_2^n) f_o, H_m respectively. In (f) and (g),the entraining and subducting stages are marked on the time axis.

example of Fig.4.7 is the water column shaded with grey in Fig.4.7f) has subducted south of f_o below the mixed layer and will never be caught by the outcrop line. In "June" (Fig.4.8d), a big pulse of subducted water is formed partly because of the subduction left behind by the northward moving outcrop line and partly because of the southward advection of the already subducted water. In this way, a big pulse of water, which is mainly formed during the rather long subducting stage, is injected into the permanent thermocline. This big pulse of water is advected southward and downward. Later, part of the water will be reentrainend in the next entraining stage $(\tau_1^{n+1}, \tau_2^{n+1})$.

The evolution of the mixed layer depth and subduction potential vorticity $q_s = f_o/[1 - H_m(t)]$ are shown in Fig.4.8f. In the figure, the H_m in the subducting stage is given by (4.14b); the H_m in the seasonally subducting stage (later than τ_0^{n+1} and before τ_1^n) is taken from (4.14a); the H_m in the entraining stage is given by the convection scheme (4.9a). The potential vorticity shown in Fig.4.8f indicates that the water subducted during the subducting stage has a lower potential vorticity while the water entrained into the mixed layer has a higher potential vorticity. Physically, this occurs because the subducted water comes from the mixed layer where water mass is well-mixed and has very small potential vorticity. In contrast, the entrained water comes from the water which was heated in the seasonally subducting season with a strong stratification. Therefore, the seasonal thermocline acts as a source of lower potential vorticity to the permanent thermocline in the subducting stage while a sink of higher potential vorticity waters during the entraining stage (Woods,1985).

Fig.4.8e compares the time-mean profile (dot-connected lines) with that derived from the steady LPS model with the outcrop line and mixed layer depth respectively as the time-mean ones (short dash line), and at the time τ_2^n when the mixed layer reaches the deepest (long dash line). It is seen that the time-mean profile is close to the steady thermocline with the early spring outcrop line and mixed layer depth. This phenomenon has been suggested by Stommel (1979). This is in sharp contrast to the nonentrainment solution if one compares the present Fig.4.8e with Fig.4.2e, where the time-mean thermocline is close to the steady thermocline with the time-mean outcrop line.

A local variation of the interface in the permanent thermocline (south of f_{0min}) is shown in Fig.4.8g. Similar to the nonentrainment solution in Fig.4.2f, the interface deepens slowly and rises

abruptly, although the outcrop line (2.11) is harmonic. The oscillation is somewhat close to the local depth of the steady thermocline with the winter mixed layer (long dashed line).

If the forcing frequency is increased, the speed of f_o increases. But v_B is still the same. Thus, f_o catches up with v_B sooner after September and the entraining stage is enlongated. As a result, more subducted water will be entrained into the thermocline and less water is left to subduct into the permanent thermocline. This is shown in Fig.4.9 with an annual frequency forcing ($\omega = 50, a = 0.4$ in (2.11)) (same as Fig.4.4e-h). Qualitatively, Fig.4.9 is similar to the lower frequency case in Fig.4.8. However, there are some important quantitative differences. First, as we expect, with a much higher frequency, much more subducted waters are reentrained into the mixed layer (the dotted lines in Fig.4.9a-d). Each year, only a small pulse of water subducts into the permanent thermocline, resulting a very wavy permanent thermocline structure. Each wave pattern represents waters subducted during one subducting stage of one year. The smaller amount of subducted water than that in Fig.4.8 is consistent with a much shorter subducting stage (about 1 month) (Fig.4.9f) than that in Fig.4.8f (about 5 months). (Here we compare the relative time normalized by the period). Second, Fig.4.9e shows that the time-mean thermocline almost coincides with the steady thermocline with the winter f_o and H_m (actually at τ_2^n which is almost March). In Fig.4.9g, we also see that the thermocline oscillates very closely around the steady thermocline with the winter f_o, H_m. All these suggest that for a higher frequency, Stommel's (1979) conjecture becomes more correct. Lastly, Fig.4.9g shows that the thermocline variability in this annual forcing case is much weaker than that in the decadal forcing case in Fig.4.8g.

Finally, it should be pointed out that the shadow zone thermocline should behavior similarly to that in the nonentrainment solution case. That is: the thermocline remains unchanged except in the western flank of the shadow zone where $x_B(f,t)$ sweeps through (as in Fig.4.2 and Fig.4.3).

5 Thermocline Variability due to Varying Surface Temperature

Now we come to our central issue: what is the thermocline variability in response to an anomalous surface buoyancy flux or a moving outcrop line ? Since our model is not fully coupled, there are an infinite number of solutions. We will choose the solution with the mixed layer depth specified by

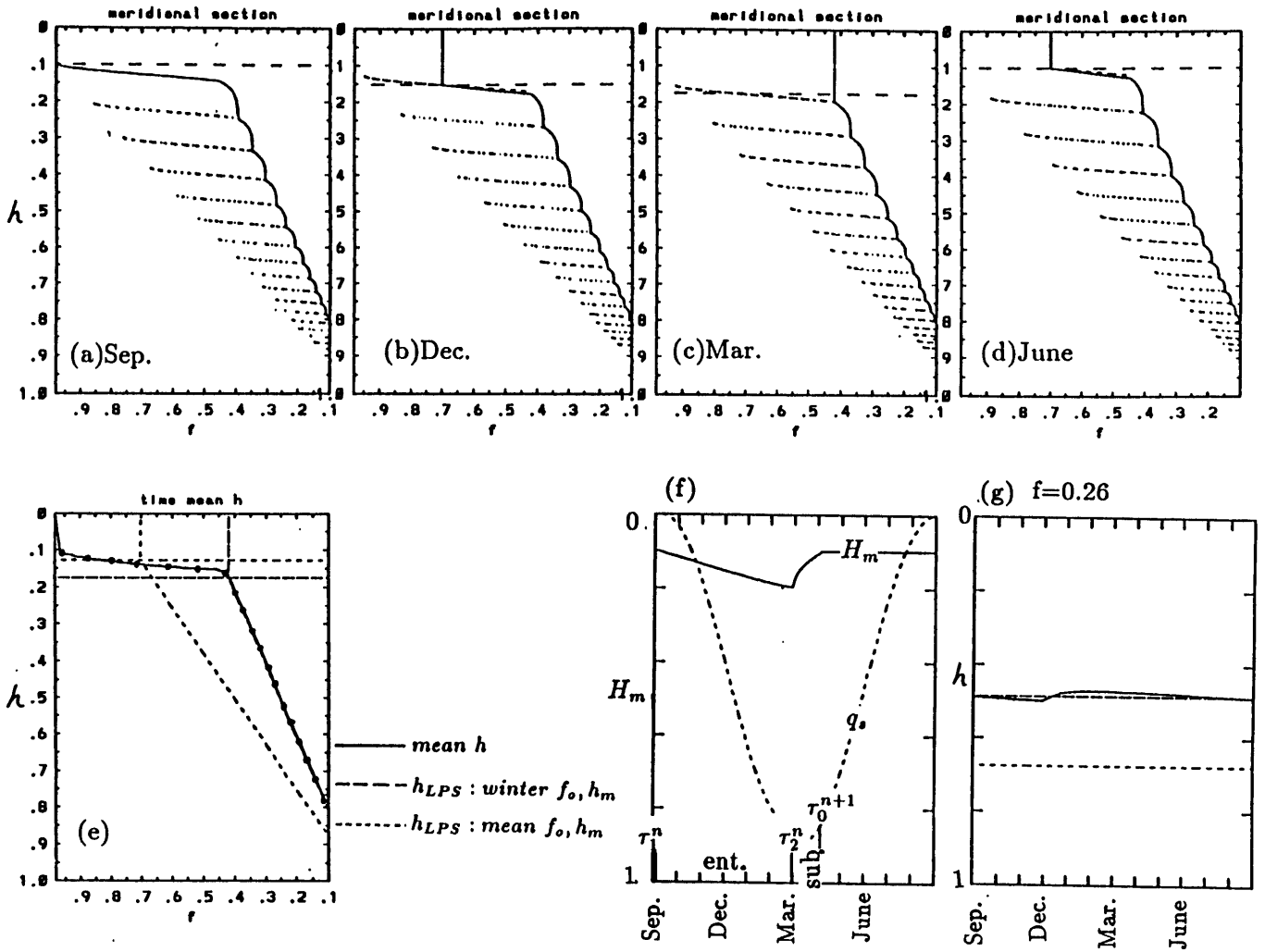

Fig.4.9: Entrainment solution with a strong annual forcing $\omega = 50, a = 0.4$ (the same as Fig.4.4e-h). Other aspects are the same as Fig.4.8. Compared with the decadal forcing case in Fig.4.8. The synoptical profiles in (a)-(d) are much more wavy, implying a much smaller pulse of waters subducted into the permanent thermocline each year. The subducting stage (τ_1^n, τ_2^n) can be seen from Fig.4.9f is much shorter than the decadal forcing case in Fig.4.8f. The time-mean thermocline in (e) almost coincides with the steady thermocline with the winter mixed layer. The thermocline variability is much smaller in (g) than in Fig.4.8g.

(4.14) because this mixed layer depth variation seems to resemble the observations well as seen in Fig.4.8f and Fig.4.9f (at least for the annual frequency case. See, for instance, Kraus and Turner (1967) and Turner and Kraus (1967).)

The magnitude of local variability can be easily derived in terms of potential vorticity because of the fixed bottom in our model. In fact, $q = f/(1-h)$ immediately gives $h(f,t_1) - h(f,t_2) = -f[1/q(f,t_2) - 1/q(f,t_1)]$. Hereafter, we concentrate on the permanent thermocline [1] i.e. south of

$$f_{omin} = min[f_0(t)] \tag{5.1}$$

The potential vorticity is conserved in the permanent thermocline and is therefore determined by waters subducted *during the subducting stage.* Therefore, the magnitude of variability in the permanent thermocline is

$$dh \leq Dh \equiv f[\frac{1}{q^s_{min}} - \frac{1}{q^s_{max}}], \tag{5.2}$$

where q^s_{min} and q^s_{max} are minimum and maximum subduction potential vorticities $q^s = f_0/(1-H_m)$ *during the subducting stage.* (5.2) suggests that the variability decreases with latitude. This occurs because at lower latitudes there is less planetary vorticity available to alter the stratification. Besides, the variability depends on the difference of subducted potential vorticities. Thus, a uniform potential vorticity in the permanent thermocline will produce no thermocline variability. [2]

Using the outcrop line in (2.11) and the mixed layer depth according to (4.9) and (4.14), with respect to the forcing amplitude a and frequency ω, we have calculated q^s_{max}, q^s_{min} and $Dh/f = \frac{1}{q^s_{min}} - \frac{1}{q^s_{max}}$ in Fig.4.10a,b and c respectively. First of all, in the parametric plane (ω, a), one sees a critical boundary separating the slow outcrop line regime (small frequency or amplitude) from the fast outcrop line regime. This is the criterion dividing the nonentrainment solution (2.15) from the entrainment solution (2.17) (i.e. these ω, a make $v_B - \dot{f}_o$ just realizable at a single time). In the nonentrainment regime, q^s_{max}, q^s_{min} and Dh/f are independent of frequency, because

[1] The permanent thermocline should be the region where the potential vorticity of each water column is always conserved. This requires that the water particle is not exposed to the mixed layer. Hence, in our model, the permanent thermocline will refer to the region south of the southernmost position of the outcrop line, i.e. $f < f_{omin} = min\{f_0\}$, where the potential vorticity of a layer two water column is conserved. In contrast, north of f_{omin}, as a water column moves, its potential vorticity will be changed by the variation of the mixed layer depth.

[2] This conclusion holds exactly in the rigid and flat bottom model here. If the bottom varies with time, even with a uniform potential vorticity, thermocline variability may exist.

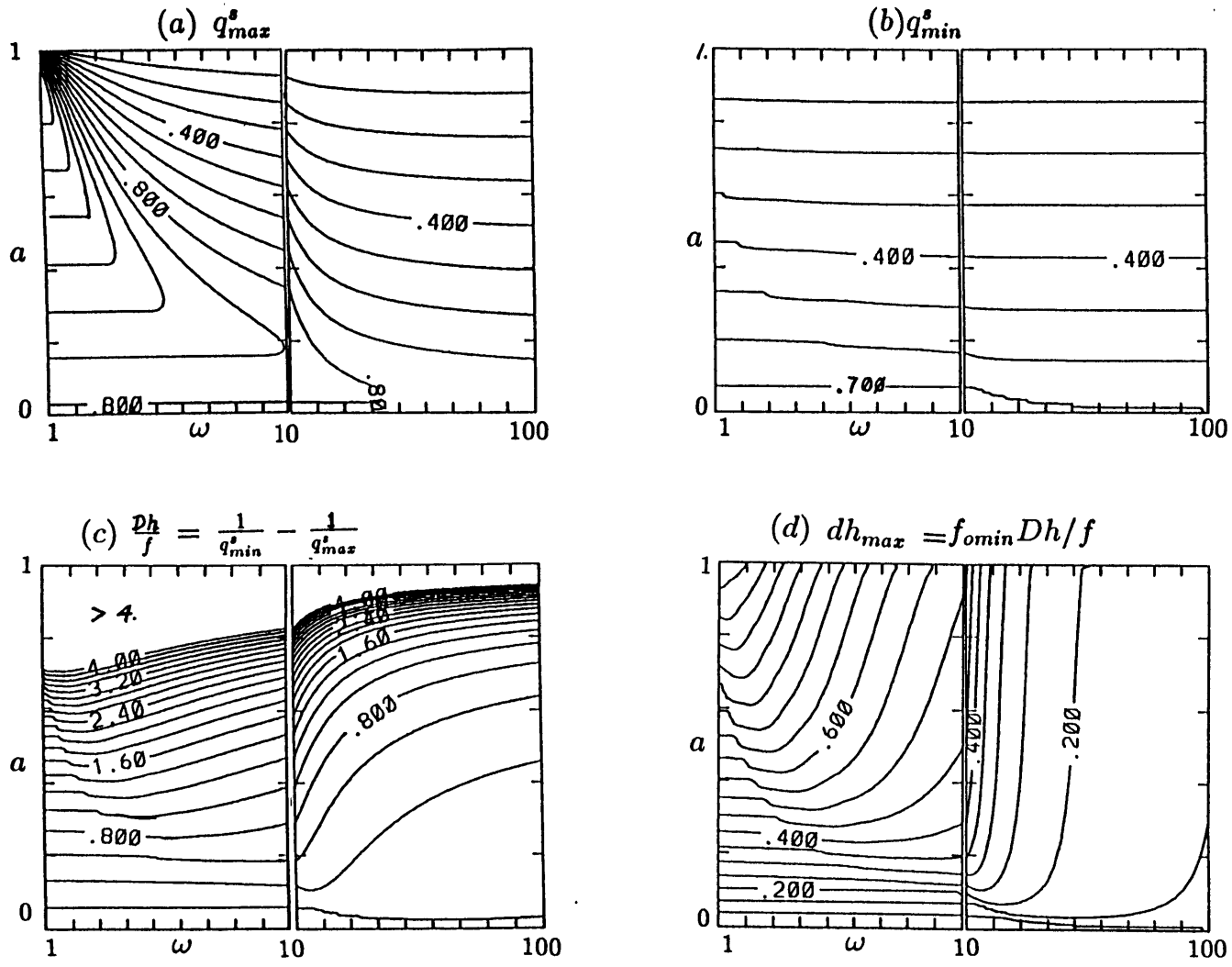

Fig.4.10: The maximum and minimum subduction potential vorticity during the subducting stage q^s_{max}, q^s_{min}, the upbound of local variability in the permanent thermocline $Dh/f = 1/q^s_{min} - q^s_{max}$, and the maximum variability in the permanent thermocline $dh_{max} = f_g(1-a)(1/q^s_{min} - q^s_{max})$. We have chosen: $f_g = 0.7, w_e(f) = -1$. The mixed layer varies according to (4.14) and (4.18).

nonentrainment solutions have neither an entraining stage nor a seasonally subducting stage. Thus, the maximum and minimum subduction potential vorticities during the subducting stage are also those in the whole cycle, i.e.

$$q^s_{max} = q_{max} = \frac{f_{omax}}{1 - H_{min}} = \frac{f_g(1+a)}{1 - H_{min}}, \quad q^s_{min} = q_{min} = \frac{f_{omin}}{1 - H_{min}} = \frac{f_g(1-a)}{1 - H_{min}}. \tag{5.3}$$

where (2.11a,b) have been used. Therefore, both q^s_{max} and q^s_{min} are independent of frequency. The variability which results (5.2) is independent of frequency, too. In contrast, the variability of most entrainment solution (in Fig.4.10c) decreases with an increasing frequency. This gives another important difference between the thermocline variability of nonentrainment and entrainment solutions.

It can also be seen in Fig.4.10b that, even in the entrainment regime, the minimum subduction potential vorticity q^s_{min} depends very weakly on frequency. In fact, if we use (4.13) in the subducting stage to replace (4.14b), we can show easily that q^s_{min} is the same as in (5.3) and therefore is independent of frequency at all. Therefore, the frequency dependency of the variability Dh is mainly caused by q^s_{max}. Roughly speaking, this is so because for different frequency, q^s_{min} usually occurs at about March but q^s_{max} varies at very different times. Thus, the planetary vorticity for q^s_{max} changes very much with frequency.

Now we concentrate on the thermocline variability. The local variability at a latitude f can be derived from multiplying the values in Fig.4.10c by f. It is seen that towards both high and low frequencies, the variability tends to be independent of frequencies. But, in the transition regime between nonentrainment solutions and entrainment solutions (actually, this is the part of entrainment solutions near the nonentrainment solution), the variability (first increases slightly and then) decreases rapidly towards high frequencies. On the other hand, the frequencies for this transition regime usually occur for about decadal frequencies ($\omega \sim 10$) unless the forcing amplitude a is very large (say, $a > 0.5$) or very small (say, $a < 0.05$). Thus, we conclude that decadal frequency forcing is the most efficient in forcing variabilities in the ventilated zone. This feature differs substantially from the wind forcing case of chapter 3, especially at high frequencies. In Fig.3.13 of chapter 3, we see that at high frequencies, the response tends to be linear, i.e. $Dh \sim a/\omega$, where the strongest frequency dependency of the variability also occurs.

Finally, one should be cautious in using Fig.4.10c, because at each different amplitude a, the range of f for the permanent thermocline is different. In fact, the northern bound of the permanent thermocline is the southernmost outcrop latitude (5.1) (noting (2.11a,b))

$$f_{omin} = f_g(1 - a). \tag{5.4}$$

For a larger amplitude a, the possible f_{omin} decreases. As $a \to 1$, the minimum potential vorticity in (5.3) approaches zero. Thus, although the variability in Fig.4.10c approaches infinity near $a = 1$, this infinity can never be achieved because then there is no permanent thermocline region , i.e.$f_{omin} = 0$. We can calculate the maximum variability with different forcings (at latitude $f = f_g(1 - a)$) as

$$dh_{max} = f_g(1 - a) \times Dh/f. \tag{5.5}$$

The results are plotted in Fig.4.10d. The most striking feature is that at higher frequencies, the maximum variability approaches a finite value at strong amplitude ($a \to 1$). Above decadal frequency, the maximum variability is almost amplitude independent and decreases with an increasing frequency. Therefore, towards high frequency, no matter how strong the forcing is, the maximum variability tends to decrease rapidly. This is in sharp contrast with the lower frequency case when the maximum variability is almost frequency independent. Thus, Dh_{max} is insensitive to frequency at lower frequency but decreases rapidly with frequency at high frequency. This fact, from another angle, suggests that a decadal buoyancy forcing (in the transition regime) is the most efficient in producing variability in the permanent thermocline.

6 Summary

In this chapter, the effect of a periodically varying surface buoyancy flux is examined in a simple model including an (essentially passive) mixed layer and two ideal fluid layers. The outcrop line is specified during the whole cycle while the mixed layer depth is specified only during part of the cycle. Some important results are found. First of all, in contrast to the surface wind stress, the surface buoyancy flux causes strong variability in the ventilated zone while it affects the shadow zone very little.

Second, there are two types of buoyancy forced solutions: the nonentrainment solution and entrainment solution. A nonentrainment solution occurs when the southward speed of an outcrop line is always slower than the partial velocity, which takes place under a weak surface cooling. The surface cooling is mainly balanced by the horizontal advection in the permanent thermocline. The mixed layer depth varies little and the mixed layer is never entrained. The time-mean profile is close to the steady thermocline with the time-mean outcrop line. The variability in the permanent thermocline is independent of frequency.

An entrainment solution occurs when the outcrop line moves southward faster than the particle during part of the period, when the horizontal advection in the permanent thermocline is no longer strong enough to balance the surface cooling. Deep cold convection must occur. The mixed layer penetrates rapidly such that water mass is entrained into the mixed layer through the bottom. The local variability of permanent thermocline is most efficiently produced by decadal forcings. At annual frequency, there is very little waters subducted into the permanent thermocline each year, causing weak variability. The time-mean thermocline resembles the steady thermocline with the early spring mixed layer.

Furthermore, for a nonentrainment solution, water always subducts into the permanent thermocline. However, for an entrainment solution, there are three stages during one period: the seasonally subducting stage, the entraining stage and the subducting stage. Waters subducted during the seasonally subducting stage will be reentrained in the following entraining stage as high potential vorticity waters to form the seasonal thermocline. The waters subducted during the subducting stage have a lower potential vorticity and establish the permanent thermocline.

For a clear comparison, the above properties of nonentrainment and entrainment solutions are listed in the following table.

Table 1: The comparison between nonentrainment and entrainment solutions:

	Nonentrainment Solutions	Entrainment Solutions
forcing	weak cooling	strong cooling
dynamics	advection $\sim$ cooling	advection+convection $\sim$ cooling
entrainment	detraining $(w_m^* < 0)$	entraining$(w_m^* < 0)$+detraining$(w_m^* > 0)$
$\rho_m(t)$ or $(f_o(t))$	$\dot{f}_o > v_B$ all the time	$\dot{f}_o < v_B$ sometimes
$h_m(t)$	weak variation	strong variation
mean structure	$< h > \approx h\ (mean\ f_o, h_m)$	$< h > \approx h\ (winter\ f_o, h_m)$
variability $(\delta h(t))$	independent of ω	strongly dependent on ω

The most important further work is to couple an active mixed layer with the permanent thermocline. A model with a further step of coupling is presented at the end of appendix A. More realistic models, such as a coupled mixed layer and a two-and-a-half-layer ideal fluid thermocline model, are also needed to further investigate the effect of the surface buoyancy effect.

A The Motion of the Outcrop Line and Surface Buoyancy Flux

The thermocline dynamic equation in the mixed layer takes the form

$$(\partial_t + \vec{v}_m \cdot \nabla)\rho_m + \partial_z(\overline{w'\rho'}) = 0. \tag{A.1}$$

where $\overline{w'\rho'}$ is the vertical turbulent buoyancy flux. It is important to notice that we have included the horizontal advection in the equation. After noting (3.2a) and (3.5), the surface velocity (after nondimensionalization) is

$$\vec{v}_{mS} \equiv \vec{v}_m - \frac{z}{f}\vec{k} \times \nabla\gamma_m = \frac{1}{f}\vec{k} \times \nabla\eta. \tag{A.2}$$

Furthermore, (A.2) enable us to write (A.1) as

$$(\partial_t + \vec{v}_{mS} \cdot \nabla)\rho_m + \partial_z(\overline{w'\rho'}) = 0, \tag{A.3}$$

where we have used $\gamma_m = (\rho_1 - \rho_m)g/\rho_0$. Integrating the equation through the mixed layer, we have

$$h_m(\partial_t + \vec{v}_{mS} \cdot \nabla)\rho_m = -(B_0 - B_m) \tag{A.4}$$

where $B_0 = \overline{w'\rho'}\,|_{z=0}$ and $B_m = \overline{w'\rho'}\,|_{z=-h_m}$ are buoyancy fluxes at the surface and bottom of the mixed layer respectively. (A.4) relates the mixed layer temperature with the buoyancy fluxes. However, since B_m is introduced as a new unknown, this relation does not close the system. But, it does provide us a better understanding. In our layered system, it is instructive to take a special surface density structure to derive the relation between the outcrop line and the buoyancy fluxes. We assume the form of $\rho_m(x, f, t)$ is such that the reduced gravity in (3.3) is that

$$\gamma_m(x, f, t) = -\Gamma_m(\theta) \quad \textit{where } \theta = f - f_o(x, t),$$

where Γ_m is an given function satisfying $\partial_f\Gamma_m = \frac{d}{d\theta}\Gamma > 0$. This gives a northward increasing surface density. Thus, (A.4) becomes the equation governing the outcrop line

$$(\partial_t + u_{mS}\partial_x)f_o(x, t) - v_{mS} = \frac{B_0 - B_m}{h_m\partial_f\Gamma_m}. \tag{A.5}$$

On the other hand, equation (3.9) suggests that the meridional characteristic speed is

$$v_c = v_B - \frac{(\gamma_m h_m^2)_x}{2f}. \tag{A.6}$$

Thus, with (A.1), (A.6) and (3.8), (A.5) can be put in the following form:

$$\frac{D}{Dt}f_o - v_c = \frac{B_0 - B_m}{h_m \partial_f \Gamma_m} + \frac{1}{f}[\gamma_m h_m - \frac{(1-h)^2}{2}]_x. \tag{A.7}$$

where $\frac{D}{Dt}f_o \equiv (\partial_t + u_{mS}\partial_x)f_o(x,t)$ gives the speed of the outcrop line. If $B_0, B_m, \gamma_m h_m$ and f_o are independent of x, in a ventilated zone (A.7) is simplified to

$$\dot{f}_o(t) - v_B = \frac{B_0 - B_m}{h_m \partial_f \Gamma_m}. \tag{A.8}$$

where we have used $v_c = v_B$ from (A.6). In addition, we have used the fact that in the ventilated zone, with a flat bottom as in our model here, a zonal outcrop line gives a ventilated zone without zonal variation of potential vorticity, which means that $h_x = 0$. (A.8) relates the motion of the outcrop line to the buoyancy fluxes at the top and bottom of the mixed layer. Thus, the nonentrainment solution and entrainment solution in (2.15) and (2.17) becomes

$$\textit{nonentrainment solution} : \quad B_0 - B_m > 0, \quad \textit{all the time} \tag{A.9a}$$

$$\textit{entrainment solution} : \quad B_0 - B_m < 0, \quad \textit{at some time.} \tag{A.9b}$$

On the other hand, in a penetrative mixed layer model (e.g.,Kraus and Turner, 1967; Turner and Kraus, 1967; Gill and Turner, 1976), there is a downward buoyancy entrainment during the deepening season while there is no buoyancy entrainment during the shallowing season, i.e.

$$B_m < 0 \qquad if \ \frac{dh_m}{dt} > 0 \tag{A.10a}$$

$$B_m = 0 \qquad if \ \frac{dh_m}{dt} < 0, \tag{A.10b}$$

From (A.9) and (A.10), we conclude that a strong surface cooling ($B_0 < B_m \leq 0$) results entrainment solution $v_B - \dot{f}_o > 0$ while a weak surface cooling ($B_0 > B_m \leq 0$) results in nonentrainment solution.

B The Mathematical Derivation of $\partial_f h \mid_{f=f_o}$.

Differentiating (4.2b) with respect to t_i yields

$$\partial_{t_i} h^* = \frac{1}{f_o^2}[f^* f_o \frac{dH_m}{dt_i} - (1 - H_m)(f^*_{t_i} f_o - \dot{f}_o f^*)], \tag{B.1}$$

where $f^*_{t_i}$ is given in (2.16). Thus, with (2.16) and using $f_o = f^*$ at $t_i = t$ and $v_B = fw_e$, we obtain

$$\partial_f h \mid_{f=f_o(t)} = \frac{\partial_{t_i} h^*}{\partial_{t_i} f^*} \mid_{t_i=t} = \frac{\frac{dH_m}{dt_i} + w_e(f_o)(1 - H_m)}{-[v_B(f_o) - \dot{f}_o]}. \tag{B.2}$$

The entrainment velocity at the bottom of the mixed layer at the outcrop line is

$$w^*_m = \frac{dH_m}{dt} + w_m \tag{B.3}$$

where where $w_m = w \mid_{f=f_o, z=-H_m}$ is the vertical velocity at the bottom of the mixed layer. This vertical velocity can be proven to be

$$w_m = (1 - H_m) w_e(f_o) \tag{B.4}$$

Indeed, since in (3.11) we assumed that the density in the mixed layer is zonally independent, the meridional velocity in the mixed layer is barotropic. Moreover, in (4.1) or the solution (4.2), we have adopted a zonal outcrop line and a zonally independent mixed layer depth. Thus, in the ventilated zone, it holds that $\partial_x h = \partial_x h_m = \partial_x \gamma_m = 0$. Consequently, in all the layers, the meridional velocities is barotropic, i.e. $v_m = v_1 = v_2 = v_B$. Integrating the vorticity equation of the mixed layer $v_m = fw_z$ from the bottom to the top of the mixed layer, we have $H_m v_B = H_m v_m = fw_e - fw(-H_m)$. Using the Sverdrup relation $v_B = fw_e$, we obtain (B.4). (B.3) and (B.4) then give

$$w^*_m = \frac{dH_m}{dt} + (1 - H_m) w_e. \tag{B.5}$$

Thus, (B.2) becomes

$$\partial_f h \mid_{f=f_o} = \frac{w^*_m}{-[v_B(f_o) - \dot{f}_o]}. \tag{B.6}$$

Chapter 5
Propagation and Breaking of Planetary Waves Radiating from the Eastern Boundary

1 Introduction

In both observations and theories, planetary waves radiating from the eastern boundary have been found to have a profound impact on the interior thermocline variability (e.g., Anderson and Gill, 1975; Kang and Magaard,1980; White and Saur,1981; Kessler, 1989; also see chapter 3 of the thesis). These planetary waves may be excited by a varying wind stress or buoyancy flux near the eastern boundary as well as vertical migration of isopycnal on the eastern boundary. In the latter case, the vertical displacement could be caused either by the variable along shore wind or by a Kelvin wave from the equator. In this chapter, we concentrate on two issues relevant to the eastern boundary waves.

1.1 Planetary Wave Penetration across a Gyre Boundary

The first issue concerns the penetration of Rossby waves across the southern boundary of a subtropical gyre. This cross-gyre wave behavior is important for the understanding of the interaction between the middle latitude and the equatorial regions. Schopf *et.al.* (1981) pointed out that linear Rossby waves forced along the eastern boundary, in the absence of a mean flow, are able to penetrate to the equator to create large equatorial variability because of the increase of zonal Rossby wave speed towards the equator. In the presence of a zonal mean flow, Cheng and Philander (1989) found that a westward mean flow tends to sweep disturbances westward before they reach the equator, while an eastward mean flow can deflect Rossby waves more equatorward.

However, previous studies lack one physical factor: the zonal variation of the mean thermocline structure. On the other hand, observations have shown that, near $15^{o}N$ (which is approximately the southern boundary of mean subtropical gyres), the mean internal Rossby radius of the first baroclinic mode almost doubles its value from the eastern sides to the western sides in both the

North Pacific and the North Atlantic (Emery *et. al.*,1984). This implies a four times increase of the planetary wave speed across the ocean. Therefore, the zonal variation of the mean thermocline structure may be important in affecting wave penetration near the southern boundary of a subtropical gyre.

In section 2, a two-layer model is used to investigate the effect of this factor on the propagation of planetary waves, particularly in the vicinity of the southern boundary of a subtropical gyre. First, we find that the meridional group velocity near the southern boundary is mainly determined by the orientation of the wave and the gradient of background potential vorticity. Then, we discuss how these two factors vary along a southern boundary due to the variation of the basic thermocline structure. Then, we find that the wave penetration is changed substantially due to the zonal variation of the basic state. For our model thermocline, the penetration of waves differs dramatically for interfaces at different depths.

1.2 Planetary Wave Breaking

The second issue addresses the breaking of planetary waves. Although we only consider the breaking of waves forced by upwelling and downwelling at the eastern boundary, the results may also apply to more general cases.

Generally, breaking can create large scale density frontal structures and baroclinic jets in the ocean, which will also be potential regions for baroclinic instability. There have been some observations of large scale fronts. The Subarctic Front and Subtropical Front in the North Pacific are two examples (Roden,1976; Roden, 1980; Levine, and White, 1981; Niiler *et. al.*,1984). There is also evidence of large scale frontal structures and baroclinic jets in the North Atlantic (McWilliams *et.al*, 1983). Vertically, some large scale fronts can extend through the main thermocline. Although these fronts seem to possess clear time-mean frontal structures, more detailed observations indicate that each front has strong temporal variabilities and finer frontal structures.

So far, the physical mechanisms for these large scale fronts are not well understood. Roden (1976) proposed that the confluence of Ekman flux is responsible for the Subtropical front in the North Pacific. Cushman-Roisin (1984) argued that the main mechanism is the external thermal

forcing that creates large scale fronts through the vertical advection. Here, it is suggested that the breaking of planetary waves may provide another mechanism. These waves may be forced by local wind or buoyancy flux as well as disturbance at the eastern boundary. Although the wave breaking mechanism may not be crucial for the mean structure, it may be important for the temporal and finer frontal structures within the mean front.

In the presence of a mean flow and an Ekman pumping, the breaking of planetary waves has hardly been studied except for some special cases (Anderson and Killworth 1980; Dewar 1987). The main difficulty lies in both the mean flow field and the two-dimensional structure. There are no general theories dealing with temporal two-dimensional fronts. In section 3 and 4, we will examine some basic aspects of wave breaking, such as when and where a breaking occurs. For simplicity, the waves are considered to be generated along the eastern boundary by the vertical displacements of isopycnals, which have been observed to have large amplitudes (Tabara *et. al*, 1986; section 4B of Kessler, 1989). We hope that the results here will shed light on wave breaking due to other mechanisms such as a diabatic cooling or a localized Ekman pumping anomaly.

A two-layer planetary geostrophic model is used to study the occurrence of breaking. There are two types of breaking to be studied: the downwelling breaking which is caused by lowering the interface at the eastern boundary, and the upwelling breaking which is forced by lifting the interface. Since a deepening of the interface at the eastern boundary causes the interface shoaling towards the west and produces a northward thermal wind, it is intuitive that a deepening breaking front will be accompanied by a northward thermal wind jet. Similarly, a shallowing breaking front is accompanied by a southward thermal wind jet.

First, in section 3, we review and further explore the breaking of a free wave. By virtue of analytical solutions, an approach is developed to calculate the first breaking time and position. In addition, the discussion of the free wave breaking will help us to understand later cases with Ekman pumping and the associated mean circulation. In section 4, we further investigate the effect of an Ekman pumping on the breaking of planetary waves. It is found that Ekman pumping changes the breaking time, position and intensity significantly. Compared with the free wave case, downwelling breaking is suppressed and the breaking time is delayed, while upwelling breaking is enhanced and

the breaking time is shortened. A downwelling breaking front occurs only for an interface near the surface while an upwelling breaking front takes place for interfaces from the bottom to the upper model thermocline. A breaking front tends to tilt northeast-southwest and the intensity of a breaking front tends to be stronger towards the north.

1.3 The Model

The model is the two-layer, planetary geostrophic model with a flat bottom, which has been developed in chapter 2. All notation in this chapter is the same as in chapter 2. Details of the model have been presented in section 1 of chapter 2.

The nondimensional form of the governing equation for the interface is derived in (1.7a) of chapter 2 as

$$h_t + v_B h_f + (u_B + C)h_x = -(1-h)w_e. \tag{1.1}$$

Here $u_B = -x(f^2 w_e(f))_f/f + u_{BE}$, $v_B = f w_e$ are barotropic velocities while the planetary wave speed is $C = -h(1-h)/f^2$, where u_{BE} is the barotropic velocity at the eastern boundary and will be assumed zero hereafter. The characteristic equations for (1.1) are

$$\frac{dt}{ds} = 1 \tag{1.2a}$$

$$\frac{df}{ds} = v_B \tag{1.2b}$$

$$\frac{dh}{ds} = -(1-h)w_e(x,f,t) \tag{1.2c}$$

$$\frac{dx}{ds} = u_B(x,f,t) - \frac{h(1-h)}{f^2}. \tag{1.2d}$$

The solution affected by eastern boundary waves should have initial conditions for characteristics starting only from the eastern boundary. If disturbances are generated along the eastern boundary $x = 0$ by the interface depth $h_e(f,t)$ at time t_i and on latitude f_i, we have the initial conditions $x_i = 0$, $h_i = h_e(f_i, t_i)$. In gneral, a planetary wave can be excited at the eastern boundary if either the Ekman pumping changes or the eastern boundary upwelling occurs. For simplicity, here we only consider the waves forced by eastern boundary upwelling $\partial_t h_e \neq 0$. Therefore, the Ekman pumping is assumed of a steady form $w_e(f)$. (If the Ekman pumping varies with time, the waves will have a more complex sturcture. We will return to this point at the end of the section.) With

the Ekman pumping, the characteristic equations (1.2) have been integrated explicitly in (4.7) and (4.8) of chapter 2 as

$$t = t_i + s, \tag{1.3a}$$

$$s = \int_{f_i}^{f} \frac{df}{f w_e(f)}, \quad or \quad f = \hat{f}(f_i, s) \tag{1.3b}$$

$$h = 1 - [1 - h_e(f_i, t_i)]\frac{f}{f_i}, \tag{1.3c}$$

$$x = \frac{h^2 - h_e^2}{2f^2 w_e(f)}. \tag{1.3d}$$

where the $\hat{f}$ is the characteristic solution for f. In the special case with $h_e = 0$, this solution is the shadow zone (5.2) in the classic LPS ventilated thermocline. In general, the lower layer pressure is $p_2 = (D^2 - h^2)/2 = h_e(f_i, t_i)^2/2$ (see (4.11) of chapter 2), where we have used (1.3d) and $D^2 \equiv 2f^2 w_2(f)x$. The f_i and t_i can be solved from (1.3a,b,c) as functions of f and t. Therefore, if the eastern boundary interface depth varies with latitude or time, it usually holds that $\vec{v}_2 \sim \nabla p_2 \neq 0$, implying a moving lower layer or an eastern boundary ventilation (Pedlosky, 1983). Nevertheless, without confusion, this solution is still called the shadow zone solution. (1.3) gives the basic solution for this chapter.

If an interface outcrops within a subtropical gyre at latitude f_0 (steady with time), the shadow zone extends westward to meet the ventilated zone on the shadow zone boundary B_2. B_2 is formed by the characteristics starting from $(x, f) = (0, f_o)$ and therefore is obtained by setting $x_i = 0, f_i = f_o, h_e(f_o, t_i) = 0$ into (1.3c,d). Then, substituting (1.3c) into (1.3d) gives

$$x_{B2} = \frac{(1 - f/f_0)^2}{2f^2 w_e(f)}. \tag{1.4}$$

For an unventilated interface, $h_e(f_n, t) > 0$ (where f_n is the northern boundary of a subtropical gyre), the shadow zone becomes adjacent to the pool zone on the western side (Pedlosky and Young, 1983). The boundary is determined by setting $x_i = 0, f_i = f_n$ in (1.3b), then eliminating s from (1.3b) by using (1.3a) and substituting (1.3c) into (1.3d) to yield parametric solutions

$$f = \hat{f}(f_n, t - t_i), \quad x_{B2} = \frac{\{1 - [1 - h_e(f_n, t_i)]f\}^2 - h_e^2(f_n, t_i)}{2f^2 w_e(f)}. \tag{1.5}$$

The disturbance starts from the eastern boundary at a time, say $t_i = T_i$, propagates to form a wave front x_F. This can be derived as follows: first, we derive the inverse function of $\hat{f}$ as $\hat{f}_i(f, s)$

such that $f \equiv \hat{f}[\hat{f}_i(f,s),s]$. Then, we substitute $t_i = T_i$ and $s = t - t_i$ into $\hat{f}_i$ and (1.3c) to derive $\hat{f}_i(f, t-T_i)$ and $h = 1 - [1 - h_e(\hat{f}_i, t-T_i)]f/\hat{f}_i$. Lastly, substituting the $\hat{f}_i$ and h into (1.3d) to yield

$$x_F(f,t) = \frac{\left\{1 - [1 - H_e(f)]\frac{f}{\hat{f}_i}\right\}^2 - H_e^2(f)}{2f^2 w_e(f)}, \tag{1.6}$$

where $\hat{f}_i = \hat{f}_i(f, t-T_i)$ and $H_e(f) = h_e[\hat{f}_i(f,T_i), T_i]$.

Finally, one should bear in mind that although it is derived for a steady Ekman pumping w_e under a varying eastern boundary interface, this wave front also applies for more general cases. Indeed, (1.6) is exactly the same wave front as that excited by a spin-up (or spin-down) from an arbitrary old Ekman pumping ($t < T_i$) to the new Ekman pumping w_e at $t = T_i$ provided that the eastern boundary stays steady at $H_e(f)$ (note that the derivation of (1.6) is independent of the Ekman pumping before T_i at all). In addition, for a periodic Ekman pumping, we have seen in chapter 3 (see (3.17) or (A.1) there) that a wave front excited along the eastern boundary can be well-approximated by (1.6). This is true particularly for frequencies higher than decadal.

2 Planetary Wave Penetration Across a Gyre Boundary

In this section, we study the penetration of planetary waves across the southern boundary f_s of a subtropical gyre in the presence of a mean thermocline, whose structure varies in both zonal and meridional directions. Since the penetration of waves can be inferred from the group velocity, we begin with re-examining the group velocity of planetary waves with particular attention to the meridional group velocity near f_s. We will concentrate on the first mode of baroclinic Rossby waves with spatial scales much longer than the deformation radius, i.e.

$$L \gg L_D = \sqrt{\gamma H/f} \sim 30\ km. \tag{2.1}$$

In this section, we start with dimensional quantities.

2.1 The Group Velocity

In the absence of mean flow, the group velocity of a long linear Rossby wave satisfying (2.1) has the approximate form

$$C_{gx} = C(1 + o[(K^2 L_D^2)]), \quad C_{gy} = -2klL_D^2 C[1 + o(K^2 L_D^2)]. \tag{2.2}$$

Here, k, l are the wavenumbers in x and y direction respectively; $K^2 = k^2 + l^2$ and $C = -\beta L_D^2$. One sees that the meridional group velocity is one order ($K^2 L_D^2 \ll 1$) smaller than the zonal one. On the other hand, in the presence of both barotropic and baroclinic structures, the evolution equation (1.1) suggests that at the lowest order, the group velocity takes the form

$$C_{gx} \approx u_B + C, \quad C_{gy} \approx v_B. \tag{2.3}$$

Here, at the lowest order, both the zonal and meridional baroclinic flows have been canceled by their accompaning pseudo-β effect. Combining (2.2) with (2.3), we may expect a group velocity accurate to the first order as

$$C_{gx} \sim (u_B + C)(1 + o[(K^2 L_D^2)]), \quad C_{gy} \sim (v_B - 2klL_D^2 C)[1 + o(K^2 L_D^2)]. \tag{2.4}$$

In (2.4), the barotropic meridional advection will dominate the meridional group velocity (as shown in (2.3)), provided that $O(v_B) \gg O(klL_D^2 C)$ or

$$L^2 \gg L_D^2 \times \left(\frac{L_D}{\sqrt{\frac{v_B}{\beta}}} \right)^2. \tag{2.5}$$

For a typical $v_B \sim 1\ cms^{-1}$, (2.5) requires that $L^2 \geq (30\ km)^2$. Even for a $v_B \sim 0.1\ cms^{-1}$, (2.5) still needs only $L^2 \geq (100\ km)^2$. These conditions are satisfied by the long waves in (2.1). As a result, within a subtropical gyre, the meridional group velocity is dominated by the Sverdrup advection. Thus, wave energy will be swept southward along the ray path in (2.3).

However, the above analysis fails in the vicinity of f_s where v_B vanishes. Instead, the group velocity should be at the order of $C_{gx} \sim u_B + C$, $C_{gy} \sim -2klL_D^2 C$. A more detailed analysis shows that at the lowest order, we have in shadow zone (see (A.19) in appendix A)

$$C_{gx} \sim u_B + C, \quad C_{gy} \sim 2kl\hat{\beta}\lambda_1\lambda_2, \quad for\ O(\frac{f - f_s}{f_s}) \ll 1. \tag{2.6a}$$

Here, the effective β is

$$\hat{\beta} = \beta R_{1y} R_{2y} / (R_{1y} + R_{2y})^2, \tag{2.6b}$$

and $R_1 = h/f \equiv 1/Q_1$, $R_2 = (H-h)/f \equiv 1/Q_2$, $\lambda_1 = \gamma h/f^2$, $\lambda_2 = \gamma(H-h)/f^2$. The derivation has allowed both the zonal and meridional variation of the quantities in the basic state, such as Q_{1yx}, Q_{2yx}, u_{Bx}. As has been noticed by Cheng and Philander (1989) in an one-and-a-half-layer model, the effect of the baroclinic structure (in R_1, R_2) on the background potential vorticity gradient exists in C_{gy} but not in C_{gx}. (2.6). This suggests that near a southern boundary, the baroclinic structure does not substantially influence the wave propagation in the zonal direction (at order 1), but it does strongly affect the wave propagation in the meridional direction (at the $K^2 L_D^2 \ll 1$ order) .

According to (2.6a), the meridional group velocity is determined by two factors: the wave front orientation (kl) and the effective $\hat{\beta}$. If there is no zonal variation of the basic state, kl and $\hat{\beta}$ will not vary along a latitude, in particular along the southern boundary. This implies that C_{gy} remains the same along the southern boundary, and thus either all waves penetrate equatorward ($C_{gy} < 0$) or all waves are trapped within the subtropic gyre ($C_{gy} > 0$). However, the basic thermocline could vary substantially in the zonal direction. This variation may change the sign of kl and $\hat{\beta}$ along the southern boundary and in turn change the sign of C_{gy}. The resulted wave penetration may exhibit a complex scenario. This is the novel point that we are going to explore.

2.2 The Zonal Variation of $\hat{\beta}$ and kl

Now, nondimensional quantities will be used (after (1.5a) of chapter 2). We first consider the $\hat{\beta}$. A flat eastern boundary interface depth

$$h_e = H_s \tag{2.7}$$

will be adopted because we are concentrated on the region near f_s, where observations show that (2.7) is a reasonable approximation. The steady LPS shadow zone solution can be derived from (1.3) as

$$h = \sqrt{2 f^2 w_e(f) x + H_s^2}, \tag{2.8}$$

which will be taken as the basic state. The Ekman pumping near the southern boundary is approximated by a linear Ekman pumping

$$w_e(f) = W_e(f - f_s), \qquad W_e = constant < 0. \tag{2.9}$$

Substituting (2.8) and (2.9) into (2.6b), we have the effective β as

$$\hat{\beta} \sim Q_{1y}Q_{2y} \sim -(W_e x - \frac{H_s^2}{f^3})[W_e x + \frac{H_s(1-H_s)}{f^3}], \ when \ f \to f_s. \tag{2.10}$$

Near the eastern boundary ($x \to 0$), (2.10) shows $\hat{\beta} \sim H_s^3(1-H_s)/f^6 > 0$, which is the same sign as β. But far away from the eastern boundary ($x \to -\infty$), (2.10) states that $\hat{\beta} \sim -(W_e x)^2 < 0$, which is the opposite sign to the β. The critical position for $\hat{\beta}$ to change sign is obtained by setting $\hat{\beta} = 0$ in (2.10) as [1]

$$x_c = H_s^2/(f^3 W_e). \tag{2.11a}$$

Thus, we see that $\hat{\beta}$ is altered substantially by the zonal variation of the basic thermocline structure. Since the effect of the surface Ekman pumping on the thermocline accumulates westward, the effect of the thermocline on $\hat{\beta}$ also accumulates westward. Consequently, $\hat{\beta}$ changes its sign far away from the eastern boundary as discussed above. In addition, one sees that x_c increases rapidly with the depth H_s. This is sensible because closer to the surface, the thermocline is more severely distorted by the Ekman pumping and therefore the thermocline will change the $\hat{\beta}$ more significantly. At the singular case with $H_s = 0$, the $\hat{\beta}$ is changed the most. Now, $x_c = 0$; $\hat{\beta}$ becomes negative along the whole southern boundary. If, on the other hand, the depth is so deep that x_c is beyond the western boundary, x_c will not appear within the basin. Then, we have $\hat{\beta} > 0$ along the whole southern boundary. Assuming $x_w \sim O(1)$, the deepest depth for x_c to occur within the basin is derived by substituting (2.11a) into $-1 \approx x_w < x_c < 0$ as

$$H_c = f_s\sqrt{f_s \mid W_e \mid}. \tag{2.11b}$$

[1] It is interesting to note that this position (which occurs for $\hat{\beta} \sim \partial_f(f/h) = 0$) is the position where the zonal velocity equals the local Rossby wave speed on the southern boundary, or $u_B(x_c, f_s) = C[h(x_c, f_s)]$. (This is different from the Rossby repellor on the northern boundary with $u_B(x(repellor), f_n) + C[h(x(repellor), f_n)] = 0$.) The physical implication is not clear to me yet.

The dimensional form of this depth is (see (1.5a) of chapter 2)

$$H_c = f_s \left(\frac{f_s \partial_f w_e \mid_{f=f_s} L_x}{\beta \gamma} \right)^{1/2}, \tag{2.11c}$$

where $L_x = \mid x_w \mid$ is the width of the basin. Thus, H_c varies with the width of the basin and the gradient of Ekman pumping.

Secondly, we briefly discuss the zonal variation of kl. A fuller discussion is left in appendix B of this chapter. Since the thermocline varies in both x and y direction, it is difficult to calculat the local k and l directly. Instead, we will infer the sign of kl from the orientation of a wave front x_F (in (1.6)) near the southern boundary. A wave front with a northeast-southwest orientation implies $kl < 0$, which will be called a β dispersion tendency as in Schopf *et. al* (1981). A front with a northwest-southeast orientation implies $kl > 0$, which, for convenience, will be called an anti-β dispersion tendency.

From (1.2d) (this is nondimensional) , one sees that the propagation of a wave front is determined by the competition among three factors: the linear β dispersion $(1/f^2)$, the stratification of the basic thermocline $(h(1-h))$ and the zonal barotropic flow (u_B). The linear β dispersion always tends to build up a β dispersion tendency since $1/f^2$ increases rapidly equatorward. Therefore, if there is no zonal variation of the stratification and the basic flow, a wave front always exhibits a linear β dispersion tendency (Schopf *et. al*, 1981) .

However, with a basic thermocline, both $h(H-h)$ and u_B are changing zonally. The change of h may provide anti-β dispersion mechanism because h shoals towards f_s. Indeed, since $\partial_f[h(1-h)] = (1-2h)h_f$, it follows that for interfaces in the upper model thermocline $h < 0.5$, the stratification factor offers an anti-β dispersion mechanism. (The opposite occurs for $h > 0.5$). As for u_B, it usually exhibits a cyclonic shear near f_s, i.e.,$\partial_f u_B \mid_{f=f_s} < 0$ (This can be varified with the Ekman pumping (2.9)). Therefore also offers an anti-β dispersion mechanism.

If a wave front exhibits a β dispersion depends on which mechanism is more important. On the one hand, the linear β dispersion effect is independent of zonal position. On the other hand, assume a flat h_e as in (2.7), the effect due to the stratification $(\partial_f h(1-h) \sim h_f)$ starts from zero along the eastern boundary and increases rapidly westward primarily because of the westward accumulation of the Ekman pumping effect on the thermocline structure. The zonal flow also starts from a zero

shear along the eastern boundary and increases linearly with distance westward since $u_B \sim x$. As a result, when a wave front propagates westward, it first exhibits a β dispersion tendency because of the linear β dispersion. As the front advances westward, the anti-β dispersion effect due to the stratification and zonal flow increases rapidly. Eventually, the wave front will change its orientation to an anti-β dispersion tendency.

If we use (2.7),(2.8) and (2.9), we can calculate the slope of the wave front x_F from (1.6). Near the eastern boundary, we will find a β dispersion ($\partial_f x_F > 0$); away from the eastern boundary, we will find an anti-β dispersion ($\partial_f x_F < 0$). The critical position for the wave front to change its orientation can be found as (see (B.4b) of appendix B)

$$x = 4x_c, \tag{2.12}$$

where x_c is given in (2.11a).

2.3 The Wave Penetration

With the above zonal variation of kl and $\hat{\beta}$, a southern boundary is divided into three parts, in each of which the wave penetration differs from its neighbors. This is illustrated schematically in Fig.5.1. Near the eastern boundary where $x_c < x < 0$, the β dispersion tendency ($kl < 0$) and the positive $\hat{\beta}$ produces a southward wave penetration ($C_{gy} < 0$). West of this region where $4x_c < x < x_c$, the β dispersion tendency remains but the $\hat{\beta}$ becomes negative. Therefore, the wave energy penetrates northward ($C_{gy} > 0$). Further west, the $\hat{\beta}$ remains negative but the wave front changes to an anti-β dispersion ($kl > 0$). Waves again radiate equatorward.

Since x_c depends on the depth of the interface, the wave penetration region (determined by x_c) will be different on interfaces at different depths. In a basin with a finite zonal width $x_w \sim -1$, according to wave penetration behavior, interfaces can be divided into three categories: (in non-dimensional form)

$$\textit{shallow}: \ 0 < H_s < 0.5H_c, \ \textit{middle}: \ 0.5H_c < H_s < H_c, \ \textit{deep}: \ H_c < H_s < 1. \tag{2.13}$$

where H_c is determined in (2.11b). Fig.5.2 presents a schematic figure for the wave penetration of the three different groups of interfaces (for the sake of simplicity, the wave rays have not been

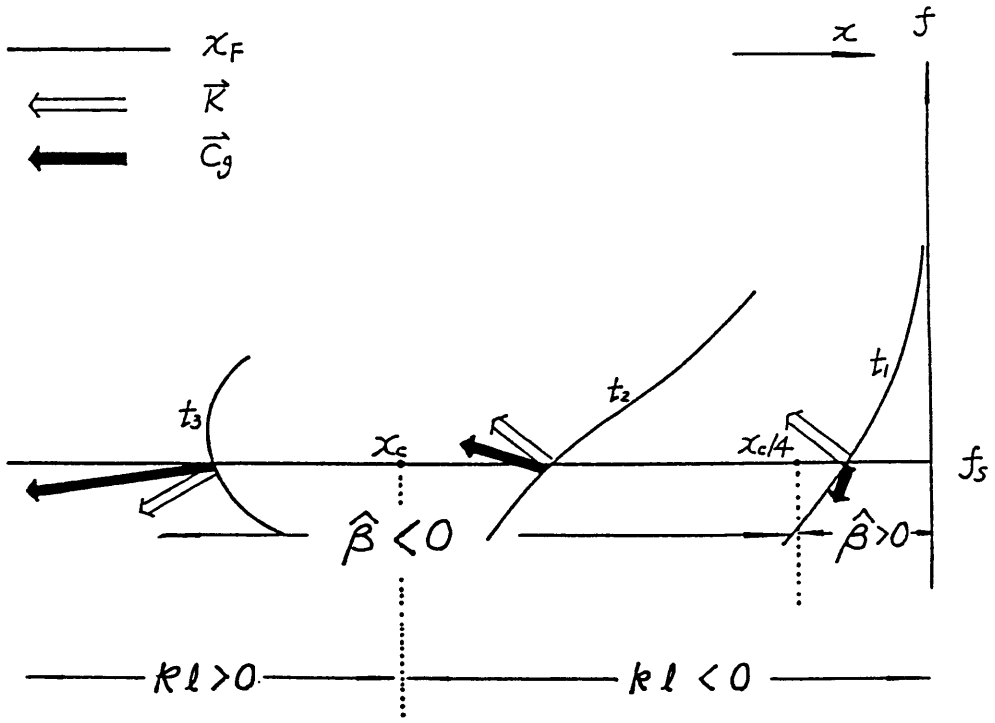

Figure 5.1: The schematic figure showing the wave propagation, the zonal variation of the effective β and the inferred wave energy penetration along the southern boundary of a subtropic gyre for an infinitely long basin. x_e is determined in (2.11a). See the text for a detailed discussion. Note that the relative orientation of the wave vector (blank arrow) and group volocity (black arrow) is drawn arbitrarily.

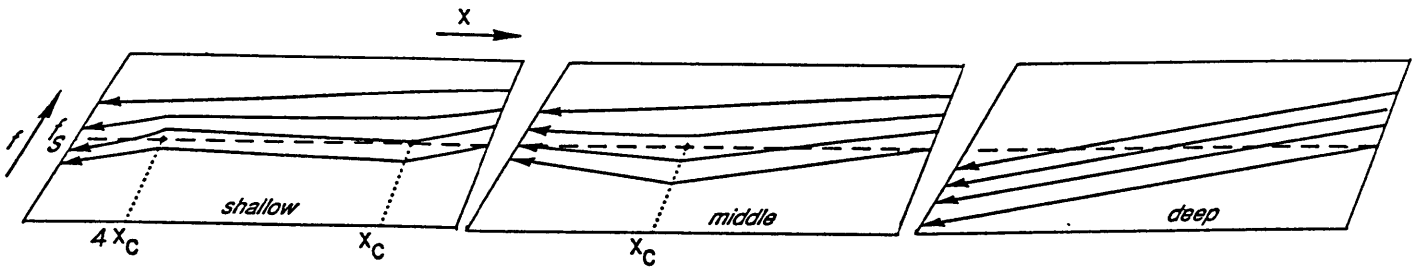

Figure 5.2: A schematic figure showing the Rossby wave penetration across the southern boundary of a subtropical gyre at different depths. The definition for shallow, middle, deep interfaces as well as x_e are given in (2.11a,b) respectively.

drawn smoothly on $4x_c$ and x_c.) On a shallow interface, it holds that $x_w < 4x_c$. Thus, all the three regions exist. On a middle interface, one has $4x_c < x_w < x_c$. The westernmost region is beyond the western boundary. On a deep interface where $x_c < x_w$, only the easternmost region appears within the basin. Hence, on deep interfaces we have full penetration, i.e. all energy penetrates into tropics along the whole southern boundary. In contrast, an interface in the middle depth has no penetration, i.e. little energy can be carried from the subtropical gyre into the tropics. (Some disturbances originating from the tropics may even penetrate into the subtropical gyre). A shallow interface presents an intermediate case of partial penetration, i.e. part of the wave energy radiates equatorward in the western part of the ocean. The full penetration for a deep interface seems sensible because a deep interface is distorted very little by the surface Ekman pumping. Thus, waves are affected by the zonal variation of thermocline very little and the linear β dispersion dominates as in Schopf *et. al.* However, the partial penetration for a near surface interface and the no penetration for middle depths are not intuitive.

For the dimensional critical depth in (2.6c), we adopt the typical dimensional quantities of a subtropical gyre $W_e = 10^{-4}\,cm/s$, $f_n = 2\Omega sin(45^o) = 10^{-4}\,s^{-1}$, $\gamma = 2cms_{-2}$, $\beta_0 = \frac{2\Omega}{a}\cos(35^o) = 1.87 \times 10^{-13}\,s^{-1}cm^{-1}$. Further, if we take f_s at 15^o, and the slope as $\partial_f w_e \approx 1\ cms^{-1}/2\Omega[sin(30^o) - sin(15^o)]$, for the Pacific with $L_x \approx 15000\ km$, we have $H_c \approx 220\ m$. For the Atlantic with $L_x \approx 6000\ km$, we have $H_c \approx 140\ m$.

To summarize, the zonal variation of the thermocline structure may play a crucial role near the southern boundary in altering the wave penetration across the gyre boundary. This zonal variation causes zonal variations in both the wave front orientation and the gradient of background potential vorticity. Consequently, for interfaces at different depths, the wave penetration near the southern boundary will be changed dramatically.

3 Planetary Wave Breaking: I. No Ekman Pumping

Now, we turn to the second topic of this chapter: the breaking of planetary waves forced by vertical displacement of interfaces at the eastern boundary. First of all, free waves (i.e. $w_e = 0$) are investigated in this section. The approach developed here will also be applied to later sections.

For simplicity, the eastern boundary interface is chosen to be flat and to vary temporally, i.e.

$$h_e = h_e(t). \tag{3.1}$$

After using this as the initial conditions for characteristics $h_i = h_e(t_i)$, the parametric solution for a free wave is readily derived from (1.2) with $w_e = 0$

$$x = -\frac{h_e(t_i)[1 - h_e(t_i)]}{f^2}(t - t_i), \tag{3.2a}$$

$$h = h_e(t_i) \tag{3.2b}$$

where $f = f_i$ has been used. Hereafter, unless otherwise specified, at the eastern boundary, interfaces are chosen to move vertically at a constant speed p, with the initial depth H_s and the final depth H_{e1}, which satisfy $0 \leq H_e,\ H_{e1} < 1$, i.e.

$$h_e(t) = \begin{cases} H_e + pt & if\ 0 \leq t \leq T \equiv (H_{e1} - H_e)/p > 0 \\ H_{e1} & if\ t > T \end{cases} \tag{3.3}$$

A downwelling is represented by a $p > 0$ and $H_e < H_{e1}$, while an upwelling is represented by a $p < 0$ and $H_e > H_{e1}$. The observed maximum speeds of interfaces varying at annual and interannual scales are no more than twice the typical Ekman pumping speed, i.e. $\mid p \mid \leq 2$. In fact, a typical dimensional Ekman speed is $w_e^* \sim 0.5 \times 10^{-4} ms^{-1} \sim 15\ meters/year$. Observations show that the maximum amplitude of interface variation is below 15 meters for annual variation and below 90 meters for interannual variation (say with period longer than 6 years) (e.g., Tabara *et. al*, 1986). The corresponding dimensional speed is then $p^* \sim 15\ meters/0.5 \times year \sim 90\ meters/0.5 \times (6\ years) \sim 2w_e^*$. Since the non-dimensional $p = p^*/w_e^*$, annual and interannual variability has the non-dimensional speed range of $\mid p \mid \leq 2 \sim O(1)$.

3.1 The Approach

After the eastern boundary perturbation (3.3), a perturbation wave is radiated from the eastern boundary. This wave may break because of the nonlinear steepening $C \sim h(1 - h)$. We are going to derive the first breaking time and positions. In order to generalize the approach here to later cases, the parametric solution (3.2) is put in a more general form

$$x = x(t, f, t_i), \qquad 0 \leq t_i \leq T, \tag{3.4a}$$

$$h = h(t, f, t_i). \tag{3.4b}$$

Physically, (3.4) says that at a time t and a latitude f, the disturbance excited along the eastern boundary at t_i reaches the zonal position $x(t, f, t_i)$. The disturbed interface now is $h(t, f, t_i)$. Indeed, (3.4a) is also the equation for the wave front x_F that leaves the eastern boundary at $t = t_i$ (see (1.6)). On a fixed latitude f, a breaking time t_b occurs when the zonal profile is vertical, i.e. $\partial_h x \mid_{f,t_b} = 0$. In (3.4), this is equivalent to

$$\partial_{t_i} x = 0. \tag{3.5}$$

Breaking times are then obtained from (3.4a) and (3.5) as

$$t_b = t_b(t_i, f) \qquad with \;\; t_b \geq t_i. \tag{3.6}$$

The physical meaning of (3.6) is clear. Along the latitude f, the interface becomes vertical at time t_b on the wave front x_F that leaves the eastern boundary at $t = t_i$. The first breaking time t_0 on the latitude f is the minimum of the family of breaking times in (3.6), i.e.

$$the\ first\ breaking\ time\ :\ \ t_0 = min\{t_b\}_{t_i \in [0,T]}. \tag{3.7a}$$

The first breaking position x_0 and depth h_0 are then obtained by substituting (3.7a) into (3.4a,b) as

$$x_0 = x(t_0, f, t_{i0}), \qquad h_0 = h(t_0, f, t_{i0}), \tag{3.7b}$$

where t_{i0} is the initial time t_i at which t_b reaches its minimum as in (3.7a). Mathematically, the above method is equivalent to deriving the envelope of the family of characteristics in (3.4a) as in classical methods.

3.2 Free Wave Breaking

Substituting the free wave solution (3.2) and the eastern boundary perturbation (3.3) into (3.5) yields the breaking time

$$t_b = t_i + \frac{h_e(t_i)[1 - h_e(t_i)]}{p[1 - 2h_e(t_i)]}, \qquad for\ 0 \leq t_i \leq T. \tag{3.8}$$

Differentiating (3.8) gives $\partial_{t_i} t_b = 2[1 + h_e(1 - h_e)/(1 - 2h_e)^2] > 0$. This means that a disturbance excited later will break later. Hence the first breaking time occurs at the earliest disturbance wave front with $t_i = 0$. With the aid of (3.3) and (3.8), the first breaking time takes the form

$$t_0 = t_b \mid_{t_i=0} = \frac{H_e(1 - H_e)}{p(1 - 2H_e)}. \tag{3.9}$$

The corresponding breaking distance x_0 is obtained by substituting (3.9) into (3.2a), and by using $t_i = 0$ in (3.3),

$$x_0 = -\frac{H_e(1 - H_e)}{f^2} t_0. \tag{3.10}$$

It is interesting to see that the first breaking time and position are independent of the disturbance amplitude $H_{e1} - H_e$ (no H_{e1} dependence in (3.9) and (3.10)). Hence, the occurrence of breaking is determined only by the speed and depth of the perturbation along the eastern boundary. For eastern boundary conditions more general than (3.3), calculation of some examples also show that the first breaking time and position are mainly determined by the depth and maximum speed of the perturbation.

To study the breaking in more detail, we plot the t_0 and x_0 against the speed and depth in Fig.5.3. As a function of $-1/p$ and H_e, Figure 5.3a displays t_0, which is independent of f as seen in (3.9). The speed range for the observed annual and interannual variation ($\mid p \mid \leq 2$) are also marked on the top. A shallowing has $-1/p > 0$ on the right half plane and a deepening has $-1/p < 0$ on the left half. The nonbreaking region is hatched. It is seen from Fig.5.3a that at the fast speed $\mid p \mid = 2$, breaking events occur within about one advective time $t_0 \leq O(1)$ for interfaces at most depths. Furthermore, Fig.5.3b,c,d give the corresponding x_0 at latitudes $f = 0.3, 0.6, 0.9$ respectively. Fig.5.3b,c,d indicate that most of the breaking is realized within the basin $\mid x_0 \mid \leq O(1)$. For a slower speed p, the H_e range for breaking gets smaller and breaking tends to be trapped on interfaces near the surface and bottom. If the speed is very slow, i.e. $p \to 0$, we have $x_0 \to -\infty$. Thus, breaking will not take place within a finite basin although in principle it may occur in an ocean unbounded to the west.

As we have seen in Fig.5.3, breaking occurs rapidly for an interface near the surface or bottom, but breaking occurs very late for an interface near the middle depth. This can be explained as

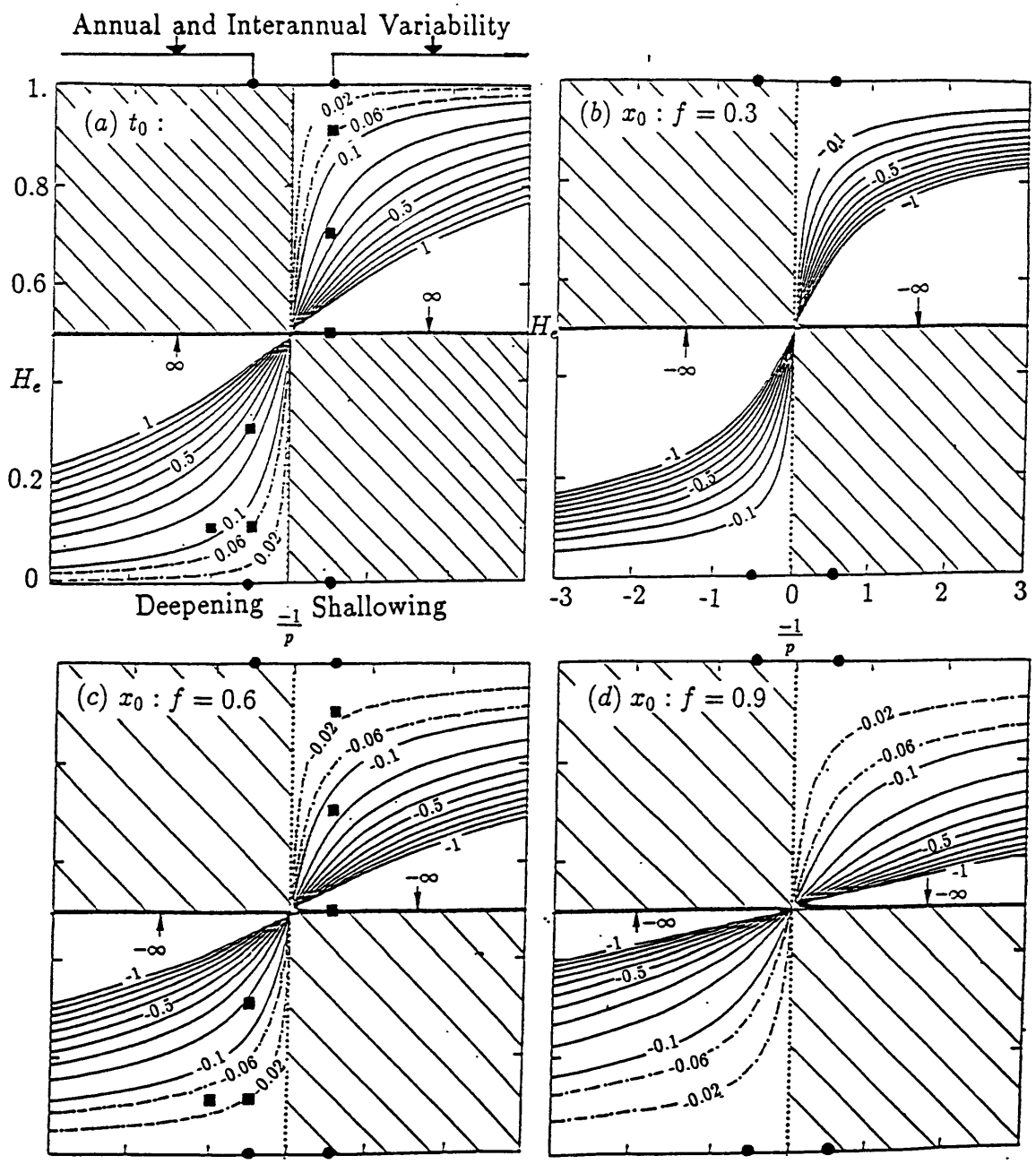

Figure 5.3: The first breaking times and positions for free waves. The horizontal axis is $-1/p$ and the vertical axis is H_e. Hatched regions are parameters no breaking will occur even in an unbounded ocean. The $t_0 > 1$ and $x_0 < -1$ contours are not drawn, where the breaking is unlikely to take place within a basin of a realistic width. a) the first breaking time. The observed maximum annual and interannual forcing speeds are marked on the top. The black squares mark the parameters later used in Fig.5.5. b) the first breaking position at $f = 0.3$. c) the first breaking position at $f = 0.6$. d) the first breaking position at $f = 0.9$.

follows. Under a perturbation δh, the local Rossby wave speed is expanded around the mean local depth h_0 as

$$C(h) = C(h_0) + \partial_{h_0} C(h_0)\delta h,$$

The first term is the local linear Rossby wave speed while the second term represents the effect of nonlinear steepening. Thus, the intensity of the nonlinear steepening can be measured by

$$\Delta = \frac{\partial_{h_0} C(h_0)\delta h}{C(h_0)} = \frac{(1-2h_0)\delta h}{h_0(1-h_0)}.$$

For an interfaces near the surface ($h_0 \to 0$) or bottom ($h_0 \to 1$), it holds that $\Delta \to \infty$, implying a strong nonlinear steepening. On the other hand, for an interface near the middle depth ($h_0 \to 0.5$), $\Delta \to 0$, suggesting a very weak nonlinear steepening.

In addition, in order to compare with later cases with Ekman pumping, several features are noteworthy in Fig.5.3. a) For a breaking to occur, the result of a shallowing $p < 0$ at the eastern boundary interface depth H_e is equivalent to the opposite deepening $-p > 0$ at the depth $1 - H_e$ (as reflected about the mid-depth $H_e = 0.5$). In particular, a downwelling causes breaking only when $H_e < 0.5$ while an upwelling causes breaking only for $H_e > 0.5$. b) Both t_0 and x_0 vary monotonically with either H_e or p. Thus, for a faster speed p, or a interface closer to the top (when $p < 0$) or the bottom (when $p > 0$) of the model ocean, the breaking occurs earlier and closer to the eastern boundary. For the special case $H_e = 0$ (when $p < 0$) or $H_e = 1$ (when $p > 0$), breaking occurs immediately at the eastern boundary, while for $H_e = 0.5$ no breaking will occur at all.

Lastly, it will be seen helpful to introduce a way of judging, directly from Fig.5.3a, if the first breaking time is at the initial front $t_i = 0$. Take the downwelling breaking as an example. In Fig.5.3a, at a fixed downwelling speed $p > 0$, t_0 increases with H_e. This implies that t_0 must occur on the initial $t_i = 0$ front. The reasoning is as follows. Examining the breaking times in (3.8), one sees that the first term on the right-hand side (t_i) increases with t_i. The second term $h_e(t_i)[1 - h_e(t_i)]/p[1 - 2h_e(t_i)]$ has the same form as the t_0 in (3.9) except with H_e replaced by h_e. Hence, an increase of t_0 with H_e in Fig.5.3a means an increase of the second term with (h_e and then) t_i (note $\partial_{t_i} h_e = p > 0$). As a result, t_b in (3.8) increases with t_i, which is consistent with the

earlier analytical calculation that $\partial_{t_i} t_b > 0$. Accordingly, the first breaking time is on the earliest wave front $t_i = 0$.

3.3 Structures and Amplitudes of Breaking Fronts

We start with examining the evolution of zonal profiles. A schematic figure of a zonal profile due to a deepening $p > 0$ at a time t is shown in Fig.5.4a. There are three parts on a typical zonal profile. The western part is the old (before-perturbation) shadow zone (now, in the absence of an Ekman pumping, the whole gyre is filled with a shadow zone in which the thermocline is flat !) which has not been affected by an eastern boundary disturbance. Behind the old shadow zone is the disturbance part forced by lowering the interface along the eastern boundary. Before the perturbation stops ($t < T$), only these two parts exist. After the perturbation stops ($t > T$), there will be a third part that is the new (after perturbation) shadow zone established near the eastern boundary. The initial ($t_i = 0$) and end ($t_i = T$) disturbance wave front x_F are marked in Fig.5.4a. Before breaking, an earlier wave front is always west of a later wave front. At the first breaking time, a later wave front catches up with an earlier one. The interface becomes vertical at a first breaking position x_0 (this case is not shown in Fig.5.4a). Fig.5.5. plots some examples of evolution of zonal profiles at $f = 0.6$ calculated from (3.2a,b) and (3.3). In all figures, the eastern boundary interface varies at an amplitude $\delta h_e = 0.2$. [1]

Fig.5.5a-e illustrate the evolution for the fastest possible annual and interannual speed $\mid p \mid = 2$. The value of t_0 and x_0 in each figure are found from Fig.5.3a,c (black squares) and are written in each figure. In each figure, the solid lines are the $t = 1$ zonal profiles while the dashed lines indicate the disturbance profiles at earlier times. Fig.5.5a depicts a downwelling case with a very shallow interface $H_e = 0.1$. One sees that a strong overturning has appeared on the first disturbance profile at $t = 0.2$. In fact, the wave has already broken long before $t = 0.2$, at $t = 0.06$. After the first breaking time, the solution in (3.2) is no longer valid because of the gravitational instability. Smaller scale process such as friction or relative vorticity will enter. (The fast breaking for shallow

[1] This is too large for observations. For $H = 800\ m$, the dimensional δh_e is about 160 m.It is chosen only for clarity of the figures. In any case, for (3.3), this large amplitude does not change the first breaking times and positions because (3.9) indicates that t_0 (and x_0) depends only on the initial depth H_e or independent of H_{e1}.

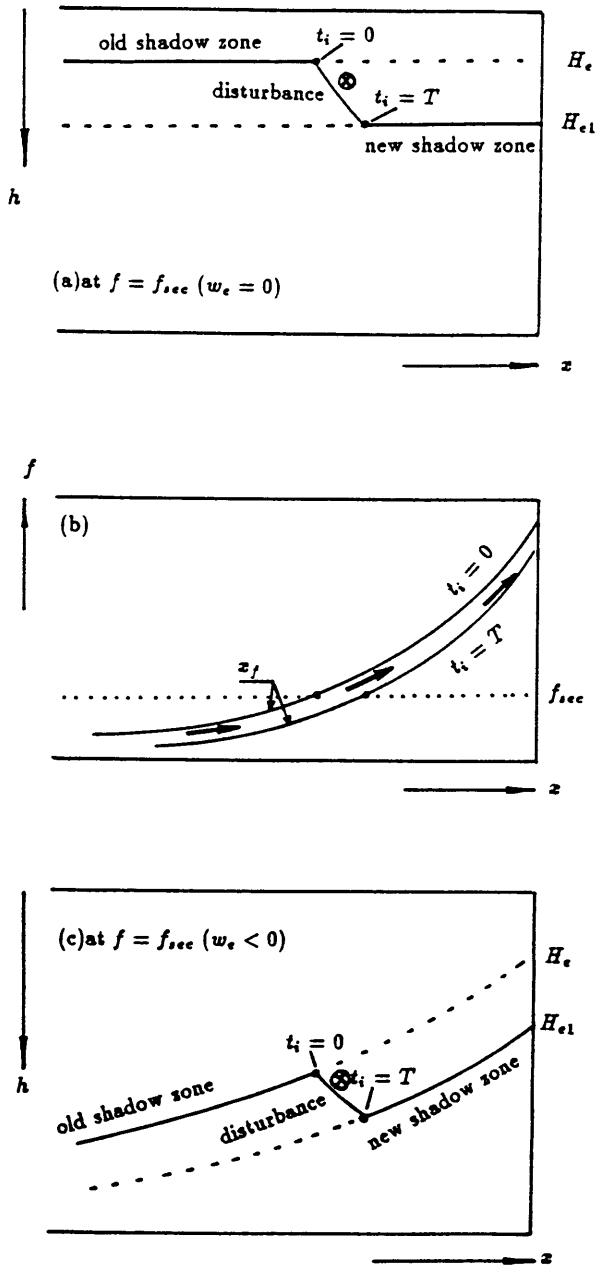

Figure 5.4: The schematic figure of a zonal profile for a downwelling eastern boundary displacement and its associated wave fronts. The solid lines are the zonal profile and the dashed lines represent the continuation of the two shadow zone profiles. a) Free wave zonal profile, b) the two-dimensional structure of the breaking front confined by the initial and last wave fronts. The black arrows indicate the thermal wind jet i.e. $\vec{v_T} = \vec{v_1} - \vec{v_2}$. c) Zonal profile with Ekman pumping. The amplitude of the maximum breaking fronts are also shown schematically.

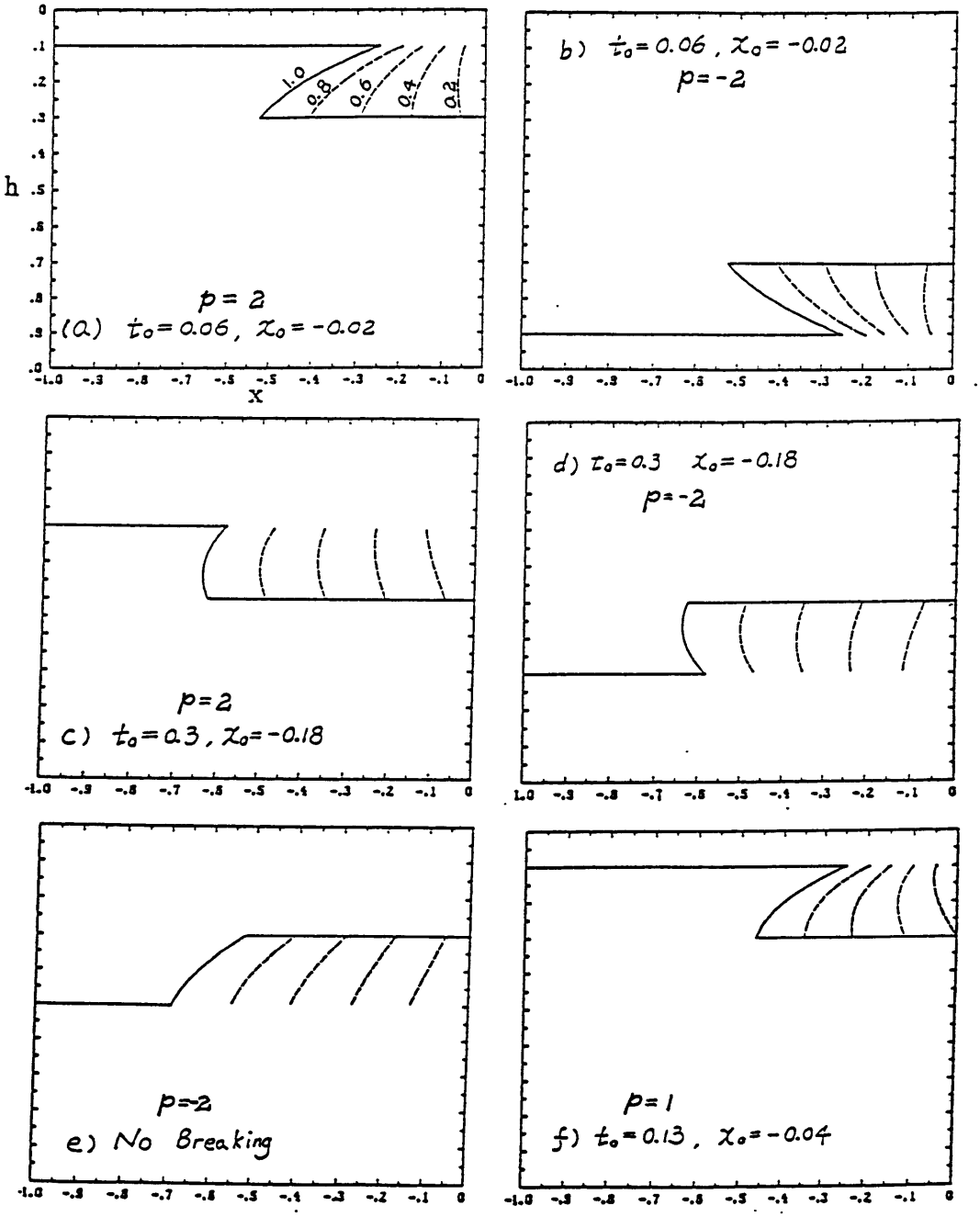

Figure 5.5 Zonal profile evolution for free waves. The eastern boundary interface moves at a constant speed p and the amplitude $\mid H_{e1} - H_e \mid = 0.2$. a)$p = 2, H_e = 0.1$. b)$p = -2, H_e = 0.9$. c)$p = 2, H_e = 0.3$. d)$p = -2, H_e = 0.7$. e)$p = -2, H_e = 0.5$. f)$p = 1, H_e = 0.1$. The profiles are all at t=0.2,0.4,0.6,0.8 and 1.

interfaces near the eastern boundary has been pointed out by Anderson and Killworth (1980).) Fig.5.5b shows the upwelling case opposite to Fig.5.5a. The profile is a mirror imagine of Fig.5.5a with respect to $H = 0.5$. The t_0 and x_0 are the same as in Fig.5.5a.

If the downwelling disturbance in Fig.5.5a starts at a deeper depth $H_e = 0.3$, Fig.5.5c indicates that the overturning has not appeared on the $t = 0.2$ profile yet. In fact, both t_0 and x_0 are delayed more then five times. Relative to the shallower case Fig.5.5a, the breaking now takes place far away from the eastern boundary. Fig.5.5d is the upwelling breaking opposite to Fig.5.5c which has the same t_0 and x_0. Fig.5.5e illustrates a shallowing perturbation forced by the same speed as that in Fig.5.5b,d but for $H_e = 0.5$. One sees that breaking will not occur. The last example is Fig.5.5f where the deepening speed in Fig.5.5a is reduced by a half to $p = 1$. (3.8) shows that the first breaking time will be twice that in Fig.5.5a. The evolution is shown in Fig.5.5f.

The reason for downwelling breaking on $H < 0.5$ and upwelling on $H > 0.5$ is simple. Descending h_e causes the disturbance profile to shallow westward. If $h < 0.5$, the local Rossby wave speed $C(h)$ is slower on the western side because $C(h) \sim h(1-h)$ reaches its maximum at $h = 0.5$. Therefore, a later disturbance on the eastern side will travel faster to catch up with a previous disturbance, causing a downwelling breaking. Ascending h_e is the opposite.

The flow field is entirely different between a downwelling breaking front and an upwelling breaking front. A downwelling breaking must produce a northward thermal wind jet along the breaking front, as drawn schematically in Fig.5.4a, while an upwelling breaking a southward thermal wind jet.

The two-dimensional structure of the breaking front is simply the linear β dispersion shape $x \sim 1/f^2$. This is because the first breaking time (3.9) is independent of latitude. So the only f dependency for the breaking position (3.10) is the $1/f^2$ factor. A schematic figure of the two-dimensional (before breaking) disturbance structure (bounded by the initial and final disturbance front (1.6) at $t_i = 0$ and $t_i = T$) is given in Fig.5.4b. Later, when the breaking occurs, the breaking front will be sandwiched by the initial and final disturbance front. The section latitude $f = f_{sec}$ of Fig.5.4a is marked on Fig.5.4b.

Although the amplitude of the breaking front is beyond the scope of our model, some preliminary results can still be obtained. We see that the disturbance is vertically bounded by the interfaces of the old and the new shadow zone

$$h_{old\ shadow\ zone} = H_e, \quad h_{new\ shadow\ zone} = H_{e1}. \tag{3.11}$$

Therefore, we can estimate the upperbound of the intensity of the breaking front as

$$\textit{the intensity of the front} \sim \mid h_{old\ shadow\ zone} - h_{new\ shadow\ zone} \mid = \mid H_{e1} - H_e \mid . \tag{3.12}$$

This shows that the intensity of a breaking front is determined by the amplitude of the perturbation (although we have seen in (3.9) and (3.10) that the occurrence of a breaking is independent of the amplitude of the perturbation). Furthermore, in the absence of an Ekman pumping, (3.11) states that the shadow zone thermocline is flat. Thus, (3.12) suggests that the intensity of the breaking front is the same everywhere on the front.

The eastern boundary perturbation (3.3) is very special because it has an infinite acceleration and deceleration at the beginning and end, respectively. A more realistic example of the eastern boundary perturbation is probably a periodic one such that

$$h_e(t) = \begin{cases} 0.5[H_e + H_{e1} + (H_e - H_{e1})cos(\omega t)] \\ H_{e1} \end{cases} \tag{3.13}$$

Some disturbance profiles under (3.13) are presented in Fig.5.6, where the maximum speed of h_e resembles the magnitude of the speed of strong annual and interannual periodic variabilities ($max(\mid dh_e/dt \mid) = 2.$) In all the cases, the breaking occurs quickly near the eastern boundary. These figures are to be compared with later cases with an Ekman pumping. It will be seen in the next section that in the presence of an Ekman pumping, significant changes will happen.

Finally, it should be pointed out that the breaking of waves on the initial wave front $t_i = 0$ is due to the peculiar vertical motion (3.3) at the eastern boundary where h_e has a constant speed. [1]

[1] For a general eastern boundary $h_e(t)$, breaking times in (3.8) has to be replaced by $t_b = t_i + h_e(t_i)[1 - h_e(t_i)]/[\frac{dh_e}{dt_i}(1 - 2h_e)]$, Thus, $\partial_{t_i} t_b = 2 + \{[2(\frac{dh_e}{dt_i})^2 - \frac{d^2h_e}{dt_i^2}(1 - 2h_e)]h_e(1 - h_e)\}/[(\frac{dh_e}{dt_i}^2(1 - 2h_e)^2]$. When h_e has a strong positive acceleration, it is possible that $\partial_{t_i} t_b < 0$. As a result, the first breaking time may occur after the earliest wave front. For the perturbation (3.13) (if we use only the half period from 0 to $T = \pi/\omega$). $\frac{dh_e}{dt_i} \mid_{t_i=0} = 0$ indicates that $t_b(t_i = 0) = \infty$. Thus, the initial wave front can not be the first breaking time. Similarly, the first breaking does not occur on $t_i = T$ wave front either.

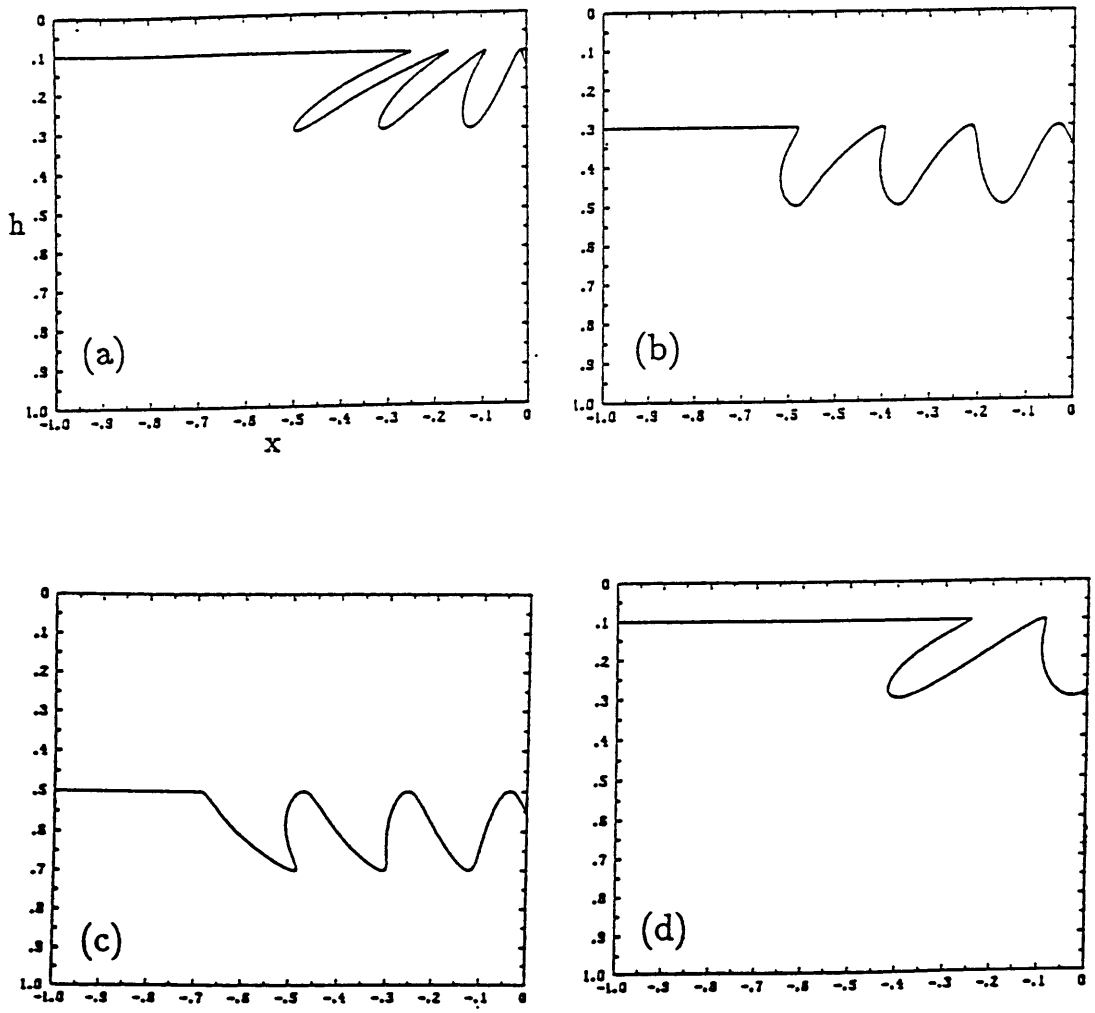

Figure 5.6: Zonal profiles at $t = 1$ for free waves with periodic eastern boundary condition in (3.11) with the amplitude 0.2. a) $max(\frac{dh_e}{dt}) = 2, H_e = 0.1$. b)$max(\frac{dh_e}{dt}) = 2, H_e = 0.9$, c) $max(\frac{dh_e}{dt}) = 2, H_e = 0.5$, d) $max(\frac{dh_e}{dt}) = 1, H_e = 0.1$.

4 Planetary Wave Breaking: II. With Ekman Pumping

In the presence of an Ekman pumping, there will be both a two-dimensional barotropic flow and an external forcing. There is no general approach and conclusion about the wave breaking in the presence of a two dimensional flow. Nevertheless, the analytical solutions (1.3) make it possible to examine the breaking condition. To understand the basic effect of an Ekman pumping on breaking, the simplest situation--a spatially uniform Ekman pumping, is examined. The Ekman pumping and its $\hat{f}_i$ characteristic solution can be derived from (1.3b) as (or see (4.9) of chapter 2)

$$w_e(f) = W_e, \qquad \hat{f}_i(f,s) = fe^{-W_e s}. \tag{4.1}$$

4.1 Forced Wave Breaking

After substituting (4.1) into (1.3), the solutions with t_i as a parameter are obtained as

$$x = \frac{\{1-[1-h_e(t_i)]e^{W_e(t-t_i)}\}^2 - h_e(t_i)^2}{2f^2W_e} = x(t,f,t_i). \tag{4.2a}$$

$$h = 1-[1-h_e(t_i)]e^{W_e(t-t_i)} = h(t,f,t_i), \tag{4.2b}$$

Similar to the free wave case, taking the eastern boundary perturbation as the linearly varying h_e in (3.3), the breaking time is determined by setting $\partial_{t_i} x = 0$ as

$$t_b = t_i + \frac{1}{W_e} ln[J(h_e, \frac{W_e}{p})], \tag{4.3a}$$

$$or \quad p(t_b - t_i) = \frac{1}{\frac{W_e}{p}} ln[J(h_e, \frac{W_e}{p})] \tag{4.3b}$$

$$where \qquad (1-h_e)J^2 - J + \frac{h_e}{1+(1-h_e)\frac{W_e}{p}} = 0 \tag{4.3c}$$

For a physically valid breaking time $t_b - t_i \geq 0$, it is required that $0 \leq J \leq 1$. J is readily solved from (4.3c) as

$$J^+_- = \frac{1}{2(1-h_e)} \left\{ 1^+_- \left[1 - \frac{4h_e(1-h_e)}{1+(1-h_e)\frac{W_e}{p}} \right]^{\frac{1}{2}} \right\}. \tag{4.3d}$$

The sign is chosen such that t_b gives the minimum and positive $t_b - t_i$ if available. The free wave limit (3.8) can be recovered from (4.3b) in the limit $\frac{W_e}{p} \to 0$.

It will be shown soon that the first breaking time occurs at the initial wave front $t_i = 0$. Therefore, from (4.3b) and (3.3) the first breaking time satisfies

$$pt_0 = \frac{1}{\frac{W_e}{p}} ln[J(H_e, \frac{W_e}{p})]. \tag{4.4}$$

The corresponding position is obtained by substituting (4.4) into (4.2a) as

$$x_0 = \frac{\{[1-(1-H_e)e^{W_e t_0}] - H_e^2\}}{2f^2 W_e}. \tag{4.5}$$

As in the free wave case of (3.9) and (3.10), the first breaking time and position are independent of the amplitude of the perturbation $H_{e1} - H_e$. Thus, the occurrence of breaking is determined only by the speed and depth of the perturbation.

With $w_e = -1$, t_0 and x_0 are plotted in Fig.5.7 which is arranged similarly to Fig.5.3. t_0 is independent of f and is displayed in Fig.5.7a. One sees that t_0 increases monotonically with H_e for deepening and decreases monotonically with H_e for shallowing. Using the argument similar to that for free waves (at the end of subsection 3.2), we know that the first breaking time must occur on the initial wave front $t_i = 0$.

The most striking difference between Fig.5.7a and the free wave case of Fig.5.3a is that t_0 is not symmetrical at all with respect to the center point $(-1/p, H_e) = (0, 0.5)$, particularly for perturbation speed comparable or slower than the Ekman pumping speed ($p \leq O(1)$) which is just the speed of interest for annual and interannual variations. In comparison with the free wave in Fig.5.3a, the upwelling breaking time is shortened and its parameter domain is substantially enlarged. On the contrary, the downwelling breaking time is delayed and its domain is severely reduced. Hence, imposing an Ekman pumping will enhance upwelling breaking but suppress downwelling breaking.

In more detail, the upwelling breaking now occurs for interfaces from the top to the bottom of the model ocean. At a fixed ascending speed p, the first breaking time increases monotonically from 0 to ∞, as H_e varies from 0 to 1 (as opposed to varying from 0 to 0.5 as in the free wave case.) Especially, near or slightly above the middle depth $H_e \approx or < 0.5$, if a shallowing is faster than or comparable to the Ekman pumping ($p \leq O(1)$), an upwelling breaking occurs within an advective time ($t_0 < O(1)$). This is in sharp contrast to the free wave case where no upwelling breaking occurs at all if $H_e \leq 0.5$ (see Fig.5.3a near $H_e = 0.5$ for shallowing) The implication is

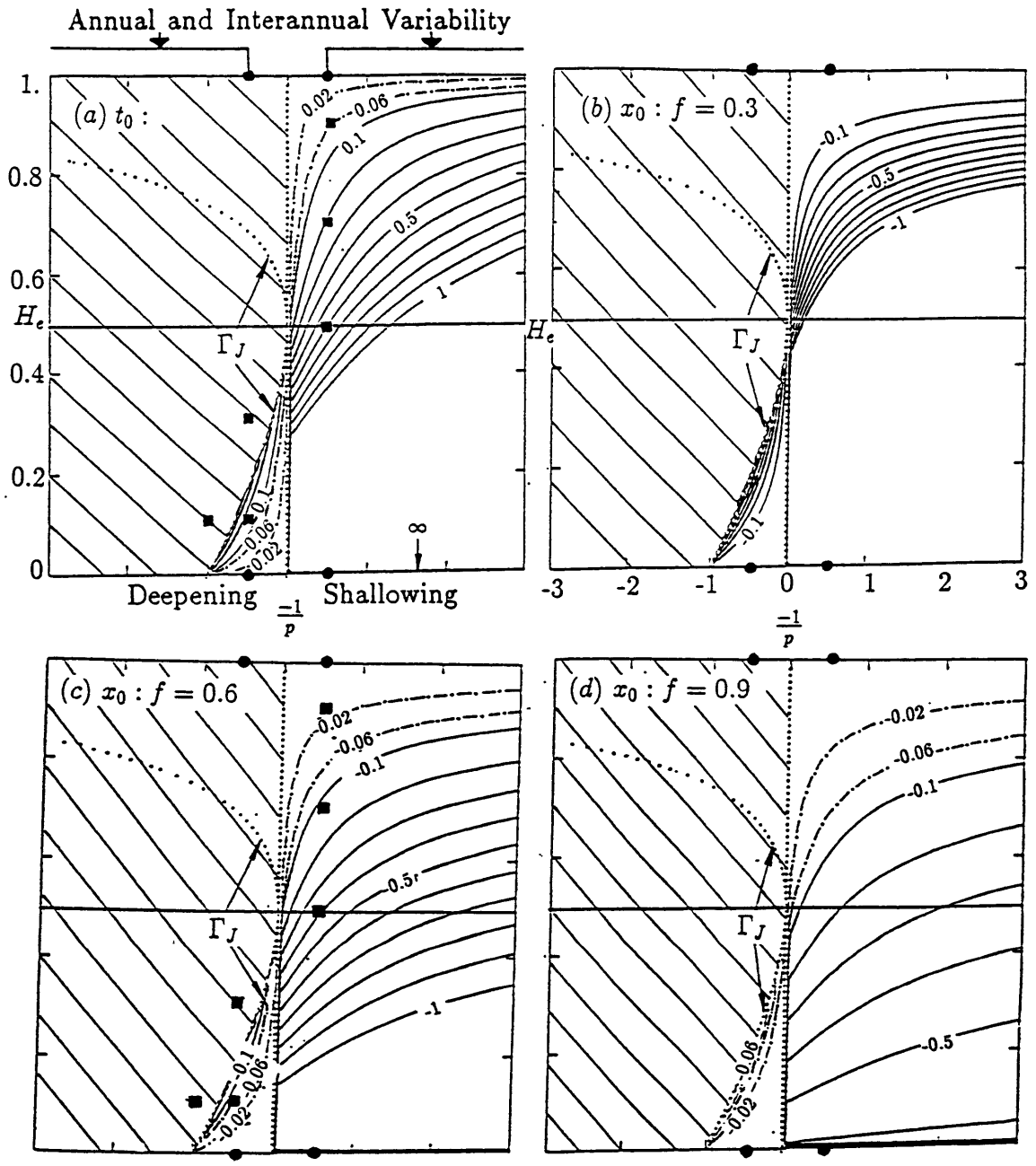

Figure 5.7: The first breaking times and positions with an uniform Ekman pumping $w_e(f) = W_e = -1$. The parameters in each figure correspond that in Fig.5.3. a)for t_0. b)x_0 at f=0.3. c)x_0 at f=0.6. d)x_0 at f=0.9. In comparison with the free wave case in Fig.5.3, the downwelling breaking domain is severely reduced while the upwelling breaking domain is greatly enhanced (see the text for a full discussion).

that for interfaces near and above the middle depth, an upwelling breaking is qualitatively changed from nonbreaking to breaking.

In contrast to an upwelling breaking, for a downwelling breaking, fast downwelling ($p \gg 1$) is similar to the free wave case. However, a qualitative difference from the free wave appears for descending speed comparable or slower than the Ekman pumping. In the parametric plane, there is a (internal) marginal curve given by the dotted line (Γ_J see Fig.5.7) on the edge of downwelling breaking domain. This curve is marked by $W_e/p = -(1-2H_e)^2/(1-H_e)$ which is derived by substituting $t_i = 0$ and (3.3) into (4.3d) and then setting the $()^{1/2}$ in (4.3d) zero. (As far as the J value is concerned, Γ_J divides the complex conjugates of J on the left from the real J on the right.) On Γ_J, the breaking time is finite. In fact, at each depth, Γ_J gives a cutoff (or slowest descending) speed

$$p_c(H_e) = -W_e(1-H_e)/(1-2H_e)^2 > 0. \tag{4.6}$$

For a descending speed slower than p_c, downwelling breaking will not occur. The minimum speed of p_c in (4.6) is

$$min\{p_c\} = -w_e$$

implying no downwelling breaking at all depths if the downwelling speed is slower than the surface Ekman pumping ($p < -w_e$). As H_e deepens from 0 to 0.5, Γ_J varies from $W_e/p = -1$ to $W_e/p = 0$ and the associated cutoff speed (4.6) increases from $-w_e$ to ∞. Thus, away from the surface the cutoff speed increases and breaking becomes less likely to take place.

Physically, it is hard to understand exactly how and why the breaking conditions are altered, partly because the effect of the mean flow is coupled with that of the external Ekman pumping. Nevertheless, a rudimentary explanation is presented. Relative to a water parcel forced downward (by the surface Ekman pumping) with a speed $w < 0$, a upwelling h_e at an ascending speed $p < 0$ has a stronger ascending speed $p + w < p < 0$. In other words, relative to the water particle, the upwelling speed is enhanced, which in turn results in a stronger upwelling breaking tendency and an earlier breaking time. However, with respect to this downward particle, a descending h_e at the speed $p > 0$ has a relatively weaker descending speed $p+w < p > 0$. Especially, when the descending is slower than the downward speed of the particle $0 < p + w < p$, h_e moves upward relative to

that particle. As a result, downwelling breaking will not occur. This offers an explanation why downwelling breaking abruptly disappears when $p < -w_e$.

In a basin with a finite zonal extent, a breaking occurs only when the x_0 is within the basin. x_0 derived from (4.5) is drawn in Fig.5.7b,c,d at latitudes $f = 0.3, 0.6, 0.9$ respectively. Similar to t_0, here x_0 differs substantially from the free wave case, especially away from the southern boundary in Fig.5.7c,d, where the breaking positions x_0 are much closer to the eastern boundary.

In summary, for annual and interannual variations, downwelling breaking is severely suppressed and the breaking time is delayed. Abruptly, for descending speeds slower than the Ekman pumping, there will be no downwelling breaking. In addition, downwelling breaking tends to be trapped on interfaces near the surface. On the contrary, upwelling breaking is greatly enhanced and the breaking times are shortened. Shallowing breaking even appears on interfaces within the upper half ocean. [1]

4.2 Structures and Amplitudes of Breaking Fronts

In the presence of an Ekman pumping, (1.3d) shows that a steady shadow zone interface deepens westward as

$$h = \sqrt{2f^2 w_e(f)x + H_e^2}. \tag{4.7}$$

Here, we have assumed a flat $h_e = H_e$. Schematically, a zonal profile after an eastern boundary disturbance is shown as in Fig.5.4c. This differs from the free wave case in Fig.5.4a in that now the disturbance is advected downward as it advances westward.

Fig.5.8 demonstrates some examples of evolution of zonal profiles at $f = 0.6$. The parameters in Fig.5.8a-f correspond to that in Fig.5.5a-f respectively except now with an Ekman pumping

[1] In the presence of a spatially varying Ekman pumping, we can also study the breaking. A detailed discussion is not presented here. We only briefly describe the conclusions. The breaking in the northern part of a subtropical gyre is similar to the free wave breaking case in section 3. On the contrary, the breaking in the southern part of a subtropical gyre is similar to the uniform Ekman pumping case studied above. Physically, this difference occurs because of the southward mean flow. In our model, the southward mean flow carries the effect of the Ekman pumping southward. In the northern part of a subtropical gyre, there is very little wave energy coming from the north which in turn results in a breaking similar to a free wave case. But, in the southern part, much wave energy arrives from the northern and middle of the basin and therefore the influence of the Ekman pumping is stronger. In addition, within each half basin, near the middle of the basin, the breaking is more similar to a uniform Ekman pumping case compared with the breaking occurring near the gyre boundaries. The physics is simple. Near the middle of the gyre, the magnitude of the Ekman pumping is stronger.

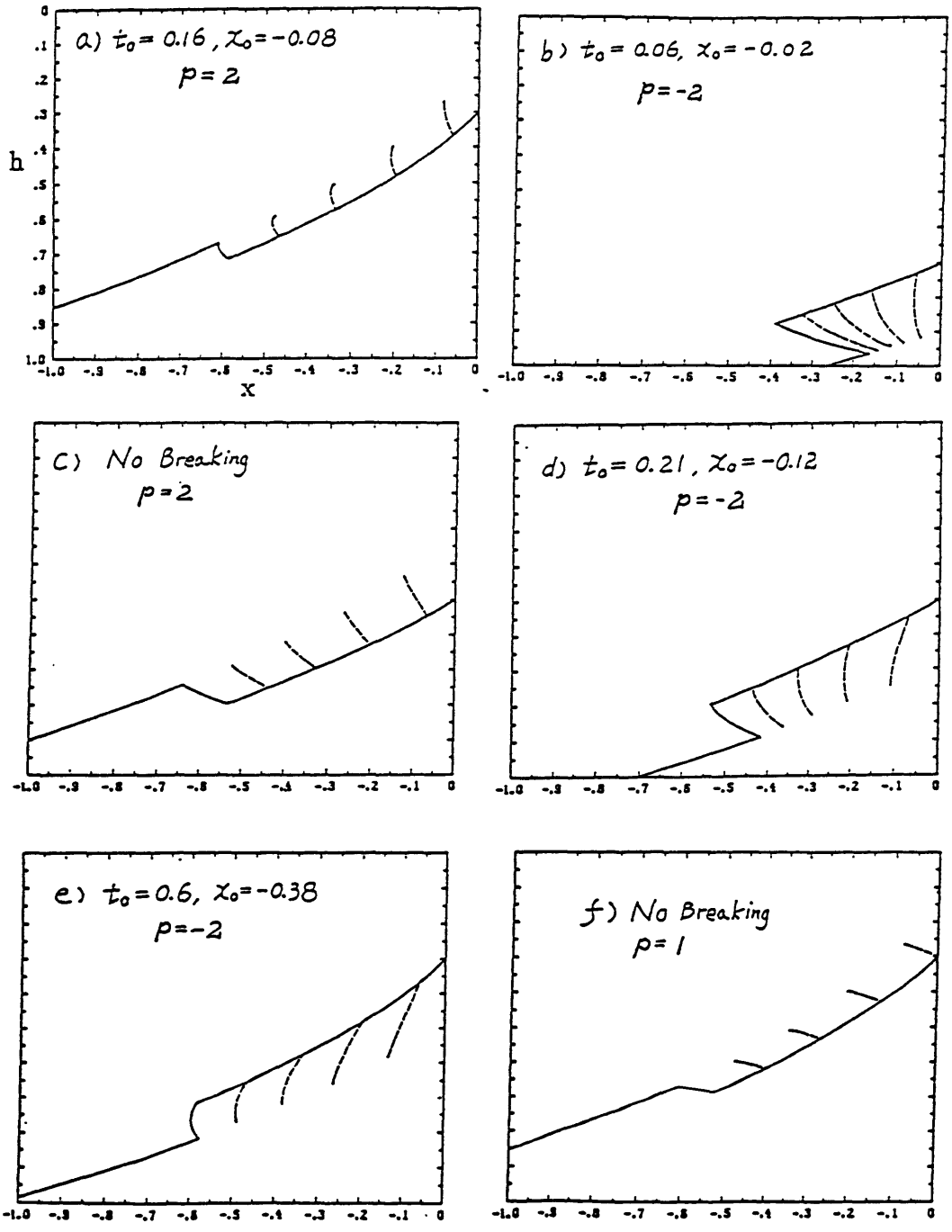

Figure 5.8: Zonal profile evolution for waves in the presence of a uniform Ekman pumping $w_e = -1$. The eastern boundary condition is the same as in Fig.5.5. Parameters in Fig.5.8a-f correspond to those in Fig.5.5a-f. a)$p = 2, H_e = 0.1$. b)$p = -2, H_e = 0.9$. c)$p = 2, H_e = 0.3$. d)$p = -2, H_e = 0.7$. e)$p = -2, H_e = 0.5$. f)$p = 1, H_e = 0.1$. The profiles are all at t=0.2,0.4,0.6,0.8 and 1.

$w_e = -1$. For the strong annual and interannual deepening on a shallow interface with $H_e = 0.1$, comparing Fig.5.8a with the free wave case in Fig.5.5a, one sees that the first breaking time and position are delayed about three times. Yet, the opposite upwelling breaking in Fig.5.8b has t_0 and x_0 only slightly earlier than the free wave case in Fig.5.5b. A dramatic change occurs if the interface is deeper, say $H_e = 0.3$ as in Fig.5.8c, or the deepening speed is reduced, say by a half, as in Fig.5.8f, now downwelling breaking does not occur even in an unbounded ocean while the free wave in Fig.5.5c or Fig.5.5f breaks early in the eastern part of the basin. These two cases are located in the parameter plane in the non-breaking domain (the hatched region in Fig.5.7a,c). The opposite upwelling case to Fig.5.8c is shown in Fig.5.8d. The first breaking time and position are shortened about 40 percent than the free wave in Fig.5.5d. If the interface starts further up within the upper half ocean, a significant change appears for the upwelling breaking. Although the free wave in Fig.5.5e will not break, upwelling breaking will take place in the presence of an Ekman pumping as shown in Fig.5.8e. Combining Fig.5.8e with Fig.5.8c, one can imagine an interesting phenomenon. Under a periodic h_e forcing, the disturbance will create a upwelling breaking front on an interface in the upper half ocean where otherwise a downwelling breaking front will be expected in the absence of an Ekman pumping, as can be seen in comparison of Fig.5.9b and Fig.5.6b.

Fig.5.9 presents some zonal profiles with the periodic h_e (3.13) (the same as in Fig.5.6 except with $w_e = -1$ now). For a near surface interface starting on the eastern boundary at $H_e = 0.1$, it is seen in Fig.5.9a that a downwelling breaking front is formed rapidly in the eastern part of the ocean, implying a northward thermal wind jet there. However, if the initial depth H_e is lowered to $H_e = 0.3$, an upwelling breaking front is developed in the middle part of the ocean, implying a southward thermal wind jet. A further deeper disturbance (in the deeper half ocean) in Fig.5.9c demonstrates that a strong upwelling breaking front is established more rapidly than in Fig.5.9b. The final example of Fig.5.9d is also interesting, in which the moving speed of h_e is reduced by a half from that in Fig.5.9a. It is seen that neither downwelling breaking nor upwelling breaking occurs. In contrast to the free wave case in Fig.5.6d where a downwelling breaking takes place quickly.

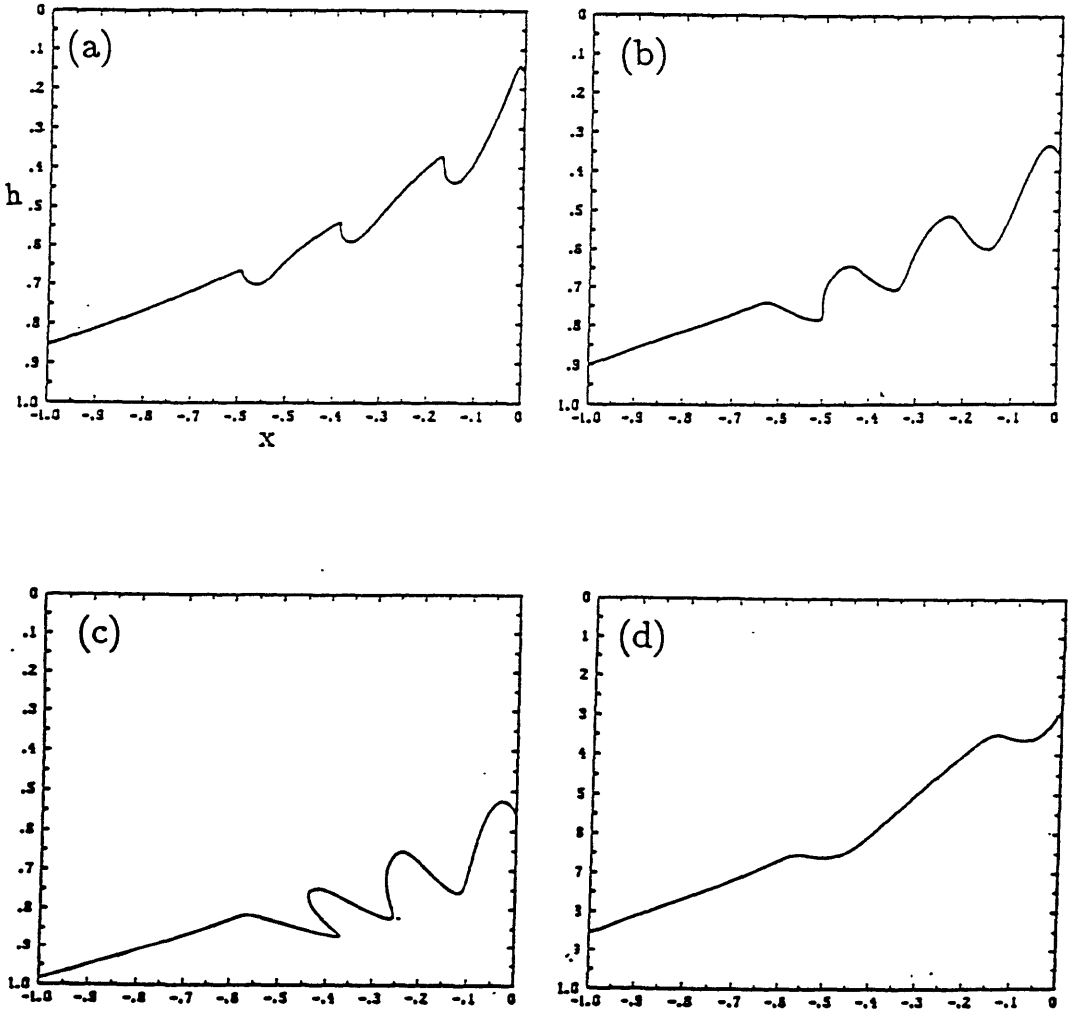

Figure 5.9: Zonal profile for waves in the presence of a uniform Ekman pumping $w_e = -1$. The eastern boundary condition is the same as in Fig.5.6. Parameters in Fig.5.9a-d correspond to that in Fig.5.6a-d.

Another difference from the free wave case is that all the disturbances now slide down along the steady shadow zone thermocline because of the downward Ekman pumping (Fig.5.8, Fig.5.9). This vertical propagation provides another explanation for the suppressed downwelling breaking and enhanced upwelling breaking. Initially, a deepening disturbance starting at $h \sim H_e < 0.5$ will of course create a downwelling breaking tendency (i.e. a westward shoaling interface) that can only break for $h < 0.5$. Its profile is becoming steeper due to the nonlinear steepening. However, the disturbance also propagates downward. The perturbation may penetrate to the deeper half ocean ($h > 0.5$) before breaking. After it descends to the lower half ocean, the perturbation with the downwelling breaking tendency (shoaling towards the west) will never break. A similar argument applies to a disturbance forced by a shallowing.

The structure of the breaking front can also be estimated according to (3.12). Now, the old and the new shadow zone are (see (4.1)) $h_{old\ shadow\ zone} = \sqrt{2f^2 w_e(f)x + H_e^2}$ and $h_{new\ shadow\ zone} = \sqrt{2f^2 w_e(f)x + H_{e1}^2}$. As a result, we can have the upper bound for the amplitude of a breaking front occurring at $x = x_0, f = f_0$ as

$$\Delta h \leq \mid h_{old\ shadow\ zone} - h_{new\ shadow\ zone} \mid = \frac{\mid H_{e1}^2 - H_e^2 \mid}{\sqrt{2f_0^2 w_e(f_0)x_0 + H_e^2} + \sqrt{2f_0^2 w_e(f_0)x_0 + H_{e1}^2}}. \quad (4.8)$$

It is seen that this upper bound is determined by two factors: the amplitude of the initial displacement $H_{e1} - H_e$ and the distance from the eastern boundary x_0. The upper bound increases with the initial amplitude and decreases westward monotonically. The zonal decay is related to the strength of the Ekman pumping ($w_e(f)$). The stronger the Ekman pumping is, the faster the decay is. In the absence of Ekman pumping, there is no zonal decay, as has been seen in the free wave case (Fig.5.4a, Fig.5.5 and Fig.5.6.) [1] The upper bound in (4.8) only gives a local upper bound and prohibits any direct estimate on the amplitude of a breaking front. Nevertheless, it still seems reasonable to speculate that the amplitude of breaking fronts will increase with initial amplitude and decrease away from the eastern boundary. Two important deductions immediately come out. One is that breaking fronts occurring far away from the eastern boundary usually are

[1] This upper bound actually applies to non-breaking waves too. Therefore, a disturbance tends to decrease its amplitude as it propagates westward and downward. This has been explained in section 3 of chapter 3. The physical mechanism for this decay is a divergent group velocity field.

weak. The other is that: although both an interannual variation and an annual variation with the same maximum speed have comparable first breaking time and positions (see discuss following (4.5)), the interannual variation will create a stronger breaking front than the annual variation, because of the larger amplitude of the interannual variation. In other words, the occurrence of the breaking (the breaking time and position) is mainly determined by the maximum vertical speed of the disturbance, while the intensity of the breaking front mainly depends on the amplitude of the disturbance.

Finally, we show that in the presence of mean flows, the breaking positions are also changed qualitatively. Re-examining the free wave in Fig.5.3 or (3.2), one sees that an infinite breaking time must take place at an position infinitely westward away from the eastern boundary (and thus beyond the basin). Therefore, free waves break only for those with $t_0 \leq O(1)$ (so that $x_0 \leq O(1)$). But now in Fig.5.7, breaking positions are finite even for breaking times approaching infinity (on the shallowing half plane near $H_e \to 0$ in Fig.5.7a-d). Particularly on the high latitude case in Fig.5.7d, the breaking positions are close to the eastern boundary ($x_0 \leq 0.6$) no matter how long the breaking time is.

These finite breaking positions are caused by the two-dimensional barotropic flow field, which tends to carry wave energy southward while they propagate westward. In fact, in the thermocline, it is this mean flow field that causes the different zones (pool zone, ventilated zone and shadow zone). Waves forced along the eastern boundary can only propagate in the shadow zone which is bounded to the west by B_2 (see (1.4) or (1.5)). Since B_2 extends south-westward, it is closer to the eastern boundary to the north. In fact, with the aid of (4.4), (4.5) says that a breaking position exhibits a linear β dispersion shape as is the case for the free wave. Therefore, breaking fronts occur closer to the eastern boundary in the north than in the south. Noting the westward decay of breaking front intensity discussed in (4.8), we come to another important conclusion: breaking fronts, if any, are usually stronger towards the north.

5 Summary

Two issues about the waves radiating from the eastern boundary have been investigated. The first addresses the penetration of planetary waves across the southern boundary of a subtropical gyre; the second relates to the breaking of planetary waves.

In the first part of this chapter, we see that the wave penetration across the southern boundary of a subtropical gyre is substantially changed by the zonal variation of the thermocline structure. The zonal variation of the basic thermocline alters both the effective β and the wave orientation kl substantially. Consequently, across a southern boundary, the wave penetration differs for different depths. For an interface near the surface with the eastern boundary depth of H_s satisfying $0 < H_s < 0.5H_c$, part of the waves penetrate into the equatorial region. For the middle depths of $0.5H_c < H_s < H_c$, most waves will be trapped within the subtropical gyre. In contrast, for the deeper depths with $2H_c < H_s$, all waves penetrate southward. (Here $H_c \approx 220$ meters for a model ocean with the width of the Pacific, and $H_c \approx 140$ meters for the width of the Atlantic.)

In the second part of the chapter, the breaking of planetary waves are discussed. We first discussed the free wave breaking. It is found that downwelling breaking occurs for an interface in the upper model ocean ($h < 0.5H$) while upwelling breaking takes place in the deeper model ocean ($h > 0.5H$). All breaking fronts tilt northeast-southwest (β dispersion). The occurrence of the breaking (or the first breaking time) is mainly determined by the speed of the vertical displacement while the strength of the breaking front depends heavily on the amplitude of the disturbance. The intensity of a breaking front or the accompanying thermal wind jet is the same everywhere along the front. For annual and interannual variations along the eastern boundary, breaking can take place within a basin of a realistic width.

Then, the breaking under an Ekman pumping is considered. It is found that the planetary wave breaking is affected significantly by an Ekman pumping and the associated mean flow. In the presence of an Ekman pumping, downwelling breaking, which is caused by an eastern boundary downwelling, is suppressed and the breaking time is delayed; upwelling breaking, which is caused by an eastern boundary upwelling, is enhanced and their times are shortened. The breaking of annual

and interannual disturbances will be significantly altered. In particularly, downwelling breaking will not occur except for interfaces near the surface.

The breaking times and positions are mainly determined by the maximum vertical perturbation speed while the intensity of the breaking front mainly depends on the amplitude of the perturbation. The intensity of a breaking front increases with the amplitude of the forcing, but decreases with the distance from the eastern boundary. The position of breaking fronts are shortened significantly by the two-dimensional mean flow in the northern part. On the other hand, the orientation of a breaking front is overall consistent with the β dispersion tendency. (This is not valid near the southern boundary of a subtropical gyre because a uniform Ekman pumping is used in section 4). Thus, the intensity of a front becomes stronger towards the north.

One should be cautious in applying the theory here to a continuously stratified thermocline. This because we are not sure what in a continuous model an interface in our two-layer model exactly corresponds to (see section 6 of chapter 2).

A Long Rossby Waves in a Two-layer PG Model

In this appendix, we derive the Rossby wave group velocity (2.6) near the southern boundary of a subtropical gyre in the presence of zonal and meridional variations of the mean thermocline. In a two-layer model, the governing equations are

$$(\partial_t + \vec{v_1} \cdot \nabla)u_1 - fv_1 = -p_{1x}, \tag{A.1a}$$

$$(\partial_t + \vec{v_1} \cdot \nabla)v_1 + fu_1 = -p_{1y}, \tag{A.1b}$$

$$\partial_t h_1 + \nabla \cdot (\vec{v_1} h_1) = -w_e, \tag{A.1c}$$

$$(\partial_t + \vec{v_2} \cdot \nabla)u_2 - fv_2 = -p_{2x}, \tag{A.1d}$$

$$(\partial_t + \vec{v_2} \cdot \nabla)v_2 + fu_2 = -p_{2y}, \tag{A.1e}$$

$$\partial_t h_2 + \nabla \cdot (\vec{v_2} h_2) = 0. \tag{A.1f}$$

Here,

$$h_1 + h_2 = H = constant, \quad p_1 - p_2 = -\gamma h_1, \tag{A.1g}$$

where a flat bottom is adopted and γ is the reduced gravity. After neglecting momentum advection, the LPS solution is derived from the steady form of (A.1). The upper layer satisfies

$$fV_1 = P_{1x}, \quad fU_1 = -P_{1y}, \quad \nabla \cdot (\vec{V_1} H_1) = -w_e, \tag{A.2a}$$

where upper case letters are used for the steady basic state. In the vicinity of the southern boundary of a subtropical gyre, a shadow zone prevails and the lower layer basic state is motionless. Thus

$$U_2 = V_2 = 0, \quad H_1 + H_2 = H, \quad P_1 - P_2 = -\gamma H_1. \tag{A.2b}$$

Small perturbations on this basic state are $h_n^* = h_n - H_n, \quad n = 1, 2$ where $h_n^* \ll H_n$. Omitting the stars for the perturbations, the linearized equations for the disturbances are then derived from (A.1) and (A.2) as

$$D_{1t}u_1 + \vec{v_1} \nabla \cdot \vec{V_1} - fv_1 = -p_{1x}, \tag{A.3a}$$

$$D_{1t}v_1 + \vec{v_1} \nabla \cdot \vec{V_1} + fu_1 = -p_{1y}, \tag{A.3b}$$

$$D_{1t}h_1 + \nabla \cdot (\vec{v_1} H_1) = h_1 w_e / H_1, \tag{A.3c}$$

$$D_{2t}u_2 - fv_2 = -p_{2x}, \tag{A.3d}$$

$$D_{2t}v_2 + fu_2 = -p_{2y}, \tag{A.3e}$$

$$D_{2t}h_2 + \nabla \cdot (\vec{v_2} H_2) = 0. \tag{A.3f}$$

where

$$D_{1t} \equiv (\partial_t + \vec{V_1} \cdot \nabla), \quad D_{2t} \equiv \partial_t, \quad and \quad h_1 + h_2 = 0, \quad p_1 - p_2 = -\gamma h_1. \tag{A.3g}$$

Also, we have used $\nabla \cdot \vec{V_1} = w_e / H_1$ in (A.3c). Cross-differentiating (A.3d,e), we obtain

$$\partial_{tt}u_2 + f^2 u_2 = -p_{2xt} - fp_{2y}, \tag{A.4a}$$

$$\partial_{tt}v_2 + f^2 v_2 = p_{2x} - p_{2yt} \tag{A.4b}$$

For lower frequencies concerned here, the ratio of the first term on the RHS to the second term is

$$(\omega / f)^2 \ll 1. \tag{A.5}$$

Therefore, the first terms in (A.4a,b) are neglected to yield

$$f^2 u_2 = -p_{2xt} - fp_{2y}, \tag{A.6a}$$

$$f^2 v_2 = p_{2x} - p_{2yt} \tag{A.6b}$$

This approximation is called geostrophic momentum approximation by Cheng and Philander (1989) in the context of an one-and-a-half-layer model. The upper layer is more complicated due to the mean flow. For the planetary scale basic state, we have

$$f \gg \partial_y U_1, \ \partial_x V_1. \tag{A.7}$$

In addition, we assume that the spatial scales of waves are much shorter than the basic state, which is necessary for WKB wave theory. Thus,

$$\frac{\partial_x U_1}{U_1 \partial_x} \sim \frac{\partial_x V_1}{V_1 \partial_x} \sim \frac{L_{wave}}{L_{mean}} \ll 1. \tag{A.8}$$

This assumption is valid for planetary waves below decadal periods. In the light of (A.7) and (A.8), the upper layer perturbation momentum equations (A.3a,b) can be rewritten as

$$D_{1t}u_1 - fv_1 = -p_{1x}, \tag{A.9a}$$

$$D_{1t}v_1 + fu_1 = -p_{1y}. \tag{A.9b}$$

Similar to the lower layer in (A.6), for disturbances with low frequencies and large scales

$$(\omega/f)^2, (u/fL)^2 \ll 1, \tag{A.10}$$

The geostrophic momentum approximation simplifies (A.9) as

$$f^2u_1 = -D_{1t}p_{1x} - fp_{1y}, \tag{A.11a}$$

$$f^2v_1 = p_{1x} - D_{1t}p_{1y} \tag{A.11b}$$

Substituting (A.6) into (A.3f), and substituting (A.11) into (A.3c), we obtain the equations for the upper and lower layer respectively

$$D_{nt}h_n + J[p_n, 1/Q_n] - \nabla \cdot [D_{nt}\nabla p_n/fQ_n] = s_n, \quad n = 1, 2, \tag{A.12}$$

where $s_1 = h_1 w_e/H_1$, $s_2 = 0$ and $Q_n = f/H_n$ represents the basic state potential vorticity in each layer. Furthermore, the WKB assumption in (A.8) ensures that the third term on the LHS in (A.12) can be approximated as

$$\nabla \cdot [D_{nt}\nabla p_n/fQ_n] \approx D_{nt}\nabla^2 p_n/fQ_n. \tag{A.13}$$

On the other hand, near the southern boundary,

$$V_1 \approx 0, \quad \partial_x H_1 \approx 0, \quad w_e \approx 0. \tag{A.14}$$

With the aid of (A.13),(A.14) and (A.3g), the equations in (A.12) reduce to a closed set in the following

$$(\partial_t + U_1\partial_x)h_1 = -p_{1x}(1/Q_1)_y - (\partial_t + U_1\partial_x)\nabla^2 p_1/(fQ_1), \tag{A.15a}$$

$$\partial_t h_1 + \gamma(1/Q_2)_y h_{1x} + \gamma\nabla^2 h_{1t}/(fQ_2) = p_{1x}(1/Q_2)_y + \nabla^2 p_{1t}/(fQ_2). \tag{A.15b}$$

Assuming the waves of the form $(h_1, p_1) = (h, p)e^{i(kx+ly-\omega t)}$ and by virtue of (A.15), the wave speed $c_p = \omega/k$ satisfies:

$$Ac_p^2 + Bc_p + C = 0, \quad c_p = \omega/k, \tag{A.16a}$$

$$A = K^2[-(\lambda_1 + \lambda_2) + K^2\lambda_1\lambda_2]/\gamma, \tag{A.16b}$$

$$B = -[(1/Q_1)_y + (1/Q_2)_y] + K^2[\lambda_1(1/Q_2)_y + \lambda_2(1/Q_1)_y + U_1(\lambda_1 + \lambda_2)/\gamma] - U_1\lambda_1\lambda_2K^4/\gamma, \tag{A.16c}$$

$$C = [\gamma(1/Q_1)_y + U_1](1/Q_2)_y - K^2\lambda_1U_1(1/Q_2)_y. \tag{A.16d}$$

where $K^2 = k^2 + l^2$ and $\lambda_n = \gamma/(fQ_n) = \gamma H_n/f^2$. Therefore, the dispersion relation is

$$(c_p)_-^+ = [-B_-^+\sqrt{B^2 - 4AC}]/(2A). \tag{A.17}$$

At the long wave limit $K^2 \to 0$, (A.16) indicates that $B > 0$. Thus, "+" sign is adopted for baroclinic mode which is finite at the long wave limit. For waves much longer than the deformation radius (long Rossby waves),

$$K^2(\lambda_1 + \lambda_2) \ll 1. \tag{A.18}$$

tedious algebraic manipulations give rise to the dispersion relation approximated to the second order as

$$c_p = c_{g0} + K^2c_{g1} + O\{[K^2(\lambda_1 + \lambda_2)]^2\}, \tag{A.19a}$$

where

$$c_{g0} = u_B - \beta\gamma H_1(1 - \frac{H_1}{H})/f^2, \quad u_B = H_1U_1/H, \tag{A.19b}$$

$$c_{g1} = \lambda_1\lambda_2\beta(1/Q_1)_y(1/Q_2)_y/[(1/Q_1 + 1/Q_2)_y]^2. \tag{A.19c}$$

Here, c_{g0} gives the non-dispersive part of the wave speed while c_{g1} the dispersive part. For long waves, the dispersion effect is weak and thus appears in the second order. However, it is this weak dispersion that causes the meridional group velocity of long Rossby waves.

In the QG limit where the depths H_n of the basic state have small deviations, the potential vorticities of the basic state is approximated as $Q_n = \frac{f}{H_n(1+\frac{H_{ny}y}{H_n})} \approx \frac{f}{H_n}[1 - \frac{H_{ny}y}{H_n}]$. Accordingly, $Q_{ny} \approx \frac{1}{H_n}[\beta + \frac{U_n}{\lambda_n}]$. It can be shown that (A.19) approaches the long wave limit (to the second order) directly derived from QG equation (e.q. section 11 of chapter 7 in Pedlosky, 1986).

B Propagation of Eastern Boundary Wave Fronts Near the Southern Boundary

As seen in equation (2.6a), the wave front orientation near the southern boundary is essential for the wave penetration across the boundary. For convenience, we will study the eastern boundary wave front (1.6), which is generated by a spin-up (or spin-down). The results also apply to more general cases as discussed below (1.6).

Examples

First, we present some examples of wave front (1.6) in Fig.5.10, where the Ekman pumping is taken to be

$$w_e(f) = W_e(1-f)(f-f_s). \tag{B.1}$$

with the maximum $w_e(f) = -1$ achieved at the middle of the gyre $f = 0.5(f_n + f_s)$. The eastern boundary interface first linearly deepens towards the south and then remains flat

$$h_e(f) = \begin{cases} \frac{2H_s}{f_0-f_s}(f_0-f) & if\ f_0 \geq f \geq (f_0+f_s)/2 \\ H_s & if\ (f_0+f_s)/2 \geq f \geq f_s \end{cases} \tag{B.2}$$

In Fig.5.10a,b and c, H_s is respectively 0, 0.1 and 0.2. Near the southern boundary, the wave front orientation varies and differs from each. In the shallowest case of Fig.5.10a, an anti-β dispersion tendency emerges at the beginning and intensifies as the front propagates westward. If the depth is slightly deeper, Fig.5.10b shows that a β dispersion tendency initially appears and then rapidly changes to an anti-β dispersion. Afterwards, the anti-β dispersion intensifies similar to that in Fig.5.10a. If the layer depth is even deeper, Fig.5.10c shows that the initial β dispersion orientation persists for a long time before it changes to an anti-β tendency. These figures suggest that a wave front initially exhibits a β dispersion orientation and later reverses the tendency. If the layer depth is very shallow, the time for reversing tendency is very short and the position is very close to the eastern boundary. On the contrary, as the layer depth gets deeper, the time for reversing tendency is delayed and the position is further away from the eastern boundary.

The reversing time and position can be estimated as follows. Since we are concentrated on the southern boundary, h_e is taken to be flat such that $h_e = H_s$. The linear Ekman pumping (2.9) is

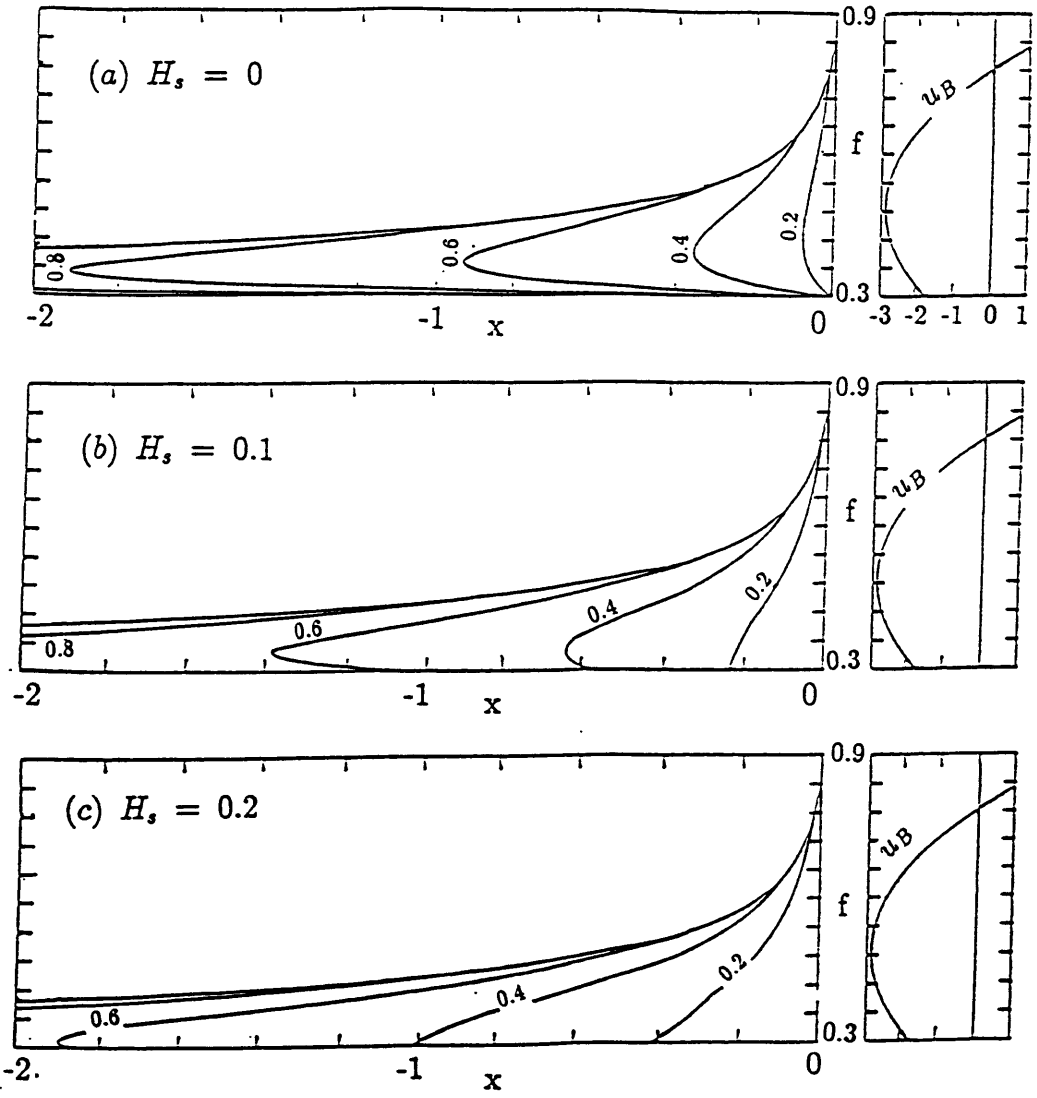

Figure 5.10: Wave front propagation in the presence of different eastern boundary condition. The parabolic Ekman pumping is $w_e(f) = W_e(f_n - f)(f - f_s)$, where the maximum Ekman pumping is -1, $f_n = 1$ and $f_s = 0.3$. All left panels are wave fronts. Solid lines are eastern boundary wave fronts x_F and the dashed lines are outcrop line wave fronts f_F. The right panels are profiles of barotropic zonal flow u_B. a) Singular eastern boundary condition $h_e = H_s = 0$. At the southern boundary, the wave front is stagnant. An anti-β dispersion tendency occurs from the beginning. b)$H_s = 0.1$. c)$H_s = 0.2$. In b) and c), the eastern boundary condition (2.4) is used. The wave fronts first exhibit a β-dispersion tendency. Later, an anti-β dispersion tendency emerges. Western boundaries are set at $x_w = -2$.

used. The $\hat{f}_i$ characteristic solution (the inverse of $\hat{f}$ in (1.3b)) is derived as

$$\hat{f}_i(f,s) = f_s/[1-(1-\frac{f_s}{f})e^{-W_e f_s s}]. \tag{B.3}$$

Substituting these functions into (1.6) and differentiating it yields the slope of the wave front at f_s as

$$\partial_f x_F \mid_{f=f_s} = -X[e^{-f_s W_e t} - 1 - H_s(3+e^{-f_s W_e t})],$$

where $X = -(e^{-f_s W_e t}-1)(1-H_s)/(2W_e f_s^4) > 0$. Initially $-f_s W_e t \ll 1$, the slope indicates that $\partial_f x_F \mid_{f=f_s} \sim 4H_s > 0$. This is the initial β dispersion tendency. Later on, when $-f_s W_e t \to \infty$, it follows that $\partial_f x_F \mid_{f=f_s} \to -\infty$, which is the ultimate strong anti-β dispersion. The reversing time occurs when $\partial_f x_F \mid_{f=f_s} = 0$, at

$$t_{reverse} = \frac{-1}{f_s W_e} ln\left(\frac{3H_s+1}{1-H_s}\right). \tag{B.4a}$$

Inserting (B.4a), (B.3) and (2.9) into (1.6) yields the position of the wave front at the reversing time as

$$x_{reverse} = x_F(f, t_{reverse}) \mid_{f \to f_s} = 4H_s^2/(f^3 W_e). \tag{B.4b}$$

In particular, if $H_s = 0$, we have $t_{reverse} = x_{reverse} = 0$, i.e. the anti-$\beta$ dispersion starts from the beginning. [1]

Physical mechanism for the evolution of the wave front

Physically, the x equation (1.2d)

$$\frac{dx}{ds} = u_B - \frac{h(1-h)}{f^2} \tag{B.5}$$

indicates that the propagation of a wave front is determined by the competition among three mechanisms: the linear β dispersion (f^{-2}), the stratification ($h(1-h)$) and the zonal barotropic flow (u_B). Here we only concentrate on the vicinity of the southern boundary.

First, the linear β dispersion always builds up a β dispersion tendency. Second, the meridional variation of stratification induces an anti-β dispersion on the part of interface in the upper half

[1] In fact, when $h_e = 0$, we can prove from (1.2) that $d^n x/ds^n \mid f = f_s, x = 0 = 0$ for $n = 0, 1, 2....$ Therefore, x_F is stagnant at the southern boundary. This always gives an anti-β dispersion tendency because away from the southern boundary $d^2x/ds^2 = w_e \mid_{z=0} /f^2 < 0$ although $dx/ds|midx = 0 = 0$.

ocean ($h < 0.5$), but does the opposite for the deeper half ocean. This is because, towards the southern boundary, an interface shoals ($h_f > 0$) due to the decreased Ekman pumping (assuming that h_e is flat there). Since $\partial_f h(1-h) = (1-2h)h_f$, it follows that for interfaces in the upper half ocean, the induced equivalent depth $h(1-h)$ and in turn the Rossby wave speed decreases southward. The opposite occurs for the deeper half ocean ($h > 0.5$). Last, the barotropic zonal velocity is also able to change the wave front orientation through the shear. For a subtropical gyre, the zonal velocity usually achieves its maximum westward velocity north of the southern boundary and therefore possesses a cyclonic shear on the southern boundary. One example of u_B profile has been presented on the right panels of Fig.5.10a,b,c. This cyclonic shear near the southern boundary is in favor of an anti-β dispersion.

Initially, (near $x = 0$), both the stratification variation and u_B are weak, for non-vanishing H_s, the wave front exhibits the linear β dispersion effect. This can be clearly seen in (B.5) because

$$\frac{dx}{ds} \mid_{x=0} = -\frac{h_e(1-h_e)}{f^2}.$$

Subsequently, both the meridional variation of stratification and the velocity shear grow rapidly in x and become the two dominant mechanisms for the wave front. (It can be easily proven from the solution (1.3) that $\mid h_f \mid$, $\mid u_B \mid \rightarrow \infty$ as $x \rightarrow -\infty$.) For $h < 0.5$, the two effects enhances each other and quickly overcome the initial linear β dispersion effect to produce a strong anti-β dispersion. For $h > 0.5$, however, these two effects are opposite. It turns out now that the shear effect is slightly larger than the stratification effect and therefore suppresses the initial linear β dispersion to slowly produce a weak anti-β dispersion. In short, initially a wave front exhibits a β dispersion due to the linear β dispersion $C \sim 1/f^2$. Later, the zonal variation of the thermocline structure and mean flow grows to overcome the linear β dispersion and eventually reverse the tendency to an anti-β dispersion.

Finally, one may notice that throughout the above study, we have assumed a meridional eastern boundary and a flat isopycnal h_e near the southern boundary. However, both assumptions may not be true. A northwest-southeast eastern boundary, as in the real North Pacific, or a southward shallowing eastern boundary isopycnal depth will enhance the anti-β dispersion tendency.

Chapter 6
Conclusions

1 Summary and Discussion

In this thesis, we have investigated some basic aspects of a time-dependent ventilated thermocline. The variability considered here is produced by three external forcings: the wind stress (chapter 3), the surface heat flux (chapter 4) and the upwelling along the eastern boundary (chapter 5). The spatial scale that we are interested in is the basin scale while the time scale extends from years to decades.

A two-layer planetary geostrophic model is developed in chapter 2 to simulate a thermocline. The model includes some novel physics which have not been previously fully explored. Above all, it captures the essential feature of ventilation and it is able to account for a time-varying surface temperature. In addition, the model considers the two-dimensional mean flow and thermocline structure; it includes the interaction between the barotropic and baroclinic flows as well as nonlinear Rossby waves; it can also be used to study both annual and decadal forcings. The governing equation is a quasi-linear equation, whose solution can be obtained analytically.

In chapter 3, the effect of a varying wind stress is investigated. Through the study of simple spin-up and spin-down cases, we find that in a shadow zone, the deepening due to the Ekman pumping is mainly balanced by the shallowing due to the westward propagation of planetary waves from the eastern boundary. This is qualitatively in accordance with previous studies. But, in a ventilated zone, the cold advection of subducted water plays the essential role in opposing the Ekman pumping. The very different dynamics also results in very different thermocline variability between the two zones. After a change of Ekman pumping, in the shadow zone, since the baroclinic Rossby wave responds to a changing Ekman pumping slowly (in years to decades), an imbalance emerges between the Rossby wave term and the Ekman pumping, which in turn excites a strong local thermocline variability. However, in the ventilated zone, both the advection and the Ekman

pumping vary rapidly after a barotropic process (about one week) to reach a new steady balance, leaving little thermocline variability.

The evolution of the thermocline also exhibits interesting features. For instance, in a shadow zone, the lower layer is no longer motionless. Instead, when the Ekman pumping intensifies, the lower layer water moves southward in the shadow zone because of the compression of planetary vortex tubes by the anomalous downward Ekman pumping. The associated lower layer circulation consists solely of an anticyclonic gyre. In contrast, when the Ekman pumping weakens, the lower layer water flows towards the north in the shadow zone due to the stretching of planetary vortex tubes by the anomalous upward Ekman pumping. The associated circulation is therefore composed of two counter-rotating gyres with an anticyclonic gyre to the north and a cyclonic gyre to the south.

Furthermore, for a strongly variable Ekman pumping (with the perturbation comparable to the mean), it is somewhat surprising to find that linear solutions are able to approximate the fully nonlinear solution well, particularly for annual forcings. However, the linear solution is strongly influenced by the basic thermocline structure and circulation. The divergent group velocity field, which is mainly caused by the divergent Sverdrup flow field in a subtropical gyre, produces a decay effect on disturbances. The mean thermocline structure also strongly affects the relative importance of the local Ekman pumping and remote Rossby waves. In a shadow zone, local response dominates for a shallow interface, because the effective Ekman pumping is strong and the Rossby wave energy flux is weak. On the contrary, the remote Rossby wave dominates for a deep interface, because the effective Ekman pumping diminishes while the Sverdrup flow still supports a finite Rossby wave energy flux.

In a shadow zone, with a strong decadal forcing, the nonlinearity becomes important, particularly in the western part. The time-mean thermocline which results, becomes shallower than the steady thermocline under the time-mean Ekman pumping. Rather than being zero, now the mean flow is southward. This mean thermocline structure and circulation are mainly caused by nonlinear Rossby waves. For a strong annual forcing, the mean flow in the shadow zone exhibits micro gyres

due to the interaction between the barotropic and baroclinic flows, as found by Dewar (1989). But, the magnitude is very weak.

Chapter 4 investigates the effect on the permanent thermocline by a periodically varying surface temperature or outcrop line, which is presumably caused by a varying surface heat flux. The two layer model is modified by adding an (essentially passive) mixed layer above. The outcrop line is specified during the whole cycle while the mixed layer depth can only be specified during part of the cycle. Some important results are found. First of all, opposite to a surface wind stress, a surface buoyancy flux causes strong variability in the ventilated zone through subducted water while it affects the shadow zone very little.

Secondly, there are two types of buoyancy forced solutions: the non-entrainment solution and entrainment solution. When the outcrop line moves slowly (always less fast than the southward particles) during a strong cooling season, the solutions are non-entrainment solutions. For these solutions, the surface heat flux is mainly balanced by the horizontal advection in the permanent thermocline. The mixed layer depth varies very little such that the mixed layer is never entrained. The time-mean profile is close to the steady thermocline with the time-mean outcrop line. When the outcrop line moves southward faster than the particles during part of a period, the solutions become gravitationally unstable near the outcrop line if the mixed layer depth remains unchanged. To overcome the instability, by deepening the mixed layer depth properly, a convective scheme is developed to entrain the unstable water into the mixed layer and assure the stablity of solutions. The solutions obtained are therefore entrainment solutions. Now, deep vertical convection must occur, because the horizontal advection in the permanent thermocline is no longer strong enough to balance the surface cooling. The mixed layer penetrates rapidly such that water mass is entrained into the mixed layer through the bottom. The time-mean thermocline resembles the steady thermocline with the early spring mixed layer, which supports the suggestion of Stommel (1979).

According to subduction processes, one period is divided into three stages: the seasonally subducting stage, the entraining stage and the subducting stage. Water subducted during the seasonally subducting stage will be re-entrained in the following entraining stage to form the seasonal thermocline. This water has a high potential vorticity because it is formed during the heating

season and therefore possesses strong stratification. The water subducted during the subducting stage will never be re-entrained into the mixed layer and therefore establishes the permanent thermocline. The water has a low potential vorticity which has been built up previously in the mixed layer by mixing (see Woods, 1985). In particular, if the outcrop line moves slowly to force a nonentrainment solution, only the subducting stage exists. Therefore, water always subducts to influence the permanent thermocline.

The local variability in the permanent thermocline is caused by the potential vorticity anomaly of the waters subducted during a subducting stage. With a harmonic migration of the outcrop line, the local interface exhibits a rapid rise and a slow descent, implying a rapid build-up and a slow destruction of the stratification. The variability is most efficiently produced by decadal forcings. At annual frequency, there is very little water subducted into the permanent thermocline each year, causing weak variability.

Finally, in chapter 5, two issues about the waves radiating from the eastern boundary have been investigated. The first is the penetration of planetary waves across the southern boundary of a subtropical gyre; the second mainly concerns with the breaking of planetary waves in the presence of an Ekman pumping and the associated two-dimensional mean flow.

For the first issue, we find that the wave penetration across the southern boundary of a subtropical gyre is substantially changed by the zonal variation of the thermocline structure. First, we show that the meridional group velocity at the southern boundary is determined mainly by the effective β and wave orientation. Then, we see that the zonal variation of the basic thermocline could substantially alter both the effective β and the wave orientation. The result is that, across a southern boundary, the wave penetration differs for interfaces at different depths. For an interface near the surface with the interface depth H_s along the eastern boundary satisfying $0 < H_s < 0.5H_c$, part of the waves penetrate into the equatorial region. Here H_c is a critical depth determined mainly by the width of the basin and the meridional gradient of the Ekman pumping along the southern boundary. For the middle depths of $0.5H_c < H_s < H_c$, most waves will be trapped within the subtropical gyre. In contrast, for the deeper depths with $2H_c < H_s$, all waves penetrate southward. (Here $H_c \approx 220$ meters for a model ocean with the width of the Pacific, and

$H_c \approx 140$ meters for the width of the Atlantic.) In the deep interface case, one may think that the thermocline structure is distorted by the surface Ekman pumping very little. Therefore, the wave propagation is similar to the case without a mean thermocline (Schopf *et. al*, 1981). However, the shallow and middle depths cases are not intuitive.

For the second issue, the breaking of planetary waves are discussed with emphasis on the effect of Ekman pumping and the associated flow on breaking. It is found that the planetary wave breaking is affected significantly by an Ekman pumping and the associated mean flow. In the presence of an Ekman pumping, downwelling breaking is suppressed and the breaking time is delayed; upwelling breaking is enhanced and their times are shortened. The breaking of annual and interannual disturbances will be significantly altered. In particular, downwelling breaking will not occur except for interfaces near the surface. The breaking times and positions are mainly determined by the maximum vertical perturbation speed while the intensity of the breaking front mainly depends on the amplitude of the perturbation. The intensity of a breaking front increases with the amplitude of the forcing, but decreases with the distance from the eastern boundary. The position of breaking fronts are shortened significantly by the two-dimensional mean flow in the northern part. On the other hand, the orientation of a breaking front is consistent overall with the β dispersion tendency (away from the southern boundary of a subtropical gyre).

In short, the variable Ekman pumping dominates the variability in the shadow zone, where the eastern boundary Rossby waves balances the local Ekman pumping to achieve the dynamic balance. On the other hand, the variable surface heat flux dominates the variability in the ventilated zone, where the advection due to the subducted water is a major mechanism to balance the surface heat flux. With a strong cooling, the vertical convection also becomes crucial. In addition, for a variable Ekman pumping, the variability is mainly linear with the disturbance being substantially influenced by the basic thermocline structure. However, for a variable surface temperature or eastern boundary upwelling (or downwelling), the response may present salient nonlinear features.

2 Relevance to Observations

So far, the observations are too poor to allow a comprehensive comparison with the theory here. Nevertheless, some observations available are consistent with the theory.

Thermocline variability in the northern part of a subtropical gyre

Analyses on observations have indicated that the annual response in the northern part of the subtropical gyres in both the North Pacific and the North Atlantic is mainly barotropic while in the southern part the response is mainly baroclinic (Gill and Niiler,1973). Later, observations (Price and Magaard, 1980;1986; White and Saur, 1983) found no signals and very weak signals of interannual baroclinic Rossby waves in the northern part of the subtropic gyre in the North Pacific and the North Atlantic, respectively. In contrast, in the southern parts of the subtropical gyres in both oceans, clear baroclinic Rossby wave signals are identified at annual and interannual frequencies.

These observations are consistent with the theory in chapter 3 about the effect of a varying Ekman pumping. The thermocline in the northern part of a subtropical gyre is mainly occupied by a ventilated zone, where the advection from the subducted water tends to balance the local Ekman pumping. As a result, little baroclinic Rossby wave exists. On the contrary, the thermocline in the southern part of a subtropical gyre is mostly occupied by a shadow zone, where advection plays little role. Baroclinic Rossby waves and local Ekman pumping dominate the response. Consequently, the activity of baroclinic waves is strong. Therefore, the different dynamic balance between a ventilated zone and a shadow zone, as found in chapter 3, may offer an explanation for the lack of baroclinic signals in the northern parts of the subtropical gyres. Furthermore, in chapter 4 which considers the effect of a varying surface temperature, we see that at interannual time scales, the variable surface heat flux is able to force strong baroclinic variability in the ventilated zone through the advection of the subducted waters from the mixed layer. This suggests that the variability in the northern part of a subtropical gyre may be forced primarily by the surface heat flux through subduction, rather than by the local Ekman pumping and Rossby waves.

If should be noticed that the β dispersion effect may also be a mechanism for the lack of baroclinic signals in the northern part of a subtropical gyre. This is so because the β dispersion effect make eastern boundary Rossby waves radiate southward. It seems to me that for annual waves, the β dispersion effect is probably important, becasue of the relatively short wave length. For interannual or decadal waves, the wave length is long. The scaling analysis in section 2 of chapter 5 (see Eq. (2.5)) shows that in a subtropical gyre, the southward advection may be more important than the effect of β dispersion. Therefore, our results here seem to be applicable. In other words, now the southward advection is the main mechanism for the lack of baroclinic signals in the northern part of a subtropical gyre. **Mode water variability**

The mode water is believed to be formed mainly by subduction in response to strong surface cooling in the northwestern part of a subtropical gyre (McCartney, 1982). Therefore, it is a good example to test the theory about the effect of surface heat flux. Talley and Raymer (1982) found that the eighteen degree mode water in the North Atlantic does have small pulses of potential vorticity at the annual period. In addition, the mode water has been observed to be not very sensitive to the strong surface annual heat flux variation. Relatively significant changes arise at interannual time scales. These observations are in accordance with the theory in chapter 4.

The frontal structures

There have been some observations of planetary frontal structures. The Subtropical Front is trapped near the surface and is accompanied by a northward baroclinic jet. The front found by McWilliams *et. al* (1983) extends very deep and is accompanied by a southward baroclinic jet. These are consistent with our theory in chapter 5. A downwelling breaking front, which is accompanied by a northward thermal wind jet, is trapped near the surface. A upwelling breaking front, which is accompanied by a southward thermal wind jet, can extend very deep. All observed fronts have slopes consistent with β dispersion tendency i.e. northeast-southwest. Finally, one should note that without a statistically steady eastern boundary (or localized wind or diabatic) forcing, it is unlikely that the temporal breaking phenomena discussed here are mainly responsible for the observed statistically stationary fronts such as the Subtropical Front. However, it is possible that some temporal behavior and finer structures observed within these mean fronts are produced by

the breaking of (more general) planetary waves which are caused not only by the eastern boundary upwelling or downwelling but also by local wind or buoyancy flux. The breaking can be caused mainly by the nonlinear steepening of a Rossby wave, which propagates in the presence of a smooth thermocline, as discussed in chapter 5. It is also possible that a breaking is produced by another mechanism which is not investigated in the thesis. That is the effect on nonlinear Rossby waves by the mean thermocline structure associated with a mean frontal structure (which is formed by some other mechanisms.) In this case, the breaking occurs because the rapid spatial variation of the basic thermocline may produce a strong variation of local Rossby wave speed within the mean front, which in turn causes breaking of the nonlinear Rossby waves.

3 Future Work

Much work is needed for a better understanding of the time-varying thermocline. One of the most important is to couple an active mixed layer with the permanent thermocline. This work is difficult but challenging because the mixed layer dynamics is not fully understood, particularly at interannual and decadal climate scales.

In addition, a two-and-a-half-layer thermocline model is particularly attractive to eliminate artificial features due to the flat bottom in both the wind forcing and surface buoyancy forcing cases.

It has been emphasized in the thesis that the thermocline variability differs dramatically between a shadow zone and a ventilated zone. In a shadow zone, Ekman pumping and Rossby waves dominate, while in a ventilated zone, surface buoyancy flux and advection dominate. It is important to test this conclusion in the presence of a more complex thermocline structure. This test is difficult for observations. One reason is that it is diffcult to separate the variability caused by the Ekman pumping from that caused by the surface buoyancy flux. (There may be other mechanisms.) However, a general circulation model seems to be very proper for the test. We can carry experiments by varying only the Ekman pumping to test the variability caused by the Ekman pumping. In this case, the theory here says that the thermocline variability in the shadow zone should be stronger than in the ventilated zone. We can also vary only the surface buoyancy flux to test the variability

produced by the surface buoyancy flux. In this case, the theory here suggests that the variability is stronger in a ventilated zone than in a shadow zone. In particular, a coarse grid model is perhaps enough because our theory does not take into account the effect of eddies and instabilities.

References

Anderson, D.L.T and A.E. Gill, 1975: Spin-up of a stratified ocean, with applications to upwelling; *Deep-Sea Research*, **22**, 583–596

Anderson, D.L.T and P.D.Killworth, 1979: Nonlinear propagation of long Rossby waves; *Deep-Sea Research*, **26**, 1033–1050

Barnett,T.P., 1983:Long-term changes in dynamic height. *Journal of Geophysical Research*, **88**(C14), 9542–9552

Charney, J.G. and G.R. Flierl, 1981: Oceanic analogues of large-scale atmospheric motions; In *Evolution of Physical Oceanography*, ed. B.A. Warren and C. Wunsch, pp. 504–548

Cheng P. and S.G.H.Philander, 1989: Rossby wave packets in baroclinic mean currents. *Deep-Sea Research*, **36**, No.1. 17–37.

Cox, M. D. and K. Bryan, 1984: A numerical model of the ventilated thermocline. *Journal of Physical Oceanography*, **14**, 674-687

Cox, M. D. , 1985: An eddy resolving numerical model of the ventilated thermocline. *Journal of Physical Oceanography*, **15**, 1312-1324

Cushman-Roisin, B., 1984: On the maintenance of the Subtropical Front and its associated countercurrent. *Journal of Physical Oceanography*, **14**, 1179-1190.

Dewar,W.,P.B.Rhines and W.R.Young, 1984: The nonlinear spinup of the ocean circulation; *Geophys. Astrophys. Fluid Dyn.*,**30**,169–197

Dewar, W., 1987: Planetary Shock Wave; *Journal of Physical Oceanography*,**17**, 470–482.

——, 1989: A theory of time-dependent thermocline ;*Journal of Marine Research*, **47**, 1–31.

Emery, W.J. and L. Magaard, 1976: Baroclinic Rossby waves as inferred from temperature fluctuations in the Eastern Pacific. *Journal of Marine Research*, **34**, 365–385

Emery, W.J., 1983: On the geographical variability of the upper level mean and eddy fields in the North Atlantic and North Pacific.*Journal of Physical Oceanography*,**13**, 269–290.

Emery, W.J., W.G.Lee and L. Magaard, 1984: Geographic and seasonal distributions of Brunt-Väisälä frequency and Rossby radii in the North Pacific and North Atlantic. *Journal of Physical Oceanography*, **14**, 294–317.

Gill, A.E. and P.P.Niiler, 1973: The theory of the seasonal variability in the ocean. *Deep-Sea Research*, **20**, 141–177.

Gill,A.E. and J.S.Turner, 1976. A comparison of seasonal thermocline models with observation. *Deep-Sea Research*,**23**,391-401.

He, Y. and W.B. White, 1987:Interannual variability of the Kuroshio frontal structure along its western boundary in the North Pacific Ocean associated with the 1982 ENSO event. *Journal of Physical Oceanography*, **17**,1494–1506.

Huang, R.X. , 1989: The generalized eastern boundary conditions and the three-dimensional structure of the ideal fluid thermocline. *Journal of Geophysical Research,94*, 4855-4865

Kang, Y.Q. and L. Magaard, 1980: Annual baroclinic Rossby waves in the Central North Pacific. *Journal of Physical Oceanography*, **10**, 1159–1167.

Keffer, T., 1985: The ventilation of the world's oceans: maps of the potential vorticity field. *Journal of Physical Oceanography*, **15**, 509-523

Kessler, W., 1989: Observations of long Rossby waves in the Northern Tropic Pacific. *NOAA Technical Memorandum.* ERL., PMEL-86, 169 pp.

Killworth,P., 1979: On the propagation of stable baroclinic Rossby waves through mean shear flow. *Deep-Sea Research*, **26A**, 997–1031.

Kraus E.B. and J.S.Turner, 1967. A one-dimensional model of the seasonal thermocline. II. The general theory and its consequences. *Tellus*, **19**, 98-105

Levine, E. R., and W. B. White, 1981. Large-scale synoptic thermal fronts in the mid-latitude North Pacific from 1976-1978. *JGR*, **86**, 6567-6579

Levitus,S., 1982: Climatological atlas of the world ocean; *NOAA Prof. Pap.*, No.**13**, [U.S. Govt. Printing Office], 173 pp.

——-, 1988: Ekman volume fluxes for the would ocean and individual ocean basins; *Journal of Physical Oceanography*, **18**, 274–279.

Liu, Z., J. Pedlosky, D. Marshall, T. Warncke, 1991: A note on the feedback of the Rhines-Young pool on the ventilated thermocline. *Journal of Physical Oceanography*, submitted.

Luyten,J.R., J.Pedlosky and H.Stommel, 1983: The ventilated thermocline; *Journal of Physical Oceanography,* **13**, 292–309.

Luyten J. and H. Stommel, 1986: Gyres driven by combined wind and buoyancy flux. *Journal of Physical Oceanography*, **16**, 1551-1560.

Marshall J. and G. Nurser, 1991: A continuously stratified thermocline model incooperating a mixed layer with variable thickness and density. *Journal of Physical Oceanography*, **21**, (Nov. issue), in press

McCartney, M. S. , 1982: The subtropical recirculation of Mode Waters. *Journal of Marine Research*, **40 (Suppl.)**, 427–464.

McCreary, J.P., 1976: Eastern tropical ocean response to changing wind systems, with application to El Nino. *Journal of Physical Oceanography*, **6**, 632–645.

McWilliams, J.C., E.D. Brown, H.L.Bryden, C.C.Ebbesmeyer, B.A.Elliott, R.H. Heinmiller, B. Lien Hua, K.D.Leaman, E.J.Lindstrom, J. Luyten, S.E.McDowell, W.Breckner Owens, H.Perkins, J.F.Price, L.Regier, S.C.Riser, H.T.Rossby, T.B.Sanform, C.Y,Shen, B.A.Taft, and J.C. Van Leer, 1983. The local dynamics of eddies in the western North Atlantic. *Eddies in Marine Science*, A.R.Robinson, Ed.,Springer-Verlag, 92-113.

Meyers, G., 1979: On the annual Rossby wave in the tropic North Pacific Ocean. *Journal of Physical Oceanography*, **9**, 664–674.

———, 1975: Seasonal variation in transport of the Pacific North Equatorial Current relative to the wind field. *JPO*,**5**, 442–449

Niiler,P.P. and E.B.Kraus, 1977. One-dimensional models. in *Modeling and Prediction of the Upper Layers of the Oceans*, edited by E.B.Kraus. pp.143-172. Pergamon, New York

Niiler, P.P. and R. W. Reynolds, 1984. The three-dimensional circulation near the Eastern North Pacific Subtropical Front. *Journal of Physical Oceanography*, **14**, 217-230

Pedlosky,J., 1983: Eastern boundary ventilation and the structure of the thermocline; *Journal of Physical Oceanography*, **13**, 2038–2044.

—— and W.R.Young, 1983: Ventilation, potential vorticity homogenization and the structure of ocean circulation; *Journal of Physical Oceanography*, **13**, 2020–2037.

——, W. Smith and J.R. Luyten, 1984: On the dynamics of the coupled mixed-layer-thermocline system and the determination of the oceanic surface density; *Journal of Physical Oceanography*, **14**, 1159–1171.

Pedlosky, J., 1986. The buoyancy and wind-driven ventilated thermocline. *Journal of Physical Oceanography*, **16**, 1077-1087.

Pedlosky,J. and P.Robbins, 1991. The role of finite mixed-layer thickness in the structure of the ventilated thermocline. *Journal of Physical Oceanography*, **21**, 1018-1031

Price, J.M. and L. Magaard, 1980: Rossby wave analysis of the baroclinic potential energy in the upper 500 meters of the North Pacific. *Journal of Marine Research*, **38**, 249–264.

———, 1983: Rossby wave analysis of subsurface temperature fluctuations along the Honolulu–San Francisco great circle. *Journal of Physical Oceanography*, **13**, 258–268.

———, 1986: Interannual baroclinic Rossby waves in the Mid-latitude North Atlantic. *Journal of Physical Oceanography*, **16**, 2061–2070.

Qiu B. and T. M. Joyce, 1991: Interannual variability in the mid- and low-latitude western North Pacific. *Journal of Physical Oceanography*, submitted.

Rhines,P.B. and W.R.Young, 1981: A theory of the wind-driven circulation I. Mid-ocean gyres. *Journal of Marine Research*, **40,(Suppl.)**, 559–596.

Rhines,P.B., 1986: Vorticity dynamics of the oceanic general circulation; *Ann. Rev. Fluid Mech.*, **18**, 433–447.

Roemmich, D. and C. Wunsch, 1984: Apparent changes in the climatic state of the deep North Atlantic Ocean. *Nature*, **307** (5950), 447–450.

Roden, G.L., 1976: On the structure and prediction of oceanic fronts. *Nav. Res. Rev.* , **29**(3), 18-35.

——-, 1977: On long-wave disturbances of dynamic height in the North Pacific. *Journal of Physical Oceanography*, **7**, 41–49.

——-, 1980. On the subtropical frontal zone north of Hawaii During winter. *Journal of Physical Oceanography*, **10**, 342-362,

Schopf, P., D. Anderson and R. Smith, 1981: Beta-dispersion of low-frequency Rossby waves; *Dynamics of Atmospheres and Oceans.*, **5**, 187–214.

Stommel H. and F. Schott, 1977: The β-spiral and the determination of the absolute velocity field from oceanographic station data. *Deep-Sea Research*, **24** , 325-329

Stommel, H., 1979: Determination of watermass properties of water pumped down from the Ekman layer to the geostrophic flow below; *Proceedings of the National Academy of Sciences, U.S.*, **76**, 3051–3055.

Tabara, B.,B.Thomas and D. Ramsden, 1986: Annual and interannual variability of steric sea level along line P in the Northeast Pacific Ocean. *Journal of Physical Oceanography*, **16**, 1378–1398.

Talley, L.D. and M.E.Raymer, 1982: Eighteen degree water variability. *Journal of Marine Research*,**40**, Suppl., 757–775.

Talley, L.D. and W.B. White, 1987: Estimates of time and space scales at 300 meters in the Mid-latitude North Pacific from the TRANSPAC XBT program. *Journal of Physical Oceanography*, **17**, 2168–2188.

Talley, L.D. , 1988: Potential vorticity distribution in the North Pacific. *Journal of Physical Oceanography*, **18**, 89-106

Turner J.S. and E.B.Kraus, 1967. A one-dimensional model of the seasonal thermocline: I. A laboratory experiment and its interpretation. *Tellus*, **19**, 88-97

Veronis G. and H. Stommel, 1956: The action of variable wind stress on a stratified ocean. *Journal of Marine Research*,**15**, 43–75 .

Wang,L.P., 1990. The dynamical effect of the mixed-layer on the interior ideal fluid thermocline. (manuscript)

Warren B.A., 1972. Insensibility of subtropical mode water characteristics to meteorological fluctuations. *Deep-Sea Research*, **19**, 1-20

White, W.B., 1977: Secular variability in the baroclinic structure of the interior North Pacific from 1950–1970. *Journal of Marine Research*,**35**, 587–607.

———, 1978: A wind-driven experiment of the seasonal cycle of the main thermocline in the interior mid-latitude North Pacific. *Journal of Physical Oceanography*, **8**, 818–824.

———,1983:Westward propagation of short-term climatic anomalies in the Western North Pacific Ocean from 1964-1974.*Journal of Marine Research*,**41**,113-125

White, W.B. and J.F. Saur, 1981: A source of annual baroclinic waves in the eastern subtropical North Pacific. *Journal of Physical Oceanography*, **11**, 1452–1462.

———, 1983: Sources of interannual baroclinic waves in the Eastern Subtropical North Pacific. *Journal of Physical Oceanography*, **13**, 531–544.

White, W and S. Tabara, 1987: Interannual westward-propagating baroclinic long-wave activity on line P in the Eastern Mid-latitude North Pacific. *Journal of Physical Oceanography*,**17**, 385-396

Woods, J.D., 1985: Physics of thermocline ventilation; *Coupled Atmosphere-Ocean Models*, J.C.J.Nihoul, ed., Elsevier.

Wunsch, C., 1991: Decade-to-century changes in the ocean. *Manuscript.*

Wyrtki, K. and J. Wenzel, 1984: Possible gyre–gyre interaction in the Pacific Ocean. *Nature*, **309**(5968), 538–540.

4523-49